

Theoretische Physik

Pattern Formation in Driven Thin Layers of Simple and Complex Liquids

Inaugural-Dissertation
zur Erlangung des Doktorgrades
der Naturwissenschaften im Fachbereich Physik
der Mathematisch-Naturwissenschaftlichen Fakultät
der Westfälischen Wilhelms-Universität Münster

vorgelegt von
Markus Wilczek
aus Höxter

2016



Dekan: Prof. Dr. Michael Klasen

Erster Gutachter: Prof. Dr. Uwe Thiele

Zweiter Gutachter: Prof. Dr. Andreas Heuer

Tag der mündlichen Prüfung: _____

Tag der Promotion: _____

Kurzzusammenfassung

Diese Arbeit modelliert und analysiert Strukturbildungsphänomene in drei Systemen, in welchen dünne Schichten einfacher und komplexer Flüssigkeiten auf festen Substraten auftreten. Im Speziellen werden Flüssigkeitsschichten unter dem Einfluss lateraler Kräfte betrachtet, welche die Systeme aus dem Gleichgewicht treiben. In dieser theoretischen Arbeit werden die Systeme durch verschiedene Dünnschichtmodelle und ein erweitertes Cahn–Hilliard-Modell modelliert. Diese lassen sich alle als Kombination einer Gradientendynamik, die von einer zu Grunde liegenden freien Energie beherrscht wird, und zusätzlichen Triebkrafttermen formulieren.

Das erste untersuchte System ist der Langmuir–Blodgett-Transfer, welcher ein geläufiges Verfahren darstellt, um monomolekulare Schichten amphiphiler *Surfactant*-Moleküle von einem flüssigen Bad auf ein festes Substrat zu übertragen. Aufgrund der Möglichkeit, dass während des Transfers ein inhomogener Phasenübergang der *Surfactant*-Schicht auftritt und regelmäßige Streifen- oder Gittermuster auf einer Mikrometerskala erzeugt werden, besteht ein breites Interesse an diesem Verfahren. Aus experimenteller Sicht sind dabei Methoden erstrebenswert, um die Qualität, d. h. die Regelmäßigkeit und Reproduzierbarkeit, der Muster zu verbessern. Zu diesem Zweck werden in dieser Arbeit zusätzliche Kontrollmöglichkeiten für den Langmuir–Blodgett-Transfer untersucht. Mit einem erweiterten Cahn–Hilliard-Modell wird der Einfluss von Substraten mit streifenförmigen Vorstrukturierungen unterschiedlicher Größe und Orientierung auf die Strukturbildung während des Langmuir–Blodgett-Transfers eingehend untersucht. Es treten *locking*-Effekte (zu Deutsch etwa *Einrasteffekte*) auf, durch welche die Muster der periodischen Vorstruktur folgen können. Dies führt zu verschiedenen einfachen und komplexen Mustern und kann zur umfassenden Kontrolle der Musterbildung genutzt werden. Speziell können die Wellenlänge und Orientierung der Muster kontrolliert werden, was sich auch in Experimenten nachweisen lässt. Weiterhin werden in Experimenten auch komplexe gebogene Muster beobachtet. Um solche theoretisch zu charakterisieren und zu erklären, wird ein zweikomponentiges Dünnschichtmodell genutzt. Dieses berücksichtigt auch die Dynamik der Flüssigkeitsschicht, um den Langmuir–Blodgett-Transfer im Falle von Vorstrukturierungen zu beschreiben, welche die Benetzbarkeit des Substrates verändern. Neben der Möglichkeit, vorstrukturierte Substrate zu verwenden, werden zwei weitere Kontrollmechanismen in direkten numerischen Simulationen untersucht: Eine zeitlich modulierte Transfergeschwindigkeit sowie eine modulierte Meniskusposition bewirken ähnliche *locking*-Effekte wie vorstrukturierte Substrate. Damit sind alle drei Möglichkeiten gleichermaßen als Kontrollmethoden für den Langmuir–Blodgett-Transfer geeignet. Die beiden letzteren haben jedoch den Vorteil, keine Veränderungen der Substrate vorauszusetzen, wodurch sie einfacher und günstiger umsetzbar sind als Vorstrukturierungen.

Im zweiten Teil dieser Arbeit wird die Dynamik eines Flüssigkeitsmeniskus untersucht, welcher sich ausbildet, wenn ein festes Substrat aus einer einfachen partiell benetzenden Flüssigkeit gezogen wird. Dabei kann sich ein statischer Meniskus ausbilden, wenn sich die auf ihn wirkenden Kräfte ausgleichen. Zu diesen gehören die von der Oberflächenspannung herrührende Kapillarkraft, die Interaktion der Flüssigkeit mit dem festen Substrat, resultierend in der Benetzbarkeit, sowie die Reibungskraft am bewegten Substrat. Durch ein inhomogenes Sub-

strat, welches beispielsweise streifenförmig vorstrukturiert ist, kann dieses Kräftegleichgewicht gestört und eine zeitperiodische Dynamik des Meniskus ausgelöst werden. Mit einer Kombination von direkten numerischen Simulationen und numerischer Pfad-Kontinuierung für ein Dünnschichtmodell werden sowohl stationäre als auch zeitlich periodische Meniskusverformungen untersucht, welche für Anwendungen mit komplexen Flüssigkeiten, wie dem Langmuir-Blodgett-Transfer, eine wichtige Rolle spielen können. Weiterhin wird ein Parameterbereich identifiziert, in welchem bereits ohne eine Vorstruktur streifenförmige Flüssigkeitsablagerungen erzielt werden können.

Im dritten Teil dieser Arbeit werden Flüssigkeitstropfen betrachtet, die auf einem geneigten Substrat rutschen. Die gesamte Bifurkationsstruktur wird mit einer zweidimensionalen numerischen Pfad-Kontinuierungsmethode analysiert, welche durch direkte numerische Simulationen für zeitlich periodische Zustände ergänzt wird. Ein besonderes Augenmerk wird dabei auf die sogenannte *pearling*-Instabilität gelegt, welche für das Aufbrechen eines einzelnen Tropfens in kleinere Tropfen sorgen kann. Wir identifizieren die in diesen Prozess involvierten Bifurkationen und das daraus resultierende zeitabhängige Verhalten in Abhängigkeit von dem Neigungswinkel des Substrates. Wenn man eine Reihe solcher instabiler Tropfen betrachtet, kann man periodische Aufbrech- und Verschmelzungszyklen beobachten, welche auch eine Periodenverdopplungsrouten hin zu chaotischem Verhalten aufweisen können, wenn der Neigungswinkel des Substrates verändert wird. Im Anschluss wird die Betrachtung auf große Ensembles rutschender Tropfen auf räumlich weit ausgedehnten Substraten erweitert und die Vergrößerung hin zu größeren Tropfen beim gemeinsamen Rutschen untersucht. Das Rutschen beschleunigt den Vergrößerungsprozess stark, da es einen sehr schnellen Massentransport darstellt, der Verschmelzungsprozesse erleichtert. Dem fortlaufenden Verschmelzen der Tropfen wirkt die *pearling*-Instabilität entgegen, welche oberhalb eines gewissen, neigungswinkelabhängigen Tropfenvolumens zum Aufbrechen der Tropfen führt. Das Wechselspiel von Verschmelzung und Aufbrechen der Tropfen kann den Vergrößerungsprozess stoppen. Die resultierenden Effekte werden anhand verschiedener Maße quantitativ untersucht, wie der zeitlichen Entwicklung der Tropfenzahl und der Verteilungsfunktion der Tropfenvolumina. Diese Erkenntnisse über Ensembles von Tropfen werden mit Stabilitätseigenschaften einzelner Tropfen verknüpft, welche durch numerische Pfad-Kontinuierung erlangt werden. Letztlich werden die gewonnenen Informationen dazu genutzt, ein statistisches Modell für die Verteilungsfunktion der Tropfenvolumina herzuleiten. Dieses erfasst trotz seiner Einfachheit die Hauptaspekte der kollektiven Dynamik von rutschenden und zugleich vergrößernden Tropfen.

Abstract

This thesis models and analyzes pattern formation phenomena in three systems that involve thin layers of simple and complex liquids on solid substrates. In particular, liquid layers are studied which are subject to lateral forces that drive the systems out of equilibrium. In this theoretical work, the systems are modeled using different thin film models and an augmented Cahn–Hilliard model, which can all be formulated as a combination of a *gradient dynamics*, which is governed by the gradient of an underlying free energy, and additional driving terms.

The first investigated system is the process of Langmuir–Blodgett transfer, a well-known technique to transfer monomolecular layers of amphiphilic (surfactant) molecules from a liquid bath onto solid substrates. A broad interest in this method stems from the fact, that the surfactant layer can undergo a spatially inhomogeneous phase transition during the transfer, resulting in regular stripe or lattice patterns on the micrometer scale. From an experimental point of view, methods are desirable to further improve the quality, i.e., the regularity and reproducibility, of the patterns. To this aim, we examine additional control possibilities. Using an augmented Cahn–Hilliard model, the influence of prestructured substrates on the pattern formation in the Langmuir–Blodgett transfer is extensively studied for differently sized and oriented stripe-like prestructures. It is found that the occurring locking effects lead to various simple and complex patterns and can be used to exert considerable control over the pattern formation process. In particular, the wavelength and orientation of the patterns can be effectively tuned, which can also be verified experimentally. In addition, complex bent stripe patterns can be observed in experiments. To characterize and explain these patterns theoretically, a two-component thin film model that also accounts for the dynamics of the liquid layer is employed to describe the Langmuir–Blodgett transfer with prestructures that change the wettability of the substrate. Besides the use of prestructured substrates, two further control mechanisms are explored. In direct numerical simulations, a temporally modulated transfer velocity as well as a modulated meniscus position are found to induce similar locking effects as a prestructured substrate. Therefore, all three approaches are similarly suited as a control method for the Langmuir–Blodgett transfer. However, the latter two have the advantage of not involving any alterations of the substrate, indicating a simpler and less expensive control mechanism as compared to prestructures.

In the second part of the thesis, the dynamics of a liquid meniscus is studied, which evolves when a solid substrate is withdrawn from a simple partially wetting liquid. A static meniscus can form if the forces balance that act on it. They comprise the capillary force stemming from surface tension, the wettability of the substrate arising from solid-liquid interactions and the viscous drag resulting from the movement of the substrate. In the case of an inhomogeneous substrate, which is, e.g., prestructured with a stripe-like pattern, this force balance can be disturbed, leading to a meniscus that exhibits a time-periodic dynamics. Using a combination of direct numerical simulations and numerical path continuation techniques for a thin film model, both stationary and time-periodic meniscus deformations are investigated, which can play an important role in applications involving complex liquids, like the Langmuir–Blodgett transfer. Furthermore, a parameter regime is identified, in which even without a prestructure

a stripe-like liquid deposition can be achieved.

In the third part of the thesis, liquid drops sliding down an inclined substrate are considered. The overall bifurcation structure is analyzed using a two-dimensional numerical path continuation technique, which is augmented by direct numerical simulations for time-dependent states. A special emphasis is put on the so-called pearling instability which forces a drop to split into two smaller drops. The bifurcations involved in this process are identified and the resulting time-dependent behavior is studied in dependence on the inclination angle. When considering a train of such unstable drops, one can observe periodic break-up and coalescence cycles, which can even exhibit a period doubling route to chaos when changing the inclination angle of the substrate. The scope is then widened to large ensembles of drops on widely extended spatial domains and their coarsening dynamics when collectively sliding down an inclined substrate. The sliding greatly accelerates the coarsening process, as it enables a very fast way of mass transport via the translation of drops, facilitating their coalescence. The ongoing coalescence is counteracted by the pearling instability active above a certain, inclination-dependent drop volume that forces a fragmentation of the drops into smaller ones. The interplay of coalescence and fragmentation can lead to a ceasing of the coarsening. These effects are quantitatively studied using different measures, such as the temporal evolution of the number and the volume distribution of the drops. These findings on drop ensembles are connected to stability properties of single drops obtained by numerical continuation techniques. Finally, this information is employed to develop a statistical model for the drop volume distribution. Despite its simplicity, this model captures the main features of the collective dynamics of sliding and coarsening drops.

Contents

Kurzzusammenfassung	iii
Abstract	v
Contents	viii
1 Introduction	1
1.1 The Langmuir–Blodgett Transfer	2
1.2 Driven Thin Layers of Simple Liquids	5
1.3 Outline of this Thesis	5
2 Mathematical Modeling	7
2.1 The Thin Film Equation	8
2.1.1 The Lubrication Approximation	9
2.1.2 The Disjoining Pressure	11
2.1.3 The Non-dimensional Thin Film Equation	13
2.1.4 Lateral Boundary Conditions	14
2.2 Gradient Dynamics Formulation	16
2.2.1 The Thin Film Equation as Gradient Dynamics	16
2.2.2 Gradient Dynamics for Multiple Coupled Order Parameter Fields	18
2.2.3 Gradient Dynamics of a Surfactant Covered Liquid Layer	19
2.2.4 Gradient Dynamics of a Thin Solution Layer	22
2.3 The Cahn–Hilliard Equation for Langmuir–Blodgett Transfer	24
2.4 Modeling of Prestructured Substrates	25
3 Numerical Treatment	29
3.1 Spatial Discretization and Approximation of Derivatives	29
3.1.1 The Finite Difference Method	30
3.1.2 The Finite Element Method	32
3.2 Time Stepping Methods	33
3.3 Practical Implementations	36
3.4 Continuation Methods	37
4 Controlling Pattern Formation in Langmuir–Blodgett Transfer	41
4.1 Langmuir–Blodgett Transfer onto Homogeneous Substrates	41
4.2 Control through Prestructured Substrates	45
4.2.1 Comparison to Experimental Results	50
4.2.2 Complex Bent Structures due to Prestructured Substrates	54
4.3 Control through a Time-periodic Forcing	56

5	Dynamics of a Dragged Meniscus	63
5.1	Bifurcation Diagrams for Homogeneous Substrates	65
5.2	Dynamics of a Dragged Meniscus on Heterogeneous Substrates	69
5.3	Pattern Formation on Homogeneous Substrates	75
6	Dynamics of Sliding Drops	79
6.1	Individual Sliding Drops	79
6.2	Collective Behavior of Sliding Drops	90
6.2.1	Coarsening Dynamics in Fourier Space	92
6.2.2	Coarsening Dynamics from an Ensemble View	95
6.2.3	Statistical Model for the Drop Volume Distribution	100
7	Summary and Conclusion	109
	List of Publications	113
	List of Figures	115
	Bibliography	117

1 Introduction

Pattern formation phenomena are ubiquitous in the world. Numerous examples can be found both in nature, e.g., in patterned animal skins [KS09], stripe-like sand ripples [Ayr10] or dendritic patterns formed by bacterial colonies [BJST⁺94], as well as in controlled man-made environments, like, e.g., in chemical reactions [ZGP93] or nonlinear optical resonators [SSM03]. These phenomena cover an enormous range of spatial and temporal scales [CH93], ranging from large scale effects like roll patterns of clouds [HJ93] over vegetation patterns occurring in semiarid regions of the world [Kla99] to microscopic stripes created in Langmuir–Blodgett transfer experiments [GCF00]. In general, these complex phenomena emerge from the interplay of many small entities, whose overall dynamics cannot be simply derived from the individual interactions of the entities with each other. *Self-organization* occurs on scales much larger than the typical time and length scales of individual entities. This leads to, e.g., millimetric spatio-temporal patterns in the famous chemical Belousov–Zhabotinsky reaction where the interacting molecules have a size below a nanometer [ZGP93] or vegetation patterns of the size of tens to hundreds of meters where the individual plants are smaller than one meter [vHMSZ01]. Self-organization also has to be distinguished from the concept of self-assembly, where the occurring patterns or structures typically are a direct consequence of the individual entities’ tendency towards energetic minima [WG02].

Besides a thorough understanding of the pattern forming mechanisms in such systems, a long-standing field of interest is influencing and in particular controlling the pattern formation. Apart from the simple tuning of system parameters, various control mechanisms have been developed. For instance, the concept of a *temporal forcing* builds on the theory of synchronization [PRK03]. Similar to, e.g., two coupled pendulums, one can expect that the temporal behavior of a certain system can be *synchronized* to an external oscillatory forcing for a sufficiently strong coupling. In this context, *synchronized* does not necessarily imply that the dynamics of the system have to follow the external forcing one-to-one, but rather that a fixed relation between the system dynamics and the external forcing emerges. Analogously, the concept of synchronization can be applied to a spatially extended pattern forming system using a *spatial forcing*, i.e., subjecting the spatially extended system to a certain spatially inhomogeneous influence. In a photosensitive chemical reaction, for instance, this could be a stripe-like illumination [DBA⁺11]. Other examples are an inhomogeneous irrigation used in the context of a vegetation pattern or a modulated system height employed in Rayleigh–Bénard convection [MBPB08]. In either case, a response of the pattern to the forcing is possible, such as an alteration of the wavelength of a stripe pattern to match the wavelength of the forcing (e.g., [Cou86, RMM⁺03, KK04, MHM08]). Such a *locking* of the pattern size to the external forcing can be seen as the spatial equivalent to temporal synchronization. In general, this kind of control has to be distinguished from the use of templates that can only force a simple reproduction of their own, like a printing plate for the production of books. In contrast, synchronization and locking phenomena are more subtle and have a larger variety of possible effects on the pattern forming system, e.g., they can lead to a pattern that has a wavelength that is exactly n -times smaller than the forcing wavelength for various possible integers n . A different control approach well-known in the field

of dynamical systems is the use of feedback loops and in particular delayed feedback [SS08]. There, the output of a system is fed back into the system as input (possibly delayed by a certain time). For suitable choices of the particular form of this feedback, like the so-called Pyragas control [PT93], this kind of control is in particular useful to change stability properties of the underlying system, e.g., to stabilize previously unstable states.

Among the multitude of different pattern forming systems, the focus of this thesis lies on systems that involve thin liquid layers on solid substrates. Typically, situations are of interest, in which the substrate is only partly covered by the liquid and a three-phase *contact line* exists, at which the liquid, the surrounding gas or air and the bare substrate meet. Pattern formation phenomena often occur when this contact line is moving with respect to the substrate. A prominent example from every-day life is the coffee-ring effect. There, the contact line of a drop recedes due to the evaporation of the liquid and leaves behind a ring-shaped deposit of previously solved particles [DBD⁺97, BHD⁺12, HL12, Thi14, Lar14]. Besides the evaporation of the liquid, various mechanisms can lead to a moving contact line, such as capillarity, the centrifugal force in spin-coating applications [DSBM14] or surface tension gradient-induced Marangoni forces [Bro89]. Often, the velocity of the contact line crucially influences the pattern formation that typically occurs in its vicinity. Therefore, different approaches are used to influence this velocity. Examples are the control of the temperature or ambient vapor pressure to control the evaporation rate, or a confinement of the liquid, e.g., between a flat surface and a solid sphere (the so-called sphere on flat geometry [XXL07]), which also influences the evaporation process. However, in the aforementioned examples, the contact line movement can only be influenced indirectly and not actively controlled, indicating these as *passive* set-ups (cf. the classification in [Thi14]). In contrast, the doctor blade technique, slot-die coating or related approaches possess an intrinsic velocity at which substrates are covered with liquid [Kre09, DSBM14, YS05]. This velocity can *entrain* the contact line, enabling an *active* control of the contact line velocity. In general, such active set-ups are more suitable to control the occurring pattern formation than passive ones. One focus of this thesis lies on dip-coating, which is another active set-up. As the name suggests, a liquid or one of its constituents is deposited onto a solid substrate by dipping the latter into the liquid and then withdrawing it at a constant velocity. For low velocities, typically, a static liquid meniscus forms at the substrate which prescribes the movement of the contact line with respect to the solid substrate. This approach can either be used with simple liquids without an inner structure, or with complex liquids like solutions and suspensions. Besides homogeneous coverages, various striped and branched deposit patterns of different thicknesses can be achieved by dip-coating [LGS⁺10, LGW⁺13]. A sub-category of the dip-coating processes is the Langmuir–Blodgett transfer for which surfactant covered liquids are used to create monomolecular deposits on solid substrates. This technique is at the center of the first part of this thesis and is therefore now discussed in more detail.

1.1 The Langmuir–Blodgett Transfer

The general set-up for the Langmuir–Blodgett (LB) transfer is sketched in Fig. 1.1. The so-called *LB trough* [Rob90] is filled with water, whose temperature is controlled by a thermostat. A monomolecular layer of amphiphilic molecules is created by letting the molecules spread on the water surface. As the molecules have one hydrophilic end and one hydrophobic end, they automatically orient themselves such that their hydrophilic ends point towards the liquid

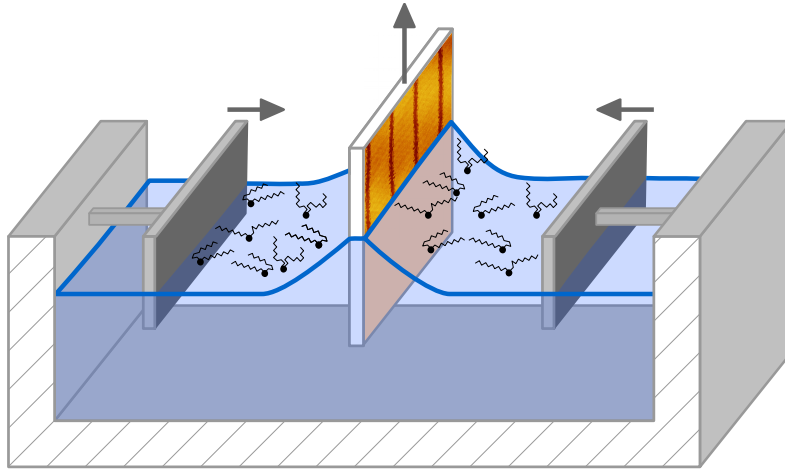


Figure 1.1: Sketch of a Langmuir–Blodgett trough used to transfer monolayers of amphiphilic molecules onto solid substrates. Movable barriers at the sides of the trough can be used to adjust the surfactant area density on the liquid surface while the substrate is withdrawn vertically at a constant velocity.

and they form a layer of only one molecule length in height (if the amount of molecules is small enough to be accommodated on the water surface). Because such amphiphilic molecules can crucially influence properties of the liquid–air interface like the surface tension, they are also denoted as **surface active agents**, or abbreviated *surfactants*. A typical example is the pulmonary surfactant 1- α -dipalmitoyl-phosphatidylcholine (DPPC), which is considered in the following. The surfactant layer can be transferred onto a solid substrate by simply withdrawing it from the LB trough at a constant velocity. Movable barriers at the sides of the LB trough can be used to restrict the accessible water surface in order to keep the area density of the molecule layer constant while being transferred onto the substrate.

The Langmuir–Blodgett technique is used for more than 80 years after its invention by Irving Langmuir (1881–1957), an American physicist and chemist, and his co-worker Katherine Burr Blodgett (1898–1979) in the nineteen-thirties [Blo34, Lan34, Blo35]. Drawing upon previous work of Agnes Pockels (1862–1935), the famous *kitchen scientist*, on the influence of surfactants on liquid surfaces [Poc91, Poc93], they developed the LB trough and were the first to achieve non-reflective monomolecular coatings of glass and metal surfaces.

Depending on experimental parameters such as the temperature and the area density, surfactants like the aforementioned DPPC may be present in different thermodynamic phases. While the phase diagram of surfactants can comprise many different phases [KMD99], the most important in the context of the LB transfer are a lower-density *liquid-expanded* (LE) and a higher-density *liquid-condensed* (LC) phase. During the LB transfer, the surfactant monolayer is not necessarily transferred as it is, but can undergo a phase transition. This transition is driven by a short-range interaction of the surfactant monolayer with the solid substrate that occurs when the thickness of the liquid layer between the substrate and the surfactant layer becomes sufficiently small. The interaction effectively lowers the coexistence pressure of the LE and LC phase and therefore energetically favors the LC phase. Accordingly, this interaction is

denoted as *substrate-mediated condensation* (SMC) [RS92, SR94].

The most interesting aspect of this method is the possibility of inhomogeneous coverages of the substrate with the surfactant monolayer. In particular, it is possible to obtain different kinds of stripe and lattice patterns which consist of alternating domains of the surfactant monolayer in phases of different density [GCF00, CLH⁺07]. As main control parameters, the surfactant layer density and the transfer velocity influence both the type of pattern that forms and the quantitative properties such as the wavelength of the stripes. Figure 1.2 presents

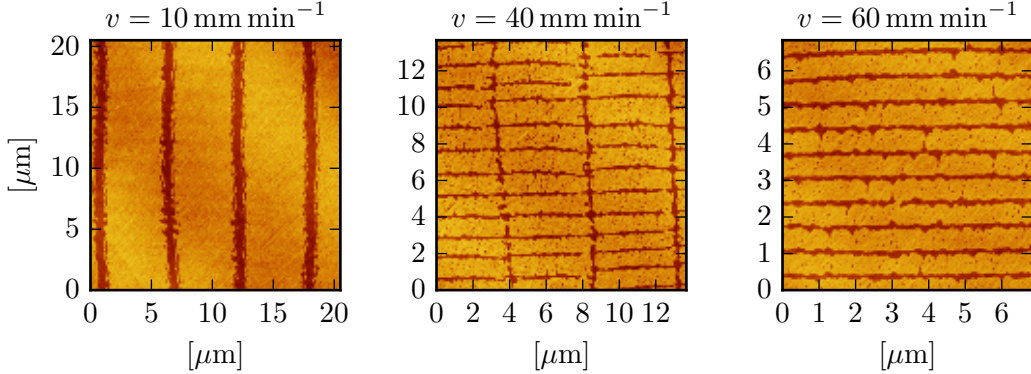


Figure 1.2: AFM images of DPPC monolayers after Langmuir–Blodgett transfer with different transfer velocities v , showing a vertical stripe pattern, a lattice structure, and a horizontal stripe pattern (left to right). The transfer direction is from bottom to top (cf. [WTG⁺15]).

atomic force microscopy images of the patterns obtained by LB transfer of DPPC onto mica substrates at different transfer velocities. For small velocities (e.g., 10 mm min^{-1}), a vertical stripe pattern with a wavelength in the order of $6 \mu\text{m}$ can be obtained, where the stripes are oriented parallel to the transfer direction. For higher velocities (e.g., 40 mm min^{-1}), rectangular lattice patterns are created, where the horizontal stripes have a wavelength of approximately $1 \mu\text{m}$ and the vertical stripes of approximately $4 \mu\text{m}$. Horizontal stripe patterns form for further increased velocities (e.g., 60 mm min^{-1}) with a typical wavelength of approximately $1 \mu\text{m}$. The velocity range in which such patterned coverages can be achieved is limited. For velocities well below 10 mm min^{-1} , a homogeneous coverage with a DPPC layer in the high-density LC phase obtained, while for high velocities beyond 60 mm min^{-1} , a homogeneous layer in the low-density LE phase is transferred onto the substrate.

Although the patterns created by LB transfer can exhibit a high regularity, this is not always the case and it is in particular sensitive to the experimental conditions. Contrarily, the stripe patterns can also exhibit defects leading to a branched pattern, whose wavelength is not perfectly regular. In addition, while the wavelength of the patterns depends on the transfer velocity, the exact form of this dependency is not known. Therefore, it is desirable to develop additional control mechanisms for this experimental method. As already mentioned above, different kinds of spatial or temporal forcing or feedback control schemes are in general conceivable. Applied to the case of LB transfer, a spatial forcing can be realized by using spatially inhomogeneous substrates. In Chap. 4, silicon substrates that are covered by thin gold stripes as prestructure will be considered and their influence on the patterns obtained by LB transfer. In addition, also a kind of temporal forcing will be studied by means of temporally

modulated parameters such as the transfer velocity.

1.2 Driven Thin Layers of Simple Liquids

The Langmuir–Blodgett transfer is one example for pattern formation phenomena occurring in a free surface film of a complex liquid that is subject to a driving force, in this case the dragging of the solid substrate. While the main interest in LB transfer lies on the resulting surfactant pattern on the solid substrate, already the transfer of the sole liquid layer onto the substrate can exhibit interesting dynamics, especially in the presence of a prestructure. Accordingly, the dynamics of a simple liquid that is dragged from a liquid reservoir by a moving solid substrate is studied intensively. Among the most prominent effects in this context is the transition from a steady, finite length liquid meniscus (that forms at very low dragging velocities of the substrate) to a transfer of a macroscopically thick layer of liquid onto the substrate, denoted as Landau–Levich film [LL42]. In the first case, the three phase contact line is static as a result of the balance of all acting forces, such as the capillary force due to the surface tension of the liquid, the wettability arising from solid-liquid interactions and the viscous drag induced by the moving substrate. This scenario is already well studied, both experimentally and from a theoretical point of view. Interesting dynamics can occur, if the force balance is disturbed, e.g., by a heterogeneous substrate. As an example, point-like defects of a wettability different to the rest of the substrate can lead to a deflection of the contact line and subsequent relaxation dynamics [DFSA08]. Accordingly, one can expect that periodic prestructures lead to periodic contact line movements. While this alone is relevant for any dip-coating method involving simple liquids, it is in addition important for set-ups with complex liquids, like the LB transfer, where the contact line dynamics can have a significant impact on the pattern formation.

Another driving force which is often important in the context of thin liquid layers is gravity. In any case where the underlying solid substrate is inclined, the gravitational force can induce a lateral movement of the liquid layer. Typical wetting or dewetting phenomena like the coarsening of liquid drops on a solid surface can be crucially influenced by such an additional driving force (e.g., [Mea92]). The effects observed in this context are typically not directly connected to the term *pattern formation*, if one only considers periodic configurations as patterns. However, one can extend this term to *structure formation* and include non-periodic structures, such as liquid drops, where one can still identify similarities to classical pattern forming systems and employ similar analysis methods. On a larger scale, such structures can then in addition also exhibit a collective behavior. In Sec. 6.2, we discuss how the sliding of drops on an inclined substrate leads to coarsening dynamics that produces an almost steady drop volume distribution with a pronounced maximum. That is, small-scale interactions (between individual drops driven by an external force) can lead to some kind of ordering on a larger ensemble scale, which is pattern formation in a wider sense.

1.3 Outline of this Thesis

The structure of this thesis is as follows. In Chap. 2, we introduce the thin film equation that is used to model thin layers of liquid on homogeneous substrates. A special emphasis lies on a gradient dynamics formulation of the models which facilitates the development and comparison of models for complex liquids like solutions or surfactant covered liquids. In addition, an augmented Cahn–Hilliard model for the description of pattern formation in Langmuir–Blodgett

transfer is presented. Suitable methods for a numerical treatment of the models are briefly discussed in Chap. 3, including finite difference and finite element methods, Runge–Kutta time stepping schemes as well as numerical continuation techniques. The methods are then employed in Chap. 4 to analyze the pattern formation in Langmuir–Blodgett transfer experiments. In particular, the influence of spatially prestructured substrates is considered in order to develop strategies for the control of pattern formation. We also compare with experimental results to verify the practical feasibility of our theoretical predictions. In Sec. 4.3, two possibilities for further control mechanisms employing temporally modulated transfer parameters are briefly explored.

In Chap. 5, the focus of the investigations is shifted from Langmuir–Blodgett transfer to the dip-coating of simple liquids. There, we discuss the influence of prestructured substrates on the dynamics of the liquid meniscus that forms between the liquid reservoir and the solid substrate. In this context, we identify settings, in which also pattern formation can occur in this simpler system (as compared to Langmuir–Blodgett transfer).

In Chap. 6, the dynamics of liquid drops sliding down an inclined substrate is analyzed. We first discuss single drops in Sec. 6.1 with a special emphasis on the so-called pearling instability which can lead to the break-up of drops into smaller ones. The underlying bifurcations and the resulting complex dynamics are analyzed in detail. In Sec. 6.2, the interplay of many sliding drops in large ensembles is considered. In particular, the influence of the inclined substrate on the coarsening dynamics is studied with a focus on the evolving drop volume distribution. Our main findings are then condensed into a minimal statistical model. Finally, the thesis is summarized and concluded in Chap. 7.

2 Mathematical Modeling

The systems under consideration in this thesis all include motile liquid layers with a free surface on solid substrates. Various approaches are conceivable to mathematically model these situations. The most detailed models describe the liquid on molecular or even atomistic levels, such as molecular dynamics or quantum mechanical ab-initio methods [Hai97, Rap04]. Advantages of such models are the very extensive abilities to include interactions of the molecules constituting the liquid with each other and their surrounding as well as forces acting on them almost without the need of phenomenological assumptions. However, their high level of detail also constitutes a major drawback, as the effort needed to solve or analyze these models is very high. In particular, the necessary computation time for numerical simulations of such models increases with the number of molecules or particles considered at least linearly, but often quadratically [Rap04]. This severely limits the number of molecules and thus also the physical size of the systems that can be considered. The phenomena that are discussed in this thesis, such as the pattern formation occurring during the Langmuir–Blodgett transfer, occur on a scale of micrometers and above. The enormous number of molecules that would need to be considered on such scales is by far larger than the maximum number of molecules that can be treated individually with the mentioned microscopic or atomistic models at present. In addition, the time scales on which atomistic or molecular dynamics are calculated, which are typically nanoseconds, are many orders of magnitudes smaller than the typical time scales of milliseconds to seconds, on which, e.g., the pattern formation in the Langmuir–Blodgett transfer occurs. Therefore, different coarse-grained models and descriptions are needed in the physical situations discussed here.

Throughout this thesis, only continuum models will be used. Information about the position of individual molecules, their movement and interactions are averaged out in such models and replaced by continuous density fields, velocity fields and effective forces, respectively. Especially the latter is also advantageous, because molecular interactions are typically much harder to measure as compared to the resulting macroscopic effects such as surface tension or viscosity.

A typical starting point for the continuum description of a liquid are the Navier–Stokes equations describing the transport of momentum in a Newtonian liquid. However, these can be simplified in the case of thin liquid layers on solid substrates discussed in this thesis. Therefore, a derivation of the so-called thin film equation is presented in Sec. 2.1. This thin film equation provides the basis for most models used throughout this thesis. To describe complex liquids, e.g., solutions or liquids covered with a surfactant layer, the thin film equation can be extended to a multi-component set of equations. Such extensions are particularly easy and consistent to implement when formulating the equations as dynamics resulting from a gradient of a certain energy functional. This will be discussed in Sec. 2.2. In some situations, the resulting multi-component models might prove to be more complex than necessary. This is, e.g., the case for the pattern formation phenomena occurring during the Langmuir–Blodgett transfer, where it is often sufficient to employ a description that neglects the dynamics of the liquid and only focuses on the dynamics of the surfactant layer. This model will be introduced in Sec. 2.3.

2.1 The Thin Film Equation

The *Navier–Stokes equations* are transport equations for the momentum of a fluid. For an incompressible fluid with constant density and without external body forces, they read together with the continuity equation (e.g., [LL87])

$$\rho \left(\partial_t \mathbf{u}^{(3)} + \mathbf{u}^{(3)} \cdot \nabla^{(3)} \mathbf{u}^{(3)} \right) = -\nabla^{(3)} p + \eta \Delta^{(3)} \mathbf{u}^{(3)}, \quad (2.1)$$

$$\nabla^{(3)} \cdot \mathbf{u}^{(3)} = 0. \quad (2.2)$$

Here, $\mathbf{u}^{(3)} = (u_x, u_y, u_z)^T$ denotes the three-dimensional velocity field, $\nabla^{(3)} = (\partial_x, \partial_y, \partial_z)^T$ is the three-dimensional del (or nabla) operator, $p(x, y, z)$ is the pressure, $\Delta^{(3)}$ the three-dimensional Laplace operator and η the dynamic viscosity. Note that we specifically indicate all three-dimensional vectors with the superscript ⁽³⁾, as we will drop superscripts for two-dimensional ones in the remainder, e.g., $\mathbf{u} = (u_x, u_y)^T$.

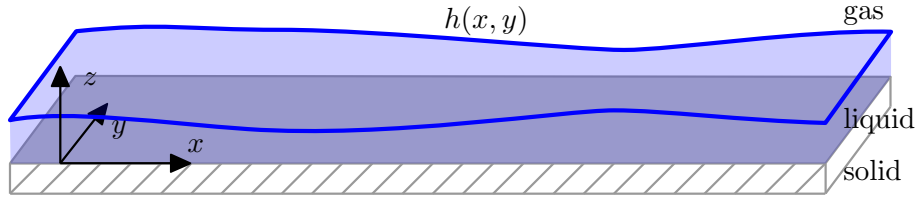


Figure 2.1: Sketch of a thin liquid layer with height profile $h(x, y)$ on a solid substrate. The used coordinate system is depicted at the left.

For the description of the physical situation involving a liquid layer with height $h(x, y, t)$ on a solid substrate with gas above the layer, Eq. (2.1)–(2.2) have to be augmented with proper boundary conditions at the liquid–solid and the liquid–gas interface (see the sketch in Fig. 2.1 for a clarification of our coordinate system). Typical assumptions for the liquid–solid interface are no-slip and no-penetration boundary conditions, which basically postulate that

$$\mathbf{u}^{(3)} \Big|_{z=0} = 0. \quad (2.3)$$

For the free boundary at the liquid–gas interface, we adopt the kinematic condition

$$u_z \Big|_{z=h} = \partial_t h + \mathbf{u} \Big|_{z=h} \cdot \nabla h, \quad (2.4)$$

which states that the dynamics of the height profile h of the liquid–gas interface is solely governed by the flux of mass given by the flow field $\mathbf{u}^{(3)}$ at the $z = h$ boundary and that no flux through this boundary is present. In addition, one has to assume a force balance at the liquid–gas interface. To this end, we introduce the *stress tensor* $\underline{\tau}$,

$$\underline{\tau} = -p \underline{I} + \eta \left(\nabla^{(3)} \mathbf{u}^{(3)} + \left(\nabla^{(3)} \mathbf{u}^{(3)} \right)^T \right), \quad (2.5)$$

where \underline{I} is the unity tensor. That is, the right hand side of the Navier–Stokes equation is the divergence of the stress tensor [LL87]. With this, the force equilibrium at the liquid–gas

interface can be formulated as

$$(\underline{\mathcal{T}} - \underline{\mathcal{T}}_{\text{gas}}) \cdot \mathbf{n}^{(3)} = \Pi \mathbf{n}^{(3)} - \sigma (\chi_1 + \chi_2) \mathbf{n}^{(3)}, \quad (2.6)$$

where $\mathbf{n}^{(3)}$ is the normal vector to the liquid-gas interface, σ is the surface tension of the liquid, χ_1 and χ_2 are the two principal curvatures of the interface, $\underline{\mathcal{T}}_{\text{gas}}$ is the stress tensor of the surrounding gas, and Π is the *disjoining pressure*, a pressure contribution that will be introduced later on.

The aim is now to derive an evolution equation for the liquid height profile $h(x, y, t)$. We start with the kinematic condition (2.4) solved for $\partial_t h$,

$$\partial_t h = u_z|_{z=h} - \mathbf{u}|_{z=h} \cdot \nabla h. \quad (2.7)$$

To substitute the vertical component of the velocity $u_z|_{z=h}$, we use the incompressibility condition (2.2) and integrate in z direction using the no-penetration boundary condition:

$$\begin{aligned} \partial_z u_z &= -\nabla \cdot \mathbf{u}, \\ \int_0^h \Rightarrow dz \quad u_z|_{z=h} &= -\int_0^h \nabla \cdot \mathbf{u} dz. \end{aligned} \quad (2.8)$$

Inserting the last equation into (2.7), one can use Leibniz's integral rule (e.g., [LP16]) to obtain

$$\begin{aligned} \partial_t h &= -\int_0^h \nabla \cdot \mathbf{u} dz - \mathbf{u}|_{z=h} \cdot \nabla h \\ &= -\nabla \cdot \int_0^h \mathbf{u} dz \\ &= -\nabla \cdot (h \bar{\mathbf{u}}), \end{aligned} \quad (2.9)$$

where in the last step we have introduced the mean velocity

$$\bar{\mathbf{u}} := \frac{1}{h} \int_0^h \mathbf{u} dz. \quad (2.10)$$

Now, the main remaining objective is to find an expression for this mean velocity. This can be obtained from the momentum equation (2.1) using the so-called *long-wave* or *lubrication approximation*, introduced in the following section.

2.1.1 The Lubrication Approximation

We will now use the fact that the liquid layers that are discussed in this thesis are thin. In this context, *thin* means that the height of the liquid layer is small as compared to typical lateral length scales. As an alternative definition, one may also choose that the height profile $h(x, y)$ only exhibits small gradients in x and y direction. The lubrication approximation exploits this fact by introducing a parameter of smallness ϵ , expanding the momentum equation (2.1) in powers of this parameter and then omitting all terms except for the lowest order in ϵ [ODB97]. To start, a scaling of all occurring variables is introduced [Thi07],

$$t = t_0 \tilde{t}, \quad (x, y) = l_0(\tilde{x}, \tilde{y}), \quad z = h_0 \tilde{z} = \epsilon l_0 \tilde{z}, \quad \mathbf{u} = \frac{l_0}{t_0} \tilde{\mathbf{u}} = u_0 \tilde{\mathbf{u}}, \quad u_z = \frac{h_0}{t_0} \tilde{u}_z = \epsilon u_0 \tilde{u}_z, \quad (2.11)$$

as well as the corresponding derivatives,

$$\partial_t = \frac{1}{t_0} \partial_{\tilde{t}}, \quad \nabla = \frac{1}{l_0} \tilde{\nabla}, \quad \partial_z = \frac{1}{h_0} \partial_{\tilde{z}} = \frac{1}{\epsilon l_0} \partial_z. \quad (2.12)$$

In addition, we define a scaling for the pressure and two dimensionless parameters,

$$p = \frac{\eta}{t_0 \epsilon^2} \tilde{p}, \quad \epsilon = \frac{h_0}{l_0}, \quad Re = \frac{\epsilon \rho l_0^2}{\eta t_0}, \quad (2.13)$$

with the density of the liquid ρ . The parameter ϵ is the aforementioned parameter of smallness relating the typical vertical length scale h_0 to the typical lateral length scale l_0 and is here assumed to be much smaller than one. The second parameter is the *Reynolds number* Re which gives the ratio of inertial to viscous forces. Adopting this scaling for the momentum equation (2.1) and immediately dropping the tildes, one obtains for the first two components and the third component, respectively:

$$\partial_t \mathbf{u} + (\mathbf{u} \cdot \nabla + u_z \partial_z) \mathbf{u} = Re^{-1} \left(-\epsilon^{-1} \nabla p + (\epsilon \Delta + \epsilon^{-1} \partial_z^2) \mathbf{u} \right), \quad (2.14)$$

$$\partial_t u_z + (\mathbf{u} \cdot \nabla + u_z \partial_z) u_z = Re^{-1} \left(-\epsilon^{-3} \partial_z p + (\epsilon \Delta + \epsilon^{-1} \partial_z^2) u_z \right). \quad (2.15)$$

In the lowest order of ϵ , the equations simplify to

$$\nabla p = \partial_z^2 \mathbf{u}, \quad (2.16)$$

$$\partial_z p = 0. \quad (2.17)$$

To solve these equations for p and \mathbf{u} , one needs again to formulate appropriate conditions at the lower $z = 0$ and upper $z = h$ boundaries of the liquid layer. At the lower boundary, we employ again the no-slip condition

$$\mathbf{u}|_{z=0} = 0. \quad (2.18)$$

For the upper boundary, one has to consider the force balance (2.6) at the liquid-air interface. This can be projected onto the normal and tangential vectors \mathbf{n} and \mathbf{t} , respectively, and then be expanded in terms of the lubrication approximation. As the derivation of the final boundary conditions is rather lengthy, we will skip it here and only refer to the literature where it is conducted in detail [ODB97, Thi07]. The resulting conditions read

$$\partial_z \mathbf{u}|_{z=h} = 0, \quad (2.19)$$

$$p|_{z=h} = -Ca^{-1} \Delta h - \Pi(h). \quad (2.20)$$

Note that the pressure at the liquid-air interface now comprises two contributions. The first one proportional to Δh is the well-known *Laplace pressure* stemming from the surface tension of the liquid, where the now-introduced *capillary number*¹

$$Ca = \frac{l_0 \eta}{\epsilon^3 \sigma t_0} \quad (2.21)$$

relates viscous friction forces to the surface tension σ [ODB97]. The second contribution is the so-called *disjoining pressure* $\Pi(h)$, also denoted as Derjaguin or conjoining pressure

¹In contrast to the classical definition of the capillary number, we absorbed the additional factor ϵ^{-3} into it. This is done to emphasize that Ca is still of order $\mathcal{O}(1)$.

[dG85, Der75, Thi07, SV09]. It accounts for effective molecular interactions of the liquid layer with the solid substrate and is in practice only relevant for extremely thin liquid layers with a thickness well below the micrometer range. The origin of this pressure as well as the particular form of $\Pi(h)$ that we employ is discussed later on in Sec. 2.1.2.

With the boundary conditions (2.18)–(2.20) we are now in the position to solve the Navier–Stokes equations in the lowest order (2.16)–(2.17) for the velocity \mathbf{u} . Integrating (2.16) once with respect to z yields

$$\partial_z \mathbf{u} = z \nabla p + \mathbf{c}_1 = z \nabla p - h (\nabla p)|_{z=h}, \quad (2.22)$$

where in the second step we already determined the integration constant \mathbf{c}_1 by demanding (2.19). A second integration with respect to z then results in

$$\mathbf{u} = \frac{1}{2} z^2 \nabla p - zh (\nabla p)|_{z=h} + \mathbf{c}_2 = \frac{1}{2} z^2 \nabla p - zh (\nabla p)|_{z=h}, \quad (2.23)$$

where the second integration constant \mathbf{c}_2 is zero because of (2.18). We can now finally evaluate the mean velocity $\bar{\mathbf{u}}$ needed for the evolution equation of the height profile h (cf. Eq. (2.9)):

$$\begin{aligned} \bar{\mathbf{u}} &= \frac{1}{h} \int_0^h \mathbf{u} \, dz \\ &= \frac{1}{h} \int_0^h \frac{1}{2} z^2 \nabla p - zh (\nabla p)|_{z=h} \, dz \\ &= -\frac{h^2}{3} (\nabla p)|_{z=h} \\ &= \frac{h^2}{3} \nabla (Ca^{-1} \Delta h + \Pi(h)), \end{aligned} \quad (2.24)$$

where in the last step Eq. (2.20) was used. Inserting this expression into (2.9) results in the *thin film equation*

$$\partial_t h = -\nabla \cdot \left[\frac{h^3}{3} \nabla (Ca^{-1} \Delta h + \Pi(h)) \right]. \quad (2.25)$$

2.1.2 The Disjoining Pressure

As already briefly introduced, $\Pi(h)$ denotes the disjoining or Derjaguin pressure that models the interaction of the solid substrate and the liquid layer and therefore accounts for the wettability properties of the solid substrate. As the name already suggests, it is a pressure contribution for the liquid in addition to the normal bulk pressure, which only arises when the liquid-gas interface is in the vicinity of a substrate, in our case the liquid-solid interface [ODB97].

On a macroscopic level, the interaction between the liquid, the solid substrate and the air results in a certain equilibrium contact angle that the liquid forms with the solid substrate at the *three-phase contact line*. Depending on this angle, one can classify the combination of the liquid and the solid as either completely wetting when the contact angle vanishes, or as non-wetting for a contact angle approaching 180° or as partially wetting for all contact angles in between. These different situations are sketched for two-dimensional drops in Fig. 2.2 (see, e.g., [dGBWQ04]).

The *equilibrium contact angle* θ_e , i.e., the contact angle that is formed at rest without additional external forces, is determined by a balance of the different interfacial tensions that

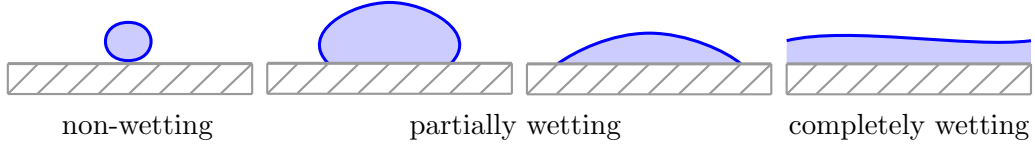


Figure 2.2: Sketch of the different possible wetting scenarios of a liquid on a solid substrate. The equilibrium contact angle decreases from left ($\theta_e = 180^\circ$) to right ($\theta_e = 0^\circ$).

meet at the contact line: the liquid-gas interfacial tension γ_{lg} , the liquid-solid interfacial tension γ_{ls} and the solid-gas interfacial tension γ_{sg} . They all act in a direction tangential to the corresponding interface, see Fig. 2.3 for a sketch. Therefore, the contact angle enters the balance equation of the interfacial tensions, the famous Young's law (see, e.g., [dG85])

$$\gamma_{sg} = \gamma_{ls} + \gamma_{lg} \cos(\theta_e). \quad (2.26)$$

However, this macroscopic approach is no longer sufficient for extremely thin layers of liquid where the effective intermolecular interactions between the solid and the liquid lead to a deviation from the behavior inside a thick bulk of liquid. These deviations can be modeled as an additional contribution $\Pi(h)$ to the pressure in the liquid that is dependent on the thickness h of the layer. This was first studied by Derjaguin in 1936 and hence this contribution is called the Derjaguin or disjoining pressure [Der75]. The specific functional form of the disjoining pressure for partially wetting liquids is difficult to obtain experimentally, and, therefore, suitable assumptions have to be made for it. For example, one can derive that attractive long-range van der Waals forces asymptotically correspond to an inverse cubic dependence $\Pi(h) \propto -h^{-3}$. Typically, a combination of both short-range and long-range interactions with different signs is assumed, for example

$$\Pi(h) = -\frac{A}{h^3} + \frac{B}{h^6}, \quad (2.27)$$

which we will use in the remainder of this thesis unless stated otherwise. Here, $A > 0$ and $B > 0$ are the Hamaker constants defining the strength of the interactions. Also other functional forms are frequently used, e.g.,

$$\Pi_S(h) = \frac{A}{h^3} - Ce^{-\chi h}, \quad (2.28)$$

as it was proposed by Sharma [Sha93], accounting for a polar interaction. Again, A and C

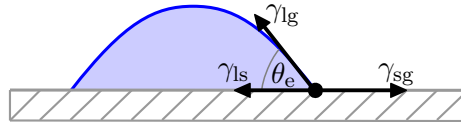


Figure 2.3: Sketch of the contact line of a partially wetting liquid. The equilibrium contact angle θ_e results from a balance of the different interfacial tensions.

are Hamaker constants and χ is an inverse interaction length. This disjoining pressure will be employed in Sec. 4.2.2 in combination with a fully hydrodynamic model for LB transfer.

The combination of long-range attractive and short-range repulsive forces in the disjoining pressure (2.27) results in the special property that $\Pi(h)$ crosses zero at the specific height

$$h_{\text{eq}} = \left(\frac{B}{A} \right)^{\frac{1}{3}}. \quad (2.29)$$

A liquid layer with constant height h_{eq} is thus a stable solution of the thin film equation (2.25). In contrast, for a layer with vanishing height, the disjoining pressure diverges. This implies that the inclusion of a disjoining pressure with this particular form leads to a model where the height never vanishes (if enough fluid mass is present or the liquid can exchange such with the surrounding vapor) and hence the whole solid substrate is always covered with a liquid layer of at least height h_{eq} . This layer is very thin for reasonable choices of the Hamaker constants and also called *precursor* layer. In fact, this can also be observed experimentally: A solid substrate is never completely dry in the vicinity of a liquid layer, but instead it is always covered by a thin layer of adsorbed liquid molecules [dG85, BEI⁺09]. Therefore, the precursor layer is also sometimes referred to as an adsorption layer.

The presence of a precursor layer also serves as a solution to an issue we have not discussed up to now, the so-called *moving contact-line problem* [dG85]. It arises when considering situations where a drop, such as the one depicted in Fig. 2.3, is subjected to a lateral force, e.g., due to gravity and an inclination of the solid substrate. Everyday experience tells us that the drop should start to move, however, this is not possible in the model without the disjoining pressure [DV79]. Without the precursor layer, the height of the liquid layer tends to zero at the contact line. There, at the solid interface, we assumed no-slip boundary conditions, effectively fixing the velocity of the liquid to zero at the contact line. Hence, it would be impossible to move the contact line. Different approaches can resolve this problem, for example allowing for a finite slip velocity at the solid substrate [Gre78, ODB97], however, with the disadvantage of the introduction of an unknown parameter that cannot be measured easily. The presence of the disjoining pressure solves the problem as well, as it guarantees that the liquid layer height never vanishes. For physically meaningful choices of the slip velocity and precursor height, i.e., in the limit of small slip velocities and precursor heights, one can show that both approaches are mathematically equivalent [SK11].

2.1.3 The Non-dimensional Thin Film Equation

When introducing the disjoining pressure (2.27) to the thin film equation (2.25), one is left with an equation with the remaining parameters Ca , A and B , but has not yet fixed the scale h_0 and the scale ratio ϵ , which can be specified with the help of A and B . The equation can be further simplified by scaling the equation differently, effectively moving the parameters into the scales of the spatial and temporal coordinates. This has not only the advantage of a more simple form of the equation, but it also reduces redundancy and emphasizes the universality of certain results irrespective of particular parameter choices. Introducing the new scaling (e.g., [TGT14])

$$t = \frac{9\eta h_{\text{eq}}}{25\sigma\theta_{\text{eq}}^4} \tilde{t}, \quad (x, y) = \frac{\sqrt{3}h_{\text{eq}}}{\sqrt{5}\theta_{\text{eq}}} (\tilde{x}, \tilde{y}), \quad h = h_{\text{eq}} \tilde{h}, \quad \theta_{\text{eq}} = \sqrt{\frac{3A}{5\sigma h_{\text{eq}}^2}}, \quad (2.30)$$

and fixing the precursor film height to $h_{\text{eq}} = \left(\frac{B}{A}\right)^{1/3}$, we arrive at the final scaled thin film equation:

$$\partial_t h = -\nabla \cdot \left[\frac{h^3}{3} \nabla \left(\Delta h - \frac{1}{h^3} + \frac{1}{h^6} \right) \right]. \quad (2.31)$$

To include further contributions in the thin film equation (2.31), one can introduce the corresponding terms into the Navier–Stokes equations and the boundary conditions and simply redo the steps of the previous derivation. For the case of an inclined solid substrate for example, one can introduce an additional body force into the momentum equation (2.1) and include the hydrostatic pressure due to gravity into the pressure term [ODB97]. For a substrate that is dragged out from a liquid bath with a certain velocity U , one has to alter the no-slip boundary conditions to fix the velocity of the liquid to this velocity at the substrate instead of setting it to zero (e.g., [SADF07]). The resulting thin film equation for a liquid layer on a substrate that is inclined by an angle α with respect to the gravity normal and is dragged with a velocity U then reads

$$\partial_t h = -\nabla \cdot \left[\frac{h^3}{3} \nabla \left(\Delta h - \frac{1}{h^3} + \frac{1}{h^6} \right) - \frac{h^3}{3} G \left(\nabla h - \begin{pmatrix} \alpha \\ 0 \end{pmatrix} \right) - \begin{pmatrix} U \\ 0 \end{pmatrix} h \right]. \quad (2.32)$$

Here, we chose the inclination and velocity to be only directed in x direction, while G is a dimensionless gravity parameter, for which we choose $G = 0.001$. Of course, the newly introduced parameters here are also subject to the scaling previously applied to the equation, e.g., the velocity U is scaled to units of l_0/t_0 . Note that the frame of reference is chosen here to be at rest in the laboratory frame, while the solid substrate moves with respect to this frame, see Fig. 2.4 for a sketch of this frame of reference.

The detailed derivation of thin film equations for the various possible additional contributions can be tedious and sometimes error-prone. In particular, this proves true when considering not only simple liquids like we did up to now, but complex ones, such as solutions or liquids covered by a surfactant layer, where an additional concentration field governed by advection-diffusion dynamics has to be included in the derivation. Therefore, this is not the approach we will pursue here further. Instead, we will reformulate the thin film equation in an appropriate way that lends itself to easy extensions. This formulation as a *gradient dynamics* is presented in the following Sec. 2.2, but before, we briefly discuss lateral boundary conditions that are needed to employ the thin film models (2.31) and (2.32) in numerical simulations or analysis.

2.1.4 Lateral Boundary Conditions

Up to now, the presented thin film models implicitly include boundary conditions in the z direction, where the no-slip and no-penetration conditions at the $z = 0$ boundary and stress balance conditions at the $z = h$ boundary entered the derivation of the equations. Boundary conditions in the x and y direction are, however, still needed. These conditions have of course to reflect the physical situation that one models. For a widely extended thin film on an uninclined substrate for example, periodic boundary conditions would be appropriate in both x and y direction, especially because of the translational symmetry of the system. If the liquid film is laterally confined, in contrast, Neumann boundary conditions for the height profile would be reasonable, as they forbid any flux through the outside boundaries. Alternatively, one can

embed such a system in a larger periodic domain and then impose the desired conditions by symmetry constraints [CGG⁺91].

In the case of a solid substrate that is withdrawn from a liquid bath under a certain angle with a constant velocity, adequate boundary conditions are more difficult to propose. In this geometry, one side of the substrate, which we will denote as the downstream end, is submerged in the liquid, while the other side sticks out, also see Fig. 2.4 for a sketch of this situation. Accordingly, the downstream side of the liquid layer profile should asymptotically approach the surface of the liquid reservoir (left side at $x = 0$ in Fig. 2.4), while at the opposing side, the thin liquid film should not be influenced by the liquid reservoir.

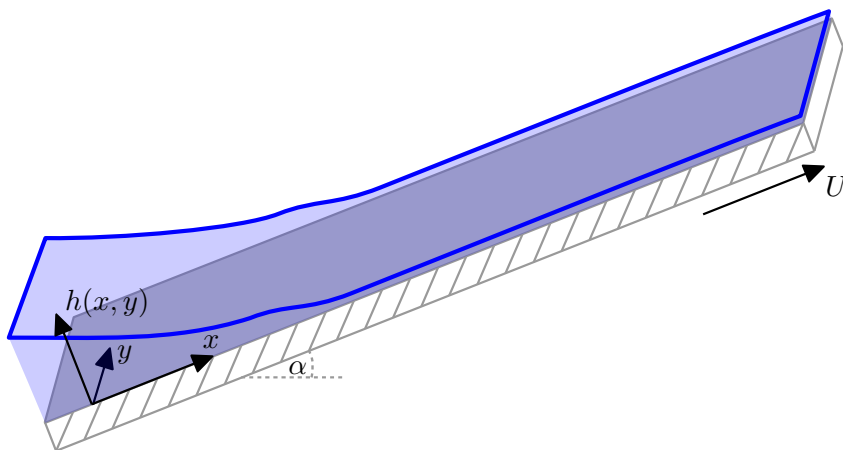


Figure 2.4: Sketch of a thin liquid layer with height profile $h(x, y)$ on a solid substrate that is dragged out from a liquid reservoir with a velocity U under an angle α with respect to the surface of the liquid reservoir.

Obviously, the behavior at the downstream side cannot be completely captured on a finite (simulation-) domain. Therefore, suitable boundary conditions were derived in [TGT14, GTLT14], which are asymptotically correct, i.e., they recover the correct behavior already on finite domains. While the boundary conditions were derived to arbitrary order, we only employ the lowest order and refer to [TGT14] for the full series, where in addition also temperature gradient-induced Marangoni forces are considered. The lowest order boundary conditions read

$$h|_{x=0} = h_b \quad \text{and} \quad \partial_x h|_{x=0} = -\alpha. \quad (2.33)$$

That is, a fixed liquid height h_b and slope $-\alpha$ are prescribed at the downstream boundary. The slope is obviously fixed by the angle that the solid substrate forms with free surface of the liquid reservoir. The height h_b , in contrast, can be chosen freely, and determines which length $L = h_b/\alpha$ of the domain is submerged in the bath.

A different approach for the boundary conditions which we mention only briefly is the one employed in, e.g., works on the Langmuir–Blodgett transfer in [KGFC10, KGF11]. There, at the downstream boundary, again the liquid height is fixed, but instead of the slope, a vanishing curvature $\partial_x^2 h = 0$ is imposed. These boundary conditions are only valid in the very vicinity of the contact line and can in particular only be valid in cases where the real liquid profile exhibits

an inflection point, as for example in slot-die coating. However, they are easy to implement and are able to deliver qualitatively similar results to (2.33), so that their usage is still justifiable.

At the upstream end of the domain, again different boundary conditions are conceivable. A common and straight forward approach is to impose a flat film, i.e., to keep the liquid height free but to demand vanishing derivatives $\partial_x h$ and $\partial_x^2 h$ of the height profile. This is typically accompanied by choosing the size of the domain large enough to exclude unwanted effects of the boundary conditions on the region of interest, which is typically located near the contact region. In addition, the advection term in the thin film equation (2.32) also acts contrary to any disturbances originating from the upstream boundary. We note that for different problems and equations also more suitable boundary conditions can be posed. In particular, so-called non-reflective conditions effectively let the solution pass the domain boundaries without affecting it. However, we are not aware of a possibility to pose such conditions for the thin film equation. Lastly, for the y direction again periodic boundary conditions are suitable when considering sufficiently large, translationally invariant domains.

We now get back again at the formulation of the thin film model in a particular way that lends itself towards further extensions for more complex liquids like solutions or liquids covered by insoluble surfactants.

2.2 Gradient Dynamics Formulation

The derivation of the thin film equation (2.31) that was presented in Sec. 2.1 can be quite involved, especially if one would include all necessary steps and considerations in detail. Still, the end result is rather similar to the well-known Cahn–Hilliard equation [Cah65, NCS84], which is used to describe the phase decomposition of a binary mixture. In general, the Cahn–Hilliard equation can be formulated as

$$\partial_t u = -\nabla \cdot \mathbf{J} = \nabla \cdot \left[M(u) \nabla \frac{\delta \mathcal{F}}{\delta u} \right], \quad (2.34)$$

for an order parameter field² $u(x, y, t)$ describing, e.g., the concentration field of one component of a binary mixture in the two-dimensional space. The dynamics of the order parameter is governed by a continuity equation with the flux \mathbf{J} , which itself comprises a mobility $M(u)$ and the gradient of the variation of a free energy functional $\mathcal{F}[u]$. In fact, by comparing the equations (2.25) and (2.34), one can see that the thin film equation *actually is* a Cahn–Hilliard type equation for a particular choice of the mobility $M(u)$ and the free energy $\mathcal{F}[u]$ [Mit93, Thi10]. In this section, this analogy will be considered in detail and used to formulate augmented thin film equations by proposing augmented free energies for different cases. Thereby, it is possible to derive the models in an easier and less error-prone way and at the same time ensure a certain inner consistency of the models. When doing this, we mainly follow the lines of [WTG⁺15].

2.2.1 The Thin Film Equation as Gradient Dynamics

The dimensionless thin film equation (2.25) can be rewritten in a form similar to the Cahn–Hilliard equation as

$$\partial_t h = \nabla \cdot \left[Q(h) \nabla \frac{\delta \mathcal{F}}{\delta h} \right], \quad \text{with } \mathcal{F}[h] = \int_{\Omega} \left(\frac{1}{2} |\nabla h|^2 + f_{\text{DP}}(h) \right) d^2 \mathbf{x}, \quad (2.35)$$

²In the following, we use the expressions *order parameter* or *order parameter field* to denote any variable or field that can be used to describe the state of a certain physical system.

where $Q(h) = \frac{h^3}{3}$ is the mobility and $f_{\text{DP}}(h)$ is the *wetting potential* related to the disjoining pressure $\Pi(h)$ by

$$\Pi(h) = -f'_{\text{DP}}(h). \quad (2.36)$$

Furthermore, Ω is the two-dimensional domain being considered, where we use the notation $\mathbf{x} = (x, y)$ and $d^2\mathbf{x} = dx dy$ for simplicity. The functional derivative with respect to h is denoted as $\frac{\delta}{\delta h}$. In this formulation, the temporal evolution of the height profile h is governed by the variation of the free energy functional $\mathcal{F}[h]$ and therefore follows gradients of $\mathcal{F}[h]$ in the function space. Accordingly, it is also denoted as *gradient dynamics*. One important property of such dynamics is that the free energy can only decrease (or stay constant) with time, as can be easily seen by calculating the total derivative of $\mathcal{F}[h]$ with respect to time,

$$\begin{aligned} \frac{d}{dt}\mathcal{F}[h(\mathbf{x}, t)] &= \int_{\Omega} \frac{\delta\mathcal{F}}{\delta h(\mathbf{x}, t)} \partial_t h(\mathbf{x}, t) d^2\mathbf{x} \\ &= \int_{\Omega} \frac{\delta\mathcal{F}}{\delta h(\mathbf{x}, t)} \nabla \cdot \left[Q(h) \nabla \frac{\delta\mathcal{F}}{\delta h(\mathbf{x}, t)} \right] d^2\mathbf{x} \\ &= - \int_{\Omega} Q(h) \left[\nabla \frac{\delta\mathcal{F}}{\delta h(\mathbf{x}, t)} \right]^2 d^2\mathbf{x} \leq 0, \end{aligned} \quad (2.37)$$

where Eq. (2.35) is used in the second step. In the third step, a partial integration is performed, where the boundary integral vanishes for suitable boundary conditions, such as periodic or Neumann boundaries. In the last step, the positive definiteness of $Q(h)$ is used.

Up to now, the free energy $\mathcal{F}[h]$ only comprises the surface energy $\frac{1}{2}|\nabla h|^2$ that accounts for the surface tension of the liquid, and the wetting potential $f_{\text{DP}}(h)$ from which the disjoining pressure originates. However, in this formulation, it is now easy to include additional physical effects by adding the corresponding contributions to the free energy. As a first example, we will again consider the case of an inclined plate that is dragged out from a liquid reservoir. For this situation, Eq. (2.32) was derived by including a hydrostatic pressure as well as a gravitational body force in the Navier–Stokes equations. In the current formalism, we just need to augment the free energy with a hydrostatic energy $\propto h^2$ and the potential energy on an inclined substrate $\propto \alpha x$:

$$\mathcal{F}_{\text{inclined}}[h] = \int_{\Omega} \left(\frac{1}{2}|\nabla h|^2 + f_{\text{DP}}(h) + \frac{1}{2}Gh^2 - G\alpha x h \right) d^2\mathbf{x}. \quad (2.38)$$

Using this free energy in Eq. (2.35), one obtains the model Eq. (2.32) described earlier, except for the advective term which cannot be embedded in the free energy. To recover the previous model, one also has to assume that the mobility remains unchanged by the new contributions. However, this can be safely assumed when the boundary conditions in vertical direction at the interfaces remain unchanged.

The approach used here can be applied whenever a particular effect that should be included can be formulated as a contribution to the free energy, such as, e.g., Marangoni forces induced by temperature gradients. This holds also true for more complex systems, where more than one order parameter field is needed for a description. For instance, for a liquid that serves as a solvent for solute molecules, the free energy should also depend on the bulk concentration of the solute. In the case of an insoluble surfactant layer covering the liquid, also the density (or per-area concentration) of the surfactants has to enter the free energy. In both cases, the

concentrations can of course be spatially varying and exhibit their own dynamics. Therefore, they have equally to be considered as order parameters, and one has to extend the gradient dynamics formulation towards multiple coupled order parameter fields.

2.2.2 Gradient Dynamics for Multiple Coupled Order Parameter Fields

The thin film model in gradient dynamics formulation can be easily extended to a set of equations describing the evolution of n coupled order parameter fields $\mathbf{u} = (u_1, u_2, \dots, u_n)^T$. To this end, the mobility $Q(h)$ in (2.35) has to be generalized to a $n \times n$ dimensional mobility matrix $\mathbf{Q}(\mathbf{u})$ which comprises the linear coupling of each component with the gradients of the variation of the free energy with respect to each component, $\nabla \frac{\delta \mathcal{F}}{\delta u_i}$. The resulting n equations then read

$$\partial_t \mathbf{u} = \nabla \cdot \left[\mathbf{Q}(\mathbf{u}) \nabla \frac{\delta \mathcal{F}}{\delta \mathbf{u}} \right]. \quad (2.39)$$

In this notation, one has to pay attention to the different dimensionalities of the vectors involved. The vector of the order parameters \mathbf{u} and the variations of the free energy with respect to the order parameters $\frac{\delta \mathcal{F}}{\delta \mathbf{u}} = \left(\frac{\delta \mathcal{F}}{\delta u_1}, \frac{\delta \mathcal{F}}{\delta u_2}, \dots, \frac{\delta \mathcal{F}}{\delta u_n} \right)^T$ are n -dimensional vectors in the order parameter space, while the nabla operator ∇ and the dot product “ \cdot ” belong to the two-dimensional coordinate space. For a clarification, we give Eq. (2.39) in index notation,

$$\partial_t u_\alpha = \nabla_i \left[Q_{\alpha\beta}(\mathbf{u}) \nabla_i \frac{\delta \mathcal{F}}{\delta u_\beta} \right], \quad \text{with } i = x, y \text{ and } \alpha, \beta = 1, \dots, n, \quad (2.40)$$

where we used the Einstein summation convention. For a thermodynamically meaningful model, the mobility matrix $\mathbf{Q}(\mathbf{u})$ has to fulfill certain criteria. On the one hand, the matrix has to be symmetric to comply with the Onsager reciprocity relations [Ons31]. On the other hand, it has to be positive definite, which can be seen in analogy to non-equilibrium thermodynamics, where this leads to a positive entropy production of the overall system [GP71], while it ensures now that the dynamics of this model can only ever decrease the free energy over time:

$$\begin{aligned} \frac{d}{dt} \mathcal{F}[\mathbf{u}] &= \int_{\Omega} \frac{\delta \mathcal{F}}{\delta \mathbf{u}} \partial_t \mathbf{u} \, d^2 \mathbf{x} \\ &= \int_{\Omega} \frac{\delta \mathcal{F}}{\delta \mathbf{u}} \nabla \cdot \mathbf{Q} \left(\nabla \frac{\delta \mathcal{F}}{\delta \mathbf{u}} \right) \, d^2 \mathbf{x} \\ &= - \int_{\Omega} \left(\nabla \frac{\delta \mathcal{F}}{\delta \mathbf{u}} \right) \cdot \mathbf{Q} \left(\nabla \frac{\delta \mathcal{F}}{\delta \mathbf{u}} \right) \, d^2 \mathbf{x} \leq 0. \end{aligned} \quad (2.41)$$

The dynamics of the n -dimensional model (2.39) is still governed by the free energy functional $\mathcal{F}[\mathbf{u}]$, which may now comprise contributions from all order parameters. In analogy to the case for the simple thin film equation, one can assume that the free energy is composed of two general parts. One accounts for effects of spatial gradients of the order parameter fields, i.e., interface energies, and the other one for bulk contributions. In line with this consideration, the free energy can be written as

$$\mathcal{F}[\mathbf{u}] = \int_{\Omega} \left[\frac{1}{2} (\nabla \mathbf{u})^T \cdot \Sigma (\nabla \mathbf{u}) + f(\mathbf{u}) \right] \, d^2 \mathbf{x}, \quad (2.42)$$

with the symmetric $n \times n$ dimensional surface energy matrix Σ and the general bulk local free energy $f(\mathbf{u})$. The formulation in index notation is

$$\mathcal{F}[\mathbf{u}] = \int_{\Omega} \left[\frac{1}{2} (\nabla_i u_\alpha) \Sigma_{\alpha\beta} (\nabla_i u_\beta) + f(\mathbf{u}) \right] d^2\mathbf{x}, \quad \text{with } i = x, y \text{ and } \alpha, \beta = 1, \dots, n. \quad (2.43)$$

Just as in the case for a single layer of a simple liquid in Eq. (2.35), the effort to derive a suitable model for a certain physical situation is now reduced to the formulation of a free energy with the appropriate contributions. Still, one additional intricacy remains, which is the mobility matrix $\mathbf{Q}(\mathbf{u})$. Often, each entry of the matrix consists of a polynomial in the order parameters, but the form of the polynomials depends on the vertical boundary conditions of the liquid layer(s) at the solid substrate, the liquid air-interface and possibly liquid-liquid interfaces for systems with multiple liquids. The mobility matrix for a particular set of boundary conditions can only be obtained by the full derivation in the framework of lubrication approximation as presented before in Sec. 2.1. Yet, this necessary derivation presents no major drawback for the complexity of the overall gradient dynamics approach, as it only has to be performed once for each set of boundary conditions. It can then be re-used in good approximation for many amendments of the free energy.

In the following section, this approach is used to propose a thin film model describing a liquid layer that is covered by an insoluble surfactant layer. This will then be augmented by appropriate boundary conditions to present a model for the pattern formation occurring in the Langmuir–Blodgett transfer.

2.2.3 Gradient Dynamics of a Surfactant Covered Liquid Layer

For the description of an insoluble surfactant layer floating on top of a liquid layer, two order parameter fields are necessary, the height of the liquid layer $h(x, y)$ as well as the (area-) density of the surfactant layer $\Gamma(x, y)$ [TAP12], see Fig. 2.5 for a sketch of this set-up. For the

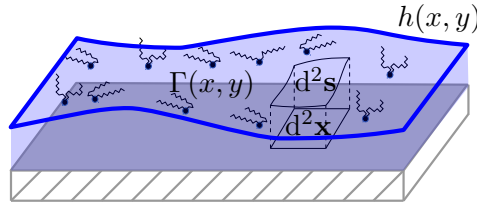


Figure 2.5: Sketch of a thin liquid layer with the height profile $h(x, y)$ covered by an insoluble surfactant layer with density $\Gamma(x, y)$. Because the liquid surface on which the surfactants are floating is not flat, one has to distinguish the surface element $d^2\mathbf{s}$ on the curved liquid surface from the flat surface element $d^2\mathbf{x}$.

formulation of a gradient dynamics, however, the area-density $\Gamma(x, y)$ defined on the curved surface $h(x, y)$ is not suitable, as it does not represent a conserved quantity on the Euclidean plane. This can be resolved by using the projection of the area-density onto the flat surface of the solid. This is accomplished using the relation

$$d^2\mathbf{s} = \xi d^2\mathbf{x}, \quad \text{with } \xi = \sqrt{1 + |\nabla h|^2} \approx 1 + \frac{1}{2} |\nabla h|^2, \quad (2.44)$$

where $d^2\mathbf{s}$ is a surface element on the curved liquid surface and $d^2\mathbf{x}$ a surface element on the Euclidean flat plane (cf. Fig. 2.5). With this, also the density Γ can be transformed by

$$\tilde{\Gamma} = \xi\Gamma. \quad (2.45)$$

The projected surfactant density $\tilde{\Gamma}$ now presents a conserved quantity suitable to be an order parameter for a gradient dynamics formulation, as $\tilde{\Gamma}$ and h can be varied independently. In all following considerations about, e.g., the free energy, one always has to distinguish between the two densities Γ and $\tilde{\Gamma}$.

The free energy in terms of the order parameters h and $\tilde{\Gamma}$ for a surfactant covered film can now be formulated as

$$\mathcal{F}[h, \tilde{\Gamma}] = \int_{\Omega} \left[f_{\text{DP}}(h) + g\left(\frac{\tilde{\Gamma}}{\xi}, h\right) \xi + \frac{\kappa}{2} \left(\nabla \frac{\tilde{\Gamma}}{\xi} \right)^2 \frac{1}{\xi} \right] d^2\mathbf{x}. \quad (2.46)$$

This free energy now comprises three contributions. The first, $f_{\text{DP}}(h)$, is the same wetting potential as for a simple liquid in Eq. (2.36). The second contribution $g(\Gamma, h)$ is the local free energy of the surfactant layer that depends both on the density Γ and the film height h . For the application of this model to the Langmuir–Blodgett transfer, one can assume that the surfactant layer has a density close to a phase transition. In this vicinity, it is reasonable to model the local free energy as a double-well potential described by a fourth-order polynomial in $\Gamma - \Gamma_{\text{cr}}$, the distance from the critical density Γ_{cr} :

$$g(\Gamma, h) = \sum_{k=0}^4 G_k (\Gamma - \Gamma_{\text{cr}})^k + D f_{\text{DP}}(h) (\Gamma - \Gamma_{\text{cr}}). \quad (2.47)$$

While the constants G_k should be chosen to describe a double-well, the zeroth order term G_0 also includes the surface energy of the bare liquid film $\frac{1}{2}G_0 |\nabla h|^2$, because $g(\Gamma, h)$ enters the free energy multiplied with the curved surface element and therefore the factor ξ . In addition, a second, height-dependent linear term with the coefficient D is included in the local free energy of the surfactant layer. This term introduces a skewness of the double-well which energetically favors one side of the double-well. This term models the *substrate-mediated condensation*, a short-range interaction between the surfactant layer and the solid substrate that can induce a phase transition of the surfactant layer as soon as it gets very close to the substrate [RS92]. In our case, the distance between the surfactant layer and the solid substrate is determined by the height h of the liquid layer, and therefore the corresponding term in Eq.(2.47), which is linear in Γ , has a height-dependence. The functional dependence of the substrate-mediated condensation on the film height h is not known, and therefore assumptions have to be made for it. In line with [KGFC10], we choose the same dependence as the wetting potential, as it fulfills two experimentally known conditions for the substrate-mediated condensation: (i) it acts on a very short length scale comparable to the one of the disjoining pressure and (ii) it decays quickly for increasing liquid film heights. However, real measurements would be needed for a more realistic modeling.

The last term in Eq. (2.46) proportional to $|\nabla\tilde{\Gamma}|^2$ describes the energy contribution due to gradients of the surfactant density. In analogy to the similar term $|\nabla h|^2$ accounting for the surface tension of the liquid, this term allows for a line tension between spatial regions of different surfactant density. The various factors of ξ or ξ^{-1} in the free energy occur due to

the projection of Γ defined on the curved surface of $h(x, y)$ to $\tilde{\Gamma}$ defined on the flat Euclidean plane, and because ∇/ξ is the gradient tangent to the free surface of the liquid.

This free energy can now be used for a two-component version of the gradient dynamics (2.39). Explicitly written for the two order parameters h and $\tilde{\Gamma}$, it reads

$$\begin{aligned}\partial_t h &= \nabla \cdot \left[Q_{hh} \nabla \frac{\delta \mathcal{F}}{\delta h} + Q_{h\Gamma} \nabla \frac{\delta \mathcal{F}}{\delta \tilde{\Gamma}} \right], \\ \partial_t \tilde{\Gamma} &= \nabla \cdot \left[Q_{\Gamma h} \nabla \frac{\delta \mathcal{F}}{\delta h} + Q_{\Gamma\Gamma} \nabla \frac{\delta \mathcal{F}}{\delta \tilde{\Gamma}} \right].\end{aligned}\tag{2.48}$$

As noted before, the mobility matrix has to be derived separately taking into account the vertical boundary conditions of the liquid and the surfactant layer. We only specify it here without a detailed justification, which can be found, e.g., in [TAP12, WTG⁺15]:

$$\mathbf{Q} = \begin{pmatrix} \frac{h^3}{3} & \frac{h^2 \Gamma}{2} \\ \frac{h^2 \Gamma}{2} & h\Gamma^2 + \tilde{D}\Gamma \end{pmatrix}.\tag{2.49}$$

Here, the constant \tilde{D} in the entry $Q_{\Gamma\Gamma}$ denotes the molecular mobility of the surfactant molecules.

In the gradient dynamics formulation (2.48), the order parameters are inherently conserved. Therefore, physical effects that lead to a loss or a gain of one or more components are not included. However, it is easily possible to extend it with non-conserved contributions such as evaporation of the liquid. To this end, an *Allen–Cahn type* term can be added to the evolution equation [KGFC10]:

$$\delta_{\text{ev}} = -E_v \left(\frac{\delta \mathcal{F}}{\delta h} - p_v \right).\tag{2.50}$$

The parameter E_v denotes an evaporation rate that relates the timescale of the non-conserved dynamics to the timescale of the conserved part. In this formulation, also the non-conserved part is governed by the same free energy functional $\mathcal{F}[h, \Gamma]$, ensuring a thermodynamic consistency with the conserved dynamics. In this approach, the evaporation is assumed to be proportional to the difference between the pressure in the liquid phase, which is given here as the variation of the free energy with respect to h , and the vapor pressure p_v in the gas phase, which is here assumed to be constant and homogeneous. Note that a similar approach can also be chosen when allowing for the adsorption and desorption of soluble surfactants [TAP16].

The final model describing the dynamics of a surfactant-covered thin liquid film can now be formulated by performing the variations of the free energy and inserting them into Eq. (2.48). Including the non-conserved term for the evaporation, it reads [TAP12, WTG⁺15]

$$\begin{aligned}\partial_t h &= \nabla \cdot \left[\frac{h^3}{3} \nabla [f'_{\text{DP}}(h) - \nabla \cdot (\gamma \nabla h)] - \frac{h^2}{2} \nabla \gamma \right] + \delta_{\text{ev}}, \\ \partial_t \Gamma &= \nabla \cdot \left[\frac{h^2 \Gamma}{2} \nabla [f'_{\text{DP}}(h) - \nabla \cdot (\gamma \nabla h)] - (h\Gamma + \tilde{D}) \nabla \gamma \right],\end{aligned}\tag{2.51}$$

where we introduced the abbreviation

$$\gamma = g(\Gamma, h) - \Gamma \partial_{\Gamma} g(\Gamma, h) - \frac{\kappa}{2} (\nabla \Gamma)^2 + \kappa \Gamma \nabla^2 \Gamma,\tag{2.52}$$

which can be interpreted as a generalized surface tension that accounts for a dependence of the surface tension on the concentration of the surfactant density. To apply this model to the

case of the Langmuir–Blodgett transfer, only two more aspects have to be considered. First, additional advection terms with the dragging velocity U have to be added to both equations to account for the transfer process. Second, appropriate boundary conditions as already discussed in Sec. 2.1.4 have to be applied. Together with these two aspects, the resulting model is the same as the model presented in [KGFC10], where it was derived with much effort starting with the Navier–Stokes equations and an advection-diffusion equation for the surfactant layer.³ We will employ this model in Sec. 4.2.2 to describe the pattern formation process in the Langmuir–Blodgett transfer with prestructured substrates. In this case, rather complex bent stripe patterns will be found as a result of the interplay of the dynamics of the liquid and the surfactant layer.

The gradient dynamics formulation presented here also facilitates the derivation of models for other similar systems, such as thin solution layers that are again described by the liquid height profile and a concentration field, which now describes a per-volume concentration of the solute molecules within the film [TTL13]. As we will not use such a model in the remainder of this thesis, we will only very briefly present the model and the contributions entering here to give an impression of the possibilities of the approach (cf. [WTG⁺15]).

2.2.4 Gradient Dynamics of a Thin Solution Layer

A thin layer of a solution on a solid substrate can also be described by two order parameters, the height of the layer $h(x, y)$ as well as the per-volume concentration of the solute molecules $c(x, y, z)$. In the framework of the lubrication approximation, it can be assumed that the z dependence of the concentration can be neglected and therefore a height-averaged concentration $\phi(x, y)$ with

$$\phi(x, y, t) = \frac{1}{h(x, y, t)} \int_0^{h(x, y, t)} c(x, y, z, t) dz \quad (2.53)$$

is a more appropriate choice as an order parameter, see also Fig. 2.6 for a sketch of the situation we are now considering. However, the choice of h and ϕ as order parameters can pose difficulties,

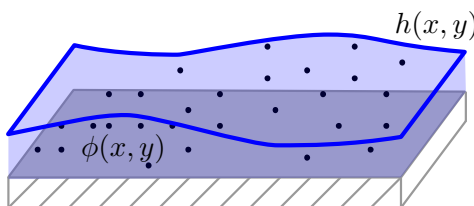


Figure 2.6: Sketch of a thin liquid solution layer with height profile $h(x, y)$ and a height-averaged per-volume concentration $\phi(x, y)$.

as they cannot be varied independently. Consider, e.g., a situation where the solvent is subject to evaporation. Then, a change of the height due to evaporation would also have to induce

³When comparing the formulation of the model here and the one presented in [KGFC10], one can identify two minor differences: In [KGFC10], the approximation $\nabla \cdot (\gamma \nabla h) \approx \gamma \Delta h$ was used and the explicit height dependence $\partial_h g(\Gamma, h)$ is missing in one term. However, this can be absorbed in a scaling of the wetting potential, also see [TAP12] for more details.

a change of the concentration ϕ . A possible way around is the usage of the local amount of solute $\Psi(x, y, t) = h(x, y, t)\phi(x, y, t)$ as order parameter [Thi11, TTL13], which can be varied independently of the film height h . For these order parameters, the gradient formulation then reads

$$\begin{aligned}\partial_t h &= \nabla \cdot \left[Q_{hh} \nabla \frac{\delta \mathcal{F}}{\delta h} + Q_{h\Psi} \nabla \frac{\delta \mathcal{F}}{\delta \Psi} \right], \\ \partial_t \Psi &= \nabla \cdot \left[Q_{\Psi h} \nabla \frac{\delta \mathcal{F}}{\delta h} + Q_{\Psi\Psi} \nabla \frac{\delta \mathcal{F}}{\delta \Psi} \right],\end{aligned}\tag{2.54}$$

with the mobility matrix

$$\mathbf{Q} = \begin{pmatrix} \frac{h^3}{3} & \frac{h^2\Psi}{3} \\ \frac{h^2\Psi}{3} & \frac{h\Psi^2}{3} + \tilde{D}\Psi \end{pmatrix}.\tag{2.55}$$

Various contributions are now conceivable for the free energy $\mathcal{F}[h, \Psi]$. Here, we specify a free energy with the same contribution for the liquid layer as before corresponding to the Laplace and disjoining pressure and an additional bulk free energy $f_B(\phi)$ for the solute:

$$\mathcal{F}[h, \Psi] = \int_{\Omega} \left[f_{\text{DP}}(h) + \frac{1}{2} |\nabla h|^2 + h f_B \left(\frac{\Psi}{h} \right) \right] d^2 \mathbf{x}.\tag{2.56}$$

A possible choice for the bulk free energy can be

$$f_B(\phi) = \frac{k_B T}{a^3} [\phi \ln(\phi) + (1 - \phi) \ln(1 - \phi)] + \alpha \phi (1 - \phi) + \frac{\kappa}{2} |\nabla \phi|^2.\tag{2.57}$$

The first two contributions account for entropic effects over the entire concentration range, where a is a microscopic length scale of the solute. The third term is a Flory interaction free energy appropriate for, e.g., polymer solutions [Flo53] with the interaction constant α . The last term penalizes spatial inhomogeneities of the concentration field. In fact, the local part of the bulk free energy (without the term $\sim |\nabla \phi|^2$) has a similar shape as the local free energy (2.47) for the surfactant layer close to a critical density. In particular, we can expand the local part of (2.57) about the critical concentration $\phi_{\text{crit}} = \frac{1}{2}$, which results in

$$\begin{aligned}\frac{k_B T}{a^3} [\phi \ln(\phi) + (1 - \phi) \ln(1 - \phi)] + \alpha \phi (1 - \phi) &= -\frac{k_B T}{a^3} \ln 2 + \frac{\alpha}{4} - \alpha \left(\phi - \frac{1}{2} \right)^2 \\ &+ \frac{k_B T}{a^3} \sum_{n=1}^{\infty} \frac{2^{2n-1}}{n(2n-1)} \left(\phi - \frac{1}{2} \right)^{2n}.\end{aligned}\tag{2.58}$$

As one can see, the bulk free energy can be expressed in terms of a polynomial symmetric about $\phi_{\text{crit}} = \frac{1}{2}$. If one now truncates the expansion after $n = 2$, one obtains a fourth order polynomial describing a double well (for reasonable choices of a , α and T). That is, the local free energy contribution proposed earlier in (2.47) is nothing but an approximation of the local bulk free energy in (2.57).

The model resulting from this free energy can now similarly to the case presented in Sec. 2.2.3 be extended by evaporation and advection terms to describe the transfer of a volatile solution onto a substrate in a dip-coating process, also see [WTG⁺15]. Plenty of additional effects can now be incorporated into the model easily and in a thermodynamically consistent way, e.g., an impact of the solute concentration on the wettability [Thi11, TTL13]. However, we will not pursue this further here. Instead we will come back to the case of Langmuir–Blodgett transfer, where the complexity of the model can be significantly reduced in certain situations.

2.3 The Cahn–Hilliard Equation for Langmuir–Blodgett Transfer

The thin film model for a surfactant covered liquid film presented in Sec. 2.2.3 has already been successfully used to describe Langmuir–Blodgett transfer experiments [KGFC10, LKG⁺12], in which the surfactant layer is transferred onto a solid substrate by withdrawing it from the liquid. In these experiments, one is in particular interested in the deposit of the surfactant layer on the solid substrate after the transfer, which can consist of differently oriented stripe patterns that are composed of the surfactant layer in two phases with varying density. The liquid layer is evaporated after the transfer and does therefore only play a role during the transfer but not afterward.

In addition, numerical simulations of the model revealed that even during the Langmuir–Blodgett transfer the liquid height profile $h(\mathbf{x}, t)$ often only relaxes to a stationary profile that exhibits no significant dynamics [KGFC10, KGFT12]. Therefore, also a *reduced model* suffices to describe the pattern formation of the surfactant layer that neglects the hydrodynamics of the liquid layer. In practice, the evolving liquid layer height is replaced by a stationary, parametric profile [KGFT12]. This results in a simpler model, which can be analyzed more easily. In addition, it can as well provide more insights into the origin of the pattern formation process, as one can then directly see the importance of hydrodynamic effects for it.

Because the dynamics of a gradient dynamics model can only reduce the free energy over time, a stationary liquid height profile implies that the free energy contributions of the liquid layer, i.e., the Laplace and disjoining pressure, have reached a minimum. Therefore, it is reasonable to neglect the corresponding terms also in the evolution equation for the surfactant layer. With this, only two more entries are present in the free energy (2.46), namely the gradient term $\propto |\nabla\Gamma|^2$ and the local free energy of the surfactant layer modeled by a double-well potential in Γ , see Eq. (2.47). In this double-well potential, a h -dependent skewness proportional to the wetting potential was incorporated accounting for the substrate-mediated condensation. Now, this is approximated by a simple parametric function. Figure 2.7 shows an exemplary height profile that results from a thin film model for a liquid layer that is dragged out of a bath and

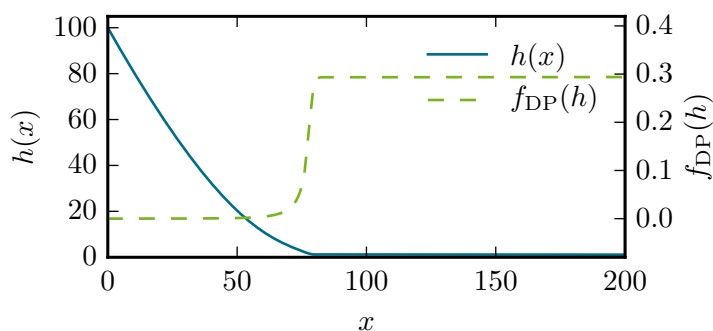


Figure 2.7: Exemplary height profile $h(x)$ of a liquid that develops on a solid substrate that is withdrawn from a liquid bath and the resulting spatial form of the wetting potential $f_{\text{DP}}(h) = \frac{1}{2h^2} - \frac{1}{5h^5}$. As can be seen from the profile, the wetting potential can be well approximated by a sigmoidal function.

the resulting spatial dependence of the wetting potential $f_{\text{DP}}(h) = \frac{1}{2h^2} - \frac{1}{5h^5}$. Obviously, this can be well approximated in a reduced model by a sigmoidal function, such as a hyperbolic tangent. Taking into account all these simplifications, one obtains an *augmented Cahn–Hilliard model*:

$$\partial_t c = \nabla \cdot \left[M(c) \nabla \frac{\delta \mathcal{F}}{\delta c} \right] + \mathbf{v} \cdot \nabla c, \quad F[c] = \int_{\Omega} \left[\frac{1}{2} |\nabla c|^2 + f(c) \right] d^2 \mathbf{x}, \quad (2.59)$$

with the local free energy $f(c)$ given by

$$f(c) = \frac{1}{4} c^4 - \frac{1}{2} c^2 + \mu \zeta(\mathbf{x}) c. \quad (2.60)$$

Now, the variable $c(\mathbf{x}, t)$ is used for the concentration of the surfactant layer to avoid confusion with the previous, fully hydrodynamic model. The concentration is now also further scaled so that the double-well potential has two minima at $c = \pm 1$ corresponding to the two phases of the surfactant. We note again, that this fourth-order polynomial is an approximation of the local free energy in (2.57) accounting for entropic effects and a Flory-type interaction. The transfer velocity is denoted as $\mathbf{v} = (v, 0)^T$ here to emphasize that particular numbers cannot be readily compared to the differently scaled velocity U in the hydrodynamic models. The spatial dependence of the substrate-mediated condensation is modeled as

$$\zeta(\mathbf{x}) = -\frac{1}{2} \left[1 + \tanh \left(\frac{x - x_s}{l_s} \right) \right], \quad (2.61)$$

where the contact line is assumed to be located at $x = x_s$ and l_s describes the width of the region in which the substrate-mediated condensation sets in. Similar to the classic Cahn–Hilliard model for phase decomposition, the mobility is also simplified to be constant,

$$M(c) = 1. \quad (2.62)$$

With the aforementioned simplifications and approximations made, the model should no longer be thought of a model for the description of Langmuir–Blodgett transfer that is capable of quantitative descriptions and predictions. In contrast, it is more of a toy-model that is complex enough to capture the main features of the pattern formation processes but is still as simple as possible to facilitate an in-depth analysis. This has also already been performed in [KGFT12, KT14], where in particular the bifurcation diagram for the transfer velocity as the main control parameter was obtained and analyzed. This also clarifies which bifurcations are involved at the onset of the pattern formation. We will also briefly review these findings in Chap. 4. However, our main focus will be on extended models that also account for spatial inhomogeneities of the substrate that are used for the Langmuir–Blodgett transfer.

2.4 Modeling of Prestructured Substrates

In real-world applications, perfectly homogeneous substrates are hardly available, either due to crystallographic defects or impurities occurring during the handling of the substrates. But inhomogeneities can also be introduced on purpose in the form of a prestructure that is employed to influence and control the pattern formation process [GHLL99, QXX⁺99, CGO06]. Different types of such prestructures are conceivable, e.g., topographical or chemical prestructures. For

a topographical prestructure, parts of the surface of the substrate are removed by etching or milling for example. This results in a substrate with a non-flat topography, whereas all chemical properties are still homogeneous across the substrate because it still consists of only one material. This is different for chemical prestructures, where the substrates are chemically altered leading to a change of interaction types and strengths. Of course, both types of prestructures can also be combined, when for example a prestructure of finite thickness and made of a different material than the substrate is deposited.

When referring to prestructures throughout this thesis, we will always consider *chemically prestructured* substrates that exhibit a flat topography. Depending on the precise type of prestructure, also different ways are possible to include them into the models that were presented. As the main objective of this thesis is the dynamics of the liquid and surfactant layers on top of the solid substrates, we will assume the prestructure to change the corresponding interactions of these layers. For the hydrodynamic models in Sec. 2.1 to Sec. 2.2.4, the most prominent interaction between the liquid layers and the solid substrate is the disjoining pressure that also determines the contact angle of the liquid on the solid. Therefore, a prestructure can be included as a spatial modulation of the strength, i.e., amplitude of the disjoining pressure (e.g., [KGF11]). Although any prefactors of these terms were previously removed by the scaling of the variables, one can now explicitly re-introduce a factor κ for the wetting potential $f_{\text{DP}}(h)$ in the free energy formulations. This factor represents the ratio of the wetting energy of a certain material combination to the one already assumed in the scaling. When including this factor, one in particular changes both Hamaker constants simultaneously, meaning that the height of the precursor layer h_{eq} is not changed. The equilibrium contact angle, however, is changed to

$$\theta_{\text{eq}} = \sqrt{\frac{3\kappa}{5}} \quad (2.63)$$

for the disjoining pressure and scaling used in the scaled thin film equation (2.31). For a prestructured substrate, the wetting energy then becomes spatially varying which can be included in a spatial modulation $m(\mathbf{x})$ of κ .

In the reduced Cahn–Hilliard model (2.59), the interactions of the liquid layer and the solid substrate only enter parametrically in the modeling of the substrate-mediated condensation in Eq. (2.60)–(2.61), for which a similar functional dependence was assumed as for the wetting potential. Consistent to the implementation for the hydrodynamic models, one can therefore include prestructures into the Cahn–Hilliard model (2.59) as a spatial modulation $m(\mathbf{x})$ of the term ζ accounting for the substrate-mediated condensation in Eq. (2.61).

For the particular shape of a prestructure, of course infinitely many possibilities exist. For the sake of simplicity, we will restrict ourselves only to periodic stripe-like prestructures with two different orientations, parallel and perpendicular to the transfer velocity. Again, various concrete implementations for such are thinkable, where we choose a train of repeated tanh-shaped rising and falling edges:

$$m(y) = 1 + \rho \tanh \left[s \left(4 \left| \text{frac} \left(\frac{y}{L_{\text{pre}}} \right) - 0.5 \right| - 1 \right) \right] \quad (2.64)$$

for a prestructure that is oriented parallel to the transfer velocity that acts in x direction and

$$m(x) = 1 + \rho \tanh \left[s \left(4 \left| \text{frac} \left(\frac{x - Ut}{L_{\text{pre}}} \right) - 0.5 \right| - 1 \right) \right] \quad (2.65)$$

for a prestructure that is oriented perpendicular to the transfer velocity. Note that in the latter case the prestructure moves with the transfer velocity U (denoted as v in the augmented Cahn–Hilliard model), while it is stationary in the case parallel to the transfer velocity, because it is homogeneous in x direction. In both cases, ρ is introduced as a parameter determining the modulation depth, L_{pre} as the spatial periodicity of the prestructure and s a parameter controlling the steepness of the edges. The function frac denotes the fractional part of the argument.

Also different, seemingly more simple prestructures such as point-defects or other single, localized structures might seem worth an investigation to study the impact of localized defects. However, our focus lies on the usage of spatially periodic forms for the prestructure, because the patterns evolving in Langmuir–Blodgett transfer are mostly periodic, too. And especially the interaction of a pattern formation process leading to periodic patterns with a periodic forcing due to the prestructure is promising, because then, synchronization phenomena can occur [PRK03]. This route will lead to interesting results, which will be presented in Chap. 4. However, before discussing the results, we will briefly introduce the methods that are employed in the thesis to analyze the models.

3 Numerical Treatment

Apart from very simple considerations about, e.g., homogeneous stationary solutions, the thin film models that were introduced in Chap. 2 can hardly be treated with exact analytical methods. In particular, most of the information about the dynamic behavior of the models can in practice only be obtained by approximations and numerical methods. In this chapter, different numerical techniques are introduced that will be used throughout this thesis to analyze the models in question.

All used models consist of nonlinear partial differential equations (PDEs) which govern the temporal evolution of order parameter fields describing the behavior of a spatially extended system. This evolution depends in particular on spatial derivatives of the order parameters. To conduct direct numerical simulations of these models in terms of an initial value problem, in principle three steps are necessary: (i) the models have to be discretized on a finite spatial mesh; (ii) a way to evaluate the spatial derivatives on this discrete mesh has to be introduced and (iii) a time stepping scheme has to be applied to advance the solution forward in time. For each step, various different methods are possible, but we only introduce the methods that will be actually used here. For the evaluation of spatial derivatives, both a *finite difference method* and a *finite element method* are described in Sec. 3.1.1 and 3.1.2, respectively. Explicit and implicit *Runge–Kutta schemes* for the time stepping will then be briefly discussed in Sec. 3.2. Besides these general concepts, also the practical implementations of the methods will be described in Sec. 3.3. One implementation of the finite difference method with an adaptive explicit Runge–Kutta scheme is done using the CUDA framework for computations on highly parallelized modern graphics processors [NVI]. A second implementation of the finite element method with an implicit Runge–Kutta scheme is conducted using the DUNE-PDELab framework [BBD⁺08b, BBD⁺08a, BHM10], again enabling parallel computations on large computer grids.

In addition to direct numerical simulations which are performed as initial value problems, also continuation methods are employed in Chap. 5 and 6 for the analysis of steady states. These methods enable one to follow stationary solutions in parameter space in terms of a boundary value problem. In particular, one can obtain bifurcation diagrams that also include unstable solution branches which could not be obtained by direct numerical simulations. The basis for such methods is explained in Sec. 3.4.

3.1 Spatial Discretization and Approximation of Derivatives

In all physical systems under consideration in this thesis, the dynamics of liquid and surfactant layers on flat solid substrates are of interest. Therefore, the spatial geometries on which the corresponding models will be solved are simple as they do not exhibit curved surfaces or temporally varying boundaries. In fact, we always restrict the two-dimensional domain Ω to a fixed rectangle

$$\Omega = [0, L_x] \times [0, L_y], \quad (3.1)$$

with the spatial domain sizes L_x and L_y in x and y direction, respectively. This rectangular domain also facilitates the discretization onto a mesh of grid points. We choose a simple approach, i.e., a mesh consisting of rectangular elements with constant size $\Delta x \times \Delta y$. The resulting grid points are then determined by

$$\mathbf{x}_{ij} = (x_i, y_j) = (i \Delta x, j \Delta y), \quad \text{with } i \in [0, N_x - 1], \quad j \in [0, N_y - 1], \quad (3.2)$$

where i, j are the integer spatial indices of the grid points that range from zero to the number of grid points $N_x - 1$, $N_y - 1$ in the corresponding direction. Obviously, this discretization fulfills the relations

$$\Delta x = \frac{L_x}{N_x - 1}, \quad \Delta y = \frac{L_y}{N_y - 1}. \quad (3.3)$$

To simplify the following descriptions in this section, we only consider one order parameter field u on a two-dimensional domain, where we introduce the abbreviation

$$u(x_i, y_j) = u_{ij}. \quad (3.4)$$

Using the finite difference method, one can now derive expressions for spatial derivatives of u on the discrete grid.

3.1.1 The Finite Difference Method

The finite difference method can be motivated in different ways. In the simplest case of a first partial derivative in x direction, it follows directly from the definition of the derivative as a difference quotient,

$$\partial_x u|_{(x,y)=(x_i,y_j)} = \lim_{\epsilon \rightarrow 0} \frac{u(x_i + \epsilon, y_j) - u(x_i, y_j)}{\epsilon}. \quad (3.5)$$

In a discrete system, the limit $\epsilon \rightarrow 0$ is approximated by $\epsilon = \Delta x$, which results in the lowest order finite difference approximation of the first derivative with respect to x ,

$$\partial_x u|_{(x,y)=(x_i,y_j)} = \frac{u(x_i + \Delta x, y_j) - u(x_i, y_j)}{\Delta x} + \mathcal{O}(\Delta x) = \frac{u_{i+1j} - u_{ij}}{\Delta x} + \mathcal{O}(\Delta x). \quad (3.6)$$

This expression is also called *forward finite difference*, because u is evaluated at the current position \mathbf{x}_{ij} and at a position advanced in positive x direction at \mathbf{x}_{i+1j} . Similarly, also a *backward finite difference* can be formulated by starting with (3.5) and a negative ϵ approaching zero. The so-called truncation error of both approximations is of order $\mathcal{O}(\Delta x)$, indicating that the error of this approximation scales linearly with Δx . A demonstrative way to derive expressions with a higher order of accuracy is to interpolate u between the grid points using a polynomial of arbitrary order which can then be derived analytically. The higher the order of the polynomial, the higher is the resulting order of the corresponding finite difference approximation. At the same time, of course, the number of neighboring grid points entering the formulas increases. For a second order finite difference scheme, one can start with a quadratic interpolation $f_{\text{interp},2}$ between the point of interest and the two neighboring points in x direction,

$$f_{\text{interp},2}(x - x_i, y - y_j) = \frac{u_{i+1j} - 2u_{ij} + u_{i-1j}}{2\Delta x^2}(x - x_i)^2 + \frac{u_{i+1j} - u_{i-1j}}{2\Delta x}(x - x_i) + u_{ij}. \quad (3.7)$$

The coefficients of the u_{ij} directly result when demanding that

$$f_{\text{interp},2}(x_i, y_j) = u_{ij}, \quad f_{\text{interp},2}(x_{i+1}, y_j) = u_{i+1j} \quad \text{and} \quad f_{\text{interp},2}(x_{i-1}, y_j) = u_{i-1j}. \quad (3.8)$$

The second order finite difference schemes now follow directly from these coefficients by calculating the derivative of $f_{\text{interp},2}$:

$$\partial_x u|_{(x,y)=(x_i,y_j)} = \partial_x f_{\text{interp},2}(x - x_i, y - y_j)|_{x=x_i, y=y_j} + \mathcal{O}(\Delta x^2) = \frac{u_{i+1j} - u_{i-1j}}{2\Delta x} + \mathcal{O}(\Delta x^2). \quad (3.9)$$

This formula is also known as *central finite difference scheme*, as values of u both left and right from the point of interest are used. In the same way, now also expressions for higher derivatives can be derived, e.g., for the second derivative with respect to x ,

$$\partial_x^2 u|_{(x,y)=(x_i,y_j)} = \frac{u_{i+1j} - 2u_{ij} + u_{i-1j}}{\Delta x^2} + \mathcal{O}(\Delta x^2). \quad (3.10)$$

For higher order derivatives and higher orders of accuracy, ansatz polynomials of higher order have to be employed, but the approach remains the same. Also derivatives with respect to other spatial directions are obtained analogously. Therefore, we do not derive further expressions here and only refer to the literature [Smi86].

The finite difference method also makes it particularly easy to implement boundary conditions which fix derivatives at the domain boundaries. To this end, so-called virtual grid points or ghost points are introduced outside the actual domain Ω and are set to specific values, such that an evaluation of the central finite difference scheme at the boundary of the domain yields the desired result. As an example, one may consider fixing the second derivative with respect to x at the $x = 0$ boundary to a fixed value

$$\partial_x^2 u|_{(x,y)=(0,y_j)} = \beta. \quad (3.11)$$

Inserting the finite difference scheme (3.10) and solving for the value at the virtual grid point u_{-1j} yields

$$\begin{aligned} \frac{u_{1j} - 2u_{0j} + u_{-1j}}{\Delta x^2} &= \beta, \\ \Leftrightarrow \quad u_{-1j} &= \beta\Delta x^2 - u_{1j} + 2u_{0j}. \end{aligned} \quad (3.12)$$

Again, this approach directly generalizes for arbitrary derivatives and can also be used to implement periodic boundary conditions by fixing the values at the virtual grid points to the values at the opposite boundary of the domain.

After discretizing a partial differential equation and replacing all spatial derivatives by their corresponding finite difference approximations, one is left with an explicit point-wise algebraic expression for the temporal evolution at each spatial grid point that depends on the values in a certain neighborhood of the grid point. The next step necessary for a numerical treatment is an approximation of the temporal derivative in the models to result in a time stepping scheme that advances from one time step to the next one. Before we introduce this in Sec. 3.2, we first introduce the finite element method as an alternative to the finite difference method.

3.1.2 The Finite Element Method

The basic idea of finite element methods is the division of the domain Ω into small and simple-shaped subdomains Ω_i , the so-called elements, on which the solution is expressed in terms of ansatz functions that only have a compact support. The partial differential equation is then formulated in a residual form on these elements, resulting in a (typically large) nonlinear set of equations for the coefficients describing the ansatz functions. The solution of this nonlinear set of equations is then equivalent to the solution of the actual partial differential equation on the whole domain. The following description is largely based on [PS05]. The description is not meant to be exhaustive or mathematically precise, but in contrast aims at providing a rather brief and demonstrative sketch of the method.

The starting point for all finite element methods is the *weak formulation* of the partial differential equation in which the equation is multiplied with a test function and then integrated across the domain. In this formulation, spatial derivatives of the order parameter can be swapped for spatial derivatives of the test function by means of integration by parts. The resulting *weak derivatives* have weaker requirements on the differentiability of the function and are therefore a generalization of the classical *strong* derivative [GT01]. We present the weak formulation here exemplary for the simple thin film equation (2.31), which we split into two equations of second order in space

$$\begin{aligned}\partial_t h &= -\nabla \cdot \left[\frac{h^3}{3} \nabla w \right], \\ w &= \Delta h + \Pi(h).\end{aligned}\tag{3.13}$$

This splitting of the equation seems arbitrary up to now. However, it is done, because we will later on employ linear ansatz and test functions on the elements which simply cannot possess non-zero derivatives of higher order. In the weak formulation for an arbitrary test function $\varphi(\mathbf{x})$ the split equations (3.13) read

$$\begin{aligned}0 &= \int_{\Omega} (\partial_t h) \varphi \, d^2 \mathbf{x} + \int_{\Omega} \nabla \cdot \left[\frac{h^3}{3} \nabla w \right] \varphi \, d^2 \mathbf{x}, \\ 0 &= \int_{\Omega} (-w + \Delta h + \Pi(h)) \varphi \, d^2 \mathbf{x}.\end{aligned}\tag{3.14}$$

All terms containing spatial derivatives can now be integrated by parts, effectively reducing the smoothness conditions on the fields h and w which can then be expressed in terms of linear ansatz functions:

$$\begin{aligned}0 &= \int_{\Omega} (\partial_t h) \varphi \, d^2 \mathbf{x} - \int_{\Omega} \left[\frac{h^3}{3} \nabla w \right] \cdot \nabla \varphi \, d^2 \mathbf{x} + \int_{\partial \Omega} \varphi \left[\frac{h^3}{3} \nabla w \right] \cdot \mathbf{ds}, \\ 0 &= \int_{\Omega} \left((-w + \Pi(h)) \varphi - \nabla h \cdot \nabla \varphi \right) d^2 \mathbf{x} + \int_{\partial \Omega} \varphi \nabla h \cdot \mathbf{ds}.\end{aligned}\tag{3.15}$$

Due to the integration by parts, integrals along the boundary of the domain $\partial \Omega$ occur, in which \mathbf{ds} denotes the line element ds along the boundary pointing in the direction of the outside unit normal \mathbf{n} , i.e., $\mathbf{ds} = \mathbf{n} ds$. If Eq. (3.15) are fulfilled for any test function φ , then they are equivalent to the strong formulation (3.13).

The integrals in the weak formulation can now be subdivided into integrals on each single element. We now choose the same equidistant discretization as in (3.2) to obtain a rectangular

decomposition of the domain

$$\Omega = \bigcup_{i,j} \Omega_{ij} \quad \text{with} \quad \Omega_{ij} = [i \Delta x, (i+1) \Delta x] \times [j \Delta y, (j+1) \Delta y]. \quad (3.16)$$

On each element, the order parameters can now be expanded in terms of local ansatz functions that only have a compact support. As mentioned earlier, we will use ansatz functions linear in both x and y direction which effectively have the values u_{ij} at the corners of the elements (the so-called nodes) as degrees of freedom. Following the classical Galerkin approach (see, e.g., [Eva10]), the same ansatz functions are used for the test functions φ . Inserting these into the weak formulation, one can also simplify the integrals to appropriately weighted sums. The result is again an algebraic set of equations for the unknown coefficients defining the ansatz functions. Boundary conditions that are posed in the models can be directly included into the weak formulation inside the boundary integrals. Particularly easy to implement are homogeneous Neumann boundary conditions, as they simply lead to vanishing boundary integrals.

Still, we have neglected the treatment of the temporal derivative up to now. In the following section we will describe how it can also be discretized. Then, the resulting set of equations can be solved for the coefficients of the ansatz functions using, e.g., a numerical Newton method. The solution to the actual problem for h and w in Eq. (3.13) can be reconstructed from the local ansatz functions using the then-found coefficients.

3.2 Time Stepping Methods

After the discretization in space and the application of a finite difference method or a finite element method, the partial differential equations under consideration are transformed into sets of coupled ordinary differential equations. To finally solve these as an initial value problem, time stepping methods are needed. For a discussion of these, we will now consider a general system of first order ordinary differential equations:

$$\frac{d}{dt} \mathbf{u}(t) = f(\mathbf{u}(t), t). \quad (3.17)$$

As an example, the vector \mathbf{u} may now comprise all the values u_{ij} of the order parameter on the spatial grid points after discretization as presented in Sec. 3.1 and $f(\mathbf{u}, t)$ would be the expression resulting from the finite difference approximation of the spatial derivatives and nonlinear contributions. The simplest way to construct a time stepping scheme is now the *explicit Euler method*, which simply replaces the temporal derivative by a forward finite difference approximation,

$$\frac{\mathbf{u}(t + \Delta t) - \mathbf{u}(t)}{\Delta t} = f(\mathbf{u}(t), t), \quad (3.18)$$

which can be solved for $\mathbf{u}(t + \Delta t)$, resulting in the Euler scheme

$$\mathbf{u}(t + \Delta t) = \mathbf{u}(t) + \Delta t f(\mathbf{u}(t), t). \quad (3.19)$$

This scheme provides an explicit rule for advancing from a given state $\mathbf{u}(t)$ by a step Δt in time. Obviously, the approximation becomes better for smaller time steps Δt and, similar to the case of the forward difference scheme in space in Eq. (3.6), the truncation error in this approximation is proportional to Δt . The so-called Runge–Kutta methods can also be derived

with a higher order of accuracy by not only calculating $f(\mathbf{u}, t)$ once in each time step and then taking it to be constant for the whole time interval $[t, t + \Delta t]$, but by approximating it with intermediate values at several so-called stages within the time interval. Explicit Runge–Kutta methods of stage s can be formulated in the form

$$\mathbf{u}(t + \Delta t) = \mathbf{u}(t) + \Delta t \sum_{i=1}^s \gamma_i \mathbf{k}_i, \quad (3.20)$$

where the \mathbf{k}_i denote the evaluation of the right-hand side $f(\mathbf{u}(t), t)$ at the intermediate steps

$$\mathbf{k}_i = f \left(\mathbf{u}(t) + \Delta t \sum_{j=1}^{i-1} \beta_{ij} \mathbf{k}_j, t + \alpha_i \Delta t \right). \quad (3.21)$$

That is, each stage builds upon the previous stages to achieve the next approximation. A specific Runge–Kutta scheme is defined by a set of the coefficients γ_i , β_{ij} and α_i , which can be handily compiled in a so-called Butcher tableau [But08], see Table 3.1. In general, Runge–

0					
α_2	β_{21}				
α_3	β_{31}	β_{32}			
\vdots	\vdots	\vdots	\ddots		
α_s	β_{s1}	β_{s2}	\cdots	$\beta_{s\ s-1}$	
	γ_1	γ_2	\cdots	γ_{s-1}	γ_s

Table 3.1: Butcher tableau for an explicit Runge–Kutta method of stage s compiling the coefficients γ_i , β_{ij} and α_i , cf. Eq. (3.21).

Kutta methods with more stages can lead to higher orders of accuracy. However, beyond $s = 4$, the order p of accuracy does not scale linearly with s anymore.

Two Runge–Kutta methods of different order can be combined to obtain a measure for the error that is made in each time step by comparing the result of the lower order method to the one of the higher order method as a reference. This estimated error can then be used to control the time step size Δt . With this, a time stepping scheme can be achieved whose error stays bounded within a desired range. We will use an embedded Runge–Kutta–Dormand–Prince method in the following, in which a fourth- and a fifth-order method are embedded in one seven stage method, see Table 3.2 for the Butcher tableau. In this context embedded means that the two solutions of different order utilize the same stages, reducing the computational costs. We skip a precise description of the time step adaptation algorithm here and refer to [Wil12], where it is also employed and discussed in detail.

The presented Runge–Kutta methods are explicit, indicating that the new state $\mathbf{u}(t + \Delta t)$ can be explicitly expressed in terms of the previous state $\mathbf{u}(t)$. This has the advantage that the new state can be easily calculated using the information from the previous step. However, such explicit time stepping schemes generally suffer from strict stability constraints concerning the possible step size Δt . This implies that errors from the time stepping can accumulate leading to a diverging solution, unless the time step size is small enough. How small it has to be strongly depends on the actual equation and also the spatial discretization size. In general, stiff equations with high orders of spatial derivatives, such as the Cahn–Hilliard equation (2.59)

0							
$\frac{1}{5}$	$\frac{1}{5}$						
$\frac{3}{10}$	$\frac{3}{40}$	$\frac{9}{40}$					
$\frac{4}{5}$	$\frac{44}{45}$	$-\frac{56}{15}$	$\frac{32}{9}$				
$\frac{8}{9}$	$\frac{19372}{6561}$	$-\frac{25360}{2187}$	$\frac{64448}{6561}$	$-\frac{212}{729}$			
1	$\frac{9017}{3168}$	$-\frac{355}{33}$	$\frac{46732}{5247}$	$\frac{49}{176}$	$-\frac{5103}{18656}$		
1	$\frac{35}{384}$	0	$\frac{500}{1113}$	$\frac{125}{192}$	$-\frac{2187}{6784}$	$\frac{11}{84}$	
	$\frac{32}{384}$	0	$\frac{500}{1113}$	$\frac{125}{192}$	$-\frac{2187}{6784}$	$\frac{11}{84}$	
	$\frac{5179}{57600}$	0	$\frac{7571}{16695}$	$\frac{393}{640}$	$-\frac{92097}{339200}$	$\frac{187}{2100}$	$\frac{1}{40}$

Table 3.2: Butcher tableau for the embedded Runge–Kutta–Dormand–Prince method. The two lowest rows present the coefficients γ_i for the fourth-order and the fifth-order solution, respectively.

and the thin film equation (2.31), typically pose particularly strong time step restrictions with explicit time stepping schemes.

Such restrictions can be resolved by implicit time stepping schemes. The simplest example is the *implicit Euler scheme*,

$$\mathbf{u}(t + \Delta t) = \mathbf{u}(t) + \Delta t f(\mathbf{u}(t + \Delta t), t + \Delta t), \tag{3.22}$$

where the only difference to the explicit Euler scheme (3.19) is the time at which f is evaluated. It can be shown that this time stepping method is A-stable [Dah63], meaning it is stable irrespective of the time step size for certain model problems. The downside of any implicit scheme is that solving for the new state $\mathbf{u}(t + \Delta t)$ involves solving a (most often nonlinear) set of equations in every time step. Also implicit methods can be derived for higher orders of accuracy. Examples are the *diagonally implicit Runge–Kutta* (DIRK) methods [Ale77] which have the same form as the Runge–Kutta methods presented above with the difference that each stage is implicit, i.e., the coefficient matrix β_{ij} has a non-zero diagonal $\beta_{ii} \neq 0$. Just as the implicit Euler scheme, they are also A-stable. In particular, there exists one DIRK method that achieves an order $p = 2$ with only $s = 2$ stages, which is depicted in the Butcher tableau in Table 3.3. This method will be used for the thin film models together with the finite element method.

α	α	0
1	$1 - \alpha$	α
	$1 - \alpha$	α

Table 3.3: Butcher tableau for the second order DIRK method with $\alpha = 1 + \frac{1}{2}\sqrt{2}$ [Ale77]. Notice the non-zero diagonal entries β_{ii} , indicating an implicit scheme.

Whether an explicit or implicit time stepping scheme should be used, strongly depends on

the particular problem at hand. In particular, stiff equations crucially benefit from an implicit scheme, i.e., the increased effort for solving the implicit set of equations is outweighed by the possible larger time step size, resulting in a smaller overall computational effort. The following section presents the combinations of methods that will be used for the different models in the remainder of this thesis.

3.3 Practical Implementations

For the models analyzed in this thesis, two different actual implementations of numerical methods are used. The first implementation utilizes a combination of second order central finite difference schemes to discretize the spatial derivatives and an adaptive explicit Runge–Kutta–Dormand–Prince time stepping method. This combination has the advantage that all resulting expressions for advancing the current state in time are explicit and therefore no solving of nonlinear sets of equations is necessary. In addition, the temporal evolution at one certain grid point only depends on the values in a finite-range neighborhood. Therefore the approach lends itself to an easy parallelization, as the interdependence between different subdomains is limited to regions close to the boundaries of these subdomains.

In particular, this approach is implemented in C++ employing the CUDA toolkit [NVI] which enables computations on modern graphics processors. Such graphics processors were developed to accelerate computer graphics applications and in particular computer games. Because a single frame of a computer game consists of several million pixels, these processors are designed with a massive parallel processing of data in mind. Therefore, current top-of-the-line graphics processors can have more than 2000 computing cores working in parallel. As the demand for complex computer graphics applications grew, also the capabilities of the graphics processors increased, making them interesting for computational tasks apart from graphics, the so-called *General Purpose Computation on Graphics Processing Units* (GPGPU). In general, all tasks that can be subdivided into many small independent sub-tasks can be suitable to be solved using GPGPU. The explicit Runge–Kutta finite difference scheme fits perfectly into this category, as the problem can be subdivided up to the level of individual grid points, where the resulting necessary computations are just simple explicit algebraic operations. This approach is used for the augmented Cahn–Hilliard model (2.59) and the fully hydrodynamic model for Langmuir–Blodgett transfer (2.51) in Chap. 4, where both models are used to describe the Langmuir–Blodgett transfer onto prestructured substrates.

The nonlinear character of the thin film equation makes it particularly stiff for height profiles with large ratios of the lowest and highest film height, i.e., it is difficult to treat it with explicit methods. Therefore, we employ a second numerical approach for all cases involving thin film equations with large film heights. For this, the finite element method is combined with an implicit Runge–Kutta scheme of order 2. This approach is implemented in C++ using the open-source framework DUNE (Distributed and Unified Numerics Environment) [BBD⁺08b, BBD⁺08a, BHM10]. The DUNE framework provides several modules that each target specific problems arising when numerically solving partial differential equations with grid-based methods. The DUNE-PDELab module, for example, facilitates the discretization of equations using, amongst others, finite element methods. Other modules provide the necessary infrastructure, such as interfaces to grid managers available in DUNE-grid or iterative solvers implemented in DUNE-istl (iterative solver template library). The framework is heavily template-based and uses generic programming techniques to facilitate both an effective

technical implementation of the underlying mathematical concepts and numerically efficient computations. In particular, DUNE is readily designed for high-performance computing, i.e., for massively parallel computations on computer grids. Most computations presented in this thesis were therefore conducted on PALMA, a Linux cluster of the University of Münster comprising more than 3000 CPU cores.

Apart from direct numerical simulations, also other methods can be employed to analyze models such as the thin film equation. In the next section, so-called *continuation techniques* are introduced that can provide an in-depth view of the bifurcation structure of such models.

3.4 Continuation Methods

Direct numerical simulations aim at the analysis of the temporal behavior of a model. This is particularly useful when the long-time dynamics of the model exhibits a time-dependent behavior, such as time-periodic solutions, e.g., in the Langmuir–Blodgett transfer corresponding to the transfer of stripes. However, the dynamics often converges to stationary solutions, i.e., solutions that have no more temporal evolution to the numerical exactness and therefore their time derivative in the constituting equation vanishes. Still, the transient time spans in which the dynamics slowly converges to such a stationary solution can be rather large. This makes direct numerical simulations computationally costly, especially if one is interested in the solutions for a whole range of control parameters. Therefore, it can be reasonable to not solve the fully dynamic problem in such situations, but the stationary problem with the time derivative fixed to zero. The resulting equations can then be solved with an iterative method, such as a Newton method. This is typically much more efficient than solving the time-dependent problem. In addition, this approach also has the advantage that it can be used to obtain *unstable* solutions which cannot be achieved with direct numerical simulations. But as the stability of a solution is a solely dynamical property, it plays no role for the stationary problem. For a full understanding of a model, knowledge about unstable stationary solutions is very valuable.

Still, the usage of a Newton method for the stationary problem has an important prerequisite: For the method to converge, one needs a sufficiently good initial guess for the solution. Without such, it is impossible to obtain a solution at all. The basic purpose of all *continuation methods* is to find a good initial guess for a certain set of parameters based on known solutions for slightly different parameters. The following description follows the lecture notes of Doedel [Doe]. The continuation approach relies on the assumption, that a solution changes only slightly for small parameter changes. The mathematical foundation for this assumption is the *Implicit Function Theorem* (IFT). If we consider any of the partial differential equations of the models we introduced in this thesis after discretization of the spatial derivatives and neglecting the time derivative, one is left with a nonlinear set of equations that can be written in the form

$$\mathbf{G}(\mathbf{u}, \lambda) = 0, \quad (3.23)$$

where \mathbf{u} is a solution vector comprising all degrees of freedom of the order parameters on the spatial discretization and λ is one of the control parameters whose influence on the solution should be studied. The IFT now states that if

- (i) $\mathbf{G}(\mathbf{u}_0, \lambda_0) = 0$ for a known solution \mathbf{u}_0 and parameter λ_0 ,
- (ii) the Jacobian matrix $(\partial_{u_j} G_i(\mathbf{u}_0, \lambda_0))_{ij}$ is non-singular, and

(iii) $\mathbf{G}(\mathbf{u}, \lambda)$ and $\partial_{u_j} G_i(\mathbf{u}, \lambda)$ are smooth near $(\mathbf{u}_0, \lambda_0)$,

then there exists an open set U_0 containing \mathbf{u}_0 and an open set Λ_0 containing λ_0 such that

$$\forall \lambda \in \Lambda_0 \quad \exists \quad \mathbf{u} \in U_0 : \mathbf{G}(\mathbf{u}, \lambda) = 0. \quad (3.24)$$

In other words, if the prerequisites of the IFT are fulfilled, then there exists a whole family of solutions $\mathbf{u}(\lambda)$ close to $\mathbf{u}_0(\lambda_0)$. The proof can be found in any textbook on multivariable calculus, e.g., [Kön04]. Using this theorem, a first simple continuation approach can use $\mathbf{u}_0(\lambda_0)$ as an initial guess for a Newton method at a slightly varied parameter $\lambda_0 + \Delta\lambda$. For a sufficiently small $\Delta\lambda$, the Newton method should converge according to the IFT. Now a next step for an again slightly varied parameter can be performed, successively following the whole solution family $\mathbf{u}(\lambda)$. This procedure is called *parameter continuation* and is already suitable to obtain complete solution families. However, it fails at a fold of the solution family, see Fig. 3.1 where such a fold is marked as $(u_{\text{SN}}, \lambda_{\text{SN}})$. There, the Jacobian $(\partial_{u_j} G_i(\mathbf{u}_0, \lambda_0))_{ij}$ is no longer invertible, i.e.,

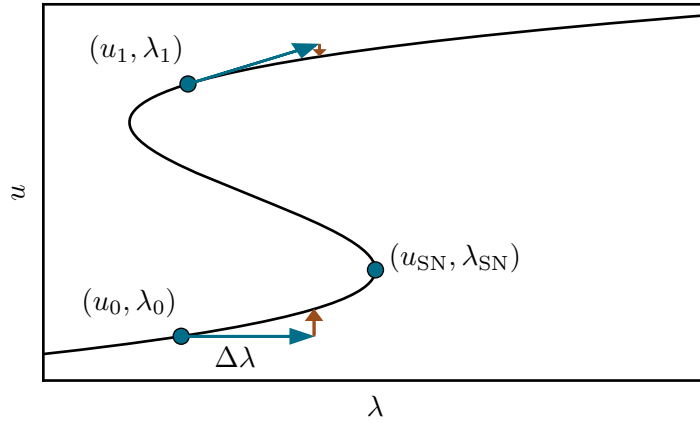


Figure 3.1: Sketch of a solution family $u(\lambda)$. For a simple parameter continuation, a known solution $u_0(\lambda_0)$ is used as an initial guess for a Newton method starting at $(u_0, \lambda_0 + \Delta\lambda)$ (indicated by an red arrow). This approach fails at a saddle-node bifurcation which occurs at a fold of the solution family, depicted by the point $(u_{\text{SN}}, \lambda_{\text{SN}})$. More advanced continuation methods provide a better initial guess for the Newton method by advancing a known solution (u_1, λ_1) tangentially to the solution branch.

singular, and therefore the IFT no longer holds. Still, this problem can be fixed by not taking λ as a parametrization of the solution family but one component of \mathbf{u} , indicating that even near a fold, the solution family $\mathbf{u}(\lambda)$ is unique. Therefore, more advanced continuation methods can also track solution families around such folds, which typically indicate a saddle-node bifurcation. One such method is the pseudo-arclength continuation invented by Keller [Kel77]. The basic idea is to augment the stationary problem (3.23) with an additional independent parameter s which represents an approximate arclength along the solution branch $\mathbf{u}(\lambda)$. This is beneficial, as the resulting Jacobian matrix can be non-singular even where the original one was singular, e.g., at a fold. Therefore, in this parametrization, also a continuation around a fold is possible. In addition, the initial guess for each new Newton iteration is obtained by extrapolating the solution family tangentially to the already known part. In contrast to simply taking the

previous solution as initial guess as suggested above, this typically provides a better guess and therefore a faster converging Newton method. Here, we do not detail the concrete math of this algorithm and refer to the corresponding literature [Kel77, Doe, Kuz10, DWC⁺14].

One remaining aspect to address is a way to obtain the very first solution $\mathbf{u}_0(\lambda_0)$ to start the continuation procedure. Sometimes an analytical solution for a certain parameter is known which can then serve as a starting solution. If this is not the case, also a solution obtained by a direct numerical simulation can be used, provided it has sufficiently converged. This has the disadvantage of being reliant on an additional numerical implementation, which might not be at hand. Therefore, an approach utilizing only the continuation method is desirable. To this end, a rather elegant ansatz is a homotopy method [AG03, TBT13]: For instance, one augments the equation of interest by an artificial parameter, e.g., μ , that multiplies the terms of the equation that hinder finding an analytical solution. Then, one determines the analytical solution for $\mu = 0$ and uses it as a starting solution for a continuation in the parameter μ from $\mu = 0$ to $\mu = 1$. The latter solution is now a solution to the original equation without the artificial parameter and can serve as a starting point for the actual continuation of interest.

In summary, continuation methods provide a very efficient way to obtain whole solution families of a given problem with the additional benefits that dynamically unstable solutions can be found and also multistable regions, i.e., regions in the parameter space where more than one stable solution exists, can be easily identified. To date, multiple ready-made software packages exist that can be conveniently employed for continuation. In particular, the software AUTO-07p [DKK91a, DKK91b] is employed in Chap. 5 to obtain a bifurcation diagram for a thin liquid layer on a substrate that is dragged out of a liquid reservoir. In addition, the `pde2path` package is used in Chap. 6 to analyze the bifurcation diagram of fully three-dimensional sliding drops on an inclined substrate.

4 Controlling Pattern Formation in Langmuir–Blodgett Transfer

When transferring monomolecular layers of surfactants onto solid substrates using the Langmuir–Blodgett (LB) transfer, interesting pattern formation phenomena can occur. These lead to an inhomogeneous coverage of the substrate with the surfactant layer in lattice or stripe patterns of different orientations on a micrometer scale. To utilize such patterns in applications, on the one hand a thorough understanding of the underlying pattern formation mechanism is needed to identify the relevant system parameters that can be used to influence the process. On the other hand, it is desirable to introduce and analyze additional mechanisms that enable a more extensive control of the system. Such control mechanisms are particularly needed for future applications that necessitate a high precision and reproducibility of the patterns.

To this end, the control possibilities using prestructured substrates for the LB transfer will be explored in Sec. 4.2, followed by a brief outlook into another control mechanism using temporally modulated control parameters in Sec. 4.3. The latter is a particularly promising approach, as it can provide a control over the process that does not involve a previous alteration of the substrate. But before these methods are discussed, in Sec. 4.1, the pattern formation mechanism during the LB transfer onto homogeneous substrates is briefly recapitulated, as it provides the basis for all other considerations.

4.1 Langmuir–Blodgett Transfer onto Homogeneous Substrates

Pattern formation during the LB transfer onto homogenous substrates has already been analyzed in detail in multiple publications using an augmented Cahn–Hilliard model (2.59) [Köp11, KGFT12, Wil12, WG14, KT14]. There, the dependence of the occurring pattern formation on experimental parameters such as the transfer velocity and the surfactant density in the LB trough was studied, including an extensive study of the bifurcation structure of the system. Here, we will only cover the basic features that are needed for an understanding of the results obtained using control mechanisms as presented in the subsequent sections.

In general, there exist four qualitatively different solution types, depending on the velocity at which the substrate is withdrawn from the LB trough. At small transfer velocities below a certain threshold, a homogeneous layer of molecules in the high-density *liquid-condensed* (LC) phase is transferred. The value of the order parameter field is always smaller than zero at the lower $x = 0$ boundary, which indicates that the surfactant molecules on the liquid reservoir in the LB trough are in the low-density *liquid-expanded* (LE) phase. This indicates that there occurs a homogeneous phase transition due to the substrate-mediated condensation (SMC, cf. Sec. 2.2.3). For larger transfer velocities, this is no longer the case and a striped deposit is produced, where the stripes are parallel to the transfer direction and consist of alternating domains in the LE and LC phase. As the stripes are then oriented vertically, this pattern will also be denoted as *vertical stripes* in the remainder. In this regime, the SMC leads to a spatially inhomogeneous phase transition at the contact line. For larger transfer velocities

beyond another threshold, this pattern becomes unstable and instead a striped deposit is formed, where the stripes are oriented perpendicular to the transfer direction, which will also be denoted as *horizontal stripes*¹. These patterns are homogeneous in the y direction and therefore represent pseudo one-dimensional structures. Here, the SMC induced phase transition occurs periodically in time at the contact line, corresponding to a temporal oscillation of the monolayer concentration at the meniscus. That is, at the meniscus, domains in the LC phase arise alternating with domains in the LE phase and are then carried away with the transfer velocity v . Also this pattern type ceases beyond another threshold velocity: At higher transfer velocities, a homogeneous layer in the LE phase is transferred and thus a phase transition is not anymore induced by the SMC. An overview of these four pattern types is shown in Fig. 4.1. Although we mentioned threshold velocities at which the pattern types change, the limits are

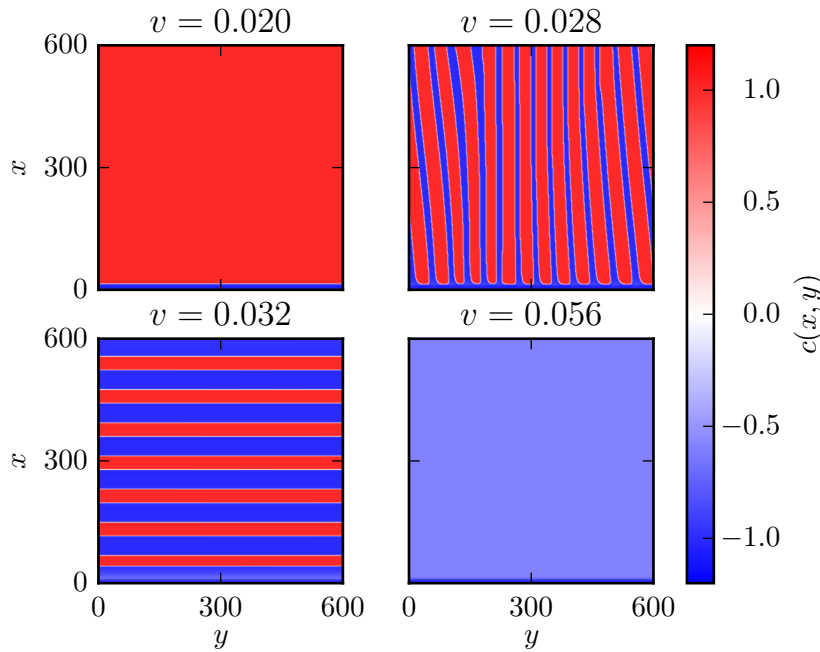


Figure 4.1: Overview of the four possible stable and periodic pattern types occurring as solutions of the augmented Cahn–Hilliard model (2.59) for different transfer velocities. For low transfer velocities, a homogeneous high-density LC layer is transferred (top left panel). For larger transfer velocities, a vertical stripe pattern occurs (top right panel), which changes to a horizontal stripe pattern for further increased velocities (bottom left panel). Beyond an upper velocity threshold, no more patterned deposits occur and instead a homogeneous, low-density LE layer is transferred (bottom right panel) (cf. [WG14]).

not sharp, as all the transitions exhibit hysteresis. That is, there are several multistable regions in which different pattern types are stable. In these regions, the multiple stable patterns are equally possible and only the initial conditions determine which pattern is chosen. This multistability can be well illustrated in a bifurcation diagram comprising all these solution

¹In fact, the horizontal stripe pattern originates from an instability of the homogeneous solution, while the vertical stripe patterns occur as a result of a secondary instability of the horizontal stripes, cf. [Wil12].

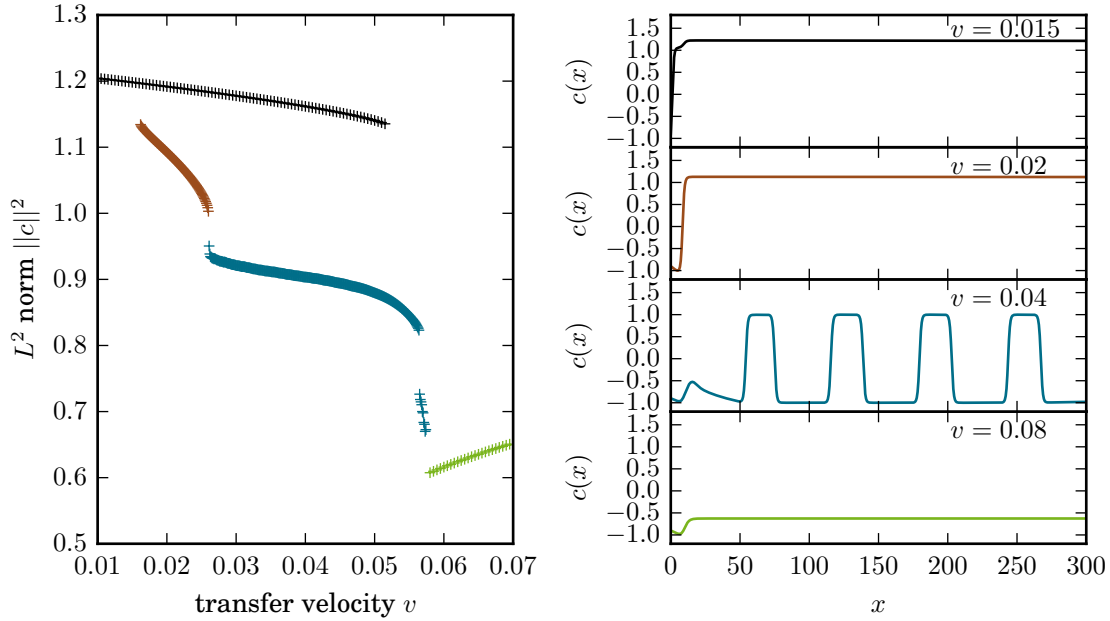


Figure 4.2: Left: Bifurcation diagram showing the L^2 -norm of the four possible stable pattern types occurring as one-dimensional solutions of the augmented Cahn–Hilliard model (2.59) for different transfer velocities. Right: Exemplary solution snapshots for each of the solution branches (cf. [KGFT12, WG14, KT14]).

types. Figure 4.2 shows the L^2 -Norm $\|c\|^2$,

$$\|c\|^2 := \sqrt{\frac{1}{L_x} \int_0^{L_x} c(x)^2 dx}, \quad (4.1)$$

of the solutions obtained by direct numerical simulations. We also refer to [KGFT12], where in addition also branches of unstable solutions obtained by numerical path continuation are discussed and included into the bifurcation diagram. There, the branches of unstable steady solutions connect the stable ones and form a heteroclinic snaking structure in the bifurcation diagram. The branch of time-dependent stripe forming solutions is found to emerge from such an unstable solution branch in a homoclinic bifurcation and to cease on the branch of steady solutions in a region where a sequence of subcritical Hopf bifurcations occurs. Beyond, a homogeneous layer in the low-density LE phase is transferred (cf. green branch in Fig. 4.2). As we mostly focus on the time-dependent stripe forming solutions, we do not discuss the unstable solution types here further. The overall bifurcation structure is also discussed in great detail in [KT14]. In particular, also (unstable) time-periodic solutions originating in Hopf bifurcations from the steady solutions and ending in global sniper and homoclinic bifurcations are identified and studied.

Besides the pattern type being dependent on the transfer velocity, also the quantitative properties of the patterns depend on the velocity. In particular, one can study its influence on the pseudo one-dimensional horizontal stripe patterns. These patterns can be characterized by their wave number and the duty cycle of the stripes. The wave number k is defined through the

wavelength λ of the stripes as $k = 2\pi/\lambda$ and the duty cycle dc is the ratio of the width l_{LC} of the stripes in the LC phase to the wavelength, $dc = l_{LC}/\lambda$. The dependence of both quantities

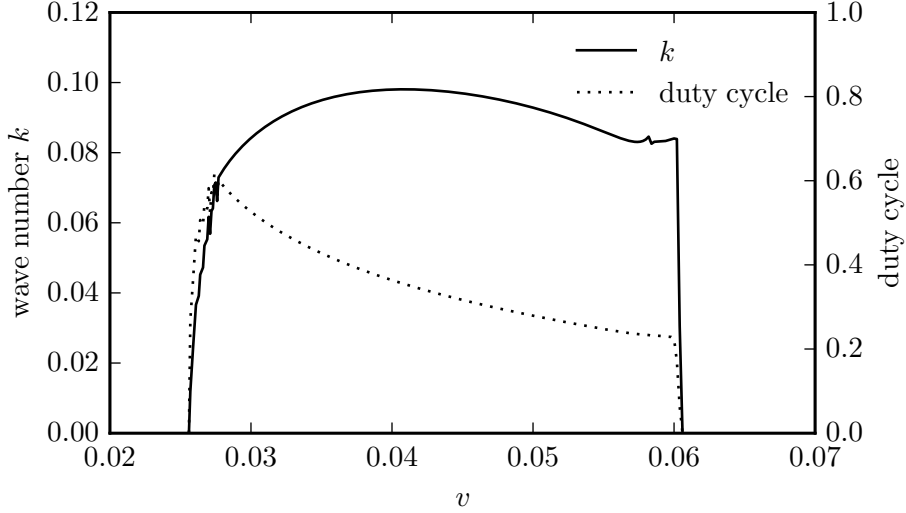


Figure 4.3: Dependence of the wave number k (solid line) and the duty cycle (dotted line) of horizontal stripe patterns on the transfer velocity v as obtained from one-dimensional simulations of the augmented Cahn–Hilliard model (2.59) for a fixed boundary concentration $c_0 = -0.9$. Zero wave numbers and duty cycles correspond to a homogeneous transfer (cf. [WG14]).

on the velocity v is shown in Fig. 4.3. The wave number develops non-monotonically with increasing transfer velocities with a global maximum at an intermediate velocity. In contrast, the duty cycle monotonically decreases with increasing transfer velocities. Therefore, patterns with the same wave number but different duty cycle can be achieved.

In addition to the transfer velocity, also the boundary concentration c_0 , i.e., the concentration of the monolayer prepared on the liquid in the LB trough, critically influences the pattern formation phenomena. This is visible in Fig. 4.4, where the wave number is shown in dependence on the transfer velocity and the boundary concentration. The overall qualitative behavior is similar to the one shown before in Fig. 4.3 for a fixed boundary concentration of $c_0 = -0.9$. However, the patterning regime, i.e., the velocity interval in which stripe patterns occur, becomes broader for increasing c_0 and becomes shifted towards larger velocities. In addition, the absolute values of the wave number are in general higher for larger values of c_0 . For rather large boundary concentrations $c_0 > -0.9$, a sharp kink becomes visible at high velocities close to the upper velocity threshold where the pattern formation ceases. In this regime, the location where the alternating stripes in the LE and LC phase are formed is no longer fixed at the meniscus, but it reaches further and further into the domain. As then the patterns occur more spontaneously similar to a spinodal decomposition, this mechanism is different to the previous one, where the decomposition is particularly induced at the meniscus position through the change of the SMC. Still, as this is rather a limiting case, we do not analyze this effect further. Now, we introduce a spatial prestructure and study its influence on the pattern formation process.

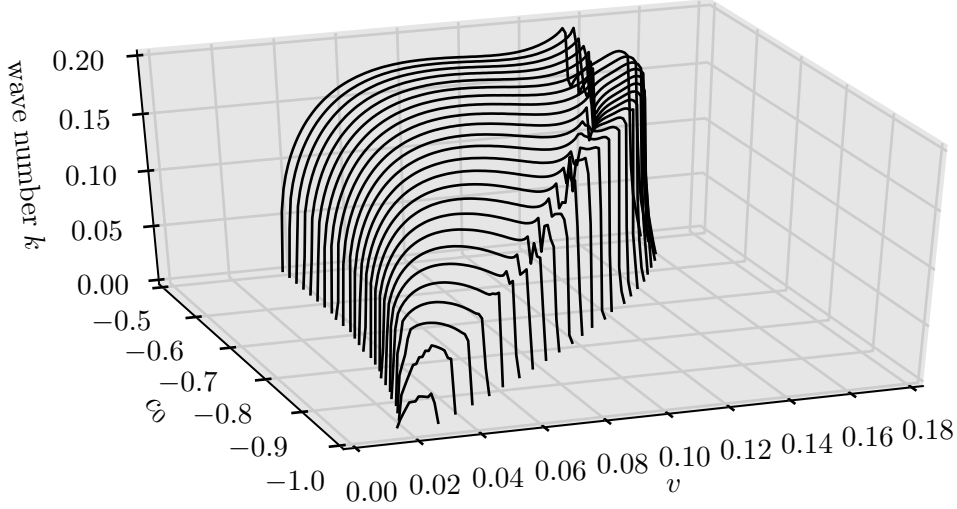


Figure 4.4: Dependence of the wave number k of horizontal stripe patterns on the transfer velocity v and the boundary concentration c_0 . An increasing boundary concentration shifts and extends the pattern forming velocity regime towards higher velocities and in general leads to higher absolute values of the wave number (cf. [WG14]).

4.2 Control through Prestructured Substrates

As already introduced in Sec. 2.4, we will now consider substrates that are chemically prestructured, i.e., substrates that are treated in a spatially inhomogeneous way altering certain properties, such as the wettability of the substrate. For the prestructures, we will restrict ourselves to stripe-like patterns either parallel or perpendicular to the transfer directory, as can be described by the functional forms (2.64)–(2.65). These functions enter the augmented Cahn–Hilliard model (2.59) as a modulation of the SMC term $\zeta(\mathbf{x})$ with an amplitude ρ . That is, we assume that the chemical prestructure influences the pattern formation process via a modulation of the strength of the SMC. When restricting the considerations to stripe-like prestructures, basically three defining parameters are of interest: (i) the strength, or contrast ρ of the modulation induced by the prestructure, (ii) the orientation of the stripes and (iii) the wavelength of the stripe prestructure. The influence of each of these control parameters will be studied in the following. Thereby, we follow along the lines of [WG14, ZWH⁺16].

We start with the consideration of a horizontal prestructure with a fixed wavelength $\lambda_{\text{pre}} = 60$ and varying contrasts ρ in one-dimensional simulations. Figure 4.5 shows the wave numbers of the resulting patterns as a function of the transfer velocity. In this presentation, the wave number is normalized to the wave number $k_{\text{pre}} = 2\pi/\lambda_{\text{pre}}$ of the prestructure, so that fractional values indicate a commensurable ratio between the wavelength of the prestructure and the wavelength of the occurring pattern. For a non-zero prestructure contrast ρ , the wave number curves deviate from the case without prestructure in certain transfer velocity intervals, in which the absolute value of the wave number jumps to a plateau and remains almost constant within the whole interval. On these plateaus, these absolute values have the aforementioned property indicating commensurability with $k/k_{\text{pre}} = 1/1$, $2/3$ or $1/2$. That is, in these velocity intervals,

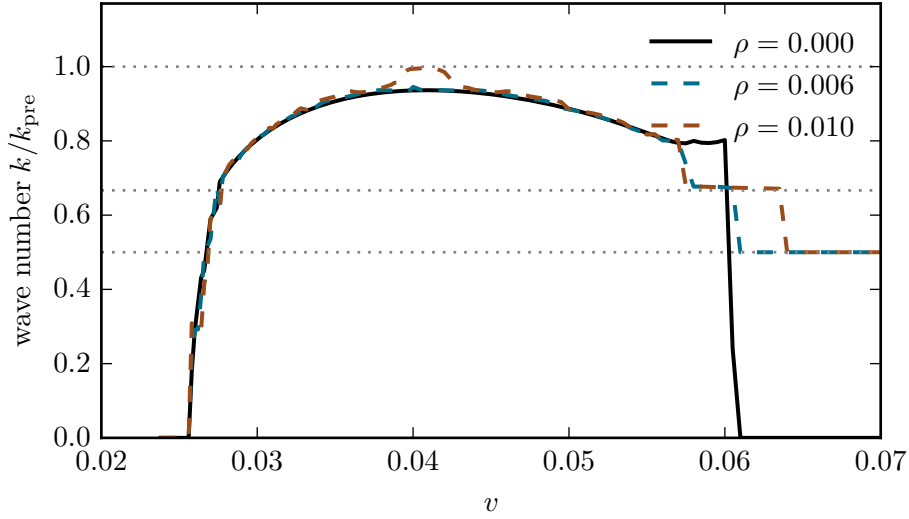


Figure 4.5: Dependence of the wave number k of horizontal stripe patterns on the transfer velocity v as obtained from one-dimensional simulations of the augmented Cahn–Hilliard model (2.59) for a prestructured substrate with wavelength $\lambda_{\text{pre}} = 60$. Each curve corresponds to a different prestructure contrast ρ (cf. [WG14]).

the stripe formation becomes *locked* to the forcing induced by the prestructure, meaning that the pattern formation process is effectively controlled by the prestructure. As one would expect, the velocity intervals exhibiting locking become larger for an increasing prestructure contrast, as can be seen when comparing the 1/2-plateaus of the red and blue curve for high transfer velocities in Fig. 4.5. In addition to this, there are two more notable effects. First, the patterning regime, i.e., the velocity interval in which a patterned deposit is possible, is also increasing with the prestructure contrast. This indicates, that a patterned deposit is particularly also possible for higher transfer velocities when using a prestructured substrate as compared to homogeneous substrates. Second, the range of achievable wave numbers is also increased by the prestructures, which becomes visible for the red curve in Fig. 4.5 at intermediate transfer velocities. There, the curve deviates upwards towards a 1/1 locking as compared to a homogeneous substrate, creating a stripe pattern that has a feature size that is smaller than what can be achieved without a prestructure.

The position and width of the locking plateaus could now be investigated more thoroughly in dependence on the prestructure contrast ρ . What then results are the so-called *Arnold tongues* of synchronization, which are tongue-shaped areas in the $\rho - v$ plane in which a certain locking ratio holds [PRK03]. As this has been already discussed in detail previously, we do not repeat it here and refer the reader to the literature [Wil12, WG14].

When now considering the full two-dimensional problem, one could expect additional instabilities that do not exist in one spatial dimension. However, for a horizontally prestructured substrate, this is not the case, as it is shown in Fig. 4.6. There, a horizontal prestructure with wavelength $\lambda_{\text{pre}} = 200$ and varying contrast ρ is considered. For all shown parameter combinations, a horizontal stripe pattern emerges. This indicates that the instability leading to vertical stripe patterns in the case of a homogeneous substrate can be effectively suppressed

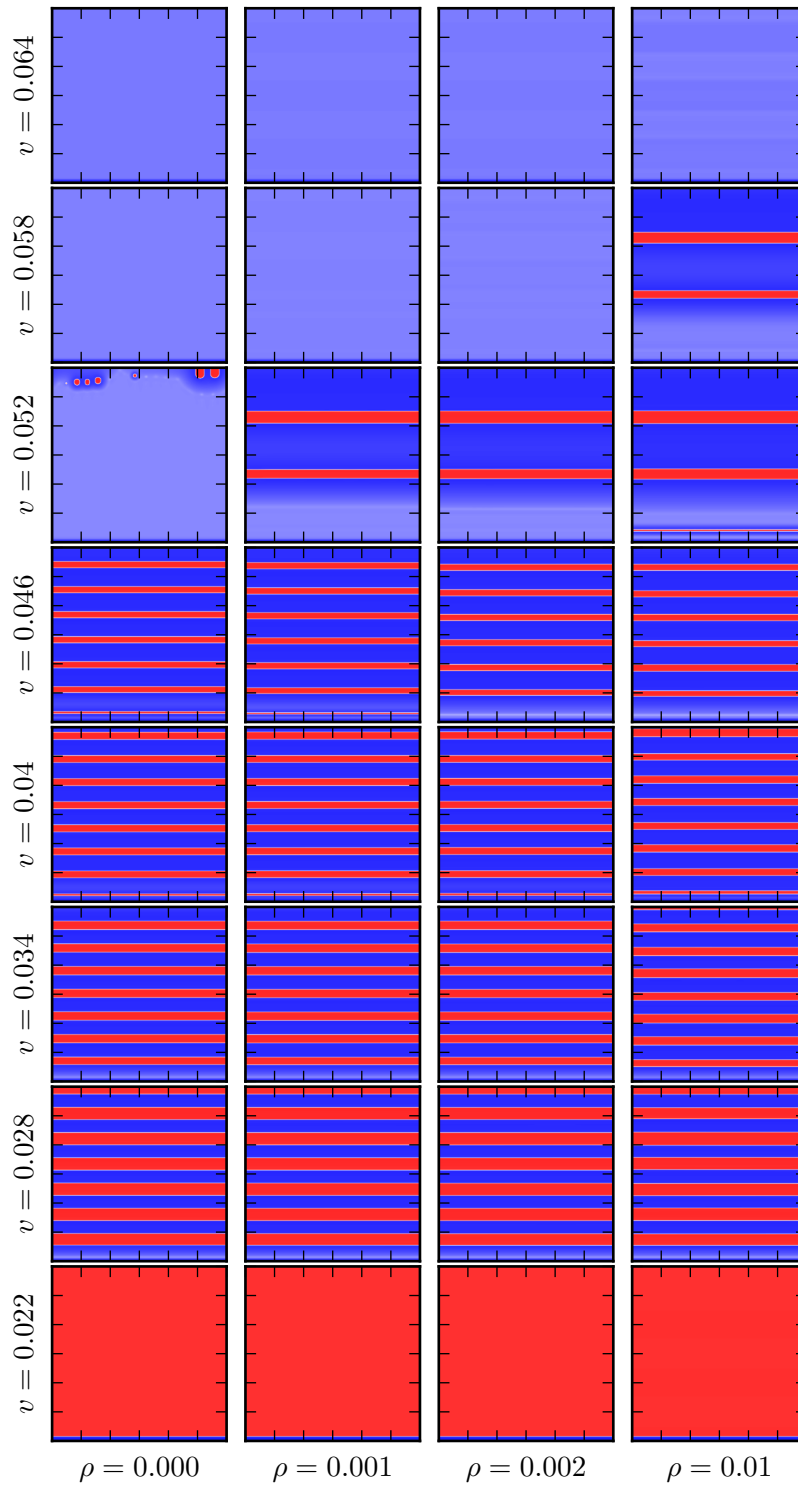


Figure 4.6: Overview of the occurring patterns in direct numerical simulations for a horizontally prestructured substrate with fixed prestructure wavelength $\lambda_{\text{pre}} = 200$ and varying transfer velocity v and prestructure contrast ρ (cf. [WG14]).

using a horizontally oriented prestructure. Just as in the one-dimensional case, one can again identify locking effects. They are particularly well seen for high velocities and prestructure contrast, such as $v = 0.052$, $\rho = 0.001$, where the stripe pattern has the same wavelength as the prestructure. Also the extension of the patterning regime towards higher velocities is achieved just as in the one-dimensional case, cf. Fig. 4.6, $v = 0.058$, $\rho = 0.000$ and $\rho = 0.010$. In addition to the results depicted in Fig. 4.6, there exist also small parameter regions, in which the horizontal stripe pattern is in fact destabilized by the horizontal prestructure (e.g., $v = 0.038$, $\rho = 0.01$, not shown here). There, the horizontal stripes decompose into smaller domains, which still exhibit an ordering along horizontal lines. This is reminiscent of similar effects found, e.g., in the Swift–Hohenberg equation [MHM08], where a forcing parallel to the natural stripe pattern induced oblique or rectangular patterns.

Next, we will consider a prestructure with different orientation, namely vertical stripes parallel to the transfer direction. In this case, a large variety of patterns can be observed, see Fig. 4.8 for an overview. For small transfer velocities, a vertical stripe pattern can be achieved, just as in the case of a homogeneous substrate. However, the wavelength can now be locked to the prestructure’s wavelength with a fixed ratio (e.g., 1:2 for $\rho = 0.001$, $v = 0.022$). For increased velocities ($v = 0.028$), oblique stripe patterns occur, whose stripes are inclined with respect to the prestructure orientation. However, this pattern is still the result of a two-dimensional locking of the wave number, which is seen when considering the projection of the wave vector of the stripe pattern onto the direction of the wave vector of the prestructure. This becomes particularly visible in the Fourier spectrum of such a pattern, as it is shown in Fig. 4.7. There, the y components of the dominant Fourier modes are integer multiples of the prestructure wave number. While this fixes the wavelength and inclination with respect to the prestructure, the direction of the inclination, i.e., if the patterns are tilted towards the left or the right, is not. Therefore, both directions can be observed, only depending on the initial conditions of the simulation.

For transfer velocities in which for homogeneous substrates only horizontal stripe patterns are observed, a vertical prestructure leads to the formation of lattice structures. These can be

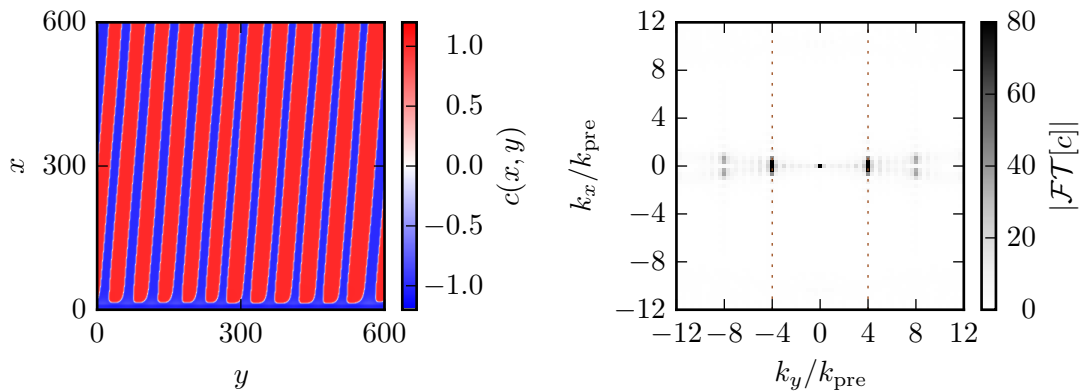


Figure 4.7: Left panel: Oblique stripe pattern occurring in a direct numerical simulation for a vertically prestructured substrate. Right panel: Fourier transform of the stripe pattern, revealing that the dominant Fourier modes in y direction are still integer multiples of the prestructure wave number k_{pre} (cf. [WG14]).

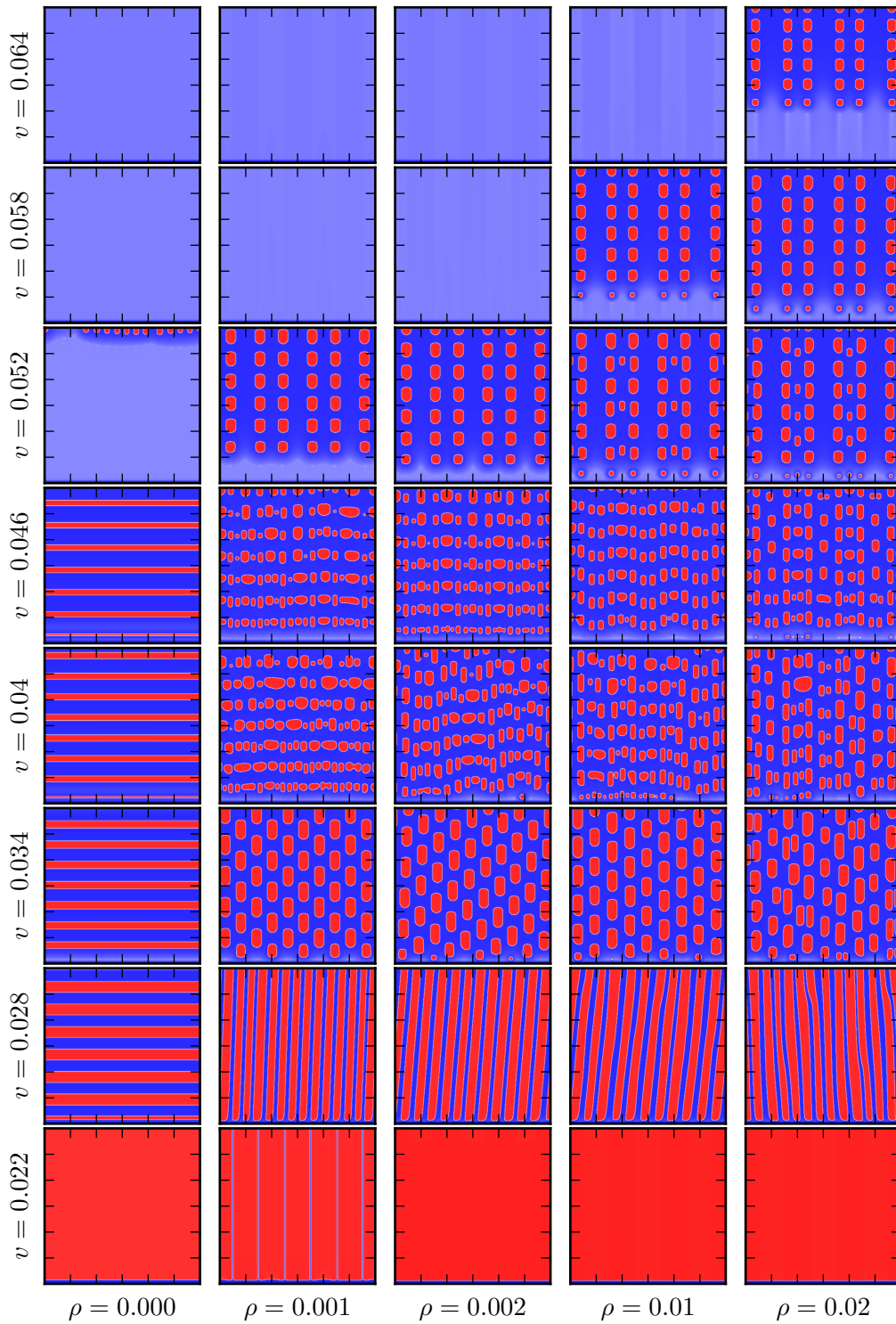


Figure 4.8: Overview of the occurring patterns in direct numerical simulations for a vertically prestructured substrate with fixed prestructure wavelength $\lambda_{\text{pre}} = 200$ and varying transfer velocity v and prestructure contrast ρ (cf. [WG14]).

either very regular (e.g., for $\rho = 0.001$, $v = 0.034$) with well aligned rows made of small domains in the LC phase, or irregular (e.g., for $\rho = 0.001$, $v = 0.04$). Still, an approximate ordering of the irregular domains in horizontal stripes can be seen. That is, the natural horizontal stripe pattern still exists, even though it is strongly disturbed by the vertical forcing due to the prestructure. At further increased transfer velocities ($v \geq 0.054$), again well-ordered lattice structures are formed. The rectangular arrangement of the domains in the LC phase can here be clearly seen as a superposition of the natural horizontal stripe pattern and the vertical prestructure.

In summary, a vertically oriented prestructure can be used to induce a multitude of complex patterns, very much in contrast to the case of a horizontally oriented prestructure. This again underlines the different nature of the horizontal and vertical stripe patterns typically occurring in LB transfer. The vertical stripe patterns emerge from a secondary instability of the horizontal stripe pattern [KGFT12] and are therefore easy to suppress with a horizontal prestructure, while the horizontal patterns cannot be suppressed with a vertical prestructure. In the latter case the complex patterns can therefore be seen as the result of the competition between the intrinsic pattern formation mechanism and the prestructure. Such a competition is also found in other pattern-forming systems that are subject to a spatial forcing (e.g., [RMM⁺03, MHM08]). There, also oblique and lattice structures are found to result from one-dimensional spatial forcings. This similarity is in fact remarkable, as the systems considered in [RMM⁺03, MHM08] have a specific intrinsic favored wave number that competes with the one of the forcing. However, this is in general not the case for any Cahn–Hilliard model, where no such distinct wave number exists. In the present case, the wave number selection arises not from the basic (undriven) model equation alone, but from the combination of it with the transfer geometry.

4.2.1 Comparison to Experimental Results

The results presented in the previous section were aimed at a broad understanding of the possible effects that a prestructured substrate can have on the pattern formation occurring in the LB transfer. Next, we apply them to specific cases that can be compared to experiments. One long-standing challenge for the productive usage of many pattern forming systems is the quality and reproducibility of the patterns [ZWH⁺16]. In the case of the LB transfer, in particular, irregularities of the stripe wavelength and the occurrence of branched patterns instead of perfectly regular stripes can hinder the usage of the pattern formation for applications. As has been shown in the previous section, prestructured substrates can exert a control over the pattern formation process and should therefore also lend themselves to improve the pattern quality.

The top row of Fig. 4.9 shows experimental results² of a LB transfer with prestructured substrates. In the cases shown, the prestructures consist of vertical 20 nm thick gold stripes parallel to the transfer direction, where the stripes have a width of 1 μm and the spacing (i.e., the distance) between the stripes (and therefore the overall wavelength of the stripe-pattern) is varied between 1 μm and 17 μm . The spacings are chosen in such a way that approximately an integer multiple of the natural wavelength fits into it. In the chosen parameter regime, a transfer onto a homogeneous substrate results in a vertically aligned, irregular branched pattern. For a spacing of 1 μm , the pattern formation process is seemingly stopped, as the whole groove between the prestructure stripes is homogeneously covered without apparent

²The experiments presented in this thesis were conducted by Juan Zhu during her PhD studies in the group of Prof. Lifeng Chi at the Physical Institute of the University of Münster.

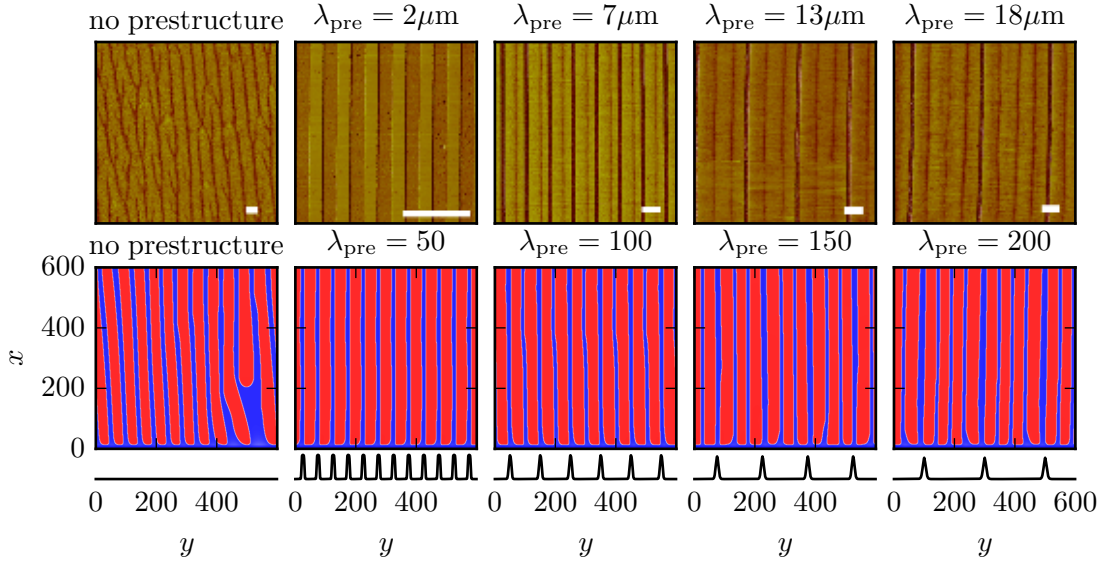


Figure 4.9: Comparison of experimental results (top row, white bars equal $5 \mu\text{m}$) and numerical simulations (bottom row) for vertically prestructured substrates used to control the naturally branched vertical pattern (cf. first column). Different spacings of the prestructure stripes lead to different locking ratios between the prestructure wavelength and the occurring pattern wavelength (1:1, 2:1, 3:1, 4:1 from left to right, numerical prestructure shown as 1d cut below the solutions, cf. [ZWH⁺16]).

pattern. Here it has to be noted, that one is only able to distinguish the phase of the surfactant layer between the prestructure stripes, but not on top of it. This is due to the fact that the prestructure stripes exhibit a roughness that is larger than the height difference between the LE and LC phase of the involved surfactant. An increased spacing of $6 \mu\text{m}$ (i.e., a wavelength $\lambda_{\text{pre}} = 7 \mu\text{m}$) is then large enough to accommodate one wavelength of the occurring LB pattern. This pattern is now perfectly regular and aligned with the prestructure. For larger prestructure spacings of $12 \mu\text{m}$ and $17 \mu\text{m}$, now two or three wavelengths of the LB pattern fit in between the prestructure stripes, respectively. Still, these patterns show a high regularity, indicating that the pattern formation is well controlled by the prestructure. The same is also true for prestructure spacings between the ones of the particular examples shown here. In the whole range of spacings from $2 - 9 \mu\text{m}$, exactly one distinct stripe of the LB pattern occurs, from $10 - 13 \mu\text{m}$, two stripes are observed and from $13 - 18 \mu\text{m}$, three stripes are achieved [ZWH⁺16]. That is, also the effective wavelength of the pattern is tunable within the given ranges. The cases in which multiple stripes of the LB pattern occur within the prestructure stripes again underline that the control of the pattern formation process is not just achieved in terms of a simple template, where the occurring pattern can only directly reproduce the pattern of the prestructure. Instead, the control mechanism is a real locking effect of variable ratio, as it was already described in the previous section for the augmented Cahn–Hilliard model (e.g., Fig. 4.5). To emphasize the analogy between the experimental results and the theoretical model, the second row of Fig. 4.9 shows snapshots from direct numerical simulations of the model (2.59) for prestructured substrates, where similar to the experimental case, thin prestructure stripes

with a variable spacing are considered (see one-dimensional sketch of the prestructure below the solution panels). Also in these simulations, a locking of the vertical pattern with different ratios can be observed, leading to well-aligned stripes with a well-controlled wavelength. Although this contrasting juxtaposition of experimental and theoretical results in Fig. 4.9 might suggest differently, the comparison is not meant in a quantitative way (which is beyond the scope of the model used here), but it should only underline the qualitative agreement. With this, we conclude that the theoretical model might not be quantitatively predictive for the experiments, but it is a valuable tool to explore the possibilities that can be then verified experimentally.

From the point of view of applications, besides the possibly achievable results, also the robustness of the method is of interest. This comprises, e.g., how strict the requirements with regard to the accuracy of certain experimental parameters are. We now want to analyze this by taking the orientation of the prestructure as example. To obtain the experimental

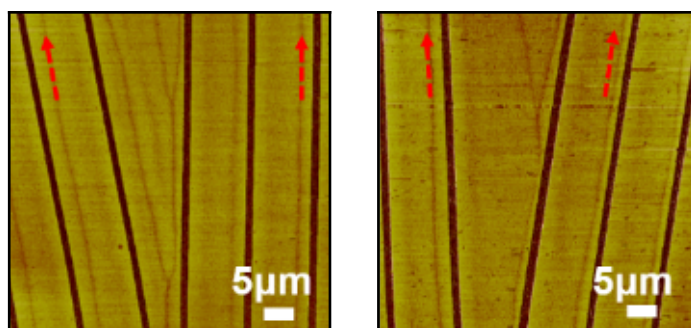


Figure 4.10: AFM images of a DPPC monolayer after LB transfer onto a prestructured substrate where the prestructure stripes are slightly inclined with respect to the transfer direction. The occurring stripe pattern (indicated by red arrows) closely follows the orientation of the prestructure (bold brown lines), even when the orientation changes (cf. [ZWH⁺16]).

results shown in Fig. 4.10, a prestructure was designed that consists of vertical stripe arrays that are not parallel to each other, but exhibit a small inclination. That is, the stripes of the prestructure are then also not perfectly parallel to the transfer direction, but slightly inclined by an angle of approximately 10° with respect to it. In a transfer velocity regime where normally a branched vertical stripe pattern would occur, this prestructure now leads to a stripe pattern that is again perfectly aligned with the prestructure stripes. This is in particular true where prestructure stripes with different inclination meet and form a wedge, leading to a stripe pattern reproducing the same shape. Whether the prestructure is inclined to the left or right with respect to the transfer direction is irrelevant, as can be seen by comparing both panels of Fig. 4.10. For an actual application of LB transfer with prestructured substrates, this presents a major advantage, as it means that the requirements regarding the needed accuracy of the orientation of the substrates used for the transfer are rather low. The very same behavior can also be observed in direct numerical simulations employing the augmented Cahn–Hilliard model. The three rows of Fig. 4.11 show snapshots at different times in a simulation, where a prestructure consisting of inclined stripes starts at a certain position and also stops again. The first row shows a snapshot shortly before the prestructure begins and the natural pattern

consists of slightly irregular vertical patterns. Quickly after the prestructure begins (middle row of Fig. 4.11), the stripe pattern becomes perfectly oriented with the inclined prestructure (always shown in the right panels of each row). After the end of the prestructure (bottom row panels), the pattern relaxes back to its non-inclined vertical stripe pattern. The case of an inclined stripe-like prestructure is therefore also well described by this model.

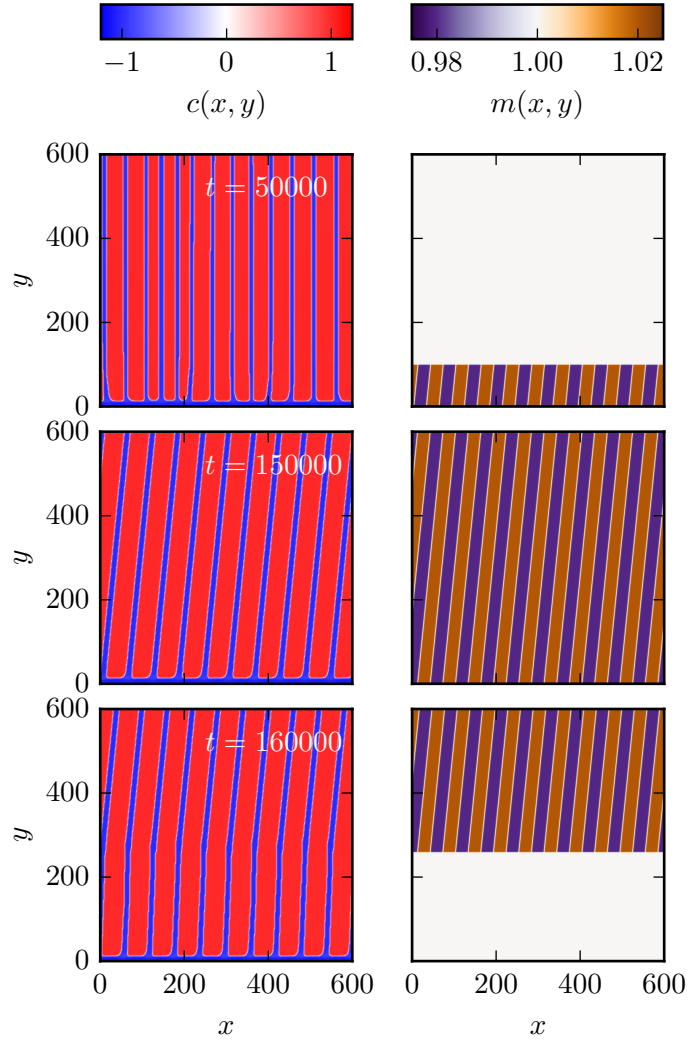


Figure 4.11: Snapshots at different times of a direct numerical simulation of Eq. (2.59) (left panels) for a prestructure that is inclined with respect to the transfer direction (right panels show modulation $m(x, y)$ of the SMC). In the absence of a prestructure, the pattern is not perfectly regular (top row), but it quickly becomes locked to the prestructure, even if it has a slightly different inclination (middle panels). At the end of the prestructure, the LB pattern quickly regains its natural vertical orientation (bottom panels, cf. [ZWH⁺16]).

In the cases we have considered up to now, the used combination of substrates and prestructures was only meant to weakly influence the pattern formation occurring during LB transfer, leading to an additional control mechanism over the natural pattern formation. In the following section, we will also cover cases, where the prestructure has a stronger influence on the pattern formation, leading to more complex patterns.

4.2.2 Complex Bent Structures due to Prestructured Substrates

One major assumption in the considerations on the control of LB patterns using prestructured substrates up to now was that the prestructure mainly influences the spatially inhomogeneous condensation of the surfactant monolayer. In contrast, an influence of the liquid layer between the surfactant layer and the substrate was assumed to be negligible. This implies that the prestructure should only induce small wettability changes as compared to the bare substrate and it is therefore thought to have only a minor impact on the hydrodynamics of the liquid layer. This is obviously a simplification which is not in general true. To cover this aspect, we now discuss a situation in which the hydrodynamics is significantly altered by the prestructure, which in turn also affects the pattern formation of the surfactant layer. An experimental

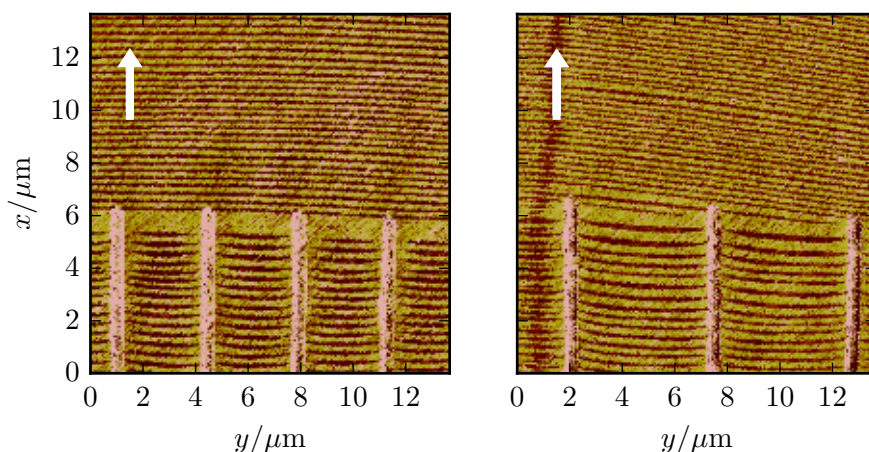


Figure 4.12: AFM phase images showing experimental results of a LB transfer of DPPC onto prestructured substrates. On the homogeneous part of the substrate (upper halves of the images), a horizontal line pattern occurs. In the presence of the prestructure (bottom half of the images, left panel $3\ \mu\text{m}$ spacing, right panel $5\ \mu\text{m}$ spacing), the patterns exhibit an upwards bend towards the gold stripes. The prestructure is visible in the lower half as vertical pinkish lines. The transfer direction is from bottom to top and indicated by the white arrows (cf. [WZC⁺17]).

situation where this is the case is shown in Fig. 4.12. There, an LB transfer is performed in a parameter regime that leads to a horizontally aligned stripe pattern on a homogeneous substrate. A vertically oriented stripe prestructure consisting of $50\ \text{nm}$ thick gold stripes on a $3\ \text{nm}$ thick chrome adhesion layer now breaks this stripe pattern, which only persists between the stripes. Interestingly, the stripe pattern consists no longer of perfectly straight horizontal stripes, but instead the stripes exhibit a curvature in a way that the left and right sides of each stripe are bent upwards in the vicinity of the prestructure stripes. With this, the occurring

stripes resemble the form of a liquid meniscus in a thin vertical tube, where the capillarity deforms the liquid-air interface. With this observation, it seems plausible that a deformation of the liquid layer due to the prestructure is involved in the formation of such a curved pattern. This assumption is further supported by the fact that the substrate-mediated condensation being responsible for the pattern formation, significantly acts only near the contact line so that a deformation of the latter should strongly influence the resulting pattern formation. However, this hypothesis is difficult to check experimentally, as only the created pattern *after* a LB transfer can be observed using AFM microscopy, but the dynamics of the liquid layer *during* the LB transfer is hardly accessible. Therefore, we will now employ direct numerical simulations of the fully hydrodynamic model (2.51) to qualitatively reproduce the experimental findings based on our assumptions. A snapshot of such a simulation is shown in Fig. 4.13, where the top panel shows the occurring pattern of the surfactant layer and the middle panel shows the liquid layer height profile. In this height profile, one can identify that the liquid layer reaches further into the domain (i.e., more upwards with the transfer direction) in the middle of the substrate which is more wettable as compared to the edges of the domain, which are less

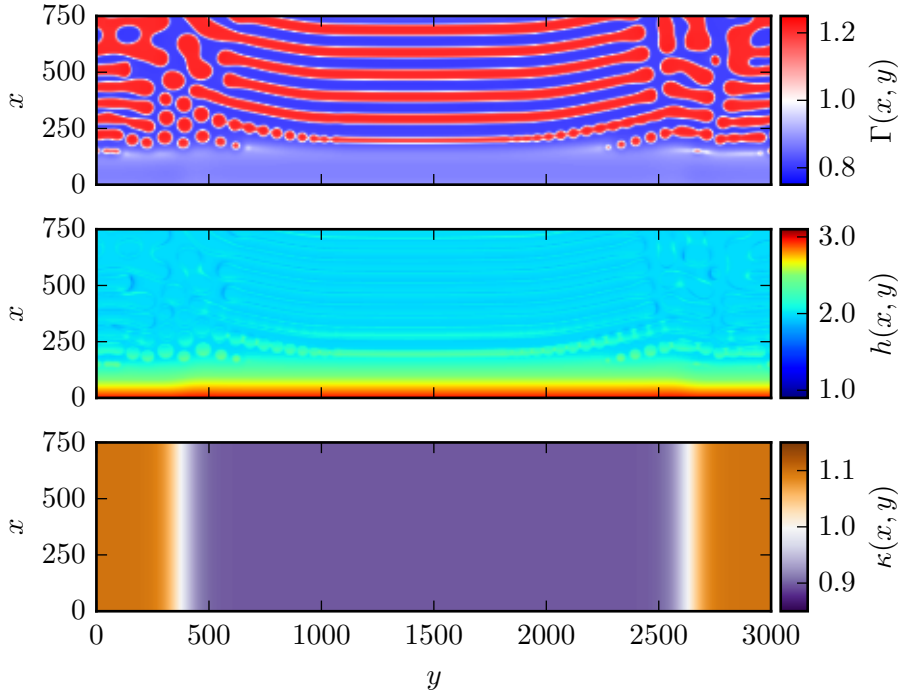


Figure 4.13: Snapshot of a direct numerical simulation of the fully hydrodynamic model (2.51) describing the coupled dynamics of the surfactant layer and the liquid layer during a LB transfer onto a vertically prestructured substrate. The stripe pattern of the surfactant density $\Gamma(x, y)$ (top panel) exhibits an upwards bend in the vicinity of the prestructure (left and right boundary). In the height profile $h(x, y)$ (middle panel), one can identify a further protrusion of the liquid layer into the domain in the more-wettable middle region as compared to the left and right less-wettable boundaries (cf. [WZC⁺17]).

wettable. The wettability is controlled by a modulation of the disjoining pressure (cf. Sec. 2.4 and Eq. (2.64)), where the modulation is depicted in the bottom panel of Fig. 4.13. The disjoining pressure (2.28) and the parameters ($U = 1.3$, $\chi_0 = 1.04$, $\rho = 0.1$) are particularly chosen in such a way that the liquid layer exhibits a sensitive reaction to the prestructure. The pattern that results from this setting exhibits horizontal stripes that are bent upwards at the edge of the more-wettable stripe in the middle of the substrate, which resembles the experimental findings, supporting our previous hypothesis about the origin of the bent stripes. Of course this is by no means a strict proof that the pattern formation and the hydrodynamics show this very same interaction with the prestructure in real-world experiments. To clarify this, two approaches are possible. On the one hand, more extensive parameter studies on both the experimental and theoretical side should be conducted. These should in particular show whether the extent to which the stripes are bent can be controlled by the wettability contrast induced by the prestructure. On the other hand, experiments could be designed that enable the *in-situ* observation of the contact line during the LB transfer (e.g., [SR94]), which would lead to a more direct understanding of the occurring effects. In this context, it would also be interesting to study the dynamics of a simple liquid when a prestructured substrate is withdrawn, i.e., looking at the dynamics during the LB transfer without any surfactants. To our knowledge, such studies have not been performed, although a good understanding of the occurring effects would lay the foundation for a deep comprehension of the pattern formation during the LB transfer onto prestructured substrates. To this end, we will discuss the dynamics of a simple liquid on a dragged prestructured substrate in Chap. 5 from the theoretical point of view. But before that, we will briefly introduce two different control mechanisms with experimentally desirable properties that could be used for the LB transfer technique.

4.3 Control through a Time-periodic Forcing

We have seen that the use of prestructured substrates is a powerful tool to gain control over the pattern formation occurring during the LB transfer. However, this control method has also disadvantages in real-world applications. The biggest one is the effort needed to fabricate the prestructures on the substrates. For the experimental results presented in, e.g., Figs. 4.9 and 4.10, first a poly(methylmethacrylate) (PMMA) layer is spin-coated onto the silicon substrate as a resist. The form of the prestructure is then written into the PMMA layer by electron beam lithography. The substrate is then developed, removing the surplus PMMA. Afterward, a 3 nm thick chrome adhesion layer and the actual 20 nm gold prestructure are created by thermal evaporation under vacuum conditions (also see [ZWH⁺16, WZC⁺17]). That is, the time, effort and cost involved in producing the prestructure easily exceed the ones for the actual LB transfer process. Therefore, it is desirable to also find alternative control techniques that are simpler and equally powerful.

In the previous section, we partly attributed the control exerted by prestructures to a spatial modulation of the strength of the substrate-mediated condensation, i.e., a spatial modulation of an important control parameter. This suggests that also other influential control parameters should lend themselves to a spatial or temporal modulation, enabling an additional control mechanism for the pattern formation process. One of the most important control parameters is the transfer velocity, i.e., the velocity at which the substrate is withdrawn from the liquid. As the velocity influences both the type of pattern that occurs, horizontal vs. vertical stripes, and its properties such as the wavelength, a periodic modulation of it could lead to similar effects

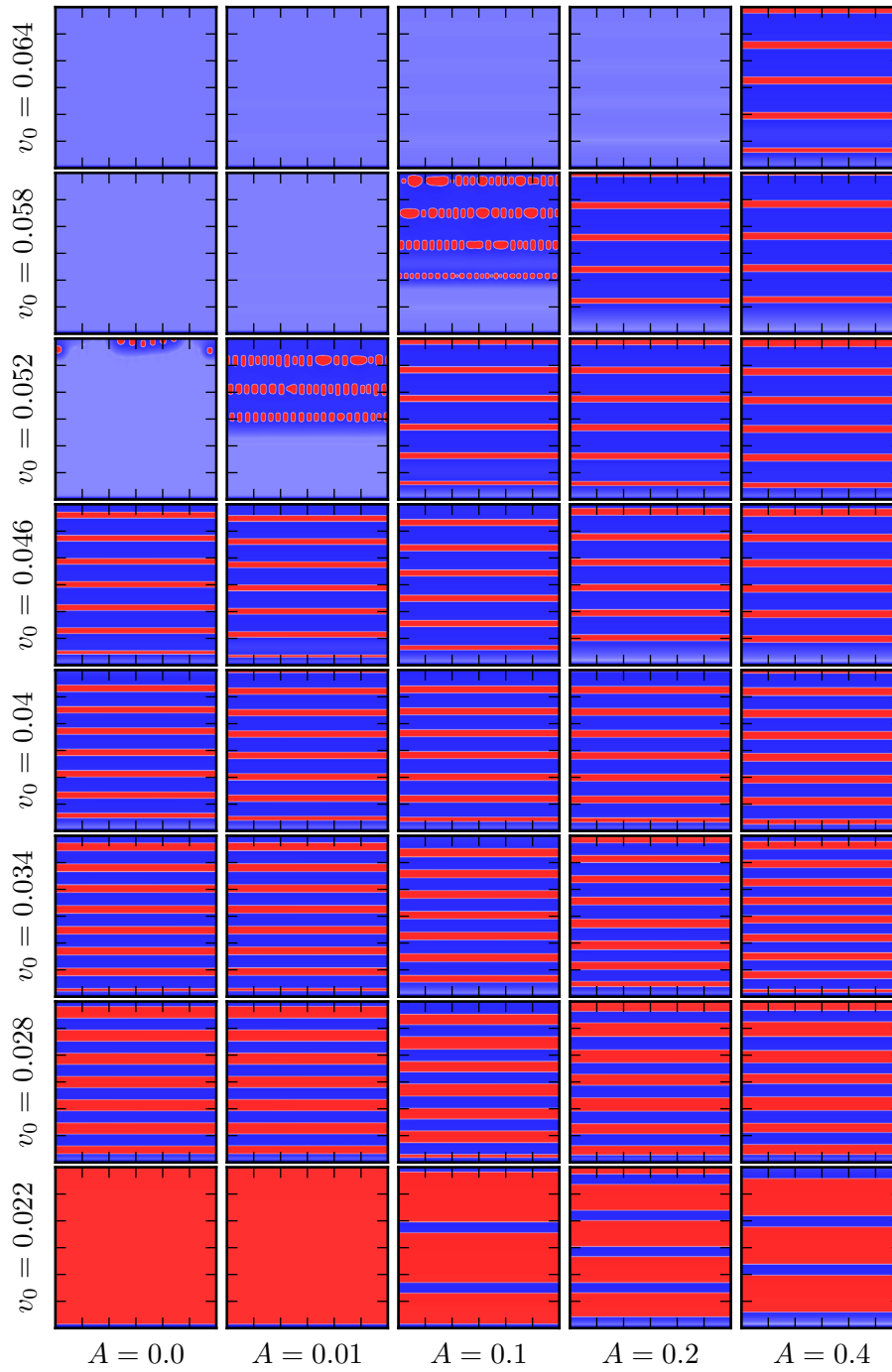


Figure 4.14: Overview of the occurring patterns in direct numerical simulations for a sinusoidally modulated transfer velocity with different modulation amplitudes A and mean velocities v_0 . The frequency of the modulation is fixed at $\omega = 0.003$. The natural horizontal stripe pattern is further stabilized by the velocity modulation and the wavelength of the pattern can be controlled (cf. Fig. 4.15).

as observed for prestructured substrates. Therefore, we will now consider the LB transfer onto a homogeneous substrate with a periodically modulated transfer velocity,

$$v(t) = v_0(1 + A \sin(\omega t)), \quad (4.2)$$

where v_0 is the average velocity, A is the amplitude and ω the frequency of the modulation. As a model we use again the augmented Cahn–Hilliard model (2.59). The results for a varying average transfer velocity v_0 and modulation amplitude A are presented in Fig. 4.14. Obviously, the horizontal stripe patterns are further stabilized by the velocity modulation. Also for velocities at which horizontal patterns can be unstable leading to a vertical pattern (not shown here), a horizontal pattern is achieved. The velocity regime in which a stripe pattern can be achieved is also extended by the modulation of the velocity, leading to a stripe pattern at both higher and lower average velocities as compared to a constant transfer velocity. This effect was also already observed for prestructured substrates in Sec. 4.2. In addition, also the wavelength of the stripe patterns becomes controlled by the velocity modulation. This can be seen in Fig. 4.15, where the wavelength of the stripe patterns depending on the mean transfer velocity is shown for the cases of a constant and a modulated velocity. The modulation leads to a linearization of the wavelength dependence. That is, the temporal frequency at which new stripes are formed is locked to the frequency of the velocity modulation in this regime (starting at $v_0 \approx 0.036$) and the simple relation

$$\lambda = \frac{2\pi}{\omega} v_0 \quad (4.3)$$

holds. That is, the slope of the linear dependence is directly governed by the modulation

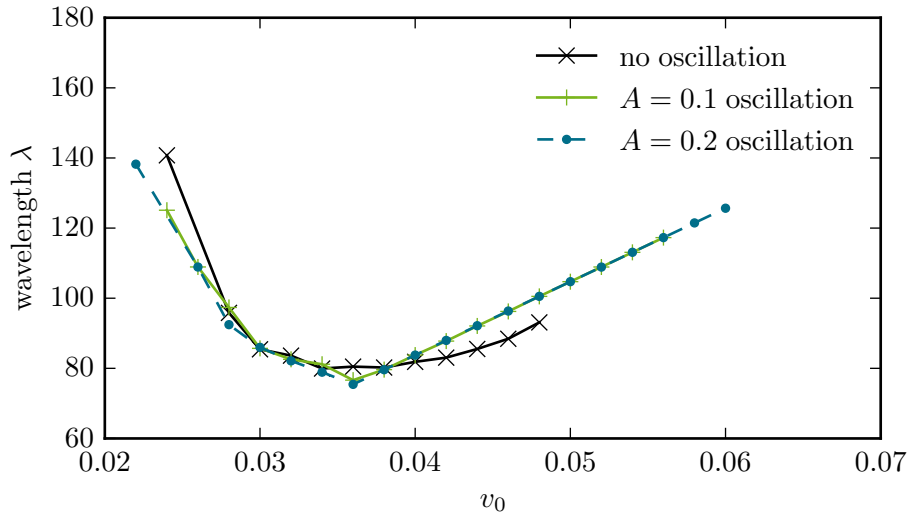


Figure 4.15: Dependence of the wavelength of horizontal stripe patterns on the mean transfer velocity v_0 for both a constant transfer velocity and a sinusoidally modulated transfer velocity with frequency $\omega = 0.003$ and amplitude A . The velocity dependence of the wavelength can be linearized by the modulation, where the slope of the linear dependence is controlled by the frequency ω .

frequency. Note that we describe the patterns here in terms of the wavelength λ and not in terms of the wave number k as in the previous sections, because a linear dependence of $\lambda \propto v$ is more easily visible than $k \propto v^{-1}$.

The observation of the frequency locking here shows that a simple temporal modulation of the transfer velocity can serve the same control purpose as the use of a prestructured substrate with the big advantage that no alterations to the substrate are needed. This would be in particular interesting for high-throughput applications, where many substrates have to be coated subsequently. Of course, these are only results obtained with a rather simplified model and, thus, experiments are needed to check this approach. But a quick consideration can already clarify the technical feasibility of this approach. To create the modulated transfer velocity, one needs an actuator that can achieve the needed sinusoidal movement of the substrate. A typical transfer velocity in LB transfer of horizontal stripes is $v_0 = 1 \text{ mm/s} = 1 \cdot 10^{-3} \text{ m/s}$ and the stripes then have a wavelength of $\lambda \approx 1 \text{ }\mu\text{m} = 1 \cdot 10^{-6} \text{ m}$. Thus, the stripes are formed at a temporal frequency of

$$f_{\text{stripe-creation}} = \frac{v_0}{\lambda} \approx 1 \text{ kHz}, \quad (4.4)$$

which is also the frequency such an actuator would need to work at. In addition, the maximum amplitude of the oscillating motion would be

$$\Delta x_{\text{modulation}} = \frac{v_0 A}{\omega} \approx 0.1 \text{ }\mu\text{m} \quad (4.5)$$

for an amplitude $A = 0.1$. An actuator suitable for this modulated-velocity approach therefore has to achieve a linear motion of roughly $0.1 \text{ }\mu\text{m}$ at a frequency of 1 kHz (in addition to the constant linear movement with $v_0 = 1 \text{ mm/s}$). Both conditions can be realistically fulfilled with a piezo actuator that can be used in combination with the traditional LB dipper for the constant velocity. That is, from a technical point of view, this approach seems feasible. Apart

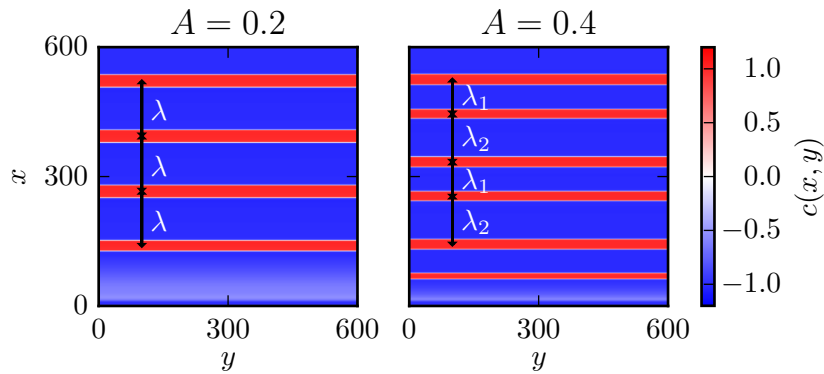


Figure 4.16: For increasing oscillation amplitudes, the patterns obtained can become more complex. For $A = 0.2$ (left panel), a stripe pattern with equidistant stripes with a single wavelength λ is obtained. For $A = 0.4$ (right panel), a period doubling occurs, due to which stripes with alternating distance λ_1 and λ_2 are created. Other parameters are kept constant ($\omega = 0.005$, $v_0 = 0.052$).

from simple regular stripe patterns, the transfer velocity modulation can also facilitate the formation of more complex patterns. One such example is shown in Fig. 4.16. Here, a simple regular stripe pattern for an amplitude $A = 0.2$ of the velocity modulation is shown (left panel) and compared to the pattern obtained for $A = 0.4$ (right panel). The pattern still consists of horizontal stripes, but the wavelength is no longer constant. In contrast, a period doubling is found, indicating that the distance between two neighboring stripes alternates between two different wavelengths λ_1 and λ_2 . As the exploration of the parameter space conducted here is far from being exhaustive, one can expect that many more interesting patterns and effects exist. Another aspect possibly worth an investigation is the use of non-sinusoidally modulated transfer velocities. If one can create arbitrary transfer velocity protocols, one is in principle in the position to create stripe patterns at will. A first exemplary realization of this method is shown in Fig. 4.17.

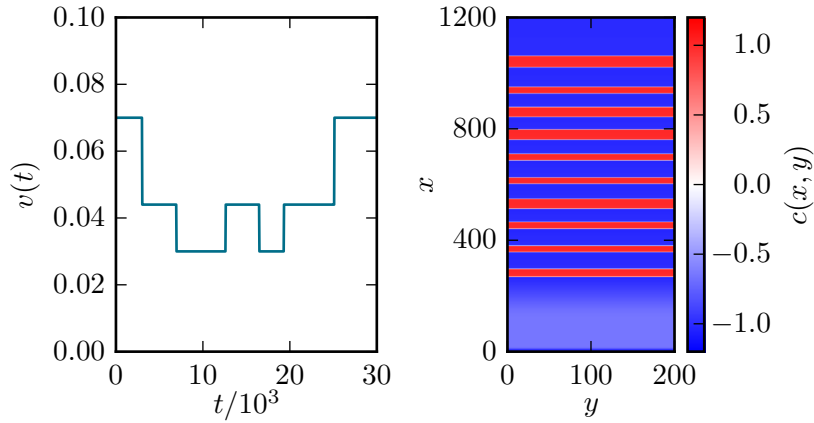


Figure 4.17: Complex barcode-like stripe pattern (right panel) obtained by a non-periodic transfer velocity modulation (left panel). By carefully tuning the transfer velocity protocol, the stripe widths and distances can be adjusted at will.

The findings up to now suggest that many control parameters can be used for a spatial or temporal modulation in order to further control the pattern formation process. We want to underline this now with a brief, third example. This time, the parameter x_s of Eq. (2.61) is employed for a spatial modulation. This parameter controls the spatial position at which the substrate-mediated condensation starts to act. That is, for the augmented Cahn–Hilliard model (2.59), it serves as a parameter for the contact line position. We now allow for a periodic modulation as

$$x_s(t) = x_{s0} \left(1 + A \left(\frac{1}{2} \sin(\omega t) + \frac{1}{2} \right) \right), \quad (4.6)$$

where again ω is the modulation frequency and A its amplitude. The modulation is now chosen to only increase x_s with respect to x_{s0} . The obtained patterns for a fixed frequency $\omega = 0.002$ and varying transfer velocity v and modulation amplitude A are shown in Fig. 4.18. The overall picture is similar to the one obtained for a modulated transfer velocity (cf. Fig. 4.14): Horizontal stripe patterns are further stabilized, the patterning regime is extended towards higher and lower transfer velocities and the wavelength of the patterns becomes controllable. This becomes visible in Fig. 4.19, where the wavelength of the stripe pattern is shown in

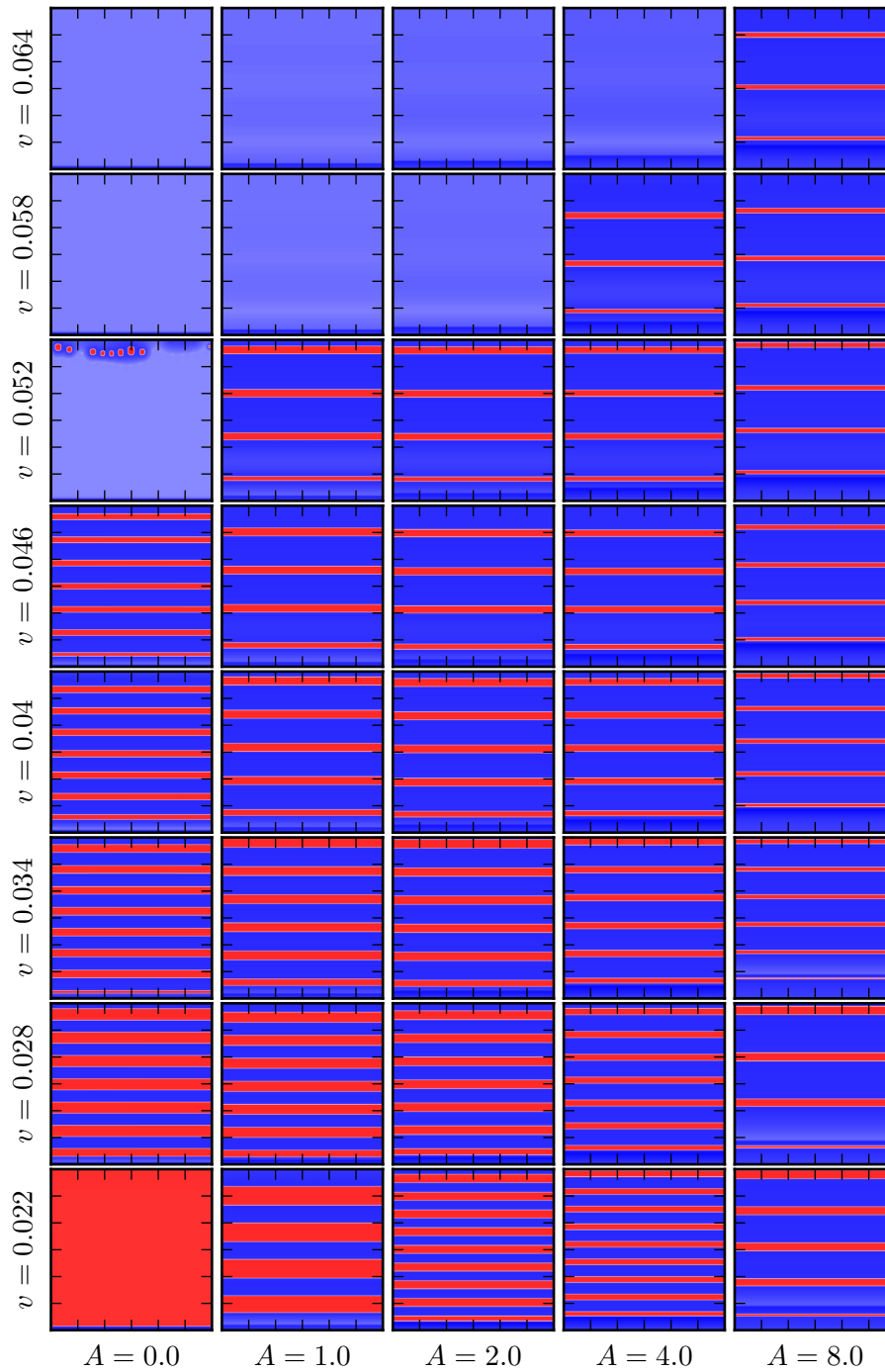


Figure 4.18: Overview of the occurring patterns in direct numerical simulations for a sinusoidally modulated contact line position with different modulation amplitudes A and transfer velocities v . The frequency of the modulation is fixed at $\omega = 0.002$. The natural horizontal stripe pattern is further stabilized by the velocity modulation and the wavelength of the pattern can be controlled (cf. Fig. 4.19).

dependence on the transfer velocity for different amplitudes of the oscillation. An oscillation of the contact line position with amplitude $A = 2.0$ leads to a completely linear dependence of the wavelength on the transfer velocity over the whole pattern forming velocity range. Just as in the case of a modulated transfer velocity, the temporal frequency at which stripes are formed is now locked to the frequency of the contact line oscillation. Therefore, the linear relation (4.3) holds again. Interestingly, also a frequency locking with a different ratio can be found for an oscillation amplitude of $A = 8.0$. In the lower velocity range up to $v \approx 0.03$, stripes are only formed at half of the frequency of the contact line oscillations, resulting in a doubled wavelength (and slope of the λ vs. v graph) as compared to the $A = 2.0$ case (cf. blue and green line in Fig. 4.19).

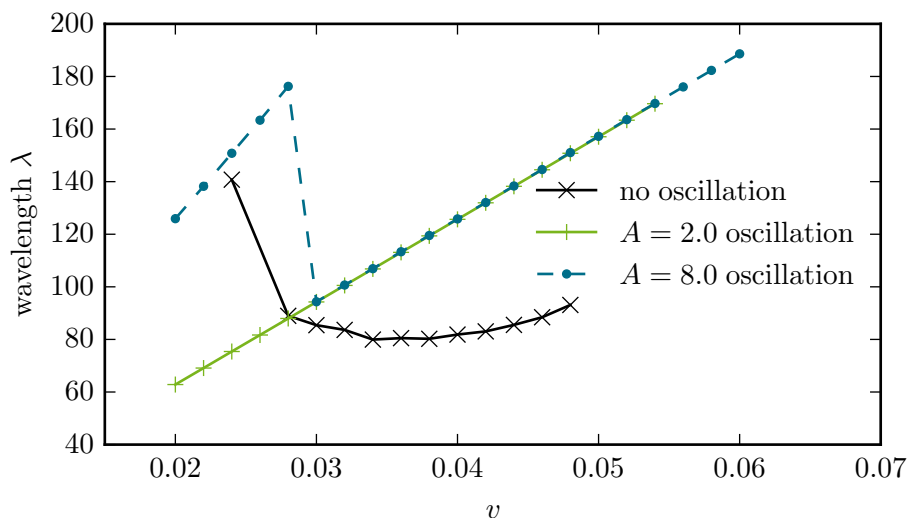


Figure 4.19: Dependence of the wavelength of horizontal stripe patterns on the transfer velocity for both a constant and a sinusoidally modulated contact line position with frequency $\omega = 0.002$ and amplitude A . The velocity dependence of the wavelength can be linearized by the modulation, where the slope of the linear dependence is controlled by the frequency ω .

This last example of the contact line position as an additional control mechanism through temporal modulation is meant as a demonstration that the range of possible control approaches is not limited to the first two cases of prestructures and modulated transfer velocities. For real-world applications, it would probably present no suitable option, as the control of the contact line position would involve an alteration of the whole hydrodynamics involved in the transfer process. However, when introducing a significant hydrodynamic motion in the LB transfer process, one can hardly expect the augmented Cahn–Hilliard model employed here to hold anymore. Still, this example shall motivate to find other experimentally well-accessible parameters and check their suitability for a control through spatial or temporal modulation.

In the next chapter, we return to the usage of prestructured substrates, but now considering the transfer of a simple liquid without any pattern forming solutes or surfactants.

5 Dynamics of a Dragged Meniscus

In the previous Sec. 4.2, we discussed the influence of prestructures on the pattern formation occurring during the Langmuir–Blodgett transfer of amphiphilic surfactant molecules onto solid substrates. The first considerations there dealt with situations, in which the liquid layer between the substrate and the surfactant layer could be assumed to be only weakly influenced by the prestructure. Instead, the prestructure was thought to only have an effect on the pattern formation of the surfactant layer. However, the experimental results and numerical simulations presented in Sec. 4.2.2 revealed that prestructures can also considerably influence the dynamics of the liquid layer during LB transfer, which consequently also affects the pattern formation. Thus, prestructures can have both a direct impact on the pattern formation of the surfactant layer and an indirect one via the liquid layer. This entanglement of effects makes systematic, reliable analyses complicated apart from phenomenological and qualitative studies as presented in the previous chapter. This gives the motivation for this chapter, in which we reduce the complexity of the LB transfer system by neglecting the surfactant layer and only consider the dynamics of a simple, one-component liquid on a prestructured substrate that is withdrawn from a liquid reservoir. Knowledge about this system can then be the basis for the complex coupled dynamics governing the LB transfer. Apart from the LB transfer, many other experimental and industrial applications can also benefit from this knowledge. In particular, there are various systems in which a solid substrate is withdrawn from a liquid bath in order to create a deposit on the substrate (e.g., [WR04, SADF07, DFSA08, Wil82]). Other examples are dip-coating techniques which are very similar to the LB transfer with the difference being that not a surfactant-covered film is transferred, but instead complex liquids like solutions and suspensions (e.g., [DG13, CBdC⁺14, DDG16]). In this context, prestructures are also already used to control the transferred deposit [DTD⁺00, BWvCD17].

In the case of homogeneous substrates being dragged out from a simple liquid, the properties of the liquid layer forming on the substrate have already been studied for a long time, both experimentally and theoretically. Among the first theoretical works is the one by Landau and Levich [LL42], in which they analyze the thickness of the liquid layer that is transferred onto the substrate in dependence on the velocity at which the substrate is withdrawn. This layer is therefore also known as *Landau–Levich film* and its thickness scales with the velocity U as $U^{2/3}$ [LL42, MRQG07]. For very low transfer velocities, no liquid layer of finite height is transferred onto the substrate, but a meniscus is formed at the three-phase contact line, where liquid, solid substrate and air/vapor meet. The particular form of the meniscus results from the forces acting on it, which are the capillary force due to surface tension, the wettability of the substrate, which originates from solid-liquid interactions with the substrate, and the viscous drag stemming from the movement of the substrate. Often, these forces can balance each other, leading to a steady meniscus shape. The properties of such a simple-liquid meniscus were already studied intensively [SADF07, ZSE09, GTLT14, TGT14, GLF⁺16], where in particular also solutions were found that exhibit a *foot-like* protrusion from the meniscus, i.e., a finite-length thin liquid layer beyond the classical meniscus region. In the work of Delon et al. [DFSA08], also heterogeneous substrates were used in dip-coating experiments with a simple liquid. There,

they explicitly created defects on the substrate to then analyze the subsequent relaxation of the liquid layer after it was deformed by the point-like defects. Apart from the latter work, it is common to most studies on dip-coating that they consider homogeneous substrates where no prestructures or defects on the substrate influence the dynamics of the liquid. Therefore, we will now systematically study the effect of regular prestructures consisting of vertically or horizontally oriented stripes on the dynamics of a simple liquid meniscus. The presentation of the results closely follows the publication [WZC⁺17].

We now consider the set-up sketched in Fig. 2.4, where a solid substrate is withdrawn from a liquid reservoir at a constant velocity U and under a constant inclination angle α with respect to the surface of the liquid reservoir. We describe this situation with the thin film model (2.32) which accounts for wettability of the substrate through a disjoining pressure, surface tension of the liquid through a Laplace pressure, the hydrostatic pressure and the force stemming from the dragging of the substrate. The analysis of this model is based on two different approaches. First, we analyze the one-dimensional stationary solutions of the model for homogeneous substrates using pseudo-arclength continuation with AUTO-07p (cf. Sec. 3.4). With this, we obtain the bifurcation diagrams and solution families for the main control parameters like the transfer velocity U , substrate wettability κ and inclination angle α . These results are augmented by one- and two-dimensional direct numerical simulations of the model for heterogeneous substrates.

To analyze substrates with (spatially) varying wettability, we introduce a wettability parameter κ into the model (2.32):

$$\partial_t h = -\nabla \cdot \left[\frac{h^3}{3} \nabla \left(\Delta h + \kappa \left(-\frac{1}{h^3} + \frac{1}{h^6} \right) \right) - \frac{h^3}{3} G \left(\nabla h - \begin{pmatrix} \alpha \\ 0 \end{pmatrix} \right) - \begin{pmatrix} U \\ 0 \end{pmatrix} h \right]. \quad (5.1)$$

In this formulation, the parameter κ scales the wetting energy with respect to the one already absorbed into the scaling of the equation. With other words, it shifts the balance between the wetting energy and the energy of the free surface. Therefore, it is also directly connected to the equilibrium contact angle (2.63):

$$\theta_{\text{eq}} = \sqrt{\frac{3\kappa}{5}}. \quad (5.2)$$

That is, an *increased value* of κ leads to an increased contact angle θ_{eq} , which would describe a *less-wettable* substrate. One has to keep this in mind when we refer to κ as the wettability, because then smaller values indicate a higher wettability and vice versa.

To obtain one-dimensional solutions of this model by means of pseudo-arclength continuation, we start with a homogeneous flat film with the precursor film height, which is a trivial solution of the model for vanishing inclination angle and transfer velocity. The latter are then increased by continuation to reasonable values, resulting in a starting solution for the investigation of our model. The control parameters can then be varied in the regions of interest by continuation, leading to the solution families and bifurcation structure. An exemplary resulting solution is presented in Fig. 5.1. As the substrate is inclined to an angle α with respect to the surface of the liquid reservoir, the solution approaches a linear behavior with slope $-\alpha$ at the left boundary (cf. the boundary conditions (2.33)). To quantitatively compare different solutions, it is necessary to introduce a measure that describes the solutions with a single number. A natural candidate for this is the length of the meniscus, i.e., the distance up to which the liquid reaches into the domain. Because the liquid layer height never becomes zero in the employed precursor model, we define the maximum of the curvature of the height profile as the contact

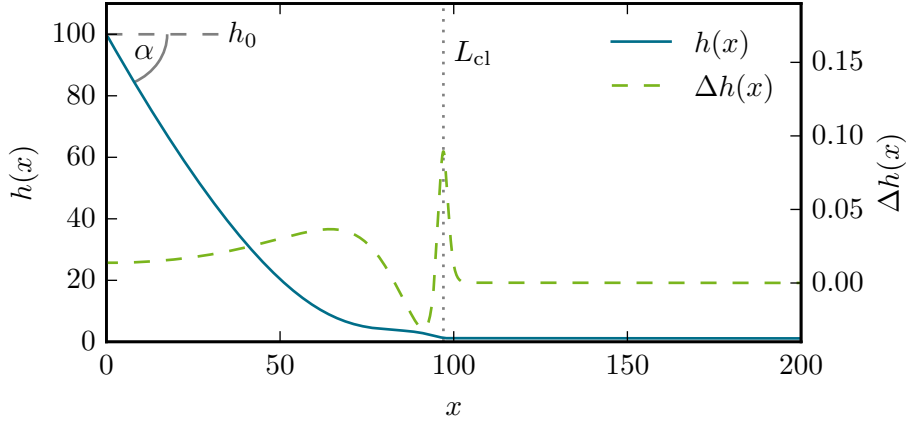


Figure 5.1: Exemplary one-dimensional numerical solution of the model (5.1) for a simple liquid on a solid substrate dragged out from a bath. In addition to the height profile $h(x)$ (blue solid line), the second derivative $\partial_{xx}h(x)$ (green dashed line) is shown. We define the contact line position L_{cl} as the position of maximum curvature, $L_{cl} = \arg \max (\partial_{xx}h(x))$ (cf. [WZC⁺17]).

line position [WZC⁺17],

$$L_{cl} = \arg \max (\partial_{xx}h(x)). \quad (5.3)$$

As one can see from the dotted line in Fig. 5.1, the measure originating from this definition coincides well with the length of the meniscus one would assign intuitively.

5.1 Bifurcation Diagrams for Homogeneous Substrates

The bifurcation diagram of model (5.1) for varying transfer velocity and homogeneous substrates has already been analyzed in detail previously [GTLT14, TGT14]. However, we employ slightly different boundary conditions¹ here and therefore re-calculate the bifurcation diagram to emphasize that the choice of boundary conditions is less important. The resulting diagram is presented in the left panel of Fig. 5.2 showing the contact line position L_{cl} in dependence on the transfer velocity U . In the right panels of Fig. 5.2, corresponding solution profiles are shown for four different locations in the bifurcation diagram marked by the labels I to IV. The bifurcation diagram comprises a lower sub-branch of simple meniscus solutions (labels I and II), whose contact line positions gradually increase with the transfer velocity. This sub-branch ends in a saddle-node (SN) bifurcation at an upper velocity threshold $U_{SN} \approx 0.07$, beyond which no meniscus solutions exist and instead Landau–Levich films with a finite thickness are formed. As these solutions cannot be reasonably characterized by a contact line position, they are not included in the bifurcation diagram. At the SN bifurcation, the branch turns backwards and forms another sub-branch of solutions for decreasing transfer velocities that exhibit the aforementioned foot-like protrusion (cf. label III). Following the sub-branch, the protrusion becomes longer up to another SN bifurcation which again connects to another sub-branch for increasing velocities. The solutions on this sub-branch are qualitatively similar to the foot-like

¹In particular, we only use the lowest order terms of the asymptotically derived conditions in [TGT14].

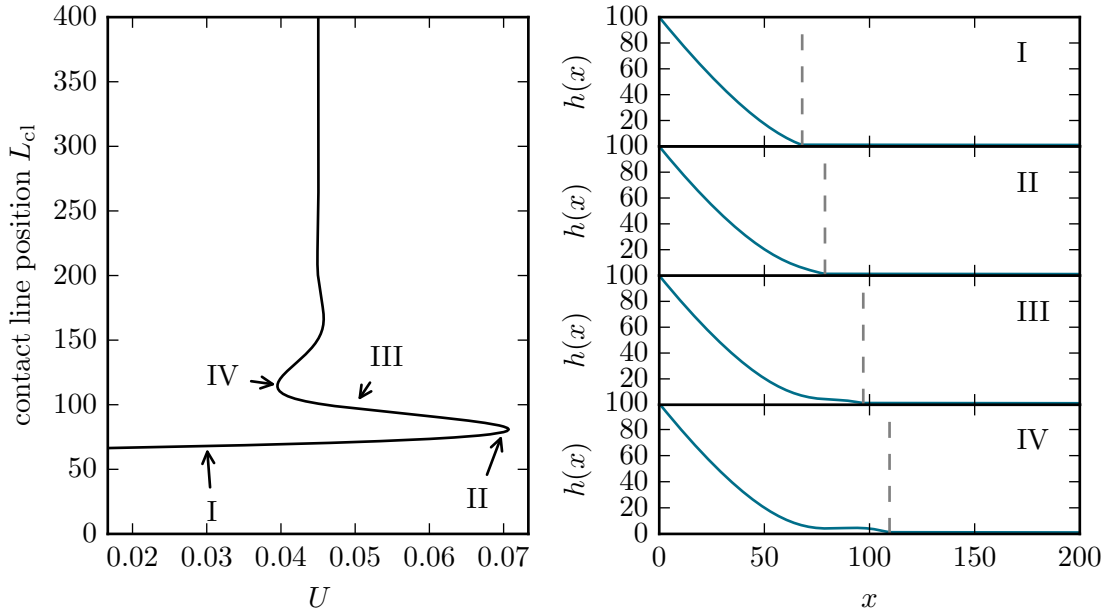


Figure 5.2: Left panel: Bifurcation diagram showing the contact line position L_{cl} of a dragged meniscus in dependence on the transfer velocity U for a fixed substrate wettability $\kappa = 1.0$ and inclination angle $\alpha = 2.0$. Right panel: Exemplary solutions along the solution branch, where the location of the solutions in parameter space is depicted by the labels I to IV. The lower sub-branch in the bifurcation diagram corresponds to simple meniscus solutions (labels I and II), whose contact line positions increase with the transfer velocity. At an upper velocity threshold $U_{SN} \approx 0.07$, this branch ends in a saddle-node bifurcation, which connects to a second sub-branch, whose solutions show a foot-like protrusion (label III). The length of this protrusion increases when following the bifurcation diagram further (label IV). The dashed lines in the solution panels mark the contact line position L_{cl} (cf. [WZC⁺17]).

solutions (cf. label IV), only with an increasing length of the foot. Following the bifurcation diagram further, it exhibits an exponential snaking behavior along which the contact line position always increases but the velocity oscillates. Upon further inspection, one can identify small-amplitude oscillations of the height profile of the solutions in the foot region. The number of oscillations increases by one with each fold of the snaking curve [TGT14]. Note that not all sub-branches correspond to linearly stable solutions, but every second sub-branch is unstable and is therefore not accessible in time simulations. However, we do not investigate the stability here in detail, as later we mostly focus on the lower sub-branch, which is linearly stable.

The bifurcation diagram presented in Fig. 5.2 was obtained for an inclination angle $\alpha = 2.0$ of the substrate with respect to the liquid reservoir. Obviously, this inclination should also have a profound influence on the obtained solutions and therefore we also analyze the bifurcation diagram in terms of a varying inclination angle α . In Fig. 5.3, the contact line position is shown in dependence on both the transfer velocity U and the inclination angle α . The graph is presented as slices, where each slice represents the same diagram as in Fig. 5.2 for a different

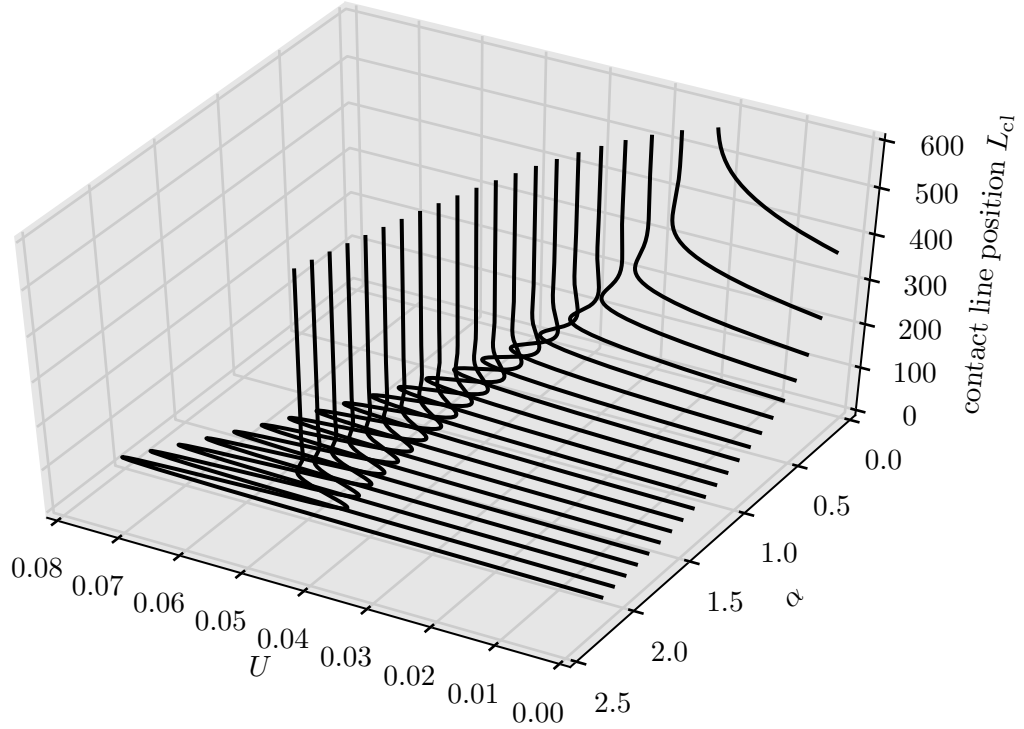


Figure 5.3: Bifurcation diagram showing the contact line position L_{cl} of a dragged meniscus in dependence on the transfer velocity U and the substrate inclination α . The presented curves are slices along various planes of fixed $\alpha = [0.2, 0.3, \dots, 2.2]$. In general, the contact line position increases for decreasing inclination angles and the position of the saddle-node bifurcation presenting the upper velocity threshold for simple meniscus solutions is shifted towards smaller velocities (cf. [WZC⁺17]).

fixed α . One can identify two major tendencies: First, the contact line position in general increases for decreasing inclination angles. This is to be expected, as the gravitational pulling decreases with the inclination angle. Second, the position U_{SN} of the first SN bifurcation, beyond which a Landau–Levich film can be transferred, is shifted towards larger velocities for larger inclination angles α . This can also be easily understood, as for larger inclination angles the gravitational pulling acts stronger against the dragging leading to a transition to a Landau–Levich film. Apart from these quantitative differences, the curves for various inclination angles are qualitatively similar². Therefore, without loss of generality, we can fix the inclination angle to $\alpha = 2.0$ and the transfer velocity to $U = 0.05$ for our following consideration of varying substrate wettabilities κ . The resulting bifurcation diagram is shown in the left panel of Fig. 5.4. Obviously, the overall structure is very similar to the one for a fixed wettability and varying transfer velocities (cf. Fig. 5.2) when flipping the horizontal axis. Also the corresponding solutions (cf. right panels of Fig. 5.4) are directly comparable. That is, an increasing wettability (or decreasing κ and equilibrium contact angle) has the same qualitative

²This is not true for very small inclination angles below $\alpha \approx 0.1$, where the snaking structure of the bifurcation diagram vanishes, leading to a continuous transition to a Landau–Levich film. This transition is analyzed in [ZSE09, GTLT14]

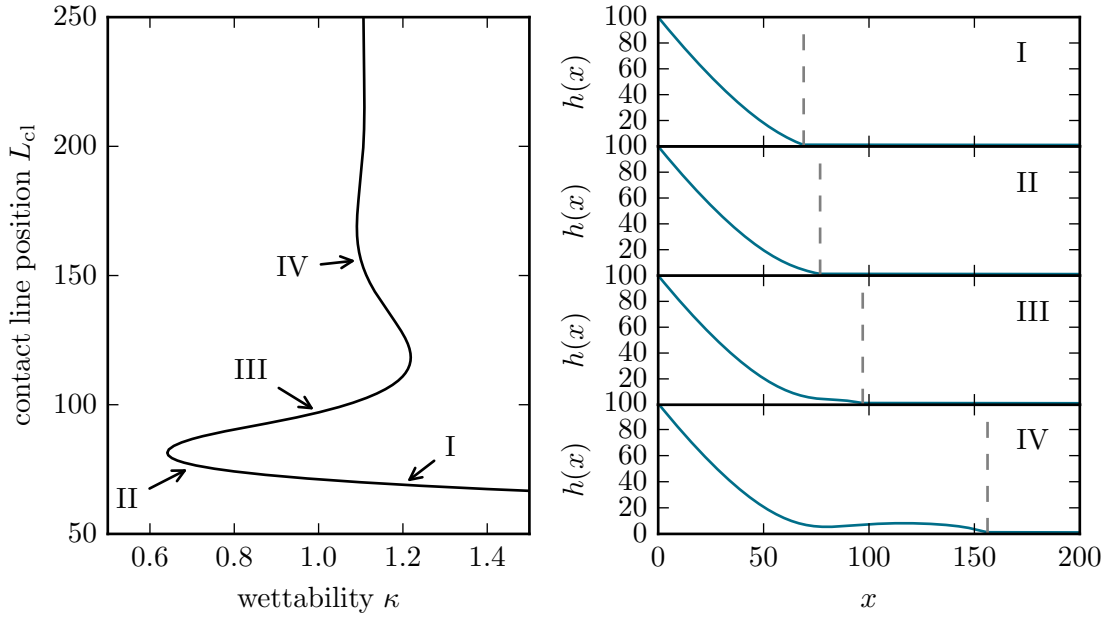


Figure 5.4: Left panel: Bifurcation diagram showing the contact line position L_{cl} of a dragged meniscus in dependence on the substrate wettability κ for a fixed transfer velocity $U = 0.05$ and inclination angle $\alpha = 2.0$. Right panel: Exemplary solutions along the solution branch, where the location of the solutions in parameter space is depicted by the labels I to IV. Apart from a horizontal flip, the overall structure of the bifurcation diagram resembles the one for fixed wettability and varying velocity closely (cf. Fig. 5.2). Here, a decreasing value of κ (equivalent to a decreasing contact angle) takes the role of an increasing transfer velocity. The dashed lines in the solution panels mark the contact line position L_{cl} (cf. [WZC⁺17]).

effect as an increased transfer velocity. In particular, there exists again a lower sub-branch of simple meniscus solutions (labels I and II) along which the contact line position increases for decreasing κ and which ends in a SN bifurcation at $\kappa_{SN} \approx 0.64$. Below this κ_{SN} , no simple meniscus solutions exist and instead Landau–Levich solutions occur (not shown here). Again, snaking sub-branches of foot-like solutions are connected to the lower sub-branch, just as in the case before. Intuitively, these similarities are not surprising, because on a more-wettable substrate the contact line region should exert less resistance against the viscous drag induced by the transfer velocity. Therefore, it was expected that a higher wettability acts similar as a higher transfer velocity. However, it is still remarkable that the whole bifurcation structure is also the same for both the wettability and transfer velocity. This is in particular of interest, as it indicates that all transitions between different solutions that can be triggered by changing the transfer velocity can be similarly induced by changing the wettability. This has consequences for possible applications, because while the transfer velocity is a fixed quantity that is the same for the whole substrate³, the wettability can be changed by physical or chemical treatments

³When introducing a temporal modulation of the transfer velocity as suggested in Sec. 4.3, the velocity can be tuned so that it has a certain value when the contact line is at a certain position of the substrate. However, this can only be changed along the direction of dragging and not in the transversal direction.

also in a spatially varying way. The shape and dynamics of the liquid meniscus when dragging such a heterogeneous substrate from a liquid reservoir can therefore also be controlled in a spatially varying way.

5.2 Dynamics of a Dragged Meniscus on Heterogeneous Substrates

We will now turn to this case of a periodically modulated substrate wettability, where we first assume a stripe-like modulation with the form (2.64) where the stripes are oriented parallel to the transfer direction. Obviously, this can no longer be captured by one-dimensional calculations and therefore we conduct two-dimensional direct numerical simulations, which are presented in Fig. 5.5. The wavelength $L_{\text{pre}} = 200$ of the prestructure is the same as the horizontal domain size and therefore there is one more-wettable stripe in the middle of the simulation domain and one half of a less-wettable stripe is at each the left and right boundary of the domain.

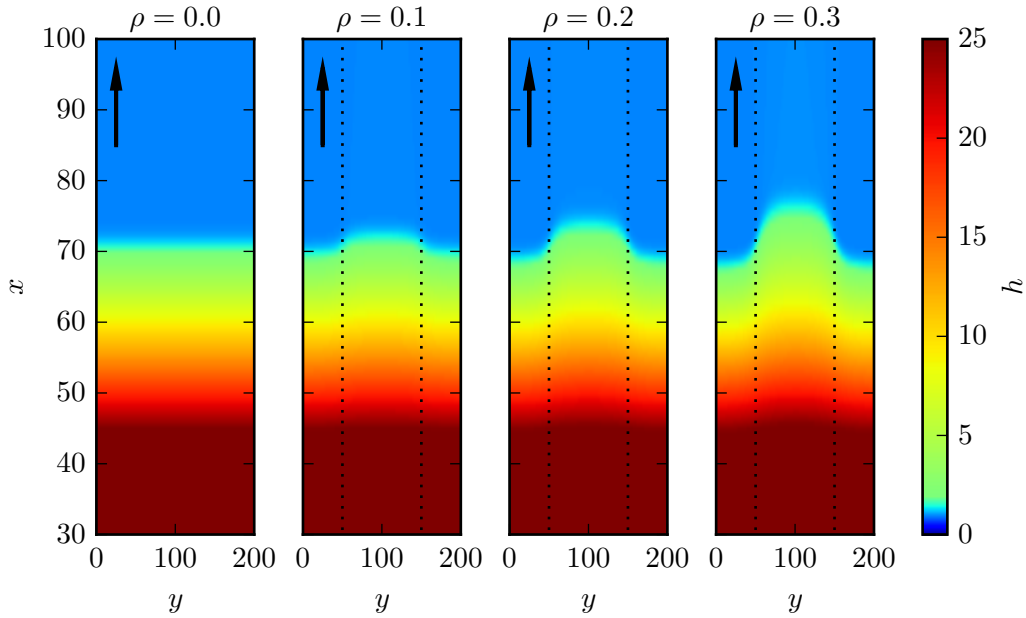


Figure 5.5: Two-dimensional solutions obtained by direct numerical simulations of a dragged meniscus for vertically prestructured substrates with different wettability contrasts ρ and fixed inclination angle $\alpha = 2.0$ and velocity $U = 0.05$. The boundaries of the vertical prestructure stripes are indicated by the dotted black lines, where the more-wettable area is in the center of the domain. The deformation of the meniscus becomes stronger for increasing ρ , as then the liquid is dragged further along the substrate with respect to the transfer direction (indicated by the black arrows) on the more-wettable part of the substrate (cf. [WZC⁺17]).

Compared to the homogeneous case for $\rho = 0.0$, where the solution is homogeneous in y direction, the meniscus is deformed for a non-zero prestructure contrast ρ . In the middle of the domain, where the wettability is $\kappa = 1 - \rho$, the liquid gets dragged further along into the domain as compared to the homogeneous reference with $\rho = 0$. At the boundaries, where the

wettability is $\kappa = 1 + \rho$, the contact line recedes as compared to the homogeneous case. Of course, this deformation becomes larger for increasing prestructure contrasts ρ . In the region close to the boundary of the prestructure stripe (i.e., at $y = 50$ and $y = 150$), there is a smooth transition between the two different deformations (receded vs. prolonged meniscus) due to the surface tension of the liquid. Distant from this transition region (e.g., at $y = 100$), the contact line reaches plateaus, in which the shape stays rather constant for a certain y interval. The particular shape of the deformation can be discussed quantitatively by again introducing the contact line position as a measure, which is now a function of the y coordinate:

$$L_{\text{cl}}(y) = \arg \max_x (\partial_{xx} h(x, y)). \quad (5.4)$$

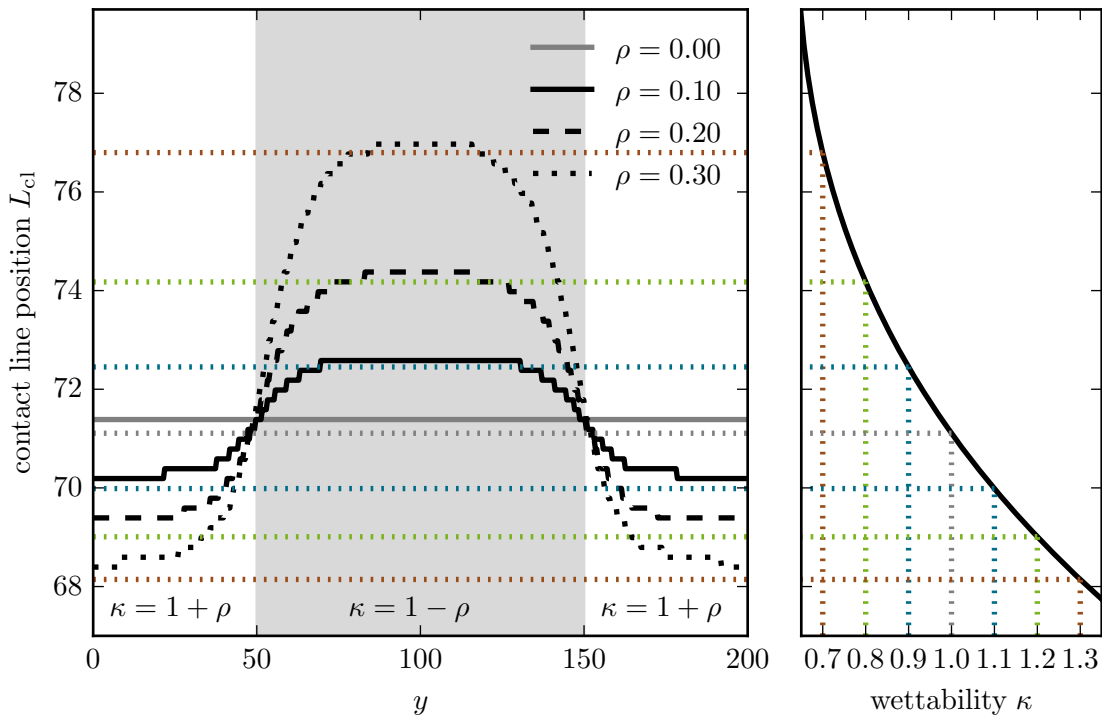


Figure 5.6: Left panel: Contact line position $L_{\text{cl}}(y)$ extracted from the direct numerical simulations in Fig. 5.5 for different wettability contrasts ρ and fixed inclination angle $\alpha = 2.0$ and velocity $U = 0.05$. Right panel: Magnification of the lower sub-branch of the bifurcation diagram in Fig. 5.4 corresponding to the 1d simple meniscus solutions. As a guide to the eye, the dotted colored lines indicate which contact line position is expected from the 1d results for homogeneous substrates with the corresponding wettability. The absolute difference between the 1d prediction and 2d simulation is smaller than $\Delta L_{\text{cl}} = 0.4$ (cf. [WZC⁺17]).

The left panel of Fig. 5.6 shows the contact line position extracted from the simulations presented in Fig. 5.5. Here, the aforementioned plateaus of the contact line position can be seen more clearly. In addition, the comparison of the curves for different ρ reveals that the plateau width becomes smaller for an increasing prestructure contrast ρ . This is due to the

fact that the surface tension of the liquid impedes strong gradients of the height profile and therefore also of the contact line. Thus, the transition region between the plateaus has to become larger as the total amplitude of the deformation grows with an increasing prestructure contrast. Although it is not studied here, one can in addition assume that the width of the transition region depends on the surface tension of the liquid and the sharpness of the assumed prestructure. However, in the case shown here, the prestructure is chosen very steep ($s = 100$ in Eq. (2.64)), so that the width of the transition region that develops here is much larger and therefore solely dependent on the surface tension of the liquid.

In addition to the contact line position L_{cl} extracted from the direct numerical simulations, the right panel of Fig. 5.6 also shows an enlargement of the lower sub-branch of the bifurcation diagram for a varying substrate wettability κ in Fig. 5.4. The contact line position axis of both panels is the same so that the absolute numbers can be compared. Using the dotted colored lines as a guide to the eye, one can inspect which contact line position is predicted by the bifurcation diagram for a one-dimensional solution on a homogeneous substrate with specific wettability κ . Obviously, this prediction from the continuation coincides well with the plateau values that the contact line position exhibits in the direct numerical simulations, when comparing the simulations with a prestructure contrast ρ with the predictions for a wettability of $\kappa = 1 + \rho$ and $\kappa = 1 - \rho$. This indicates that the dynamics of the meniscus on a prestructured substrate are - inside the plateau regions - well described by the simple one-dimensional solutions for homogeneous substrates. This fact also directly permits predictions for different prestructures. For an increased wavelength L_{pre} of the prestructure for example, one can expect the transition region to maintain its width and only the plateau regions to grow accordingly. For a smaller wavelength of the prestructure, the prediction should break down as soon as the width of the transition region is approximately half the wavelength of the prestructure. Although the results from one-dimensional continuation and two-dimensional simulations agree well, small deviations can be identified upon closer inspection. The plateau values of the contact line position in the direct numerical simulations always deviate slightly towards higher values ($\Delta L_{cl} < 0.4$) from the continuation prediction. However, this is a systematic error that also occurs for a homogeneous substrate (cf. gray line in Fig. 5.6) and therefore does not limit the reliability of the overall approach here. As the numerical methods used to obtain the direct numerical results and the bifurcation diagram are rather distinct⁴, we attribute the found deviations to the different numerical techniques.

Next, we discuss the case of a horizontally oriented prestructure of the form (2.65). As this prestructure is now homogeneous in y direction, we can restrict ourselves to one-dimensional simulations for simplicity. However, the prestructure is fixed to the substrate and therefore also moves with the same velocity U and the resulting solutions are hence no longer steady but typically periodic in time. Four snapshots at different times of such a simulation are shown in Fig. 5.7. As soon as a more-wettable region of the substrate comes into the vicinity of the contact line, it begins to move along with the dragging (i.e., in positive x direction). This stops, when the contact line has reached a certain plateau value (cf. $t = 4800$ and $t = 5200$ in Fig. 5.7), until the more-wettable stripe on the substrate has passed, after which the contact line recedes again (not shown here). Due to the periodic stripe pattern of the prestructure,

⁴The direct numerical results are obtained with time simulations of the dynamic problem with a finite element method on a fixed two-dimensional equidistant grid, while the numerical continuation solves the stationary problem on an adaptive one-dimensional grid using finite difference approximations of the spatial derivatives.

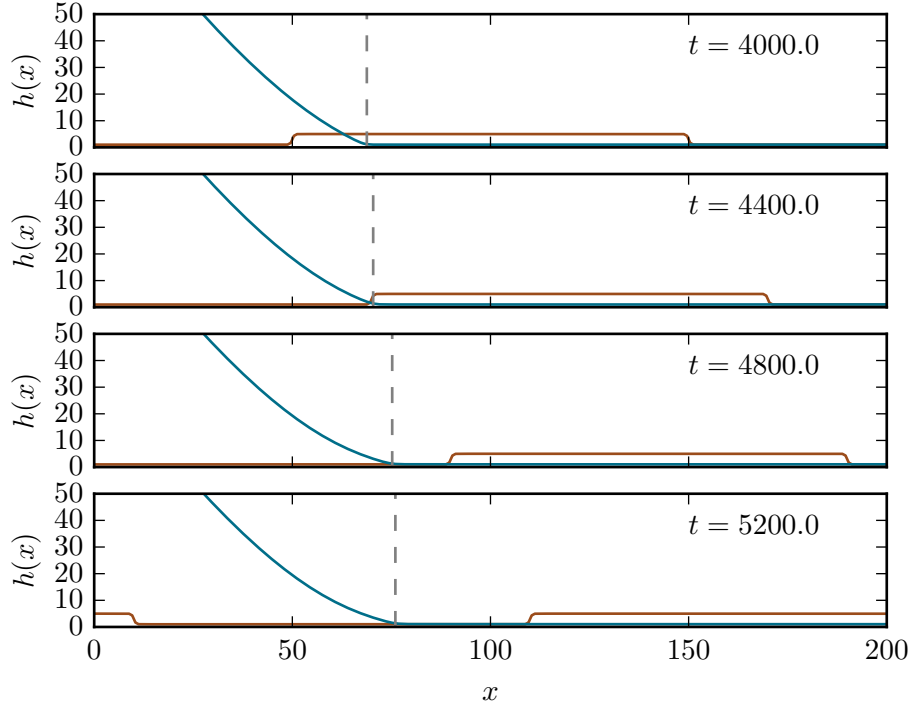


Figure 5.7: Snapshots at different times of a one-dimensional direct numerical simulation of a dragged meniscus on a horizontally prestructured substrate with a wavelength $L_{\text{pre}} = 200$ and wettability contrast $\rho = 0.3$ withdrawn at a velocity $U = 0.05$ and inclination angle $\alpha = 2.0$. The height profiles are shown as blue lines while the prestructures are indicated by red lines (showing κ). The contact line position is marked by dashed gray lines (cf. [WZC⁺17]).

this leads to a periodic movement of the contact line position, which is now a function of time,

$$L_{\text{cl}}(t) = \arg \max_x (\partial_{xx} h(x, t)). \quad (5.5)$$

The time series of the contact line position for substrates with different wettability contrasts ρ are shown in the left panel of Fig. 5.8. At first sight, the curves are very similar to the ones obtained previously for the case of vertically prestructured substrates, where the spatial y axis is now replaced by the temporal t axis. The contact line position periodically varies between two plateau values which depend on the wettability contrast ρ . The quick transitions between the plateaus exhibit a difference to the previous case of vertically prestructured substrates, as now the transition is always faster when leaving one plateau and slower when approaching the next plateau. Therefore, an asymmetry is visible in the time series. This difference to the vertically prestructured case could also be expected, as in the latter case the spatial symmetry $y \rightarrow -y$ holds, which does not translate to a temporal symmetry $t \rightarrow -t$ here for obvious reasons. The plateau values that the contact line position reaches can again be readily compared to the predictions from the one-dimensional bifurcation diagram, which is shown in the right panel of Fig. 5.8. Despite the small systematic deviations already discussed above, the plateau values of the time series are again well predicted by the bifurcation diagram for stationary solutions

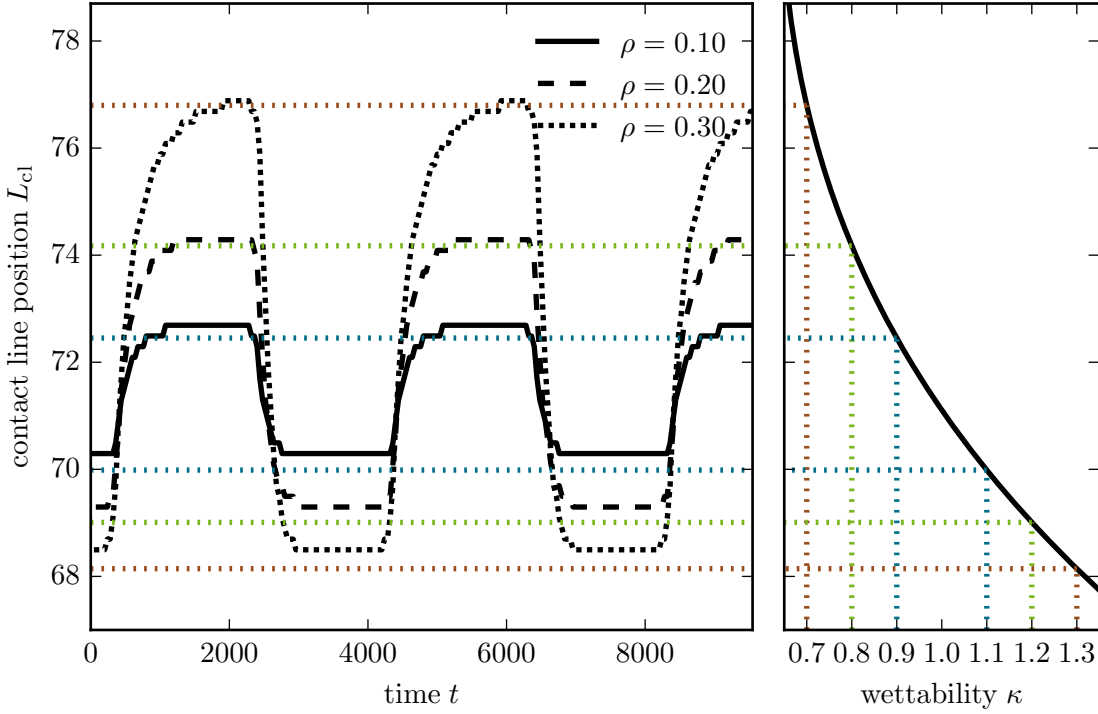


Figure 5.8: Left panel: Time series of the contact line position $L_{\text{cl}}(t)$ extracted from the direct numerical simulations in Fig. 5.7 for different wettability contrasts ρ and fixed inclination angle $\alpha = 2.0$ and velocity $U = 0.05$. Right panel: Magnification of the lower sub-branch of the bifurcation diagram in Fig. 5.4 corresponding to the 1d simple meniscus solutions. As guides to the eye, the dotted colored lines indicate which contact line position is expected from the stationary 1d results for homogeneous substrates with the corresponding wettability. The absolute difference between the stationary prediction and time simulation is smaller than $\Delta L_{\text{cl}} = 0.4$ (cf. [WZC⁺17]).

with constant wettability. From this, one can conclude that also for horizontally prestructured substrates, the meniscus shape reaches almost steady states in the plateau phases which are very similar to the ones for homogeneous substrates with according wettability. The particular form of the transition phases again results from the steepness of the prestructure stripes and the surface tension of the liquid. The concrete dependence of both parameters should also be analyzed elsewhere for a full picture of the dynamical behavior.

Qualitatively, the effects found in the direct numerical simulations for the dynamics of a dragged meniscus on a prestructured substrate could have been expected by physical intuition. In contrast, the comparison of the results with the bifurcation diagrams for one-dimensional homogeneous substrates reveals to which extent the dynamics on prestructured substrates can be quantitatively predicted. This knowledge could now be used, e.g., to formulate a parametric ansatz for the contact line position on prestructured substrates that can then be employed in the augmented Cahn–Hilliard model (2.59) in order to account for the wettability contrast of the substrate. But also apart from only studying this system of a dragged simple liquid

meniscus in order to gain insights for more complex systems like the LB transfer or dip-coating, this system exhibits many interesting features on its own. Examples are settings where the wettability contrast is rather high or where the transfer velocity is chosen only slightly below the transition threshold U_{SN} for a Landau–Levich film. In these cases, a Landau–Levich film would be formed in the more-wettable regions of the substrate, while this is not the case on the less-wettable regions of the substrate. For a horizontally oriented prestructure, this is

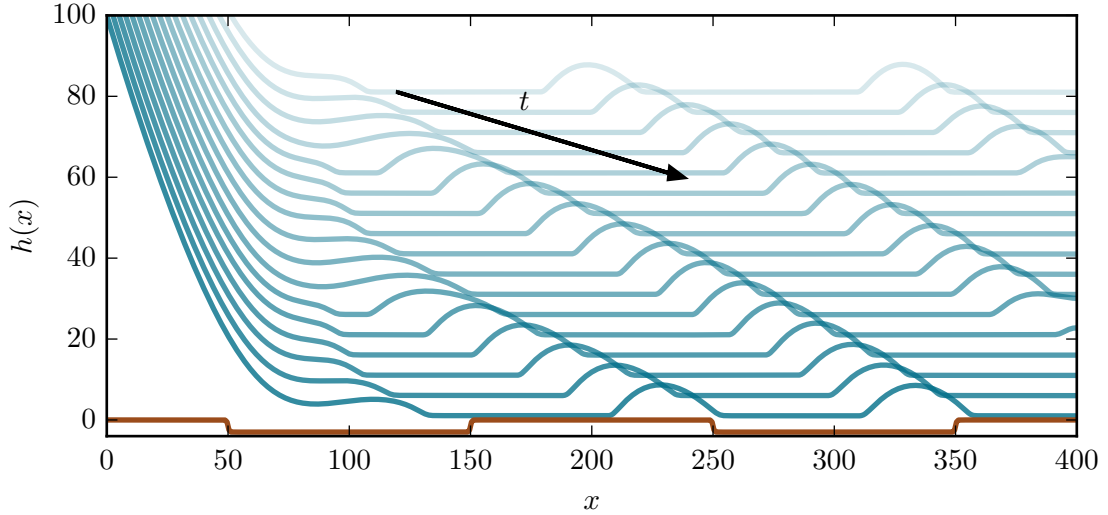


Figure 5.9: Time series of snapshots from a one-dimensional simulation of a dragged meniscus on a prestructured substrate with wettability contrast $\rho = 0.2$, prestructure wavelength $L_{\text{pre}} = 200$, velocity $U = 0.07$ and inclination $\alpha = 2.0$. The wettability contrast is large enough to trigger the transfer of liquid ridges, leading to a stripe pattern deposit on the substrate. The snapshots at different times ($\Delta T = 400$) are shifted along the h axis for better visibility ($\Delta h = 5$) with the latest snapshot shown at the bottom. The black arrow has the slope $\frac{-\Delta h}{U\Delta T}$ indicating the dragging velocity U . The prestructure at the latest time is depicted by the red curve (cf. [WZC⁺17]).

presented in Fig. 5.9. As the prestructure is oriented perpendicularly to the transfer direction, there is a temporal oscillation of the solution alternating between a meniscus solution and a Landau–Levich solution. This leads to horizontal liquid ridges parallel to the prestructure that form a stripe pattern on the substrate, which is similar to the observations made in [BWvCD17], where a prestructure with quadratic patches is considered. Interestingly, the stripe pattern has a wavelength that is smaller than the one of the prestructure. This is due to the fact that the liquid ridges are created with the temporal frequency at which the prestructure stripe pattern passes the contact line, but they are then not transported with the same velocity as the prestructure, but instead they slowly slide down the substrate due to its inclination. That is, the ridges are not *pinned* to the prestructure stripes and therefore do not reproduce its wavelength. After the stripes are formed at the contact line, they are in principle one-dimensional drops sliding down a heterogeneous inclined plate and the mechanism how

they were produced does not influence their dynamics anymore. Hence, work on this topic could be readily applied to our situation here (e.g., [TK06]), which we will not pursue further at this point.

5.3 Pattern Formation on Homogeneous Substrates

The formation of a liquid stripe pattern that was discussed in the last section and Fig. 5.9 might be reminiscent of the pattern formation in the augmented Cahn–Hilliard model discussed in Chap. 4 and in LB transfer in general. However, one must keep in mind that the pattern formation occurring in the previous Sec. 5.2 originates from a strongly heterogeneous substrate that forces the transfer of liquid at some times and hinders it at the others. Hence, the stripes do not occur due to an intrinsic pattern forming mechanism. Nevertheless, such an intrinsic mechanism, which is also present *without* any prestructure, can also be found in the dragged meniscus system. When doing time simulations in a small velocity range slightly above the upper threshold velocity U_{SN} for simple meniscus solutions, no homogeneous Landau–Levich film is transferred, but a stripe pattern perpendicular to the transfer direction. Four snapshots

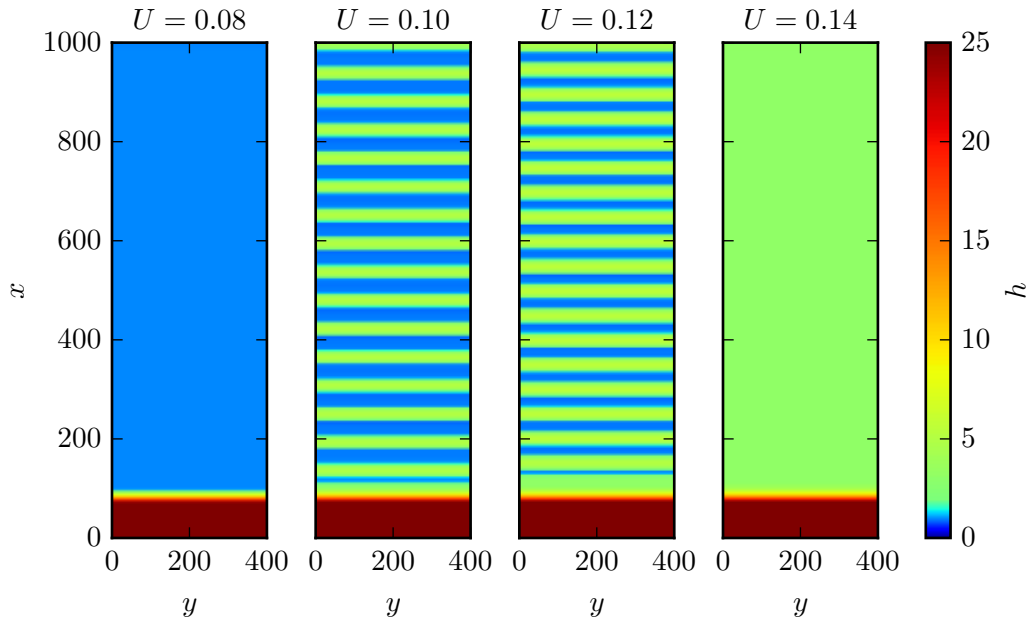


Figure 5.10: Snapshots from two-dimensional simulations for different transfer velocities and fixed inclination angle $\alpha = 3.0$ and homogeneous wettability $\kappa = 1.0$. For intermediate velocities such as $U = 0.10$ and $U = 0.12$, a horizontal stripe pattern parallel to the contact line forms without any prestructure.

of such simulations for different transfer velocities are shown in Fig. 5.10. The velocity $U = 0.08$ of the first snapshot lies below the threshold U_{SN} and therefore a steady meniscus solution is obtained in which no liquid layer (beyond the precursor height) is transferred onto the substrate. For a velocity $U = 0.10$ slightly above the threshold, stripes parallel to the contact line form spontaneously. This is true for a range of velocities, e.g., also in the case of $U = 0.12$. The

wavelength λ of the pattern slightly decreases with an increasing velocity U . Note that the liquid ridges are again slowly sliding downwards with respect to the moving substrate and therefore their net velocity upwards is always smaller than the transfer velocity U . For further increased $U = 0.14$, a homogeneous Landau–Levich layer with finite height is transferred. Starting with a simple meniscus solution as initial condition in this parameter regime, at first a striped deposit is created. Then, the location at which the stripes originate is slowly moving away from the previous contact line position, until it reaches the upper end of the computational domain. Within the pattern forming regime, i.e., the velocity range in which stripes are formed,

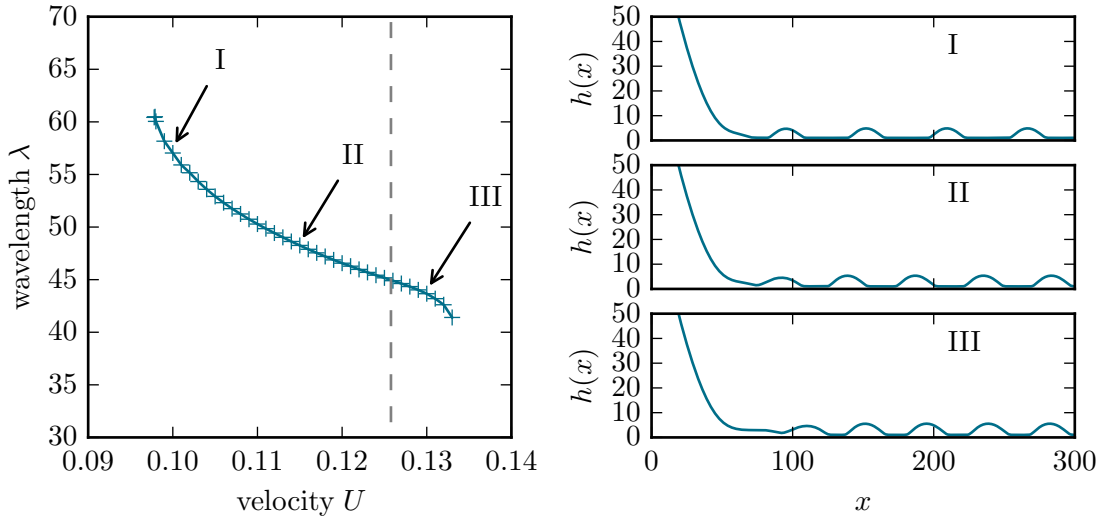


Figure 5.11: Left panel: Wavelength λ of the stripe pattern deposited from a simple liquid meniscus dragged at a varying velocity U and an inclination $\alpha = 3.0$. The wavelength decreases monotonically within the pattern forming regime. The dashed gray line shows the threshold velocity calculated by a marginal stability analysis of Landau–Levich films, which coincides with an inflection point of the λ vs. U curve. Right panels: Exemplary snapshots at different velocities (cf. labels I to III in left panel).

the wavelength of the stripe pattern decreases monotonically with the transfer velocity, which can be seen in Fig. 5.11. The steepest slopes of the λ vs. U curve are found at the lower and upper limit of the pattern forming regime with an inflection point at $U \approx 0.125$ close to the upper limit. When inspecting the simulations beyond this inflection point, a qualitative change of the pattern forming mechanism can be identified. While the stripes were previously formed very close to the position where the contact line was for a normal meniscus solution (cf. first two panels of Fig. 5.10), now a short film of finite height protrudes from the meniscus, at which the stripes are formed. This can also be identified in the bottom right panel of Fig. 5.11 as compared to the other two solution panels. The position where the stripes are formed moves further upwards with increasing velocity U until it moves outside the domain. The solution then represents the transfer of a Landau–Levich film, which marks the upper limit of the pattern forming regime.

At the upper limit of the pattern forming regime there is a competition between two solution

types: One is the homogeneous Landau–Levich film and the other is the striped pattern. When neglecting the downstream end of the domain with the meniscus, this situation is reminiscent of other systems in which a (unstable) homogeneous solution can be invaded by a front, leading to a different solution (in our case the stripe pattern). Probably the most prominent example of such a system is the Fisher-Kolmogorov equation [Fis37, KPP37]:

$$\partial_t \varphi(x, t) = \Delta \varphi(x, t) + \varphi(x, t) - \varphi(x, t)^3. \quad (5.6)$$

This equation has three homogeneous solutions, $\varphi_1 = 1$, $\varphi_2 = -1$ and $\varphi_3 = 0$, where the first two are linearly stable and φ_3 is linearly unstable. When a front connects a stable state with the unstable state, the front moves towards the unstable state. In analogy to our case, the stable state φ_1 would correspond to the stripe pattern, while the unstable state φ_3 would be the homogeneous Landau–Levich film. We discuss this analogy because in the case of the Fisher-Kolmogorov equation, one is able to calculate the velocity at which this front invades the unstable state using a method termed *linear marginal stability analysis* [DL83, vS88, vS03]. The concept is based on the assumption, that from a range of possible velocities of the front, the one will be selected that is linearly *marginally stable*, i.e., that a front moving faster would be stable and all fronts moving slower would be unstable with respect to perturbations within the comoving frame. An example of relevance in the context of this thesis is the augmented Cahn–Hilliard model (2.59). In [KGFT12], the marginal stability analysis could nicely predict the upper velocity limit of the patterning regime in which horizontal stripe patterns are formed. As a starting point of this method, one considers the leading edge of the front, where one can perform an ansatz for the evolution of a perturbation $\tilde{\varphi}$ of the field φ_3 at this point as

$$\tilde{\varphi} \propto e^{\omega t - kx}, \quad (5.7)$$

and consider the dispersion relation $\omega(k)$ of the equation linearized about the unstable state. The marginal stability criterion then reads in terms of this complex dispersion relation [vS88]

$$U^* = \frac{\operatorname{Re} \omega(k^*)}{\operatorname{Re} k^*}, \quad U^* = \left. \frac{d\omega(k)}{dk} \right|_{k=k^*}, \quad \operatorname{Im} \left. \frac{d\omega}{dk} \right|_{k=k^*} = 0. \quad (5.8)$$

Here, U^* is the marginal velocity at which the front moves. Coming back to our case of stripes formed at a dragged meniscus, the front is also subject to the dragging, i.e., to an additional advection velocity. The idea is now that the stripe formation is only possible if the marginal velocity (at which the stripe creating front can invade the unstable Landau–Levich film) is higher than the dragging velocity. Thus, the marginal stability analysis should deliver the upper velocity limit of the pattern forming regime. The calculations involve the dependency of the height of the Landau–Levich film on the transfer velocity, which can be obtained by numerical continuation as it was also used to obtain the bifurcation diagrams in the previous section. With this and the linearized operator one can solve Eq. (5.8) for the marginal velocity. This calculation will be part of an upcoming work [TWGT17] and the resulting velocity $U \approx 0.12577$ is also shown as a gray dashed line in Fig. 5.11. Obviously, the marginal velocity does not perfectly mark the upper velocity limit of the pattern forming regime, but quite precisely the inflection point of the λ vs U curve. This deviation is possibly due to the qualitative change in behavior occurring there. In particular, the protrusion that forms does not necessarily have the same liquid layer height as a Landau–Levich layer would have for the same velocity. However, as the latter enters the calculation of the marginal velocity, a deviation of this layer height from

the assumed one is a source of errors. In addition, one has to remember that after the liquid stripes are formed they are sliding downwards with respect to the moving substrate. Their sliding velocity should enter the threshold velocity in addition to the marginal velocity as a positive offset as it counteracts the dragging velocity. This effect and the validity of the whole approach apart from the single example studied here will be the topic of an upcoming work [TWGT17].

When considering the stripe patterns discussed in this section far away from the meniscus, i.e., neglecting how they were formed, they represent trains of perfectly arranged pseudo one-dimensional liquid ridges sliding down an inclined plane. This general setting of a liquid on an incline is very familiar to everyone, e.g., in the form of rain drops on a car's windshield. However, one almost never encounters straight liquid ridges sliding perpendicular to their long axis, not to mention a perfectly periodic train of them. In contrast, one is used to more or less oval-shaped drops of different sizes, sliding at various velocities and showing complex interactions with each other. Despite the simple set-up, one can therefore expect interesting phenomena already from physical intuition and everyday experience. Thus, we will analyze the dynamics of single drops on an inclined plate as well as large ensembles of such drops in the following chapter.

6 Dynamics of Sliding Drops

The dynamics of liquids on inclined substrates can be observed on a daily basis, such as rain drops on a windshield or water running down a plate after washing the dishes. Besides their appearance in everyday life, similar effects are also the subject of scientific interest, dealing with the dynamics of small droplets on inclined substrates due to the gravitational force [HM91, RQ99, PFL01] or droplets moving because of thermal or chemical gradients along the substrate inducing Marangoni forces [Gre78, Bro89, CW92]. In this chapter, we will study droplets on a homogeneous inclined substrate with a similar thin film approach as the one employed in the previous Chap. 5. However, here, we now no longer consider an active transfer geometry with special boundary conditions and an advection term, and we also neglect the hydrostatic pressure. In consequence, the thin film model (2.32) is reduced to

$$\partial_t h = -\nabla \cdot \left[\frac{h^3}{3} \nabla \left(\Delta h - \frac{1}{h^3} + \frac{1}{h^6} \right) + \frac{h^3}{3} G \begin{pmatrix} \alpha \\ 0 \end{pmatrix} \right], \quad (6.1)$$

with periodic boundary conditions in both x and y direction. That is, we still consider a partially wetting simple liquid subject to a Laplace pressure accounting for surface tension and a disjoining pressure accounting for wettability and resulting in a precursor film model.

Drops sliding due to gravity have already been studied intensively in experiments [PFL01, KLK02, LGDL05, SLGPL⁺07], analyzing the shape and dynamics of the drops depending on experimental parameters such as the drop volume and the inclination angle of the solid substrate. Among the most prominent effects observed is the so-called *pearling instability* [PFL01]: Above a critical inclination angle of the substrate at fixed drop volume or above a critical drop volume for fixed inclination angle, the drops deform strongly and break up into a large drop and a small satellite drop which is emitted at the back of the drop. The resulting large drop can then still be unstable and emit one or more subsequent satellite drops.

On the theoretical side, also much work has been conducted on the topic of sliding drops [BACP01, TVN⁺01, TNB⁺02, SLW⁺02, BACP03, LS04, SRCW05, BB15, XD16], focusing on various aspects, such as the morphological change with increasing inclination angles and the velocity of the drops depending on their volume and the inclination of the substrate. However, a thorough analysis of the bifurcations and the pearling dynamics of three-dimensional drops has not been conducted to our knowledge. This will be presented in the following Sec. 6.1, which bases on the publication [EWGT16]. Thereafter, in Sec. 6.2, we will discuss the dynamics of large ensembles of sliding drops and the resulting drop volume statistics.

6.1 Individual Sliding Drops

In a first step, we will now consider the stationary and time-dependent solutions for a single sliding drop on a periodic domain. Besides being advantageous for the numerical treatment, the periodic setting also represents the experimental situation in [PFL01], where drops are time-periodically placed on an inclined substrate. This means that in the case of unstable drops,

each drop can interact with the satellite drops of the previous drop, as is the case for a single drop on a periodic domain. Our analysis is based on two approaches. Using two-dimensional numerical path-continuation¹ (cf. [UWR14] and Sec. 3.4), we will analyze the steady drop solutions of the model (6.1) and their stability properties in dependence on the inclination angle α . This reveals both the possible solution types, i.e., drop shapes, as well as the bifurcations leading to instabilities. In addition, we conduct two-dimensional direct numerical simulations to investigate the dynamic behavior of unstable drops and in particular the pearling instability. All considerations in this section are done for a fixed volume $V = 3 \cdot 10^4$ of the drops on a fixed rectangular domain $\Omega = [0, 200] \times [0, 100]$ and the remaining control parameter of interest is the inclination angle α . Figure 6.1 presents the bifurcation diagram of such drops showing

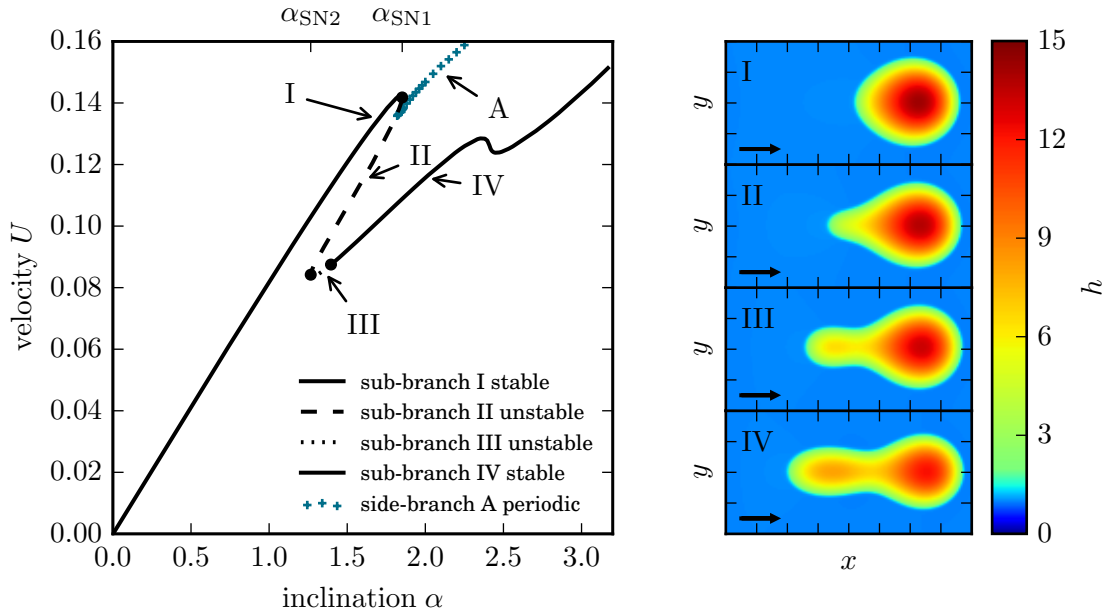


Figure 6.1: Left panel: Bifurcation diagram of sliding drop solutions of Eq. (6.1) with volume $V = 3 \cdot 10^4$ showing the sliding velocity U in dependence on the inclination angle α . There exist several sub-branches of steady drops with different shape and behavior, see labels I to IV and the corresponding exemplary solutions in the right panels (the black arrows denote the sliding direction). In addition, the side-branch A corresponding to time-periodic solutions exhibiting repeated break-up and coalescence cycles is shown (the bifurcation diagram of steady solutions was obtained by Sebastian Engelnkemper, cf. [EWGT16]).

their sliding velocity U in dependence on the inclination angle α . In the following, we divide the branch of all possible steady solutions into different *sub-branches* which we classify by their characteristic shapes and stability properties.

The first sub-branch I starts at the origin $(\alpha, U) = (0, 0)$, which corresponds to a circular

¹The results from numerical continuation in this chapter were achieved by Sebastian Engelnkemper [EWGT16]. To obtain drop solutions that slide with a constant shape and velocity U as solutions of a stationary problem, the continuation is performed with an additional advective term $-(U, 0)^T \cdot \nabla h$ in Eq. (6.1).

drop at rest on a non-inclined substrate. For a large inclination interval up to $\alpha \approx 1.5$, the velocity of the drop grows linearly with the inclination α . In this regime, the drop is only slightly deformed to an oval shape (cf. panel I in Fig. 6.1). Towards the end of sub-branch I, the deformation of the drop becomes stronger, also leading to a front-back asymmetry. The sub-branch ends in a saddle-node bifurcation at an inclination angle α_{SN1} , where the solution becomes linearly unstable. The left panels of Fig. 6.2 show the solution as well as the corresponding eigenfunction to become unstable at this bifurcation. The shape of the eigenfunction reveals that at the instability, mass of the drop is transferred from the sides of the drop to the front and particularly the back (with respect to the sliding direction). That is, the eigenfunction corresponds to an elongation of the drop. Beyond the bifurcation inclination angle α_{SN1} , there no longer exist steady simple drop-shaped solutions. When performing direct numerical simulations beyond α_{SN1} with a simple drop shape as initial conditions, the drop is unstable and deforms until it splits into a large drop and a smaller one, which is emitted at the back of the drop. That is, one observes the aforementioned *pearling instability*. The right

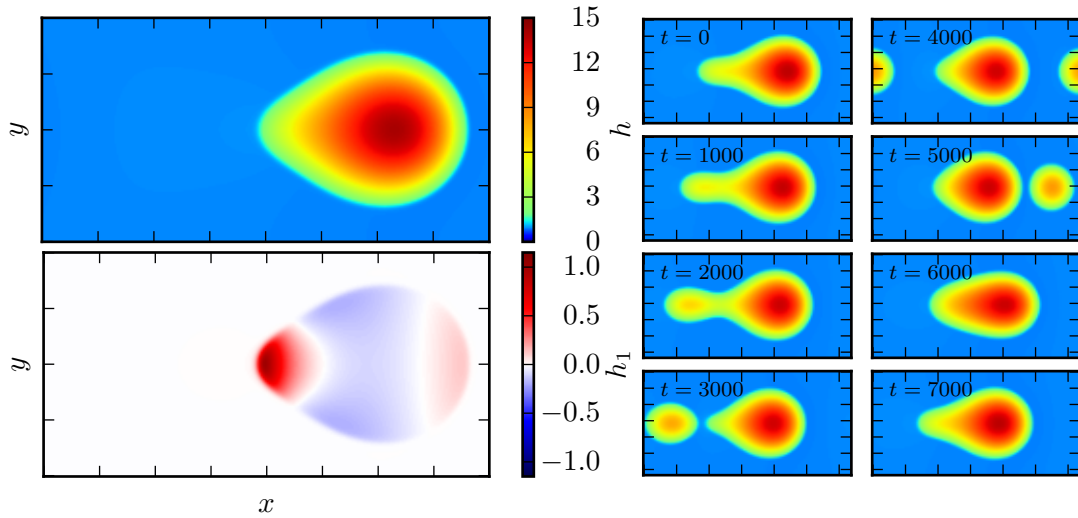


Figure 6.2: Left panels: Drop solution (top) and corresponding eigenfunction (bottom) that becomes unstable at the first saddle-node bifurcation α_{SN1} connecting the stable sub-branch I and the linearly unstable sub-branch II. The right panels show snapshots at different times of a direct numerical simulation of a drop for an inclination beyond the saddle-node bifurcation. The drop is unstable, emits a small satellite drop and coalesces with it again after one revolution in the periodic domain. The solutions are shifted to a co-moving frame for better visibility (cf. [EWGT16]).

panels of Fig. 6.2 show a time series of this process. After the break-up, the larger drop is sliding faster than the smaller one and due to the periodic boundary conditions it can reach the smaller one again and finally coalesce with it. The resulting drop is then unstable again and it splits into two drops. This occurs repeatedly, leading to periodic break-up and coalescence cycles. These cycles are truly periodic, indicating that the drop always breaks up into two drops with the same volumes in each cycle. The sliding velocity $U(t)$ of the drops varies greatly over the course of one cycle, as presented in Fig. 6.3. Because the drop shape changes over time,

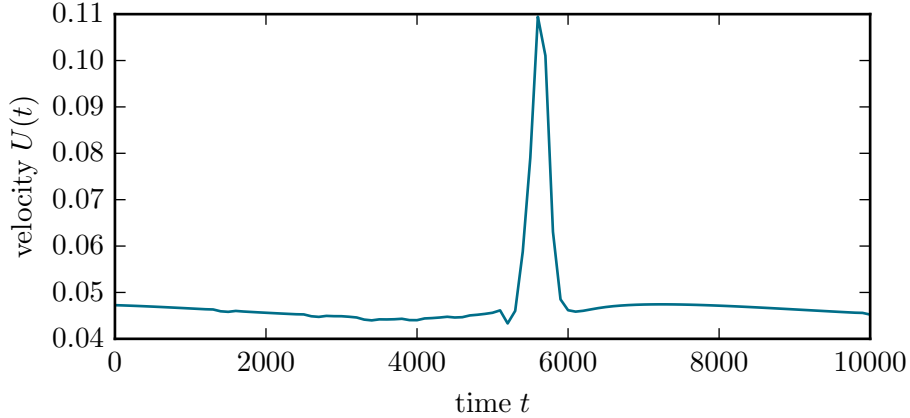


Figure 6.3: Time series of the drop velocity during one break-up and coalescence cycle. The velocity is highest during the coalescence process and lowest when the drop is split, cf. $t \in [3000, 4000]$ here and in Fig. 6.2 [EWGT16].

we define the sliding velocity as the velocity of the point with maximal height. This velocity is lowest, when there are two split-up drops sliding separately. In contrast, it is higher, when the drop is coalesced and highest during the coalescence process. To compare these periodic solutions with the steady drop solutions in the bifurcation diagram in Fig. 6.1, the sliding velocity is averaged over multiple cycles and plotted as blue crosses. Upon closer inspection of the bifurcation diagram, one notes that the side-branch A of the periodic solutions does not emerge from the saddle-node bifurcation at α_{SN1} but it also coexists with sub-branch I for smaller inclination angles. In this regime one can either obtain a periodic solution on side-branch A or a stable steady solution on sub-branch I, depending on the initial conditions of a simulation. The origin of side-branch A at low α is seemingly located on the sub-branch II of linearly unstable steady solution, which will be discussed later on. As there is no change of linear stability at this point of sub-branch II, one can already assume that the onset of side-branch A is a *global bifurcation* [Str14].

Along side-branch A, the average velocity of the drop increases with the inclination angle. In addition, the temporal period T_{per} of the break-up and coalescence cycles is decreasing, which is shown in Fig. 6.4. Close to the onset of sub-branch II, the period exhibits a particularly strong decrease. The dependence of the period on the inclination angle can be well described with a logarithmic function

$$T_{\text{per}} = a \ln(\alpha - \alpha_{\text{bif}}) + b, \quad (6.2)$$

where α_{bif} is a fit parameter describing the onset inclination of side-branch A, a is an amplitude parameter, and b is an offset parameter. The logarithmic dependence of T_{per} on the inclination angle α indicates a *homoclinic bifurcation* at the onset of side-branch A [Str14].

The periods T_{per} that are shown in Fig. 6.4 are averaged over ten periods, and in addition the resulting standard deviation is also shown as error bars. For inclination angles above $\alpha \approx 2.1$, both the mean period and the standard deviation increase. The latter indicates that the period T_{per} is no longer constant, but varies from cycle to cycle. In the inclination range from $\alpha \approx 2.15$ to $\alpha \approx 2.20$, a *period doubling* can be observed, meaning that the period always

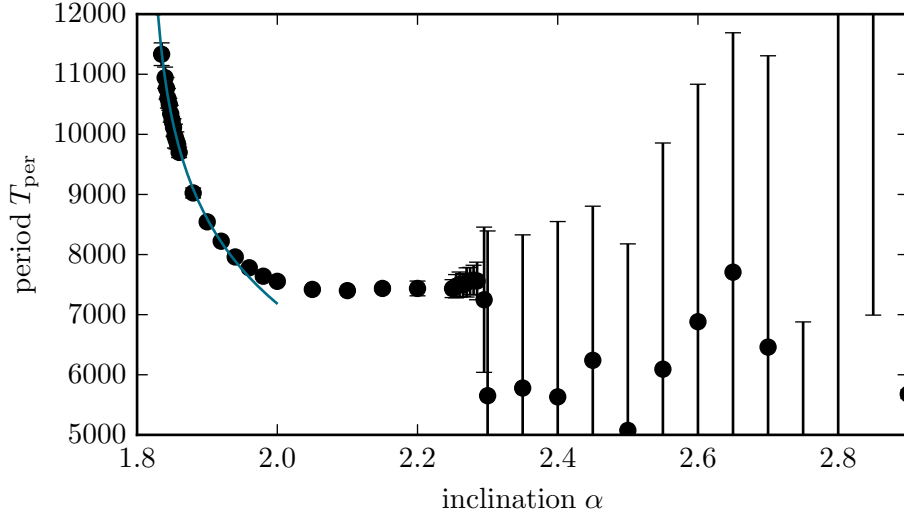


Figure 6.4: Period of one break-up and coalescence cycle depending on the inclination angle α . For low velocities, the dependence is nicely reflected by a logarithmic fit $T_{\text{per}} \propto \ln(\alpha - \alpha_{\text{bif}})$ (blue line). This indicates a homoclinic bifurcation at the onset. The standard deviation (indicated by error bars) increases after the first period doubling at $\alpha \approx 2.15$ (cf. [EWGT16]).

alternates between two different values. As the term “period doubling” suggests, the overall temporal period of the system is therefore doubled, because it now takes *two* break-up and coalescence cycles before the initial state is reached again. Beyond the period doubling, the standard deviation is steadily increasing. The dynamics that appear in this regime can be best identified by considering the volume of the drops in the split state. To this end, we determine the volume of the drops at each time step by integrating over the footprint Ω_{drop} of each drop,

$$V_{\text{drop}} = \int_{\Omega_{\text{drop}}} (h - h_{\text{thres}}) d^2\mathbf{x}. \quad (6.3)$$

To this end, we identify the footprint of the drops as connected areas in the simulation domain in which the liquid height exceeds a threshold height $h_{\text{thres}} = 1.05$. To ensure that drops with equal real volume, but different base area are assigned the same V_{drop} , the threshold height is subtracted in the integration. This leads to slightly underestimated drop volumes, but as we only quantitatively compare volumes within the simulations with the same method, this effect is negligible.

The period doubling becomes easily notable when looking at the time series of the drop volumes in a single simulation, which is presented in Fig. 6.5 for an inclination $\alpha = 2.2$. The break-up and coalescence cycles are visible as the alteration between times in which only one volume near $V \approx 30000$ is found and others, in which two volumes at $V \approx 22000$ and $V \approx 80000$ occur (cf., $t = 10000$ and $t = 14000$ in Fig. 6.5). The period doubling leads to different volumes in the split state when comparing two consequent cycles (cf., $t = 10000$ and $t = 18000$ in Fig. 6.5). The size of the smaller drop is larger at $t = 18000$ than at $t = 10000$, and vice versa for the larger drop, as can also be seen in the top four panels of Fig. 6.5. Each

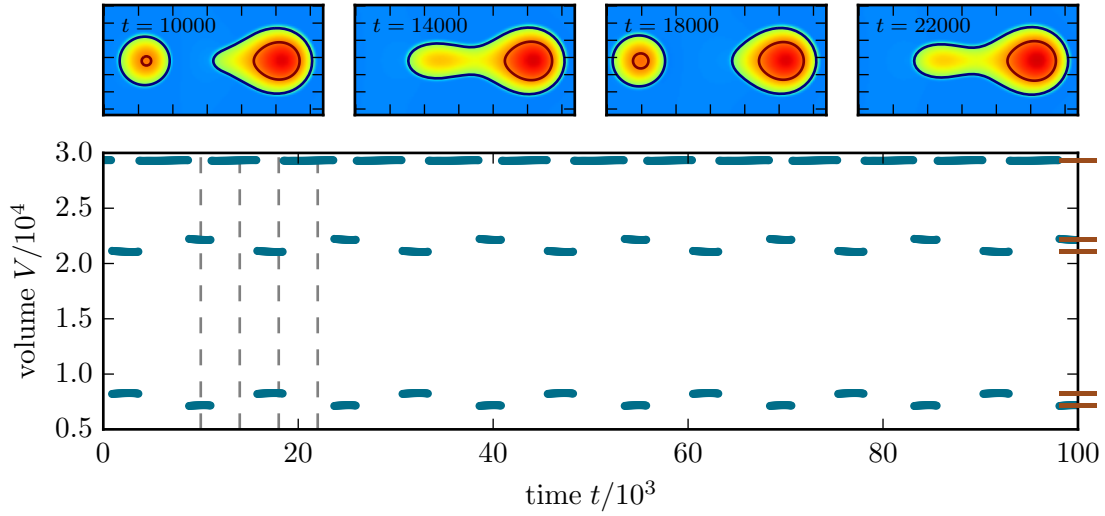


Figure 6.5: Bottom panel: Time series of the drop volumes occurring in a direct numerical simulation of Eq. (6.1) for $\alpha = 2.2$ on the periodic side-branch A. Volumes around 30000 correspond to a single coalesced drop, while volumes at $V \approx 22000$ and $V \approx 80000$ represent the larger and smaller drop after break-up, respectively. The particular volumes in the split phase alternate from cycle to cycle. The red bars at the right boundary of the bottom panel mark all volumes that occur during the whole simulation. The top four panels show snapshots at different times (marked by dashed lines in the bottom panel) indicating the different sizes of the drops in two consecutive cycles (cf. [EWGT16]).

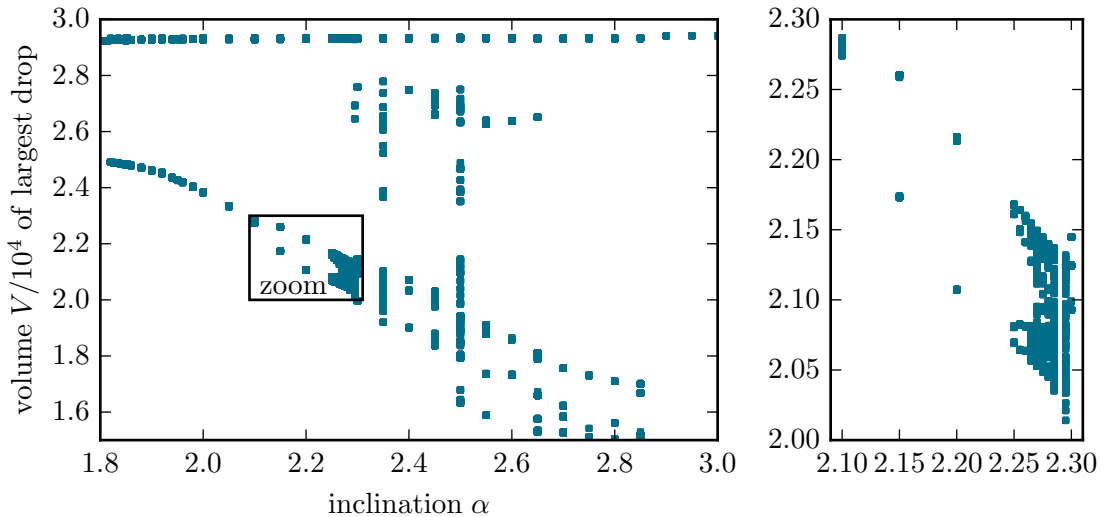


Figure 6.6: All volumes of the largest drop occurring during one simulation in dependence on the inclination angle α . For each α , multiple volumes occur during the course of a simulation of Eq. (6.1) (cf. red bars in Fig. 6.5), corresponding to the coalesced and split states (cf. [EWGT16]). The right panel is a zoom of the left panel into the period-doubling regime.

two following cycles exhibit the same behavior, meaning that the overall temporal periodicity comprises two break-up and coalescence cycles.

In order to compare simulations for different inclination angles, we now collect all drop volumes occurring in one simulation (cf. the red bars at the right edge of Fig. 6.5), and study their dependence on the inclination angle. The result is presented in Fig. 6.6. where the volume axis now only embraces the volumes of the largest drop. Here, one can now identify different regimes. Up to $\alpha \approx 2.10$, two different volumes occur, corresponding to the coalesced state and a single split state. Hence, drops in this region show a simple periodic behavior. Between $\alpha \approx 2.15$ and $\alpha \approx 2.20$, the split state exhibits two different volumes, marking the period doubling. At $\alpha \approx 2.25$, a second period doubling occurs and each of the two volumes of the split state separates into two different volumes, i.e., a period four solution is obtained here. For slightly increased inclination angles, further period doublings seem to occur, leading to a broad distribution of different volumes (cf. right panel of Fig. 6.6). In this region, the break-up and coalescence cycles are no longer periodic, but chaotic. That is, the sliding drops exhibit the well-known period doubling route to chaos, which is one of the classical routes to chaos [Str14]. A typical property of such systems is also the existence of *periodic windows*, where again periodic solutions can be found. For large inclination angles, also solutions can exist, in which the larger drop is still unstable after the first break-up and emits a second satellite drop. Then, three distinct drops can be found simultaneously.

Beyond an inclination $\alpha \approx 2.9$, the drops have a very elongated shape and they therefore span the whole simulation domain. They then no longer represent drops, but modulated rivulets. The modulations can still be periodic in time or chaotic. However, the dynamics of such liquid ridges is not within the scope of this thesis.

For all results presented up to now, we considered a single drop on a periodic spatial domain of size $\Omega = [0, 100] \times [0, 200]$. As mentioned before, the periodic domain also resembles the experimental setting in [PFL01], where drops are created periodically in time on the substrate by a nozzle which translates to a periodic train of drops sliding down the inclined substrate. In this setup, individual drops can be subject to different perturbations and therefore exhibit different behavior. In the pearling regime, adjacent drops can interact via the satellite drops that are emitted by an unstable drop and then coalesce with the consequent drop. Variations of the satellite drop size induced by perturbations could now either be damped through the interaction with neighboring drops or they could be amplified, possibly leading to new instabilities. To investigate this possibility, we perform a simulation of four identical drops on a four times larger domain $\Omega_4 = [0, 100] \times [0, 800]$. Snapshots at different times are shown in Fig. 6.7. The simulation is conducted for an inclination angle $\alpha = 1.9$, which is above the first saddle-node bifurcation of simple oval drops at α_{SN1} but well below the onset of the period doubling. In a first phase of the simulation corresponding to approximately 20 break-up and coalescence cycles, the dynamics is the same as expected from the simulations of a single drop on a larger domain, i.e., all four drops exhibit the same behavior (cf. first two panels of Fig. 6.7). For later times, a small asymmetry between each two neighboring drops becomes apparent, where the pearling occurs at slightly different times. This asymmetry grows with time (cf. third and fourth panel of Fig. 6.7), until the satellite drop of one large drop already reaches the neighboring drop before the latter broke up. This then leads to a case in which only one satellite drop exists for two large drops. This configuration then exists for the remainder of the simulation and is seemingly stable (cf. last two panels of Fig. 6.7). Such kinds of configurations are of course not possible when considering single drops on smaller domain, because the volume conservation has to be fulfilled for the single drop, while on a larger domain it only has to be fulfilled for

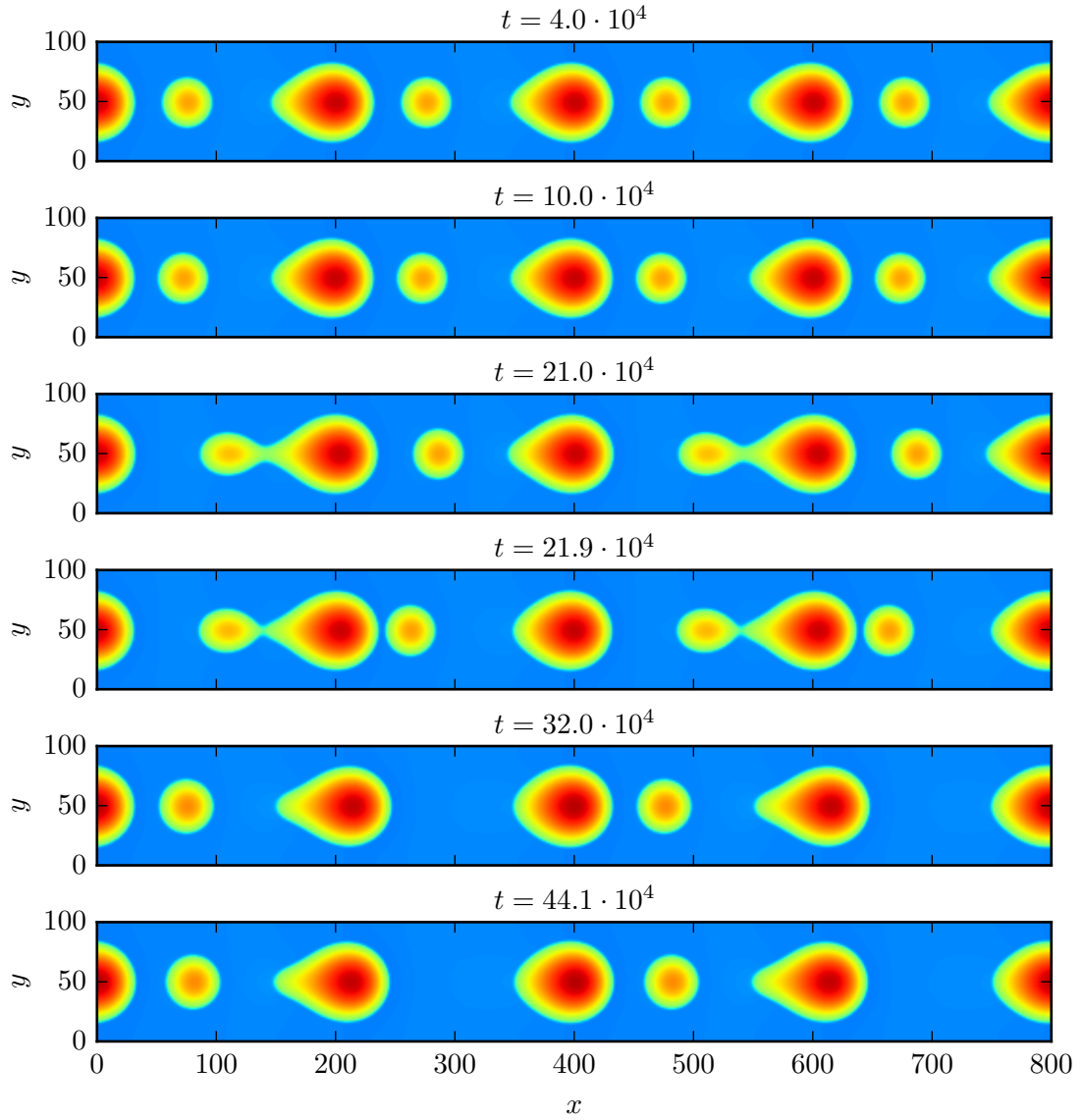


Figure 6.7: Snapshots at different times of an array of sliding drops at $\alpha = 1.9$ in a direct numerical simulation of Eq. (6.1). The drops first exhibit the same periodic break-up and coalescence cycles as a single drop on a smaller domain would show. At later times (third and fourth row), an asymmetry between two neighboring drops develops, and finally each two large drops share just one satellite drop (fifth and sixth row). The times of the snapshots are chosen to display the same stage of the break-up and coalescence cycle, and the solutions are shifted along the x axis for better visibility.

many drops together. This example should point out that for dynamic effects like the break-up and coalescence cycles, one has to keep in mind that the periodic boundary conditions can pose restrictions that limit the accessible solutions.

After this discussion of solutions on the periodic side-branch A, we will come back to the other branches of steady solutions in the bifurcation diagram in Fig. 6.1. The saddle-node bifurcation at α_{SN1} connects the stable sub-branch I to the linearly unstable sub-branch II. The drop solutions of this sub-branch exhibit a protrusion at their back which grows for decreasing inclination angle when following the branch. Direct numerical simulations of solutions on this sub-branch can show two different behaviors: Either the protrusion at the back of the drop shrinks until a shape corresponding to the solutions on sub-branch I is reached, or the protrusion can grow in size until a satellite drop is formed. After one revolution, this satellite drop coalesces with the main drop and also forms a simple drop corresponding to sub-branch I.

At a lower inclination angle α_{SN2} , another saddle-node bifurcation occurs. However, the stability of the solutions on this branch is not changed here, as a second real eigenvalue becomes positive at this point, i.e., the solutions are still linearly unstable. Following the branch a little further for increasing α , both positive real eigenvalues meet and form a pair of complex conjugate eigenvalues. As this qualitatively changes the dynamics of the solutions, we define this as the beginning of the next sub-branch III. The solutions of this sub-branch exhibit an oscillatory instability due to the complex pair of unstable eigenvalues. Figure. 6.8 shows an exemplary

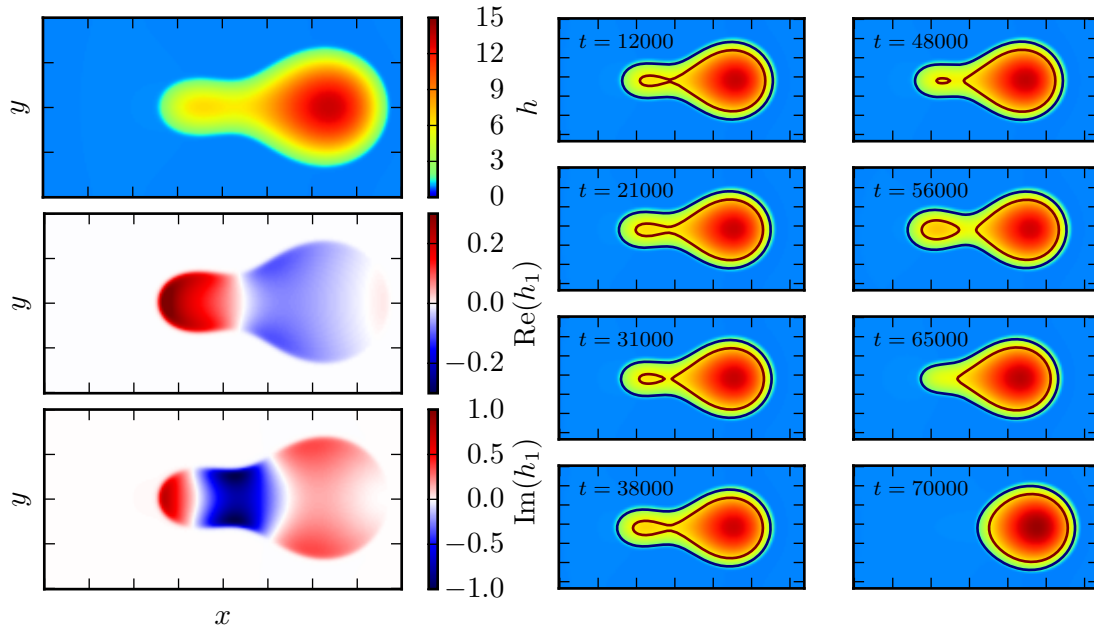


Figure 6.8: Left panels: Height profile of a drop solution for $\alpha = 1.35$ on sub-branch III (top panel) and the real and imaginary part of the unstable eigenfunction (middle and bottom panel, respectively). Right panels: Snapshots at different times of a direct numerical simulation of the same solution of Eq. (6.1) as in the left panels. An oscillatory mass transport between the front and back of the drop leads to a repeated swelling and shrinking of the tail, which becomes notable when looking at the contour lines on the tail of the drop (cf. [EWGT16]).

drop solution on sub-branch III and the unstable complex eigenfunction (left panels). The shape of the eigenfunction corresponds to a mass transfer between the bulk of the drop and the elongated tail. Direct numerical simulations using such a drop as initial condition exhibit an oscillatory, *breathing-like* behavior. Mass is repeatedly moved between the front and the back of the drop and vice versa. The amplitude of this oscillation grows with time, until the deformation of the drop is large enough that it either directly relaxes to a simple drop shape corresponding to sub-branch I, or the drop undergoes a single break-up and coalescence cycle and then obtains the simple drop shape. The oscillatory instability can be further analyzed by looking at the time series of the height $h_{\max}(t)$ and the sliding velocity $U(t)$ of the drops in this regime. This is presented in Fig. 6.9 for the same simulation as shown in Fig. 6.8. Both

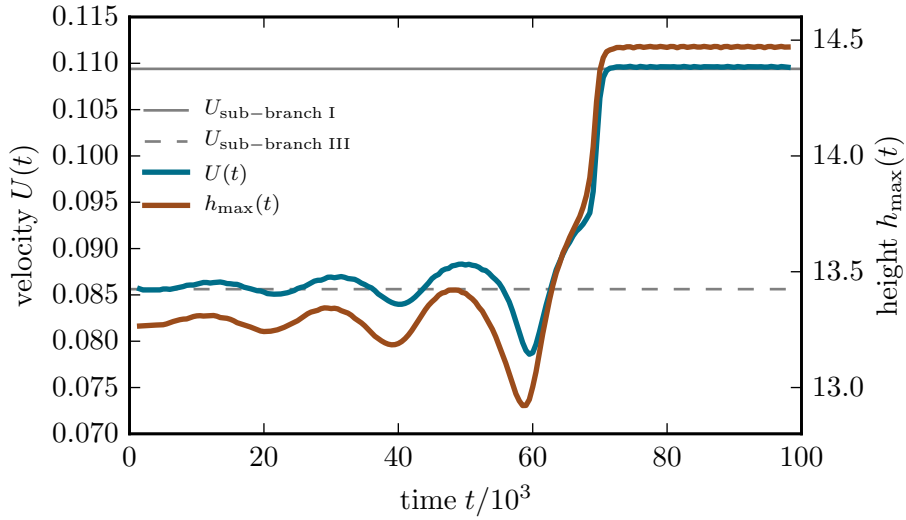


Figure 6.9: Temporal evolution of the height $h_{\max}(t)$ and the sliding velocity $U(t)$ of an oscillatory unstable drop at $\alpha = 1.35$ on sub-branch III (cf. Fig. 6.8). Both measures oscillate with an increasing amplitude until the deformation of the drop is large enough so that it relaxes to the shape and velocity corresponding to sub-branch I (cf. [EWGT16]).

the height and the velocity of the drop exhibit harmonic oscillations with a growing amplitude for approximately two periods (up to $t \approx 50000$). Afterward, the oscillations become clearly non-harmonic, which indicates that the dynamics is then no longer governed by the linear eigenfunctions. The amplitude of the oscillation is growing for one more period until the drop relaxes to a steady simple drop shape, which is sliding with constant velocity and height.

The sub-branch III ends in a Hopf bifurcation at a certain angle α_{Hopf} where the real parts of the previously unstable eigenvalues become zero. The solutions on the following sub-branch IV are therefore linearly stable. The drops on this sub-branch have a pronounced protrusion on their back, which grows for increasing inclination angle α . Simultaneously, the main body of the drop shrinks, as the overall volume of the drop is conserved. The lower end of sub-branch IV at α_{Hopf} is below the location of the first saddle-node bifurcation of sub-branch I at α_{SN1} . That is, in the interval $[\alpha_{\text{Hopf}}, \alpha_{\text{SN1}}]$, both stable solution types coexist. This indicates a *multistability* of the solutions of this system. Both solution types are equally possible and

stable in this regime and which solution is obtained in a time simulation depends solely on the initial conditions. Beyond α_{SN1} , there is a similar coexistence between the pearling solutions of the periodic side-branch A and the stable steady solutions of sub-branch IV.

Following sub-branch IV to larger inclination angles, the drops are further elongated until they span the whole domain and the front of the drop interacts with its own back. The solutions then no longer represent drops, but modulated liquid ridges. We will not discuss this type of solutions here any further and only refer to [EWGT16] for details.

The steady and dynamic drop solutions we discussed in this section up to now were all calculated for a fixed volume $V = 3 \cdot 10^4$. Of course one can expect that properties such as the sliding velocity or the instability threshold α_{SN1} will also depend on the volume of the drop. To study this, one can re-calculate all results in this section for different volumes, in particular the bifurcation diagram in Fig. 6.1. It turns out that, despite obvious quantitative differences, the overall structure of the bifurcation diagram persists for drop volumes over several orders of magnitude (up to $V > 2 \cdot 10^6$). Furthermore, one can find scaling laws for the quantitative properties, such as the sliding velocity and the instability threshold α_{SN1} which can be used to collapse the bifurcation diagrams for various drop volumes onto a single master curve. The validity of the scaling laws can be seen in Fig. 6.10, where the data obtained from the bifurcation diagrams for various drop volumes are plotted together with fitted power law ansatz functions. In particular, one can find that the location of the first saddle-node bifurcation α_{SN1} scales as

$$\alpha_{\text{SN1}} = a_1 V^{\beta_1} \quad \text{with } \beta_1 = -0.713 \pm 0.005 \text{ and } a_1 = (2.9 \pm 0.1) \cdot 10^3 \quad (6.4)$$

with the volume V . For the velocity U of simple-shaped drops corresponding to the sub-branch I,

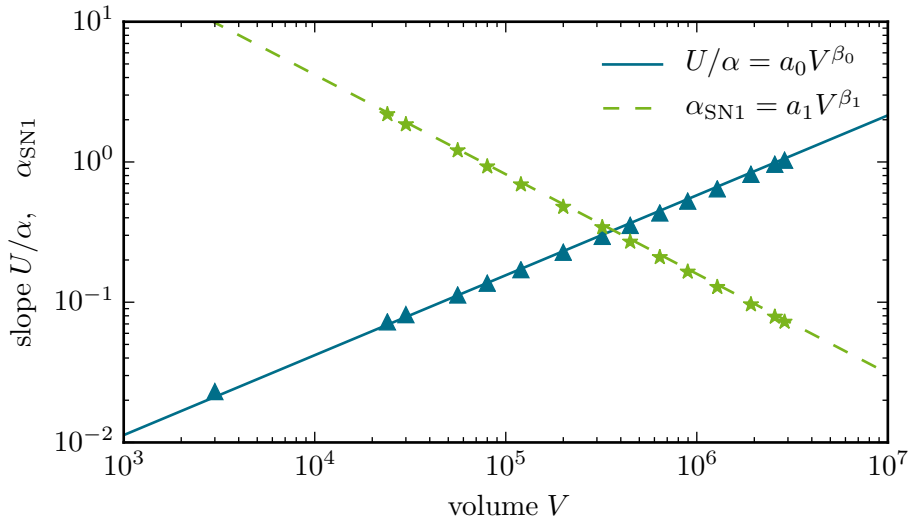


Figure 6.10: Scaling behavior of the velocity U of sliding drops (blue) and the instability inclination α_{SN1} (green) with the drop volume V . The markers indicate the data obtained from numerical continuation for different drop volumes, while the lines indicate a fitted power law (the data was obtained by Sebastian Engelnkemper, cf. [EWGT16]).

we find

$$U = \alpha a_0 V^{\beta_0} \quad \text{with } \beta_0 = 0.569 \pm 0.005 \text{ and } a_0 = (2.2 \pm 0.2) \cdot 10^{-4}. \quad (6.5)$$

The existence of these scaling laws generalizes all results from this section to a broad range of drop volumes. For more details, we again refer to [EWGT16].

The break-up and coalescence cycles of drops on side-branch A and in particular the example of four drops on a large domain in Fig. 6.7 already proved that multiple drops on the same domain can exhibit interesting interactions. Still, the settings we discussed up to now are rather artificial. Mostly, they are useful for fundamental studies of situations encountered in controlled laboratory experiments, but they do not reflect typical everyday experience. In contrast, we will now turn to the case of large ensembles of interacting drops on large spatial domains, which closely resembles, e.g., the case of rain drops on an inclined windshield.

6.2 Collective Behavior of Sliding Drops

To study the dynamics of large ensembles of sliding drops, we employ the same thin film model (6.1) as in the previous section. We now consider a much larger periodic spatial domain $\Omega = [0, 4000] \times [0, 4000]$ which is discretized on a quadratic mesh with 1024×1024 elements². In combination with the long time spans that are considered (up to $T = 5 \cdot 10^5$), this results in a considerable numerical effort. Therefore, the simulations were conducted on the parallel cluster PALMA at the University of Münster, with each simulation taking approximately 5000 CPU hours.

In the following, we are in particular interested in the *coarsening dynamics* of the ensembles of drops [Mea92, GW03, GW08, Kit14]. Already in the case of a horizontal substrate without inclination, liquid drops have the tendency to form larger structures with time at the expense of smaller ones. This process is also denoted as Ostwald ripening [Ost96, GW03, GORS09]. This is induced by the surface tension, which, at a fixed overall mass, energetically favors fewer but larger structures as compared to many smaller ones. Therefore, mass is transported from small drops to larger ones until the small ones vanish. Over time, this reduces the number of drops and enlarges the average drop size until only one large drop would accommodate all the mass. In practice, this is a very slow process which is limited by the mass transfer between the drops. When assuming the existence of a precursor film covering the whole substrate, as we do using the thin film model (6.1), mass transport is possible in terms of a flux through this precursor. In addition, this flux can lead to a movement of the drops with respect to each other [GW03]. For volatile liquids, also a transport via evaporation and adsorption can occur, which we do not study here. However, these transport possibilities are rather slow. When we now consider an inclined substrate on which the drops can slide, we in practice introduce an additional mechanism of mass transport and exchange. As we have seen in the previous section, large drops on an inclined substrate slide with a higher velocity than smaller ones and can therefore overtake the latter and also merge with them. Such a coalescence process corresponds to a mass flux from the smaller drop into the larger one that is much larger than typical fluxes through the precursor or the vapor phase. Hence, one can expect accelerated coarsening dynamics on inclined substrates as compared to non-inclined ones [Mea92]. In addition, we have already

²We are aware of the fact that the resulting spatial resolution is rather low and is not in general sufficient to resolve the contact line of the drops. This can have an influence on, e.g., the sliding velocity. However, we only focus on statistical properties of large ensembles in the following and we checked that these properties are not significantly changed for better spatial resolutions.

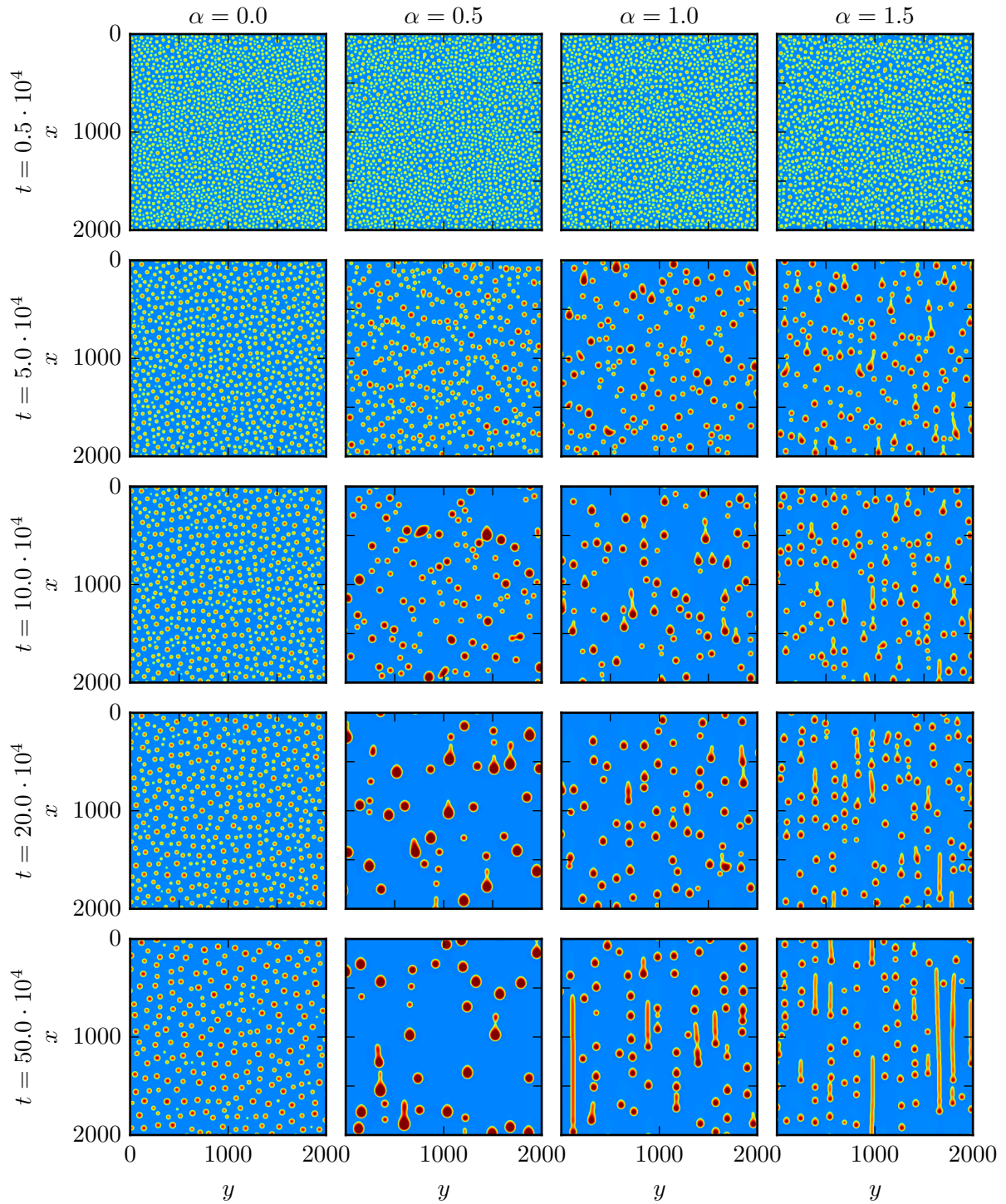


Figure 6.11: Snapshots at different times (rows) of numerical simulations of the model (6.1) for ensembles of sliding drops for various inclination angles (columns). Each panel only shows one quarter of the actual simulation domain for better visibility.

discussed the pearling instability of sliding drops in the previous section, which is a process that counteracts the coarsening dynamics, as it leads to the transition from a large drop to two or more smaller ones. In the following, we will discuss the different kind of dynamics emerging from this interplay of different processes.

Figure 6.11 presents an overview of the coarsening dynamics depending on the inclination angle of the substrate. Shown are snapshots at different times (rows) for the inclination angles $\alpha = 0.0$, $\alpha = 0.5$, $\alpha = 1.0$ and $\alpha = 1.5$ (columns, left to right). All simulations are performed using a homogeneous liquid layer of height $h_0 = 2.0$ perturbed by small amplitude noise as initial conditions. The reference case for $\alpha = 0.0$ shows the aforementioned typical coarsening dynamics where the number of drops decreases with time and the average drop size increases. However, the process is slow and therefore only small differences are visible when comparing the different snapshots. At the end of the time simulation, the domain is still filled with a large number of small drops. The overall picture is very different for non-zero inclinations. While the first snapshots at $t = 0.5 \cdot 10^4$ look very similar for all inclination angles, this does not hold for $t = 5.0 \cdot 10^4$. The typical drop size at a given time becomes larger for increased inclination angles. This difference to the reference case increases with time. For $\alpha = 0.5$, the typical drop size continuously increases up to $t = 20.0 \cdot 10^4$. However, in this snapshot one can already identify large drops that are unstable and break up. These instabilities hinder the further coarsening process and, accordingly, the last snapshot at $t = 50.0 \cdot 10^4$ looks similar to the previous one at $t = 20.0 \cdot 10^4$ with equally sized drops. For larger inclination angles $\alpha = 1.0$ and $\alpha = 1.5$, a similar behavior can be identified. However, the time span after which the coarsening process seemingly stops is shorter and the average drop size is smaller. That is, the pearling instability counteracting the coarsening process occurs already for smaller drops if the inclination is increased.

After rather large time spans, e.g., in the snapshots for $t = 50.0 \cdot 10^4$, one also notes the formation of very elongated drops which accommodate a large liquid volume. In the previous section, we have already seen that this type of drops (cf. sub-branch IV in Fig. 6.1) is stable and can coexist with the typical oval drops.

After this phenomenological description of the coarsening dynamics of the ensembles of sliding drops, we next discuss measures that can be employed to quantitatively investigate the effect of inclination on the coarsening.

6.2.1 Coarsening Dynamics in Fourier Space

The Fourier spectrum $\mathcal{FT}[h]$ of a snapshot of the height profile $h(x, y)$ can be used to determine the typical length scales of the whole drop structure. In general, the Fourier spectrum $\mathcal{FT}[h]$ is a two-dimensional function of the wave numbers k_x and k_y . Since we consider an inclined substrate, the x direction parallel to the inclination and the y direction perpendicular to it are distinguished directions. Thus, we expect an anisotropy of the Fourier spectra along the two directions. In particular, we will consider the one-dimensional power spectra for $k_x = 0$ and $k_y = 0$, which corresponds to the absolute square of the Fourier spectra of the x - and y -averaged height profile, respectively. Such spectra typically exhibit a maximum at a certain wave number k_{\max} which directly translates into a predominant wavelength $\lambda = \frac{2\pi}{k_{\max}}$, which in our case is a typical distance between the drops. As the overall volume is conserved in the system, this wavelength also contains information about the typical drop size. In general, smaller dominant wave numbers indicate larger typical distances between the drops and therefore also larger

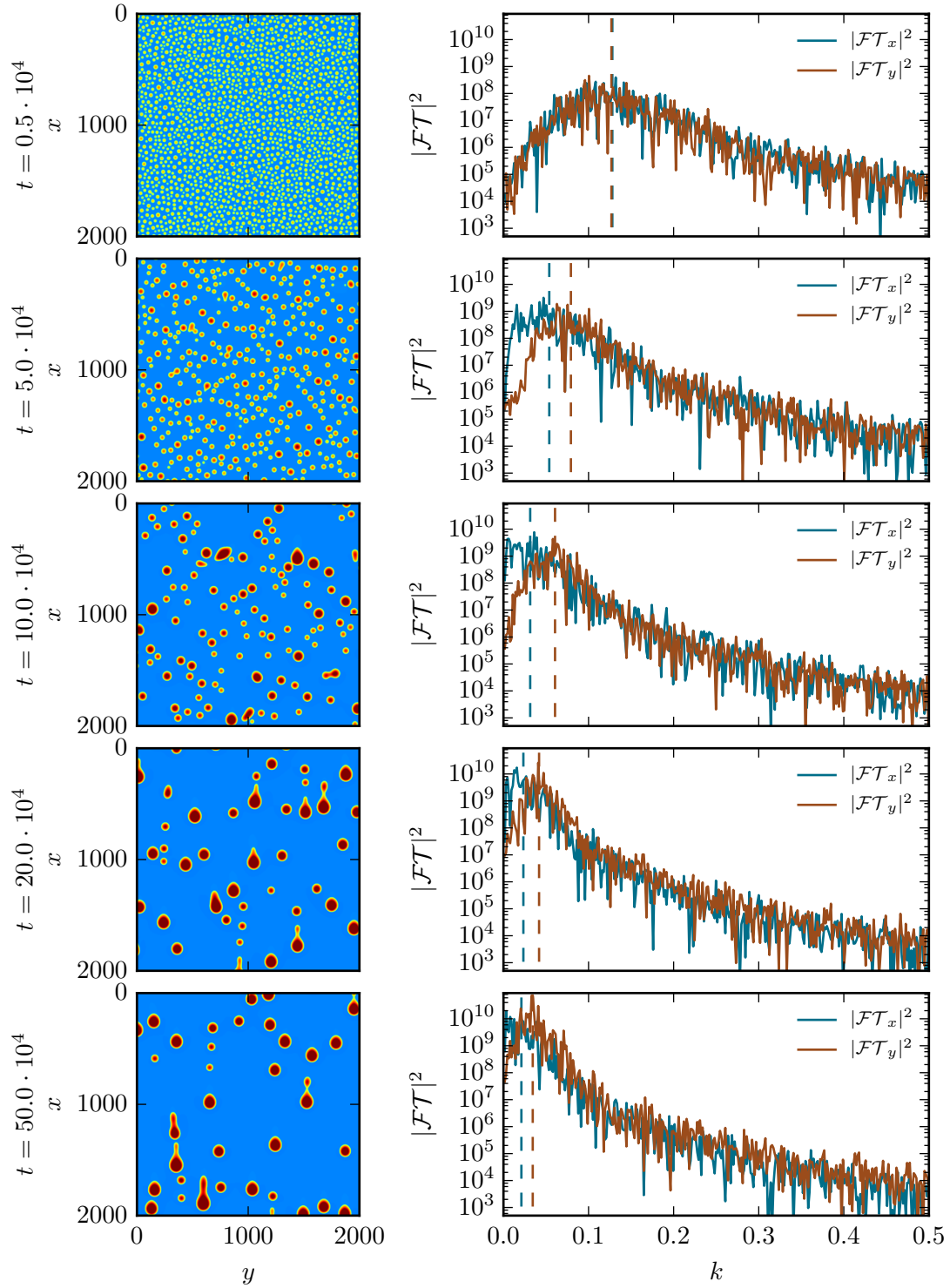


Figure 6.12: Left panels: Snapshots at different times of a direct numerical simulation of Eq. (6.1) for drops sliding on an inclined substrate with $\alpha = 0.5$. Right panels: Corresponding power spectra $|\mathcal{FT}_x|^2$ (blue lines) and $|\mathcal{FT}_y|^2$ (red lines) in logarithmic presentation. The positions of the mean wave numbers, cf. Eq. (6.7), are indicated by dashed lines.

drops. Figure 6.12 shows the absolute square of the Fourier spectra

$$\mathcal{FT}_x(k_x) := \mathcal{FT}[h](k_x, k_y = 0) \quad \text{and} \quad \mathcal{FT}_y(k_y) := \mathcal{FT}[h](k_x = 0, k_y) \quad (6.6)$$

at the same times as the snapshots in Fig. 6.11 for an inclination $\alpha = 0.5$. As the power spectra are typically rather noisy, the identification of the dominant wave number as the location of a maximum is not reliable. Therefore, we introduce the *mean wave numbers* k_{mean} in x and y direction as an alternative measure and define

$$k_{\text{mean},x} = \frac{\int_0^\infty k_x |\mathcal{FT}_x|^2 dk_x}{\int_0^\infty |\mathcal{FT}_x|^2 dk_x}, \quad (6.7)$$

$$k_{\text{mean},y} = \frac{\int_0^\infty k_y |\mathcal{FT}_y|^2 dk_y}{\int_0^\infty |\mathcal{FT}_y|^2 dk_y}.$$

The positions of the mean wave numbers are also marked in Fig. 6.12 by dashed lines. In general, the power spectra are shifted towards smaller wave numbers for increasing time. For later times (cf. last two rows of Fig. 6.12), this stops and a rather stationary spectrum is reached. While the spectra for the x and y direction are very similar for early times up to $t = 0.5 \cdot 10^4$ (cf. first row of Fig. 6.12), an anisotropy becomes noticeable for later times, where the power spectrum $|\mathcal{FT}_x|^2$ for the x direction is always shifted further towards smaller wave numbers than $|\mathcal{FT}_y|^2$. This indicates that the typical distance between the drops is smaller in y direction than in x direction which is due to the fact that the accelerated coarsening induced by the sliding and coalescence of the drops only acts in the sliding direction x . The coarsening in y direction is less affected by the sliding. These effects can be best observed by considering the temporal evolution of the mean wave numbers for different inclination angles, which is presented in Fig. 6.13. Up to $t \approx 3000$, the mean wave numbers k_{mean} for non-zero inclination angle do not deviate from the reference case for $\alpha = 0.0$, which supports the visual impression

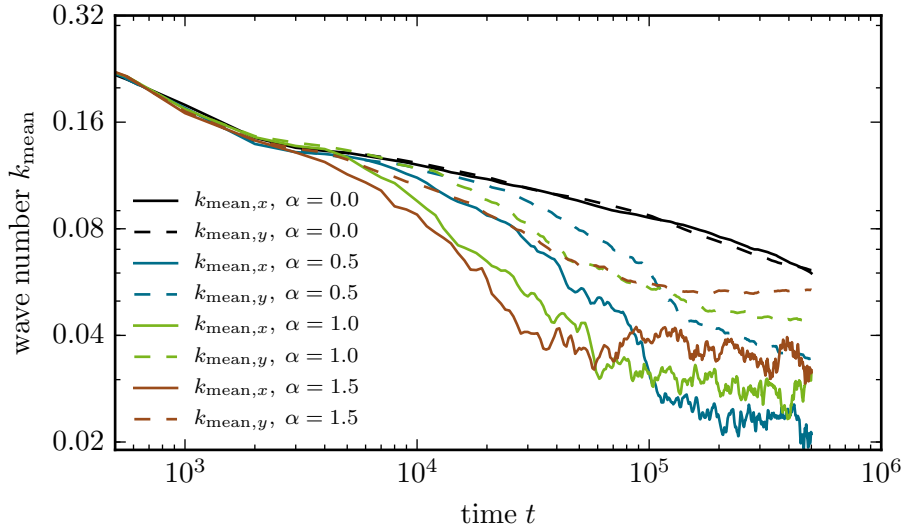


Figure 6.13: Temporal evolution of the mean wave numbers $k_{\text{mean},x}$ and $k_{\text{mean},y}$ in x and y direction for different inclination angles.

one gets from the first row of Fig. 6.11. Beyond this time, the mean wave numbers decrease faster for larger inclinations α . In addition, with increasing α , there is an increasing asymmetry between the wave numbers k_{mean} in x and y direction. As discussed before, this indicates an accelerated coarsening in the sliding direction x as compared to the perpendicular direction y . For each inclination angle, one can determine a point in time beyond which the mean wave number remains almost constant, i.e., beyond which the coarsening is stopped. This is the time, after which the coarsening and coalescence processes are balanced by the pearling processes of drops that are unstable as their volume is too large. This point in time occurs earlier at larger inclination angles and later for smaller inclination angles. Interestingly, this leads to the fact that the final mean wave numbers are smallest for small inclination angles despite that the coarsening process is slower than for larger inclination angles.

While the inspection of the coarsening process in Fourier space provides valuable insights regarding mean distances between the drops and in particular the anisotropy of the x and y direction, this kind of description is rather abstract. Therefore, we now change our point of view from properties of the continuous liquid height profile to the level of drops as individual entities.

6.2.2 Coarsening Dynamics from an Ensemble View

When looking at the coarsening process as an interaction of individual drops during which drops merge and split up, obviously, the number of drops represents a very clear measure to quantify the coarsening. To this end, we again identify drops as connected areas in which the height exceeds a certain threshold height $h_{\text{thres}} = 1.08$ that is chosen slightly above the precursor layer height. With this, we can simply count the drops by counting the number of such areas in the domain. This is done in each individual time step, resulting in a time series of the number of drops $N_{\text{D}}(t)$. These time series are shown in Fig. 6.14 for different inclination angles α . In this representation, the different stages of the coarsening process on an inclined substrate can be very easily distinguished. Up to $t \approx 3 \cdot 10^3$, the number of drops N_{D} is similar for all shown inclination angles. Beyond this time, N_{D} decreases faster for larger inclination angles. This accelerated coarsening stops at a certain inclination-dependent time ($t_{\text{c}} \approx 3.7 \cdot 10^4$ for $\alpha = 1.5$, $t_{\text{c}} \approx 6.5 \cdot 10^4$ for $\alpha = 1.0$, and $t_{\text{c}} \approx 1.4 \cdot 10^5$ for $\alpha = 0.5$, indicated by dotted lines in Fig. 6.14). This is very similar to the information we obtained from the Fourier spectra in the previous section. However, one can now identify an additional very slow decrease of the number of drops also for later times, which was hardly visible in the more noisy Fourier spectra. This behavior reflects the slow tendency of the system to form very elongated stable drops, which accumulate much more mass than the typical oval-shaped drops. That is, the time series of the number of drops is well suited to distinguish and quantify the different phases of the coarsening on an incline. However, in this representation we discard much information from the full simulations, such as the spatial distribution of the drops and in particular their shape and size. Now we want to include information about the latter into our description.

As a first step, we again determine the volumes of the individual drops by integrating their height over their footprints (cf. Eq. (6.3)). The resulting set of drop volumes $\{V_i\}_{i=1..N_{\text{D}}}$ in each time step can be further processed in different ways. A typical approach is the calculation of a *histogram*, for which the drops are grouped into volume intervals called bins and the occurrences per bin are counted. A disadvantage of such a histogram is its dependence on the bin size. For large bin sizes, much information about the drop volumes is lost, while small bin sizes necessitate large numbers of drops for reasonable results. An alternative method is the

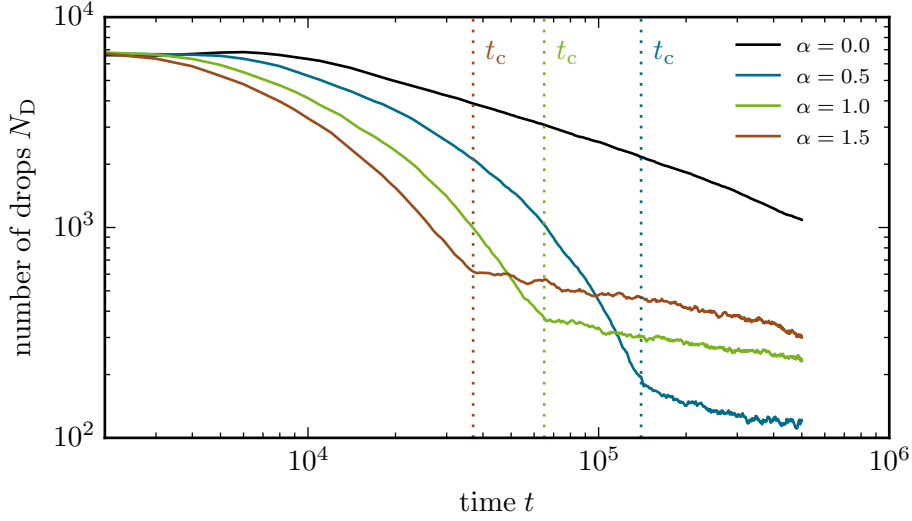


Figure 6.14: Time series of the number of drops during the coarsening process on an inclined substrate with inclination angle α . The dotted lines indicate the times t_c after which the coarsening process almost stops.

so-called *kernel density estimation* (KDE, e.g., [Sco15]). The idea of KDE is to reconstruct the continuous distribution function by summing appropriately weighted and shifted continuous *kernels*. That is, each drop i is represented by a continuous volume distribution $k(V - V_i)$ centered about its own volume V_i . Here, we employ a Gaussian kernel

$$k(V) = \frac{1}{\sqrt{2\pi}} e^{-\frac{V^2}{2}}. \quad (6.8)$$

The normalized drop volume distribution $f(V)$ of the whole ensemble then results from the summation of the kernels,

$$f(V) = \frac{1}{N_D w} \sum_{i=1}^{N_D} k\left(\frac{V - V_i}{w}\right), \quad (6.9)$$

where N_D is the number of drops in the current snapshot and w is the bandwidth of the kernel which can be chosen in different ways. We employ *Scott's rule* [Sco15], which is a rule of thumb for a one-variable distribution,

$$w = N_D^{-1/5}. \quad (6.10)$$

This results in a normalized distribution, which we calculate separately for each time step, i.e., we obtain a drop volume distribution $f(V, t)$, where $f(V_0, t) dV$ is the probability that a randomly picked drop of the current ensemble has a volume $V \in [V_0, V_0 + dV]$. Figure 6.15 presents the result of this procedure for an inclination angle $\alpha = 1.0$. At early times, the drop volume distribution is sharply peaked at small volumes, indicating that the first phase of the coarsening process leads to very uniform drop volumes. The distribution then broadens and simultaneously shifts towards larger volumes, which corresponds to the phase of accelerated coarsening due to the inclination of the substrate. Interestingly, the distribution then develops a second peak at $V \approx 6 \cdot 10^4$ for $t \approx 1 \cdot 10^5$, resulting in a bimodal distribution. In the remainder

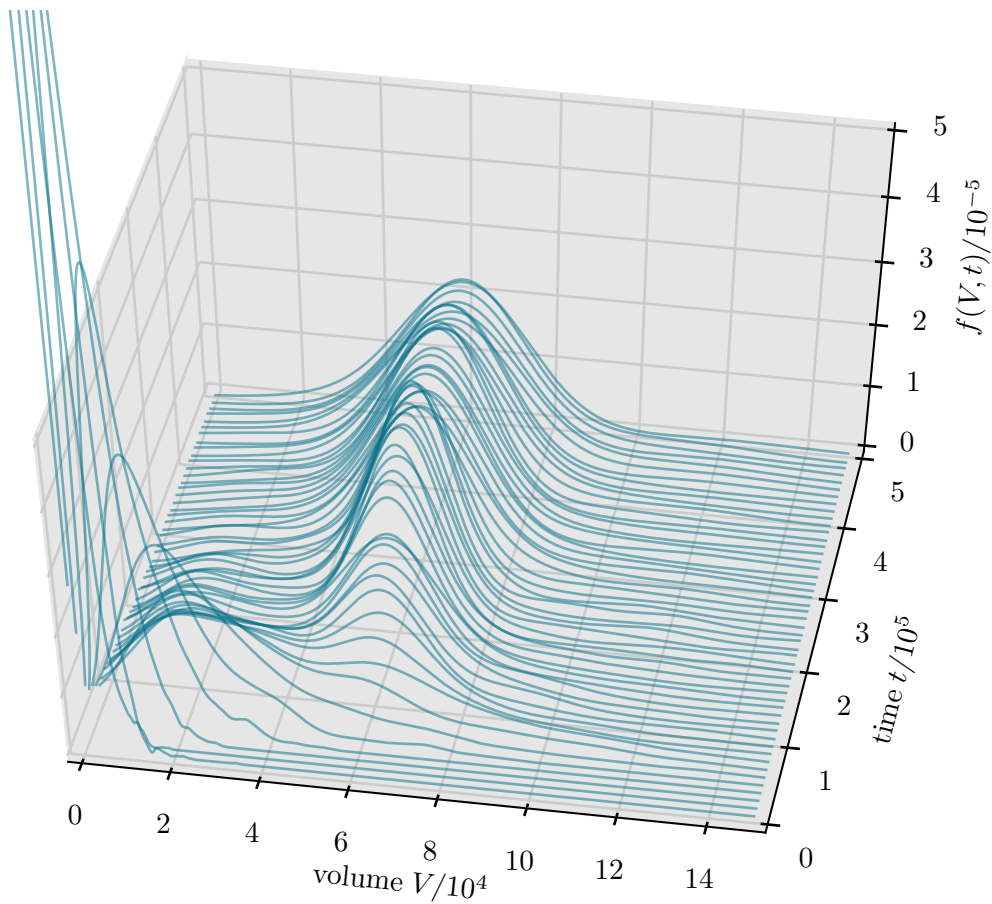


Figure 6.15: Temporal evolution of the drop volume distribution $f(V, t)$ obtained by kernel density estimation for a direct numerical simulation of Eq. (6.1) for an inclination angle $\alpha = 1.0$. The distribution is calculated and normalized individually for each time step. The distribution is sharply peaked at small drop volumes at the beginning of the simulation. For later times, it broadens and shifts towards larger volumes until it reaches an almost stationary state.

of the simulation, this peak grows in size at the expense of smaller volumes until it reaches an almost stationary distribution that is well localized. The information contained in this drop volume distribution is much more complete than the sole number of drops which we discussed previously. In particular, one can see that the balance of coalescence and break-up processes that governs the late stage of the coarsening dynamics indeed leads to a rather constant and uniform volume distribution, i.e., similarly sized drops.

We already reasoned that the coarsening process on an inclined substrate stops when the drops become too large and therefore unstable, leading to a break-up into smaller drops. In fact, we already analyzed this *pearling* instability in Sec. 6.1 of this chapter. However, there, we analyzed a drop with constant volume on differently inclined substrates and determined the inclination angle α_{SN1} beyond which simple-shaped drops become unstable. Now, the question is posed differently and we are interested in the volume at which a drop becomes unstable for a fixed inclination angle of the substrate. Therefore, we now consider the bifurcation diagram in terms of the sliding velocity in dependence on the drop volume for a fixed inclination angle. This bifurcation diagram is shown in Fig. 6.16 for a fixed inclination angle $\alpha = 1.0$

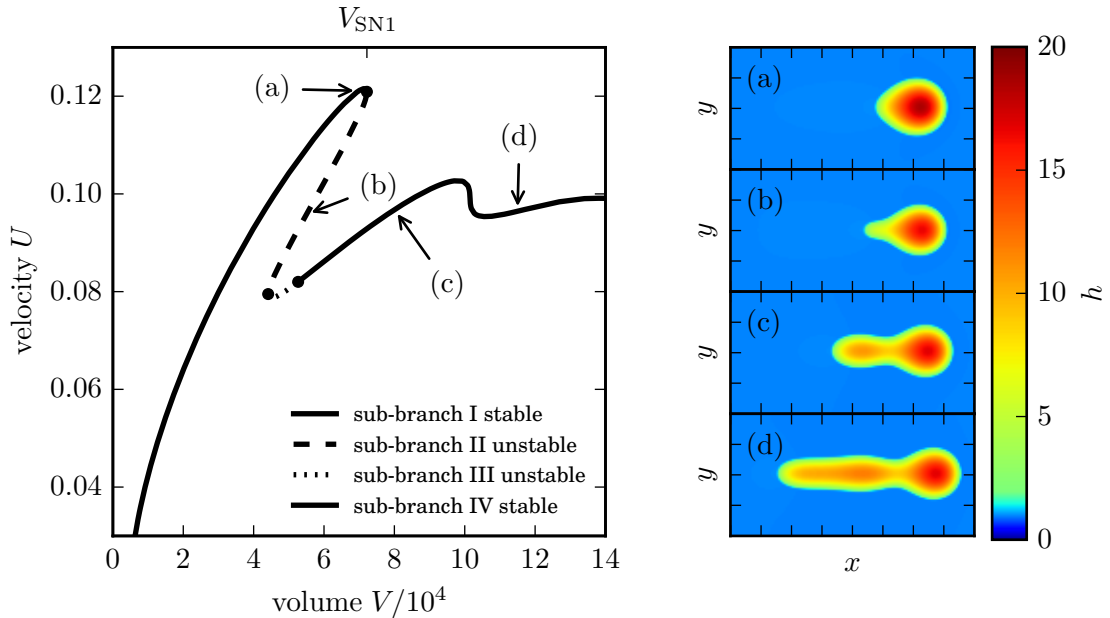


Figure 6.16: Left panel: Bifurcation diagram of sliding drop solutions of Eq. (6.1) on an inclined substrate with inclination $\alpha = 1.0$ showing the sliding velocity U in dependence on the drop volume V . There exist several sub-branches of steady drops with different shape and behavior, see labels (a) to (d) and the corresponding exemplary solutions in the right panels. The bifurcation diagram was obtained by Sebastian Engelnkemper.

together with exemplary solutions along the solution branch. The overall solution structure is very similar to the case for fixed drop volume and varying inclination (cf. Fig. 6.1). The solution branch consists of multiple sub-branches that exhibit the same stability properties and solution shapes as their counterparts that we discussed in detail in Sec. 6.1. For our current

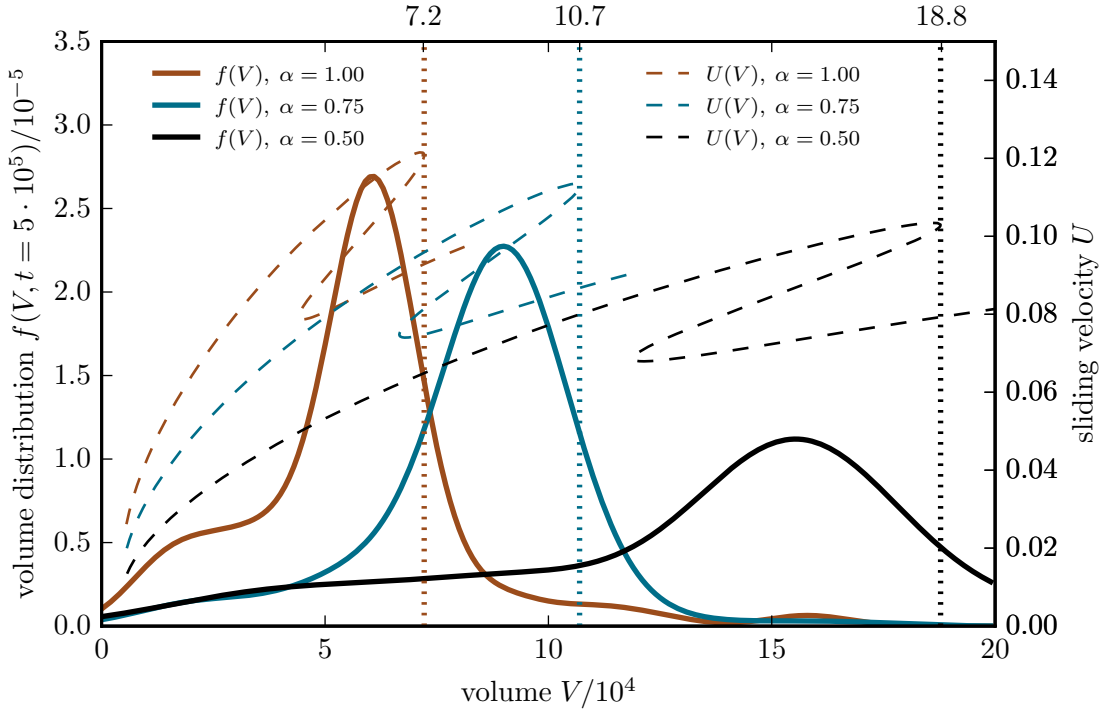


Figure 6.17: Comparison of the final drop volume distribution $f(V, t = 5 \cdot 10^5)$ obtained by kernel density estimation from the direct numerical simulations of Eq. (6.1) shown in Fig. 6.11 (solid lines) and the bifurcation diagrams $U(V)$ showing the sliding velocity in dependence on the drop volume for different inclination angles (dashed lines). The dotted lines indicate the positions of the stability thresholds V_{SN1} .

discussion, the sub-branch I corresponding to simple oval-shaped drops is the most important one. In particular, we are interested in the end of the sub-branch occurring in a saddle-node bifurcation at an upper volume V_{SN1} . Beyond this volume, there exist no stable simple-shaped drops. Translated to our situation of ensembles of sliding drops, this means that one should not encounter drops with a larger volume than V_{SN1} . Drops with a larger volume are only possible with a very elongated shape (corresponding to the stable solutions of sub-branch IV), or in other, unstable, shapes when they are not yet split-up. Therefore, we can now compare the ensemble statistics obtained from the large scale simulations with the stability threshold V_{SN1} obtained from the bifurcation diagram for a single drop. To this end, Fig. 6.17 combines the bifurcation diagrams for different inclination angles (dashed lines) with the final drop volume distributions (solid lines) obtained from the direct numerical simulations for the same inclination angles. Looking at the positions of the thresholds V_{SN1} (marked by vertical dotted lines), one notes that their positions roughly mark the upper inflection points of the corresponding distributions, i.e., volumes beyond which the drop volume distributions decay rapidly. For increasing inclination angles, the final drop volume distribution shifts towards smaller volumes and also becomes more sharply peaked. Similarly, the solution branch for the corresponding inclination angle is also deformed, so that it gives a nice prediction of a cut-off

volume for the drop volume distribution for all presented inclination angles. In addition, this comparison also explains why for larger inclination angles one obtains ensembles of smaller drops: For larger inclination angles α , the maximal stable drop volume V_{SN1} becomes smaller, so that the coarsening process effectively stops earlier.

At the end of Sec. 6.1, we introduced a scaling law (6.4) that relates the location of the first saddle-node bifurcation α_{SN1} to the volume of the drop V . This scaling law is also of interest for the discussion of the drop ensembles on an inclined substrate with fixed inclination, as it can also be reformulated to predict the location of the saddle-node bifurcation V_{SN1} depending on the inclination angle α :

$$V_{\text{SN1}} = (a_1^{-1} \alpha_{\text{SN1}})^{\frac{1}{\beta_1}}. \quad (6.11)$$

This is due to the fact that the point $(\alpha_{\text{SN1}}, V_{\text{SN1}})$ always marks the location of the saddle-node bifurcation in the (α, V) parameter space, independent of the chosen continuation path (varying V at fixed α or vice versa). That is, this power law can be readily used to predict the stability threshold V_{SN1} for single drops sliding on an inclined substrate which we found to be in close relation to the drop volume distribution that evolves for large ensembles of sliding and coarsening drops (cf. Fig. 6.17).

From the combination of statistical analysis of the direct numerical simulation and the continuation techniques used to determine stability properties of the drops depending on the inclination angle α and the drop volume V , we could identify the main mechanisms that govern the coarsening dynamics of sliding drops. As a final step of the investigation, we will now employ the findings to develop a reduced statistical model.

6.2.3 Statistical Model for the Drop Volume Distribution

In order to develop a simplified model for the coarsening dynamics of sliding drops, various approaches with different levels of description are conceivable. Coming from the thin film model describing the liquid layer height that was analyzed in the previous sections, a first simplification would be the treatment of the drops as discrete particles. For such a system, one could model the interaction of drops as a set of rules depending on the particle properties, such as volume, position, velocity and interaction range. This level of description would be still very detailed and permit the same types of analysis as we performed up to now. However, we now want to formulate a model on a further simplified level in which we do not treat individual drops and also neglect the spatial distribution of them. In particular, we aim at a model that directly describes the temporal evolution of the drop volume distribution. Such a model can be formulated as a kind of continuous Smoluchowski coagulation equation [Smo16], i.e., an integro-differential equation that describes the temporal evolution of a distribution based on transition rates. Originally, this was formulated in the context of coagulation of small particles to larger ones. However, the same kind of equation has already been applied to the case of coarsening droplets on a substrate [Mea92] and freely flying drops [LH00]. Common to the mentioned literature is that it only considers the coalescence of particles and not instabilities leading to their break-up. Still, also the splitting of particles was discussed in the wider context of coagulation processes [FMD86, ME88], mostly focusing on long-term scaling properties. We now propose a Smoluchowski-type model for sliding drops on an inclined substrate accounting for both coalescence and fragmentation events. The model describes the temporal evolution of the non-normalized drop volume distribution $\tilde{f}(V, t) = N_{\text{D}} f(V, t)$, where N_{D} is the total number of drops and $f(V, t)$ the normalized drop volume distribution. For simplicity, we drop

the tilde from now on and always refer to $f(V, t)$ as the non-normalized distribution in the context of the statistical model. The model reads

$$\begin{aligned}
 \partial_t f(V, t) = & + \underbrace{\int_0^\infty \int_0^\infty \frac{1}{2} K(V_1, V_2) f(V_1) f(V_2) \delta(V_1 + V_2 - V) dV_1 dV_2}_{\text{gain due to coalescence}} \\
 & - \underbrace{\int_0^\infty K(V, V_1) f(V) f(V_1) dV_1}_{\text{loss due to coalescence}} \\
 & + \underbrace{\int_0^\infty J(V_1, V) f(V_1) dV_1}_{\text{gain due to fragmentation}} - \underbrace{\int_0^\infty \frac{1}{2} J(V, V_1) f(V) dV_1}_{\text{loss due to fragmentation}}. \tag{6.12}
 \end{aligned}$$

The dynamics allows for the two processes coalescence and fragmentation (i.e., break-up of unstable drops), which can each lead to the gain and loss of drops with a certain volume V . At the core of the model are the rate kernels $K(V_1, V_2)$ and $J(V_1, V_2)$. $K(V_1, V_2)$ is the rate of coalescence processes at which two drops with the volumes V_1 and V_2 merge and form a single drop with volume $V_1 + V_2$. Similarly, $J(V_1, V_2)$ models the rate of fragmentation processes at which a single drop with volume V_1 breaks up into two drops with the volumes V_2 and $V_1 - V_2$. The transition rates then result from products of these kernels with the current distribution. For example, the transition rate accounting for gain due to coalescence is proportional to $K(V_1, V_2)$ and the current distribution at the volumes V_1 and V_2 , which are $f(V_1)$ and $f(V_2)$, respectively. This leads to a production of drops with volume V for any V_1 and V_2 that fulfill $V_1 + V_2 = V$. Therefore, the integration is carried out over all V_1 and V_2 with the restriction by the *delta distribution* $\delta(V_1 + V_2 - V)$, while the factor $\frac{1}{2}$ is introduced because we will formulate $K(V_1, V_2)$ as a symmetric function with respect to the arguments. The other contributions for gain and loss due to coalescence and fragmentation are analogously constructed. Again, a factor $\frac{1}{2}$ occurs in the contribution for loss due to fragmentation, because else each possible fragmentation process would be counted twice.

For the construction of the rate kernels $K(V_1, V_2)$ and $J(V_1, V_2)$, we will use the information that we obtained in the previous sections about the dynamics of sliding drops. For the coalescence kernel $K(V_1, V_2)$ we propose an ansatz

$$K(V_1, V_2) = k_1 \frac{|U(V_1) - U(V_2)|}{\Lambda}, \tag{6.13}$$

where Λ denotes the mean distance between the drops in the sliding direction, which we assume to be proportional to the length L of the domain³

$$\Lambda = \frac{L}{2}. \tag{6.14}$$

³Note that Λ is not the typical distance to the *nearest next* drop, which would scale with the number of drops. As $K(V_1, V_2)$ is the coalescence rate of each drop with *all* others, one has to assume the mean distance to all others, which is independent of the overall number of drops.

To incorporate a finite interaction radius of the drops *perpendicular* to the sliding direction, we include the prefactor $k_1 < 1$ in the kernel (6.13). For the sliding velocity $U(V)$ of the drops, we employ the scaling law (6.5),

$$U(V) = k_2 V^{\beta_0}, \quad (6.15)$$

with an inclination-dependent prefactor $k_2 = 2.2 \cdot 10^{-4} \alpha$ and the exponent $\beta_0 = 0.569$.

The form of the fragmentation kernel $J(V_1, V_2)$ is based on the assumption that drops below a critical volume V_{crit} are stable (i.e., $J(V_1 < V_{\text{crit}}, V_2) = 0$) and break up with a constant rate above this volume (i.e., $J(V_1 > V_{\text{crit}}, V_2) = \text{const.}$). For practical reasons, we approximate this with a smooth sigmoidal function,

$$J(V_1, V_2) = j \frac{1}{2} \left(1 + \tanh \left(\frac{V_1 - V_{\text{crit}}}{b_V} \right) \right) \Theta(V_1 - V_2). \quad (6.16)$$

Here, j is a free rate parameter that can be used to tune the fragmentation rate to typical timescales of the instability observed in direct numerical simulations, b_V models the width of the transition interval between stable and unstable volumes, and Θ denotes the Heaviside function. The latter ensures that the fragments V_2 and $V_1 - V_2$ in $J(V_1, V_2)$ are smaller than the previous drop with volume V_1 . The critical volume V_{crit} can be directly chosen according to the location of the saddle-node bifurcation V_{SN1} (cf. (6.11)) which we obtained from the bifurcation diagrams. We set $V_{\text{crit}} = V_{\text{SN1}} + 2b_V$ to account for the width of the tanh function and to prevent an instability of drops smaller than V_{SN1} . The width of the smooth transition between unstable and stable is chosen as $b_V = V_{\text{SN1}}/10$. In the formulation (6.16), we do not specify into which drop volume V_2 a drop of volume V_1 breaks up, i.e., we assume that all resulting volumes V_2 are equally probable. We choose this most simple assumption, because in direct numerical simulations the drop volumes resulting from pearling depend on many factors, such as the volume and shape of the original drop (which also results from possible previous coalescence or pearling events). These fine details cannot be sensibly incorporated⁴ into the definition of $J(V_1, V_2)$. For a better impression of our definitions, both kernels $K(V_1, V_2)$ and $J(V_1, V_2)$ are illustrated in Fig. 6.18.

In the model (6.12), the drop volume distribution is not a conserved quantity, i.e., $f(V)$ is not normalized. However, the mass conservation of the underlying physical system still holds, as the overall volume, which corresponds to the first moment of the non-normalized distribution,

$$V_{\text{total}} = \int_0^{\infty} V f(V) dV \quad (6.17)$$

is conserved by the dynamics of (6.12). This can be shown by calculating $\partial_t V_{\text{total}}$ and exploiting

⁴In practice, one would have to conduct huge parameter studies by direct numerical simulations, in which the different coalescence settings would need to be prepared and the resulting fragmentation products identified. As a mean over various realizations one could then assume a more detailed fragmentation product distribution. In terms of an exhaustive description of the fragmentation, one might even need history terms to account for the past of the drops.

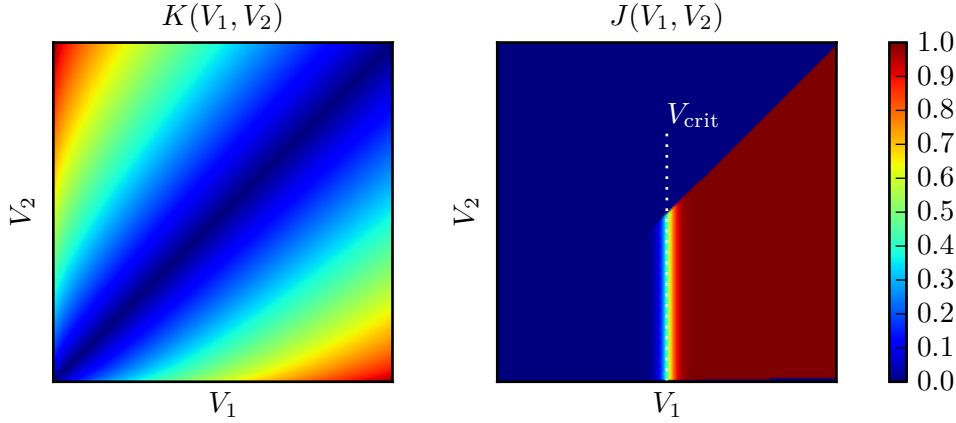


Figure 6.18: Illustration of the coalescence and fragmentation kernels $K(V_1, V_2)$ and $J(V_1, V_2)$ given by Eq. (6.13)–(6.16). For a better visibility, both kernels are normalized to their maximal value.

symmetry properties of the kernels J and K :

$$\begin{aligned}
 \partial_t V_{\text{total}} = & + \int_0^\infty \int_0^\infty \int_0^\infty V \frac{1}{2} K(V_1, V_2) f(V_1) f(V_2) \delta(V_1 + V_2 - V) dV_1 dV_2 dV \\
 & - \int_0^\infty \int_0^\infty V K(V, V_1) f(V) f(V_1) dV_1 dV \\
 & + \int_0^\infty \int_0^\infty V J(V_1, V) f(V_1) dV_1 dV - \int_0^\infty \int_0^\infty V \frac{1}{2} J(V, V_1) f(V) dV_1 dV. \quad (6.18)
 \end{aligned}$$

For more clarity, we consider each contribution separately. The first contribution accounting for gain due to coalescence can be reformulated by

$$\begin{aligned}
 & \int_0^\infty \int_0^\infty \int_0^\infty V \frac{1}{2} K(V_1, V_2) f(V_1) f(V_2) \delta(V_1 + V_2 - V) dV_1 dV_2 dV \\
 \stackrel{(1)}{=} & \int_0^\infty \int_0^\infty (V_1 + V_2) \frac{1}{2} K(V_1, V_2) f(V_1) f(V_2) dV_1 dV_2 \\
 \stackrel{(2)}{=} & \int_0^\infty \int_0^\infty V_1 \frac{1}{2} K(V_1, V_2) f(V_1) f(V_2) dV_1 dV_2 + \int_0^\infty \int_0^\infty V_2 \frac{1}{2} K(V_1, V_2) f(V_1) f(V_2) dV_1 dV_2 \\
 \stackrel{(3)}{=} & \int_0^\infty \int_0^\infty V K(V, V_1) f(V) f(V_1) dV dV_1, \quad (6.19)
 \end{aligned}$$

which exactly cancels with the term accounting for loss due to coalescence. In the first step (1), the integration over V was carried out, for (2) the sum $(V_1 + V_2)$ was split and for (3),

in the first integral the transformations $V_1 \rightarrow V$ and $V_2 \rightarrow V_1$ and in the second integral the transformation $V_2 \rightarrow V$ were performed and the symmetry $K(V_1, V_2) = K(V_2, V_1)$ was exploited. The contribution accounting for gain due to fragmentation can be reformulated by

$$\begin{aligned}
 & \int_0^\infty \int_0^\infty V J(V_1, V) f(V_1) dV_1 dV \stackrel{(1)}{=} \int_0^\infty \int_0^\infty V J(V_1, V_1 - V) f(V_1) dV_1 dV \\
 & \stackrel{(2)}{=} \int_{-\infty}^{V_1} \int_0^\infty (V_1 - \tilde{V}) J(V_1, \tilde{V}) f(V_1) dV_1 d\tilde{V} \stackrel{(3)}{=} \int_0^\infty \int_0^\infty (V_1 - \tilde{V}) J(V_1, \tilde{V}) f(V_1) dV_1 d\tilde{V} \\
 & \stackrel{(4)}{=} \int_0^\infty \int_0^\infty V_1 J(V_1, \tilde{V}) f(V_1) dV_1 d\tilde{V} - \int_0^\infty \int_0^\infty \tilde{V} J(V_1, \tilde{V}) f(V_1) dV_1 d\tilde{V} \\
 & \stackrel{(5)}{=} \frac{1}{2} \int_0^\infty \int_0^\infty V J(V, V_1) f(V) dV dV_1, \tag{6.20}
 \end{aligned}$$

which exactly cancels with the term accounting for loss due to fragmentation, and therefore $\partial_t V_{\text{total}} = 0$. In the first step (1), the symmetry $J(V_1, V) = J(V_1, V_1 - V)$ was used, then in (2), the transformation $\tilde{V} = V_1 - V$ was performed. For (3), the integration boundaries were shifted, which is possible, as $J(V_1, \tilde{V}) = 0 \forall \tilde{V} \notin [0, V_1]$. The difference $(V_1 - \tilde{V})$ was then split and the second resulting integral can be identified with the original contribution accounting for gain due to fragmentation. In (5), the transformation $V_1 \rightarrow V$ and $\tilde{V} \rightarrow V_1$ was performed.

The model resulting from (6.12), (6.13), and (6.16) has two main parameters left, which are the general rate constants k and j , one of which can be essentially eliminated by rescaling the time in (6.12). One is then left with a free parameter determining the ratio of the two rate constants. We use these parameters to calibrate the statistical model to the typical timescales that one can observe in the direct numerical simulation for the coalescence and break-up processes.

Because it is typically not possible to solve models such as (6.12) analytically, we conduct direct numerical simulations of it using a classical fourth-order Runge–Kutta scheme for the time stepping and by discretizing the volume axis on an equidistant grid. With this, all integrals in (6.12) are reduced to sums. Of course, one can only consider a finite volume domain $\Omega_V = [0, V_{\text{max}}]$ and therefore these sums are finite. The upper boundary V_{max} has to be chosen sufficiently large to ensure volume conservation in the simulations. Otherwise, the coalescence terms might produce drops with a volume above the upper boundary V_{max} which are not considered and their corresponding volume would be lost in the simulation. As initial conditions, we employ the drop volume distribution determined by the KDE of the direct numerical simulation at an early time $t = 3000$. As this distribution is normalized, it has to be multiplied with an appropriate amplitude factor to control the overall volume which in particular influences the nonlinear coalescence terms. Figure 6.19 presents the result of a direct numerical simulation of the statistical model (6.12) along with the temporal evolution observed in a direct numerical simulation of the thin film model (6.1) (cf. Fig. 6.15). The statistical model exhibits features very similar to the statistics resulting from the thin film simulations. In an initial phase up to $t \approx 0.5 \cdot 10^5$, the volume distribution broadens and gradually shifts towards larger volumes. Then, the distribution broadens much stronger towards large volumes up to $V \approx 7 \cdot 10^4$. Until $t \approx 1 \cdot 10^5$, the peak at small volumes has mostly decayed and

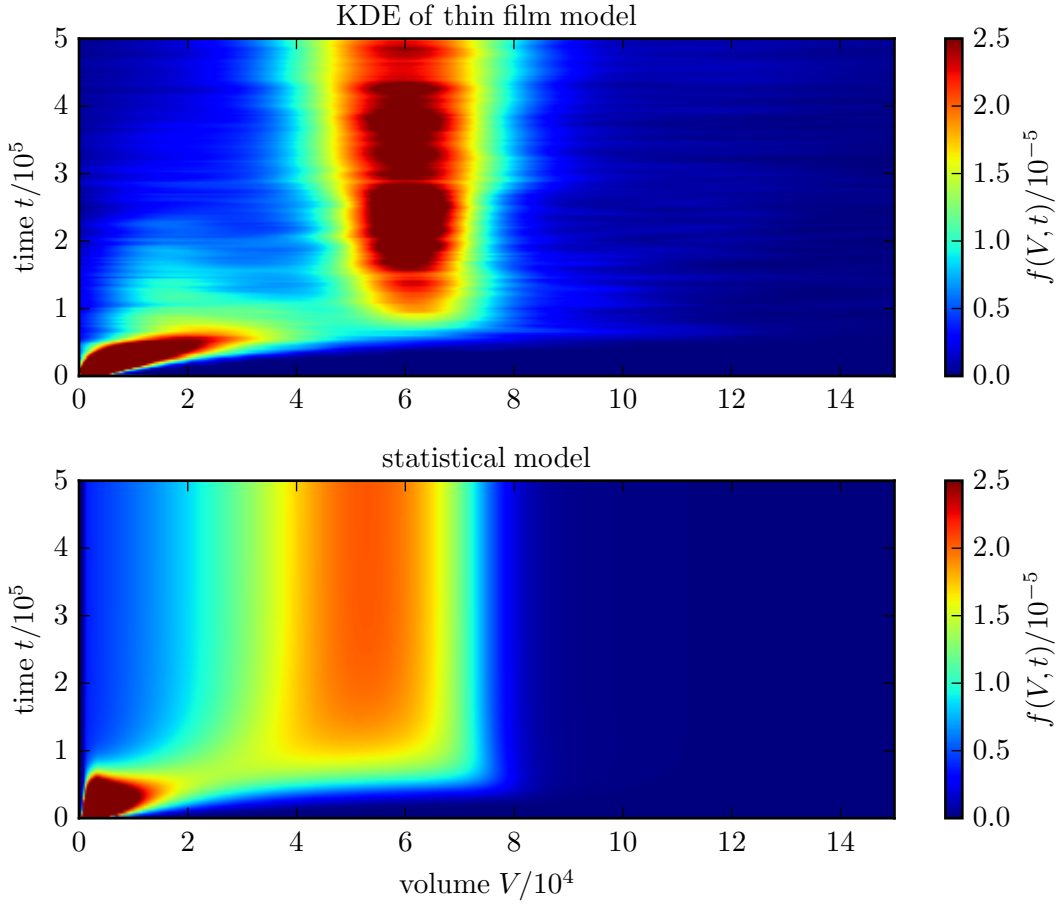


Figure 6.19: Temporal evolution of the drop volume distribution $f(V,t)$ obtained by kernel density estimation of a simulation of the thin film equation (6.1) (top panel, cf. Fig. 6.15) and as a result of a simulation of the statistical model (6.12) (bottom panel). Parameters are $\alpha = 1.0$, $j = 6.25 \cdot 10^{-6}$, $k = \frac{1}{30}$.

a distribution peaked at large volumes $V \approx 5 \cdot 10^4$ forms. Beyond $t \approx 1 \cdot 10^5$, the volume distribution shows no more visible dynamics. A quantitative difference between the results of the statistical model (6.12) and the data from the thin film model (6.1) can be seen in the location of the maximum of the distribution for later times. The final distribution obtained by the statistical model is strongly bounded by the upper instability threshold $V_{\text{crit}} \approx 7 \cdot 10^4$, while the resulting distribution in the thin film model has significant contributions beyond the threshold. This indicates that the instability of drops beyond the threshold either occurs slower than assumed in our statistical model or that a significant fraction of the drops has a different shape (cf. solution type IV in Fig. 6.16) and can therefore also be stable for larger volumes. However, the overall agreement of the main features in both the statistical model and the KDE of the thin film simulations is a strong indicator that the statistical model captures the main effects of the coarsening dynamics of sliding drops.

In the previous Sec. 6.2.2, we have seen that the temporal evolution of the drop number is a

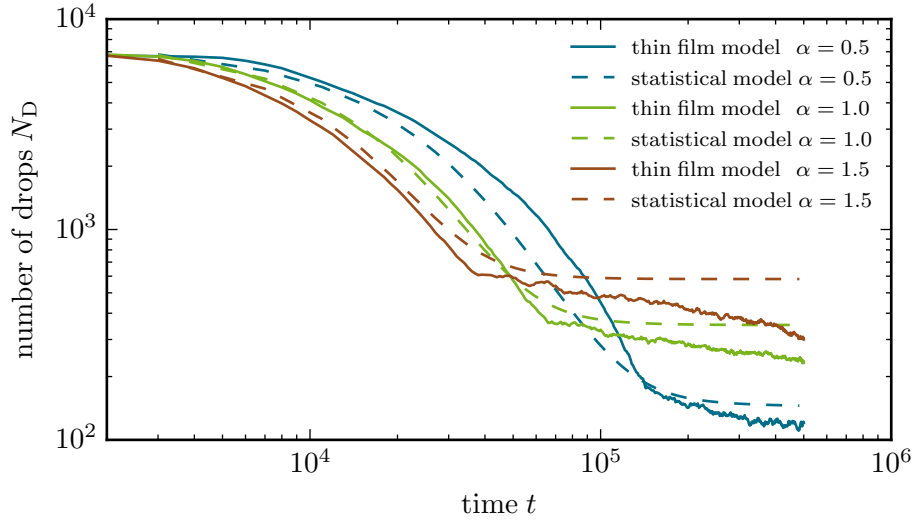


Figure 6.20: Temporal evolution of the number of drops observed in simulations of the thin film equation (6.1) (solid lines, cf. Fig. 6.14) and as a result of numerical simulations of the statistical model (6.12) (dashed lines) for different inclination angles.

simple but insightful measure to investigate the coarsening process and in particular to identify the different coarsening stages in the direct numerical simulations of the thin film model (6.1). Hence, we also apply this measure to the statistical model (6.12). The number of drops N_D can be directly calculated from the drop volume distribution $f(V, t)$ via

$$N_D(t) = \int_0^{\infty} f(V, t) dV. \quad (6.21)$$

The resulting temporal evolution of the number of drops in the statistical model can be readily compared to the one obtained directly from the thin film simulations (cf. Fig. 6.14). This comparison is presented in Fig. 6.20 for the three inclination angles $\alpha = 0.5$, $\alpha = 1.0$, and $\alpha = 1.5$. The statistical model shows the same characteristic accelerated coarsening behavior that stops at a certain time and number of drops. Both coincide well with the ones observed in the simulations of the thin film model. This is in particular true when comparing the results for the different inclination angles: The model parameters were not adjusted individually, but all parameters except for the inclination angle were kept constant. Still, one notes a tendency that the coarsening is slightly too slow at large inclination angles and slightly too fast at small inclination angles. This shows that the approximations and assumptions made in the statistical model do not fit every inclination angle equally well. A further difference can be observed for large times after the stage of accelerated coarsening. A very slow coarsening happens in the simulation of the thin film model because very large elongated stable drops form. This is not the case in the statistical model. There, the drop number converges towards a constant, because stable drops beyond the critical volume V_{crit} are simply not considered. Despite these small quantitative differences, the agreement of the results obtained with the statistical model (6.12) with the thin film model (6.1) is remarkable given the simplicity of the statistical model.

In particular, this underlines the fact that the complex dynamics of sliding drops in a thin film model can be strongly abstracted in an ensemble view with an emphasis on statistical properties.

The analysis of an ensemble of sliding drops in this section has provided interesting insights into the coarsening process under the influence of an additional driving force which enables an additional coarsening mechanism. But apart from the knowledge gained about this particular system, the used approach combining different techniques, such as direct numerical simulations, numerical continuation and a simplified statistical model, is also interesting from a methodical point of view. The starting point of the examination were direct numerical simulations on large-scale domains containing a whole ensemble of drops that reveal the overall temporal evolution of the system and the most important features. This has then been augmented by the bifurcation diagram for *single* drops obtained by numerical continuation in order to study their stability properties and quantitative features such as the inclination- and volume-dependent sliding velocity. This information demonstrated how the properties of individual entities can be used to predict the behavior of a whole ensemble (cf., e.g., the stability threshold in Fig. 6.17). As the last step of the investigation, we have developed a statistical model that comprises the two effects we found to be dominant during the coarsening (coalescence due to velocity differences of the sliding drops) and break-up processes (instability above a certain drop volume). This model has then nicely reproduced the evolution of the drop volume distribution and the number of drops as observed in the thin film simulations. This represents a final verification of our assumptions about the main mechanism in the coarsening of sliding drops, which could only be obtained by the combination of the very different approaches and methods.

7 Summary and Conclusion

In addition to the conclusions that we have already given at the end of each chapter, we now summarize and conclude the whole thesis and present brief outlooks for possible future research. In this thesis, we have considered three different settings involving thin liquid layers on solid substrates which exhibit pattern formation and other complex phenomena. The systems have been analyzed employing gradient dynamics models, in our case, nonlinear partial differential equations describing the temporal evolution of a field, such as a liquid height profile or a surfactant density, in terms of gradients of an underlying free energy. After an introduction to the topic in Chap. 1, the theoretical basis for these models has been established in Chap. 2, where we have first introduced the thin film (or lubrication) equation to describe the height profile of a three-dimensional thin layer of a simple liquid on a solid substrate. Suitable boundary conditions have been proposed for both a horizontal substrate and an inclined substrate that is withdrawn from a liquid reservoir. We have then reformulated this model as a gradient dynamics which could be extended to complex fluids, e.g., a surfactant-covered liquid layer or a solution, which are described by more than one field, e.g., the liquid layer height profile and the surfactant area density. The gradient dynamics approach facilitates the formulation of such models and ensures their inner consistency. In particular, this becomes important when introducing additional physical effects, such as a surfactant density-dependent surface tension leading to Marangoni forces. Further examples for possible extensions are an additional solubility of the surfactant molecules [TAP16], temperature gradient-induced Marangoni forces [TGT14] or colloidal interactions in a suspension. However, to describe the pattern formation in Langmuir–Blodgett transfer experiments, we have presented further approximation leading to a Cahn–Hilliard-type model that still covers the main features occurring in experiments.

The models that have been used within this thesis can hardly be analyzed using purely analytical methods. Therefore, suitable numerical approaches have been introduced in Chap. 3. On the one hand, the finite differences and finite elements methods together with time stepping techniques have been presented, which have been used to perform direct numerical simulations of the models. On the other hand, numerical path-continuation methods have been established. The latter can be employed to analyze the bifurcation structure of the models comprising stable as well as unstable steady solutions and their bifurcations and instabilities.

The first major subject of this thesis has been the pattern formation occurring in Langmuir–Blodgett (LB) transfer experiments and, in particular, ways to control it. Therefore, Chap. 4 has started with a brief overview of the typical patterns observed in the augmented Cahn–Hilliard model for the LB transfer and their dependence on experimental parameters like the transfer velocity. Then, the influence of prestructured substrates on the pattern formation has been discussed. Depending on the size, orientation and strength of the prestructure, two main effects have been shown: (i) the inherent stripe patterns formed by LB transfer can be further controlled and their properties, such as their wavelength, can be tuned by means of locking effects between the forming pattern and the prestructure, and (ii) more complex structures, e.g., oblique or lattice patterns, can be created as a result of a two-dimensional locking and a competition of the intrinsic pattern forming mechanism in the LB transfer and the external

spatio-temporal forcing exerted by the prestructure. In close collaboration with Juan Zhu from the group of Prof. Lifeng Chi, the control of the pattern formation in the LB transfer using prestructured substrates has also been confirmed in experiments designed after the theoretical predictions. Further, to describe experimental results exhibiting bent horizontal stripes due to vertically aligned prestructure stripes, a two-component thin film model accounting for prestructure-induced wettability changes has been employed. This model could be used to qualitatively reproduce the experimental findings and to explain them as a consequence of the hydrodynamics of the liquid layer on the heterogeneous substrate. Due to the combined experimental and theoretical efforts, a profound understanding of the control capabilities of prestructured substrates for patterns obtained by LB transfer has been achieved. In future applications of LB structures, this can greatly facilitate the production of patterns with the desired properties.

The final part of Chap. 4 has explored alternative approaches to control the pattern formation during the LB transfer without the use of prestructures. Employing direct numerical simulations, we have shown that both a periodically modulated transfer velocity and a periodic oscillation of the meniscus position can induce locking effects and therefore enable an extensive control over the pattern formation process. These control mechanisms have the desirable property that they do not necessitate any elaborate manipulations of the used substrates. Therefore applications involving a high throughput of substrates could greatly benefit from such control strategies. Whether they can be realized in practice will have to be examined in upcoming experimental studies. But even if these particular examples could not be successfully implemented in experiments, they can still serve as examples motivating the search for other kinds of control mechanisms using temporally or spatially modulated control parameters. The general concept is also applicable to other pattern forming systems. One example are solute deposits from an evaporating solution under the influence of surface acoustic waves [MZAM16]. A temporal modulation of, e.g., the amplitude of the surface acoustic waves might lead to similar locking effects as discussed in this thesis for LB patterns.

The case of bent stripes created by LB transfer on prestructured substrates in Sec. 4.2.2 has illustrated the importance of interactions of the liquid layer with the prestructured substrate for the pattern formation. Therefore, the second major topic of this thesis presented in Chap. 5 has been the study of this interaction in more details for the case of a simple liquid, i.e., without considering any surfactants or solutes. We have analyzed the behavior of the liquid meniscus that forms when a solid, prestructured substrate is withdrawn from a liquid reservoir under a constant angle and at a constant velocity. The considered prestructures consist of differently wettable stripes oriented either parallel or perpendicular to the transfer direction. As a result, we have identified stationary and time-periodic solutions that show a deformation due to the prestructures. The obtained meniscus profiles for prestructured substrates have been further explained by comparing them to profiles for homogeneous substrates with varying wettability obtained by numerical continuation. In particular, this has created insights on possible ways to expand the findings to, e.g., differently sized prestructures. This knowledge about the dynamics of a dragged simple liquid meniscus on prestructured substrates could now be used to formulate approximate parametric meniscus profiles that, e.g., could be used in the simplified Cahn–Hilliard model for Langmuir–Blodgett transfer to account for deformations of the liquid layer due to a prestructure. In addition, the results are of interest for other related systems, such as dip-coating of substrates with solutions and suspensions [WZH⁺15], or other techniques such as the doctor-blade method and slot-die coating [DSBM14].

Apart from the usage of prestructured substrates, we have also identified a regime in which

pattern formation on homogeneous substrates withdrawn from a simple, partially wetting liquid can be observed. Within a small velocity range slightly below the transition to a Landau–Levich film, a striped deposit perpendicular to the transfer direction has been observed, which results from an intrinsic pattern formation mechanism. For future work, it would be interesting to further investigate this intrinsic mechanism, e.g., the bifurcations at the onset and ceasing of the regime of pattern formation, and to quantitatively estimate experimental conditions where this pattern formation is encountered. Again, related experimental set-ups such as the doctor-blade technique or slot-die coating with partially wetting liquids present natural targets to transfer these findings to.

The third major topic of this thesis has been the dynamics of drops of a simple liquid on inclined substrates. In a first part considering the dynamics of single drops, we have analyzed the bifurcation structure of the system. A special emphasis has been put on the so-called *pearling* instability which is observed experimentally [PFL01]. This instability occurs, when the drop volume exceeds a certain threshold (on a substrate of fixed inclination angle) or when the substrate inclination angle is increased beyond a certain value (for a drop of fixed volume), and leads to a break-up of the drop where it emits a single or multiple small satellite droplets at its back. We have identified the bifurcations and unstable eigenmodes connected to this instability and have also studied the dynamical behavior of a periodic train of pearling drops. Starting from periodic break-up and coalescence cycles, one can find a typical period doubling route to chaos for increasing inclination angles. While the calculations were initially conducted for a single, rather small drop volume, the results could be generalized to a broad range of drop volumes over several orders of magnitude using scaling laws. With this, the results should be applicable to experimentally achievable scales. An experimental examination would also be interesting for two special drop solution that have been found, namely, drops that show an oscillatory instability and very elongated stable drops. As these different drop solutions can – at least in the thin film model employed here – exhibit a multistability, it is challenging to observe all of them in experiments. In general, an experimental realization of our findings probably necessitates considerable effort to implement the setting of our simulations, such as perfectly homogeneous substrates on which the drops do not pin and do not show any contact angle hysteresis.

In the final section of the thesis, the scope on sliding drops has been extended to large ensembles of drops on the same substrate that can interact with each other. While the underlying model is the same thin film equation as for the individual sliding drops, the computational effort is drastically increased if one considers sufficiently large spatial domains. Among the most prominent interactions of liquid drops on solid substrates is the coarsening that lets the typical drop size grow at the expense of smaller drops that shrink and vanish. Therefore, a focus has been the effect of inclined substrates on the coarsening. In general, the coarsening is considerably accelerated due to the inclination of the substrate, as the sliding and the resulting coalescence possibilities of the drops introduce a new, fast way of mass exchange between the drops. Naturally, this effect becomes stronger for increasing inclination angles of the substrate, as the sliding velocities increase, too. However, the accelerated coarsening is counteracted by the pearling instability of the drops above a certain size, which we found to effectively stop the coarsening process at a certain stage. Using different measures such as the number of drops in the domain or the drop volume distribution, the overall dynamics have been quantitatively examined. To obtain a more profound knowledge about the balance of the coarsening mechanism and the pearling instability, the latter has been again studied, in particular to obtain the dependence of the stability threshold volume on the substrate inclination angle. A comparison

of this threshold with the drop volume distribution observed in the numerical simulations has revealed that the statistical properties of the drop ensembles are governed by the stability properties of individual drops.

To verify that the coarsening dynamics of the sliding drops is mainly governed by the coalescence and break-up events, a minimal statistical model for the temporal evolution of the drop volume distribution has been developed. Formulated as a continuous Smoluchowski equation, it employs information about the drop sliding velocity and stability properties obtained by numerical continuation of single drops. Despite its simplicity, the model has been able to reproduce the main findings from the simulations of the thin film model. In particular, the temporal evolution of the drop volume distribution and the resulting number of drops shows a good qualitative agreement. To achieve a more detailed, quantitative modeling, several approaches would be conceivable. On the one hand, a further refinement of the coalescence and break-up rates would be possible, e.g., allowing for stable elongated drops with large volumes, or a more detailed modeling of the break-up products. On the other hand, completely different model types could be formulated, like a particle based approach, in which each drop is represented by a discrete entity with properties such as their position, velocity and size (i.e., interaction radius). The dynamics based on interaction rules could then be calibrated extensively to observations in experiments or simulations. Such a detailed modeling, however, is typically accompanied by a loss of generality and, therefore, the necessary level of detail has to be carefully pondered.

Another natural extension to the analysis of sliding drops would be the introduction of substrate roughness or inhomogeneities. As typically encountered in everyday life, such imperfect substrates can lead to the pinning of the drops on inhomogeneities preventing their sliding below a certain volume or inclination angle (see, e.g., [BKHT11]). Just as in the case of homogeneous substrates, a combination of numerical continuation for stationary solutions and bifurcation analysis with direct numerical simulations for the dynamics should provide a powerful set of tools for a thorough investigation. The statistical model could also be readily extended to account for the pinning of drops.

In summary, we have analyzed three related systems involving thin (simple or complex) liquid layers on solid substrates that exhibit pattern formation phenomena. The systems were investigated employing different types of model equations and different kinds of numerical and statistical methods. In general, the systems covered in this thesis provide demonstrative examples how the treatment of pattern formation phenomena can profit from the usage of different analysis approaches. The most typical case is probably the combination of experiments with theoretical predictions from direct numerical simulations, as it was successfully employed in Chap. 4 to develop control strategies for the pattern formation in Langmuir–Blodgett transfer. In cases where suitable experiments are not easily feasible, different theoretical approaches complementing each other can provide insights, such as the combination of numerical continuation revealing the bifurcation structure of a particular system along with direct numerical simulations to obtain the full dynamical behavior. This approach has proven its capabilities in the analysis of both dragged menisci in Chap. 5 and sliding drops in Chap. 6. Therefore, our work provides a good starting point for similar approaches in related systems showing similar phenomena, such as dip-coating or the doctor-blade technique.

List of Publications

This list comprises the manuscripts published based on the work presented in this thesis. Authors marked with an asterisk contributed equally to the publication.

- [WG14] M. Wilczek and S. V. Gurevich. Locking of periodic patterns in Cahn-Hilliard models for Langmuir-Blodgett transfer. *Phys. Rev. E*, 90:042926, 2014.
- [WTG⁺15] M. Wilczek, W. B. H. Tewes, S. V. Gurevich, M. H. Köpf, L. Chi, and U. Thiele. Modelling pattern formation in dip-coating experiments. *Math. Model. Nat. Phenom.*, 10:44–60, 2015.
- [ZWH⁺16] J. Zhu*, M. Wilczek*, M. Hirtz, J. Hao, W. Wang, H. Fuchs, S. V. Gurevich, and L. F. Chi. Branch suppression and orientation control of Langmuir-Blodgett patterning on pre-structured surfaces. *Adv. Mater. Interf.*, 3:1600478, 2016.
- [EWGT16] S. Engelnkemper*, M. Wilczek*, S. V. Gurevich, and U. Thiele. Morphological transitions of sliding drops: Dynamics and bifurcations. *Phys. Rev. Fluids*, 1:073901, 2016.
- [WZC⁺17] M. Wilczek, J. Zhu, L. F. Chi, U. Thiele, and S. V. Gurevich. Dip-coating with prestructured substrates: transfer of simple liquids and Langmuir-Blodgett monolayers. *J. Phys.: Condens. Matter*, 29:014002, 2017.

In addition to the already published manuscripts, the following ones are in preparation based on the work presented in this thesis.

- [TWGT17] W. Tewes, M. Wilczek, S. V. Gurevich, and U. Thiele. Self-assembled coating patterns by meniscus-induced dewetting of a Landau-Levich film. (*in preparation*), 2017.
- [WTE⁺17] M. Wilczek, W. Tewes, S. Engelnkemper, S. V. Gurevich, and U. Thiele. Ensembles of sliding drops: Dynamics and statistics. (*in preparation*), 2017.

List of Figures

1.1	Sketch of a Langmuir–Blodgett trough.	3
1.2	AFM images of DPPC monolayers after Langmuir–Blodgett transfer.	4
2.1	Sketch of a thin liquid layer with height profile $h(x, y)$ on a solid substrate. . .	8
2.2	Sketch of the different possible wetting scenarios of a liquid on a solid substrate.	12
2.3	Sketch of the contact line of a partially wetting liquid.	12
2.4	Sketch of a solid substrate that is dragged out from a liquid reservoir.	15
2.5	Sketch of a thin liquid layer covered by an insoluble surfactant layer.	19
2.6	Sketch of a thin liquid solution layer.	22
2.7	Height profile and wetting potential of a liquid withdrawn from a liquid bath. .	24
3.1	Sketch of a solution family $u(\lambda)$	38
4.1	Overview of the pattern types occurring in the augmented Cahn–Hilliard model.	42
4.2	Bifurcation diagram of the augmented Cahn–Hilliard model.	43
4.3	Dependence of the wave number k and the duty cycle on the transfer velocity. .	44
4.4	Dependence of the wave number k on the transfer velocity v and the boundary concentration c_0	45
4.5	Dependence of the wave number k on the transfer velocity v for a prestructured substrate.	46
4.6	Overview of the occurring patterns for a horizontally prestructured substrate. .	47
4.7	Oblique stripe pattern occurring for a vertically prestructured substrate. . . .	48
4.8	Overview of the occurring patterns for a vertically prestructured substrate. . .	49
4.9	Comparison of experimental results and numerical simulations for vertically prestructured substrates	51
4.10	AFM images of a DPPC monolayer after LB transfer onto a substrate with inclined prestructure.	52
4.11	Snapshots of a direct numerical simulation for an inclined prestructure.	53
4.12	AFM images of bent stripes after a LB transfer of DPPC onto vertically prestructured substrates.	54
4.13	Simulation of the hydrodynamic model showing bent structures on a vertical prestructure.	55
4.14	Overview of the patterns for a sinusoidally modulated transfer velocity.	57
4.15	Dependence of the wavelength on the transfer velocity for a sinusoidally modulated transfer velocity.	58
4.16	Period-doubled stripe pattern due to a modulated transfer velocity.	59
4.17	Complex barcode-like stripe pattern obtained by a non-periodic transfer velocity modulation.	60
4.18	Overview of the patterns for a sinusoidally modulated contact line position. . .	61
4.19	Dependence of the wavelength on the transfer velocity for a sinusoidally modulated contact line position.	62

5.1	Exemplary solution of a liquid layer on a solid substrate dragged out from a bath.	65
5.2	Bifurcation diagram of a dragged meniscus in dependence on the transfer velocity.	66
5.3	Bifurcation diagram of a dragged meniscus in dependence on the transfer velocity and the substrate inclination.	67
5.4	Bifurcation diagram of a dragged meniscus in dependence on the wettability.	68
5.5	Simulations of a dragged meniscus for vertically prestructured substrates.	69
5.6	Contact line position $L_{cl}(y)$ extracted from the simulations in Fig. 5.5.	70
5.7	Simulation of a dragged meniscus for a horizontally prestructured substrate.	72
5.8	Contact line position $L_{cl}(t)$ extracted from the simulations in Fig. 5.7.	73
5.9	Simulation of a dragged meniscus on a prestructured substrate exhibiting a striped deposit.	74
5.10	Simulations of a dragged meniscus showing horizontal stripe patterns.	75
5.11	Wavelength of the pattern deposited from a dragged meniscus at varying velocity.	76
6.1	Bifurcation diagram of a sliding drop showing the sliding velocity U in dependence on the inclination angle α .	80
6.2	Drop solution and corresponding eigenfunction at the first saddle-node bifurcation.	81
6.3	Time series of the drop velocity during one break-up and coalescence cycle.	82
6.4	Period of one break-up and coalescence cycle depending on the inclination angle.	83
6.5	Time series of the drop volumes in a simulation on the periodic side-branch A.	84
6.6	Volumes of the largest drop occurring during one simulation in dependence on the inclination angle.	84
6.7	Snapshots at different times of an array of sliding drops at $\alpha = 1.9$.	86
6.8	Height profile of a drop solution on sub-branch III and the unstable eigenfunction.	87
6.9	Temporal evolution of the height and the sliding velocity of an oscillatory unstable drop.	88
6.10	Scaling behavior of the velocity of sliding drops and the instability inclination with the drop volume.	89
6.11	Simulations of ensembles of sliding drops for various inclination angles.	91
6.12	Power spectra $ \mathcal{FT}_x ^2$ and $ \mathcal{FT}_y ^2$ of an ensemble of sliding drops for $\alpha = 0.5$.	93
6.13	Temporal evolution of the mean wave numbers for different inclination angles.	94
6.14	Time series of the number of drops during the coarsening process on an inclined substrate.	96
6.15	Temporal evolution of the drop volume distribution $f(V, t)$ obtained by kernel density estimation for a direct numerical simulation.	97
6.16	Bifurcation diagram of sliding drops on an inclined substrate showing the sliding velocity U in dependence on the drop volume V .	98
6.17	Comparison of the final drop volume distribution and the bifurcation diagrams for different inclination angles.	99
6.18	Illustration of the coalescence and fragmentation kernels $K(V_1, V_2)$ and $J(V_1, V_2)$.	103
6.19	Temporal evolution of the drop volume distribution $f(V, t)$ obtained by kernel density estimation and as a result of a simulation of the statistical model.	105
6.20	Temporal evolution of the number of drops observed in thin film simulations and as a result of simulations of the statistical model.	106

Bibliography

- [AG03] E. L. Allgower and K. Georg. *Introduction to Numerical Continuation Methods*. Classics in Applied Mathematics. Society for Industrial and Applied Mathematics, Philadelphia, 2003.
- [Ale77] R. Alexander. Diagonally implicit Runge-Kutta methods for stiff ODE's. *SIAM J. Numer. Anal.*, 14:1006–1021, 1977.
- [Ayr10] H. Ayrton. The origin and growth of ripple-mark. *Proc. R. Soc. Lond. A*, 84:285–310, 1910.
- [BACP01] M. Ben Amar, L. Cummings, and Y. Pomeau. Singular points of a moving contact line. *C. R. Acad. Sci. Ser. IIB*, 329:277–282, 2001.
- [BACP03] M. Ben Amar, L. J. Cummings, and Y. Pomeau. Transition of a moving contact line from smooth to angular. *Phys. Fluids*, 15:2949–2960, 2003.
- [BB15] E. S. Benilov and M. S. Benilov. A thin drop sliding down an inclined plate. *J. Fluid Mech.*, 773:75–102, 2015.
- [BBD⁺08a] P. Bastian, M. Blatt, A. Dedner, C. Engwer, R. Klöforn, R. Kornhuber, M. Ohlberger, and O. Sander. A generic grid interface for parallel and adaptive scientific computing. Part II: Implementation and tests in DUNE. *Computing*, 82:121–138, 2008.
- [BBD⁺08b] P. Bastian, M. Blatt, A. Dedner, C. Engwer, R. Klöforn, M. Ohlberger, and O. Sander. A generic grid interface for parallel and adaptive scientific computing. Part I: Abstract framework. *Computing*, 82:103–119, 2008.
- [BEI⁺09] D. Bonn, J. Eggers, J. Indekeu, J. Meunier, and E. Rolley. Wetting and spreading. *Rev. Mod. Phys.*, 81:739–805, 2009.
- [BHD⁺12] G. Berteloot, A. Hoang, A. Daerr, H. P. Kavehpour, F. Lequeux, and L. Limat. Evaporation of a sessile droplet: Inside the coffee stain. *J. Colloid Interf. Sci.*, 370:155–161, 2012.
- [BHM10] P. Bastian, F. Heimann, and S. Marnach. Generic implementation of finite element methods in the distributed and unified numerics environment (DUNE). *Kybernetika*, 46:294–315, 2010.
- [BJST⁺94] E. Ben-Jacob, O. Schochet, A. Tenenbaum, I. Cohen, A. Czirok, and T. Vicsek. Generic modelling of cooperative growth patterns in bacterial colonies. *Nature*, 368:46–49, 1994.

- [BKHT11] P. Beltrame, E. Knobloch, P. Hänggi, and U. Thiele. Rayleigh and depinning instabilities of forced liquid ridges on heterogeneous substrates. *Phys. Rev. E*, 83:016305, 2011.
- [Blo34] K. B. Blodgett. Monomolecular films of fatty acids on glass. *J. Am. Chem. Soc.*, 56:495, 1934.
- [Blo35] K. B. Blodgett. Films built by depositing successive monomolecular layers on a solid surface. *J. Am. Chem. Soc.*, 57:1007–1022, 1935.
- [Bro89] F. Brochard. Motions of droplets on solid surfaces induced by chemical or thermal gradients. *Langmuir*, 5:432–438, 1989.
- [But08] J. C. Butcher. *Numerical Methods for Ordinary Differential Equations*. John Wiley & Sons, 2008.
- [BWvCD17] B. J. Brasjen, H. M. J. M. Wedershoven, A. W. van Cuijk, and A. A. Darhuber. Dip- and die-coating of hydrophilic squares on flat, hydrophobic substrates. *Chem. Eng. Sci.*, 158:340 – 348, 2017.
- [Cah65] J. W. Cahn. Phase separation by spinodal decomposition in isotropic systems. *J. Chem. Phys.*, 42:93–99, 1965.
- [CBdC⁺14] T. P. Corrales, M. Bai, V. del Campo, P. Homm, P. Ferrari, A. Diama, C. Wagner, H. Taub, K. Knorr, M. Deutsch, M. J. Retamal, U. G. Volkmann, and P. Huber. Spontaneous formation of nanopatterns in velocity-dependent dip-coated organic films: From dragonflies to stripes. *ACS nano*, 8:9954–9963, 2014.
- [CGG⁺91] J. D. Crawford, M. Golubitsky, M. G. M. Gomes, E. Knobloch, and I. M. Stewart. Boundary conditions as symmetry constraints. In *Singularity Theory and its Applications, Part II*, volume 1463 of *Lecture Notes in Mathematics*, pages 63–79, New York, 1991. Springer.
- [CGO06] A. Checco, O. Gang, and B. M. Ocko. Liquid nanostripes. *Phys. Rev. Lett.*, 96:056104, 2006.
- [CH93] M. C. Cross and P. C. Hohenberg. Pattern formation outside of equilibrium. *Rev. Mod. Phys.*, 65:851, 1993.
- [CLH⁺07] X. Chen, S. Lenhert, M. Hirtz, N. Lu, H. Fuchs, and L. Chi. Langmuir–Blodgett patterning: A bottom–up way to build mesostructures over large areas. *Acc. Chem. Res.*, 40:393–401, 2007.
- [Cou86] P. Coulet. Commensurate-incommensurate transition in nonequilibrium systems. *Phys. Rev. Lett.*, 56:724–727, 1986.
- [CW92] M. K. Chaudhury and G. M. Whitesides. How to make water run uphill. *Science*, 256:1539–1541, 1992.
- [Dah63] G. G. Dahlquist. A special stability problem for linear multistep methods. *BIT Numerical Mathematics*, 3:27–43, 1963.

-
- [DBA⁺11] M. Dolnik, T. Bánsági, S. Ansari, I. Valent, and I. R. Epstein. Locking of Turing patterns in the chlorine dioxide–iodine–malonic acid reaction with one-dimensional spatial periodic forcing. *Phys. Chem. Chem. Phys.*, 13:12578–12583, 2011.
- [DBD⁺97] R. D. Deegan, O. Bakajin, T. F. Dupont, G. Huber, S. R. Nagel, and T. A. Witten. Capillary flow as the cause of ring stains from dried liquid drops. *Nature*, 389:827–829, 1997.
- [DDG16] M. Dey, F. Doumenc, and B. Guerrier. Numerical simulation of dip-coating in the evaporative regime. *Eur. Phys. J. E*, 39:1–9, 2016.
- [Der75] B. V. Derjaguin. Untersuchungen des Spaltdruckes dünner Filme, deren Entwicklung, Ergebnisse und zu lösende aktuelle Probleme. *Colloid Polym. Sci.*, 253:492–499, 1975.
- [DFSA08] G. Delon, M. Fermigier, J. H. Snoeijer, and B. Andreotti. Relaxation of a dewetting contact line. Part 2. Experiments. *J. Fluid Mech.*, 604:55–75, 2008.
- [dG85] P.-G. de Gennes. Wetting: Statics and dynamics. *Rev. Mod. Phys.*, 57:827–863, 1985.
- [DG13] F. Doumenc and B. Guerrier. Numerical simulation of an evaporative meniscus on a moving substrate. *Eur. Phys. J.-Spec. Top.*, 219:25–31, 2013.
- [dGBWQ04] P.-G. de Gennes, F. Brochard-Wyart, and D. Quéré. *Capillarity and Wetting Phenomena: Drops, Bubbles, Pearls, Waves*. Springer, New York, 2004.
- [DKK91a] E. Doedel, H. B. Keller, and J. P. Kernevez. Numerical analysis and control of bifurcation problems (I) Bifurcation in finite dimensions. *Int. J. Bifurcation Chaos*, 1:493–520, 1991.
- [DKK91b] E. Doedel, H. B. Keller, and J. P. Kernevez. Numerical analysis and control of bifurcation problems (II) Bifurcation in infinite dimensions. *Int. J. Bifurcation Chaos*, 1:745–772, 1991.
- [DL83] G. Dee and J. S. Langer. Propagating pattern selection. *Phys. Rev. Lett.*, 50:383, 1983.
- [Doe] E. Doedel. Lecture notes on numerical analysis of nonlinear equations. <http://indy.cs.concordia.ca/auto/notes.pdf>. last visited on August 28th, 2016.
- [DSBM14] Y. Diao, L. Shaw, Z. Bao, and S. C. B. Mannsfeld. Morphology control strategies for solution-processed organic semiconductor thin films. *Energy Environ. Sci.*, 7:2145–2159, 2014.
- [DTD⁺00] A. A. Darhuber, S. M. Troian, J. M. Davis, S. M. Miller, and S. Wagner. Selective dip-coating of chemically micropatterned surfaces. *J. Appl. Phys.*, 88:5119–5126, 2000.
- [DV79] E. B. Dussan V. On the spreading of liquids on solid surfaces: Static and dynamic contact lines. *Annu. Rev. Fluid Mech.*, 11:371–400, 1979.

- [DWC⁺14] H. A. Dijkstra, F. W. Wubs, A. K. Cliffe, E. Doedel, I. F. Dragomirescu, B. Eckhardt, A. Y. Gelfgat, A. Hazel, V. Lucarini, A. G. Salinger, E. T. Phipps, J. Sanchez-Umbria, H. Schuttelaars, L. S. Tuckerman, and U. Thiele. Numerical bifurcation methods and their application to fluid dynamics: Analysis beyond simulation. *Commun. Comput. Phys.*, 15:1–45, 2014.
- [Eva10] C. E. Evans. *Partial Differential Equations*. American Mathematical Society, Providence, Rhode Island, 2nd edition, 2010.
- [EWGT16] S. Engelnkemper, M. Wilczek, S. V. Gurevich, and U. Thiele. Morphological transitions of sliding drops: Dynamics and bifurcations. *Phys. Rev. Fluids*, 1:073901, 2016.
- [Fis37] R. A. Fisher. The wave of advance of advantageous genes. *Ann. Eugenics*, 7:355–369, 1937.
- [Flo53] P. J. Flory. *Principles of Polymer Chemistry*. Cornell University Press, Ithaca, 1953.
- [FMD86] F. Family, P. Meakin, and J. M. Deutch. Kinetics of coagulation with fragmentation: Scaling behavior and fluctuations. *Phys. Rev. Lett.*, 57:727–730, 1986.
- [GCF00] M. Gleiche, L. F. Chi, and H. Fuchs. Nanoscopic channel lattices with controlled anisotropic wetting. *Nature*, 403:173–175, 2000.
- [GHLL99] H. Gau, S. Herminghaus, P. Lenz, and R. Lipowsky. Liquid morphologies on structured surfaces: From microchannels to microchips. *Science*, 283:46–49, 1999.
- [GLF⁺16] P. Gao, L. Li, J. J. Feng, H. Ding, and X.-Y. Lu. Film deposition and transition on a partially wetting plate in dip coating. *J. Fluid Mech.*, 791:358–383, 2016.
- [GORS09] K. Glasner, F. Otto, T. Rump, and D. Slepčev. Ostwald ripening of droplets: The role of migration. *Euro. J. Appl. Math.*, 20:1–67, 2009.
- [GP71] P. Glansdorff and I. Prigogine. *Thermodynamic theory of structure, stability and fluctuations*. Wiley-Interscience, London, 1971.
- [Gre78] H. P. Greenspan. On the motion of a small viscous droplet that wets a surface (relevant to cell movement). *J. Fluid Mech.*, 84:125–143, 1978.
- [GT01] D. Gilbarg and N. S. Trudinger. *Elliptic Partial Differential Equations of Second Order*. Springer-Verlag, Berlin, 2001.
- [GTLT14] M. Galvagno, D. Tseluiko, H. Lopez, and U. Thiele. Continuous and discontinuous dynamic unbinding transitions in drawn film flow. *Phys. Rev. Lett.*, 112:137803, 2014.
- [GW03] K. B. Glasner and T. P. Witelski. Coarsening dynamics of dewetting films. *Phys. Rev. E*, 67:016302, 2003.

-
- [GW08] M. B. Gratton and T. P.P. Witelski. Coarsening of unstable thin films subject to gravity. *Phys. Rev. E*, 77:016301, 2008.
- [Hai97] J. M. Haile. *Molecular Dynamics Simulation*. John Wiley & Sons, Inc., New York, 1997.
- [HJ93] R. A. Houze Jr. *Cloud Dynamics*, volume 53 of *International Geophysics Series*. Academic Press, San Diego, 1993.
- [HL12] W. Han and Z. Lin. Learning from "Coffee Rings": Ordered structures enabled by controlled evaporative self-assembly. *Angew. Chem. Int. Ed.*, 51:1534–1546, 2012.
- [HM91] J. A. M. Huethorst and J. Marra. Motion of Marangoni-contracted water drops across inclined hydrophilic surfaces. *Langmuir*, 7:2756–2763, 1991.
- [Kel77] H. B. Keller. Numerical solution of bifurcation and nonlinear eigenvalue problems. In P.H. Rabinowitz, editor, *Applications of Bifurcation Theory. Proceedings of an Advanced Seminar Conducted by the Mathematics Research Center*, pages 359–383. The University of Wisconsin at Madison, Academic Press, New York, 1977.
- [KGF11] M. H. Köpf, S. V. Gurevich, and R. Friedrich. Controlled nanochannel lattice formation utilizing prepatterned substrates. *Phys. Rev. E*, 83:016212, 2011.
- [KGFC10] M. H. Köpf, S. V. Gurevich, R. Friedrich, and L. F. Chi. Pattern formation in monolayer transfer systems with substrate-mediated condensation. *Langmuir*, 26:10444–10447, 2010.
- [KGFT12] M. H. Köpf, S. V. Gurevich, R. Friedrich, and U. Thiele. Substrate-mediated pattern formation in monolayer transfer: a reduced model. *New J. Phys.*, 14:023016, 2012.
- [Kit14] G. Kitavtsev. Coarsening rates for the dynamics of slipping droplets. *Euro. J. Appl. Math.*, 25:83–115, 2014.
- [KK04] A. P. Krekhov and L. Kramer. Phase separation in the presence of spatially periodic forcing. *Phys. Rev. E*, 70:061801, 2004.
- [Kla99] C. A. Klausmeier. Regular and irregular patterns in semiarid vegetation. *Science*, 284:1826–1828, 1999.
- [KLK02] H.-Y. Kim, H. J. Lee, and B. H. Kang. Sliding of liquid drops down an inclined solid surface. *J. Colloid Interf. Sci.*, 247:372–380, 2002.
- [KMD99] V. M. Kaganer, H. Möhwald, and P. Dutta. Structure and phase transitions in Langmuir monolayers. *Rev. Mod. Phys.*, 71:779, 1999.
- [Kön04] K. Königsberger. *Analysis 2*. Springer-Verlag, Berlin, 5th edition, 2004. pages 113–114.

- [Köp11] M. H. Köpf. *On the dynamics of surfactant covered thin liquid films and the formation of stripe patterns in Langmuir-Blodgett transfer*. PhD thesis, Westfälische Wilhelms-Universität Münster, 2011.
- [KPP37] A. Kolmogorov, I. Petrovsky, and N. Piskunov. Study of the diffusion equation coupled to an increase in mass and its application to a problem in biology. *Bull. Uni. Moscow, Ser. Internat. A1*, 6:1–26, 1937.
- [Kre09] F. C. Krebs. Fabrication and processing of polymer solar cells: a review of printing and coating techniques. *Sol. Energ. Mat. Sol. C.*, 93:394–412, 2009.
- [KS09] S. Kondo and H. Shirota. Theoretical analysis of mechanisms that generate the pigmentation pattern of animals. *Sem. Cell Dev. Biol.*, 20:82–89, 2009.
- [KT14] M. H. Köpf and U. Thiele. Emergence of the bifurcation structure of a Langmuir-Blodgett transfer model. *Nonlinearity*, 27:2711–2734, 2014.
- [Kuz10] Y. A. Kuznetsov. *Elements of Applied Bifurcation Theory*. Springer, New York, 3rd edition, 2010.
- [Lan34] I. Langmuir. Mechanical properties of monomolecular films. *J. Franklin Inst.*, 218:143–171, 1934.
- [Lar14] R. G. Larson. Transport and deposition patterns in drying sessile droplets. *AIChE J.*, 60:1538–1571, 2014.
- [LGDL05] N. Le Grand, A. Daerr, and L. Limat. Shape and motion of drops sliding down an inclined plane. *J. Fluid Mech.*, 541:293–315, 2005.
- [LGS⁺10] L. Li, P. Gao, K. C. Schuermann, S. Ostendorp, W. Wang, C. Du, Y. Lei, H. Fuchs, L. De Cola, K. Müllen, and L. Chi. Controllable growth and field-effect property of monolayer to multilayer microstripes of an organic semiconductor. *J. Am. Chem. Soc.*, 132:8807–8809, 2010.
- [LGW⁺13] L. Li, P. Gao, W. Wang, K. Müllen, H. Fuchs, and L. Chi. Growth of ultrathin organic semiconductor microstripes with thickness control in the monolayer precision. *Angew. Chem. Int. Ed.*, 52:12530–12535, 2013.
- [LH00] J. C. Lasheras and E. J. Hopfinger. Liquid jet instability and atomization in a coaxial gas stream. *Annu. Rev. Fluid Mech.*, 32:275–308, 2000.
- [LKG⁺12] L. Q. Li, M. H. Köpf, S. V. Gurevich, R. Friedrich, and L. F. Chi. Structure formation by dynamic self-assembly. *Small*, 8:488–503, 2012.
- [LL42] L. Landau and B. Levich. Dragging of a liquid by a moving plane. *Acta Physicochim. U.R.S.S.*, 17:42, 1942.
- [LL87] L. D. Landau and E. M. Lifshitz. *Fluid Mechanics*. Volume 6 of Course of Theoretical Physics. Pergamon Press, Oxford, 2nd edition, 1987.
- [LP16] C. B. Lang and N. Pucker. *Mathematische Methoden in der Physik*. Springer Spektrum, Berlin, 3rd edition, 2016. p. 241.

-
- [LS04] L. Limat and H. A. Stone. Three-dimensional lubrication model of a contact line corner singularity. *Europhys. Lett.*, 65:365, 2004.
- [MBPB08] J. H. McCoy, W. Brunner, W. Pesch, and E. Bodenschatz. Self-organization of topological defects due to applied constraints. *Phys. Rev. Lett.*, 101:254102, 2008.
- [ME88] P. Meakin and M. H. Ernst. Scaling in aggregation with breakup simulations and mean-field theory. *Phys. Rev. Lett.*, 60:2503–2506, 1988.
- [Mea92] P. Meakin. Droplet deposition growth and coalescence. *Rep. Prog. Phys.*, 55:157, 1992.
- [MHM08] R. Manor, A. Hagberg, and E. Meron. Wave-number locking in spatially forced pattern-forming systems. *Europhys. Lett.*, 83:10005, 2008.
- [Mit93] V. S. Mitlin. Dewetting of solid surface: Analogy with spinodal decomposition. *J. Colloid Interf. Sci.*, 156:491–497, 1993.
- [MRQG07] M. Maleki, E. Reyssat, D. Quere, and R. Golestanian. On the Landau-Levich transition. *Langmuir*, 23:10116–10122, 2007.
- [MZAM16] S. Mhatre, A. Zigelman, L. Abezgauz, and O. Manor. Influence of a propagating megahertz surface acoustic wave on the pattern deposition of solute mass off an evaporating solution. *Langmuir*, 32:9611–9618, 2016.
- [NCS84] A. Novick-Cohen and L. A. Segel. Nonlinear aspects of the Cahn-Hilliard equation. *Physica D*, 10:277–298, 1984.
- [NVI] NVIDIA. CUDA C Programming Guide Version 7.5. <http://docs.nvidia.com/cuda/cuda-c-programming-guide/index.html>. last visited on August 18th, 2016.
- [ODB97] A. Oron, S. H. Davis, and S. G. Bankoff. Long-scale evolution of thin liquid films. *Rev. Mod. Phys.*, 69:931–980, 1997.
- [Ons31] L. Onsager. Reciprocal relations in irreversible processes. I. *Phys. Rev.*, 37:405–426, 1931.
- [Ost96] W. Ostwald. *Lehrbuch der Allgemeinen Chemie*, volume 2. Leipzig, Germany, 1896.
- [PFL01] T. Podgorski, J. M. Flesselles, and L. Limat. Corners, cusps, and pearls in running drops. *Phys. Rev. Lett.*, 87:036102, 2001.
- [Poc91] A. Pockels. Surface tension. *Nature*, 43:437–439, 1891.
- [Poc93] A. Pockels. Relations between the surface-tension and relative contamination of water surfaces. *Nature*, 48:152–154, 1893.
- [PRK03] A. Pikovsky, M. Rosenblum, and J. Kurths. *Synchronization: A Universal Concept in Nonlinear Sciences*. Cambridge Nonlinear Science Series. Cambridge University Press, 2003.

- [PS05] J. Peiró and S. Sherwin. Finite difference, finite element and finite volume methods for partial differential equations. In S. Yip, editor, *Handbook of Materials Modeling*, pages 2415–2446, Dordrecht, The Netherlands, 2005. Springer.
- [PT93] K. Pyragas and A. Tamaševičius. Experimental control of chaos by delayed self-controlling feedback. *Phys. Lett. A*, 180:99–102, 1993.
- [QXX⁺99] D. Qin, Y. Xia, B. Xu, H. Yang, C. Zhu, and G. M. Whitesides. Fabrication of ordered two-dimensional arrays of micro- and nanoparticles using patterned self-assembled monolayers as templates. *Adv. Mater.*, 11:1433–1437, 1999.
- [Rap04] D. C. Rapaport. *The Art of Molecular Dynamics Simulation*. University Press, Cambridge, 2nd edition, 2004.
- [RMM⁺03] S. Rüdiger, D. G. Míguez, A. P. Munuzuri, F. Sagués, and J. Casademunt. Dynamics of Turing patterns under spatiotemporal forcing. *Phys. Rev. Lett.*, 90:128301, 2003.
- [Rob90] G. Roberts, editor. *Langmuir-Blodgett Films*. Plenum Press, New York, 1990.
- [RQ99] D. Richard and D. Quéré. Viscous drops rolling on a tilted non-wettable solid. *Europhys. Lett.*, 48:286–291, 1999.
- [RS92] H. Riegler and K. Spratte. Structural changes in lipid monolayers during the Langmuir-Blodgett transfer due to substrate monolayer interactions. *Thin Solid Films*, 210:9–12, 1992.
- [SADF07] J. H. Snoeijer, B. Andreotti, G. Delon, and M. Fermigier. Relaxation of a dewetting contact line. Part 1. A full-scale hydrodynamic calculation. *J. Fluid Mech.*, 579:63–83, 2007.
- [Sco15] D. W. Scott. *Multivariate density estimation: theory, practice, and visualization*. John Wiley & Sons, Hoboken, New Jersey, 2nd edition, 2015.
- [Sha93] A. Sharma. Relationship of thin film stability and morphology to macroscopic parameters of wetting in the apolar and polarsystems. *Langmuir*, 9:861–869, 1993.
- [SK11] N. Savva and S. Kalliadasis. Dynamics of moving contact lines: A comparison between slip and precursor film models. *Europhys. Lett.*, 94:64004, 2011.
- [SLGPL⁺07] J. H. Snoeijer, N. Le Grand-Piteira, L. Limat, H. A. Stone, and J. Eggers. Cornered drops and rivulets. *Phys. Fluids*, 19:042104, 2007.
- [SLW⁺02] H. A. Stone, L. Limat, S. K. Wilson, J. M. Flesselles, and T. Podgorski. Corner singularity of a contact line moving on a solid substrate. *C. R. Phys.*, 3:103–110, 2002.
- [Smi86] G. D. Smith. *Numerical Solution of Partial Differential Equations: Finite Difference Methods*. Oxford Applied Mathematics And Computing Science Series. Oxford University Press, USA, 1986.

-
- [Smo16] M. V. Smoluchowski. Drei Vorträge über Diffusion, Brownsche Bewegung und Koagulation von Kolloidteilchen. *Z. Phys.*, 17:557–585, 1916.
- [SR94] K. Spratte and H. Riegler. Steady state morphology and composition of mixed monomolecular films (Langmuir monolayers) at the air/water interface in the vicinity of the three-phase line: model calculations and experiments. *Langmuir*, 10:3161–3173, 1994.
- [SRCW05] L. W. Schwartz, D. Roux, and J. J. Cooper-White. On the shapes of droplets that are sliding on a vertical wall. *Physica D*, 209:236–244, 2005.
- [SS08] E. Schöll and H.G. Schuster, editors. *Handbook of chaos control*. Wiley-VCH, Weinheim, Germany, 2008.
- [SSM03] K. Staliunas and V. J. Sanchez-Morcillo. *Transverse patterns in nonlinear optical resonators*. Springer, Berlin, 2003.
- [Str14] S. H. Strogatz. *Nonlinear Dynamics and Chaos*. Westview Press, Boulder, Colorado, 2nd edition, 2014.
- [SV09] V. M. Starov and M. G. Velarde. Surface forces and wetting phenomena. *J. Phys.: Condens. Matter*, 21:464121, 2009.
- [TAP12] U. Thiele, A. J. Archer, and M. Plapp. Thermodynamically consistent description of the hydrodynamics of free surfaces covered by insoluble surfactants of high concentration. *Phys. Fluids*, 24:102107, 2012.
- [TAP16] U. Thiele, A. J. Archer, and L. M. Pismen. Gradient dynamics models for liquid films with soluble surfactant. *arXiv*, 1609.00946, 2016.
- [TBT13] D. Tseluiko, J. Baxter, and U. Thiele. A homotopy continuation approach for analysing finite-time singularities in thin liquid films. *IMA J. Appl. Math.*, 78:762–776, 2013.
- [TGT14] D. Tseluiko, M. Galvagno, and U. Thiele. Collapsed heteroclinic snaking near a heteroclinic chain in dragged meniscus problems. *Eur. Phys. J. E*, 37:1–17, 2014.
- [Thi07] U. Thiele. Structure formation in thin liquid films. In S. Kalliadasis and U. Thiele, editors, *Thin Films of Soft Matter*, pages 25–93, Wien, 2007. Springer.
- [Thi10] U. Thiele. Thin film evolution equations from (evaporating) dewetting liquid layers to epitaxial growth. *J. Phys.: Condens. Matter*, 22:084019, 2010.
- [Thi11] U. Thiele. Note on thin film equations for solutions and suspensions. *Eur. Phys. J.-Spec. Top.*, 197:213–220, 2011.
- [Thi14] U. Thiele. Patterned deposition at moving contact line. *Adv. Colloid Interface Sci.*, 206:399–413, 2014.
- [TK06] U. Thiele and E. Knobloch. On the depinning of a driven drop on a heterogeneous substrate. *New J. Phys.*, 8:313, 2006.

- [TNB⁺02] U. Thiele, K. Neuffer, M. Bestehorn, Y. Pomeau, and M. G. Velarde. Sliding drops on an inclined plane. *Colloids Surf. A*, 206:87–104, 2002.
- [TTL13] U. Thiele, D. V. Todorova, and H. Lopez. Gradient dynamics description for films of mixtures and suspensions: Dewetting triggered by coupled film height and concentration fluctuations. *Phys. Rev. Lett.*, 111:117801, 2013.
- [TVN⁺01] U. Thiele, M. G. Velarde, K. Neuffer, M. Bestehorn, and Y. Pomeau. Sliding drops in the diffuse interface model coupled to hydrodynamics. *Phys. Rev. E*, 64:061601, 2001.
- [TWGT17] W. Tewes, M. Wilczek, S. V. Gurevich, and U. Thiele. Self-assembled coating patterns by meniscus-induced dewetting of a Landau–Levich film. (*in preparation*), 2017.
- [UWR14] H. Uecker, D. Wetzel, and J. D. M. Rademacher. pde2path - a Matlab package for continuation and bifurcation in 2D elliptic systems. *Numer. Math. Theory Me.*, 7:58–106, 2014.
- [vHMSZ01] J. von Hardenberg, E. Meron, M. Shachak, and Y. Zarmi. Diversity of vegetation patterns and desertification. *Phys. Rev. Lett.*, 87:198101, 2001.
- [vS88] W. van Saarloos. Front propagation into unstable states: Marginal stability as a dynamical mechanism for velocity selection. *Phys. Rev. A*, 37:211, 1988.
- [vS03] W. van Saarloos. Front propagation into unstable states. *Phys. Rep.*, 386:29–222, 2003.
- [WG02] G. M. Whitesides and B. Grzybowski. Self-assembly at all scales. *Science*, 295:2418–2421, 2002.
- [WG14] M. Wilczek and S. V. Gurevich. Locking of periodic patterns in Cahn-Hilliard models for Langmuir-Blodgett transfer. *Phys. Rev. E*, 90:042926, 2014.
- [Wil82] S. D. R. Wilson. The drag-out problem in film coating theory. *J. Eng. Math.*, 16:209–221, 1982.
- [Wil12] M. Wilczek. Pattern formation in Cahn-Hilliard models for Langmuir-Blodgett transfer. Master’s thesis, Westfälische Wilhelms-Universität Münster, 2012.
- [WR04] S. J. Weinstein and K. J. Ruschak. Coating flows. *Annu. Rev. Fluid Mech.*, 36:29–53, 2004.
- [WTG⁺15] M. Wilczek, W. B. H. Tewes, S. V. Gurevich, M. H. Köpf, L. Chi, and U. Thiele. Modelling pattern formation in dip-coating experiments. *Math. Model. Nat. Phenom.*, 10:44–60, 2015.
- [WZC⁺17] M. Wilczek, J. Zhu, L. Chi, U. Thiele, and S. V. Gurevich. Dip-coating with prestructured substrates: Transfer of simple liquids and Langmuir-Blodgett monolayers. *J. Phys.: Condens. Matter*, 29:014002, 2017.

- [WZH⁺15] B. Wang, T. Zhu, L. Huang, T. L. D. Tam, Z. Cui, J. Ding, and L. Chi. Addressable growth of oriented organic semiconductor ultra-thin films on hydrophobic surface by direct dip-coating. *Org. Electron.*, 24:170–175, 2015.
- [XD16] Y. Xu, X. Di and M. Doi. Variational method for liquids moving on a substrate. *Phys. Fluids*, 28:087101, 2016.
- [XXL07] J. Xu, J. Xia, and Z. Lin. Evaporation-induced self-assembly of nanoparticles from a sphere-on-flat geometry. *Angew. Chem.*, 119:1892–1895, 2007.
- [YS05] H. Yabu and M. Shimomura. Preparation of self-organized mesoscale polymer patterns on a solid substrate: Continuous pattern formation from a receding meniscus. *Adv. Funct. Mater.*, 15:575–581, 2005.
- [ZGP93] D. Zhang, L. Györgyi, and W.R. Peltier. Deterministic chaos in the Belousov–Zhabotinsky reaction: Experiments and simulations. *Chaos*, 3:723–745, 1993.
- [ZSE09] J. Ziegler, J.H. Snoeijer, and J. Eggers. Film transitions of receding contact lines. *Eur. Phys. J.-Spec. Top.*, 166:177–180, 2009.
- [ZWH⁺16] J. Zhu, M. Wilczek, M. Hirtz, J. Hao, W. Wang, H. Fuchs, S.V. Gurevich, and L.F. Chi. Branch suppression and orientation control of Langmuir-Blodgett patterning on pre-structured surfaces. *Adv. Mater. Interf.*, 3:1600478, 2016.

Danksagung

Während meiner Promotionszeit und auch bereits in der Zeit des Studiums zuvor, habe ich durch viele Menschen große Unterstützung erfahren. Daher möchte ich hier meinen Dank ausdrücken an:

- Prof. Dr. Uwe Thiele für seine engagierte und unkomplizierte Betreuung meiner Promotion.
- Prof. Dr. Andreas Heuer für die weitere Betreuung bereits seit meiner Masterarbeit.
- Dr. Svetlana Gurevich für ihre unschätzbare wertvolle Rolle als immer ansprechbare Betreuerin und hilfsbereite Mentorin seit mehr als fünf Jahren.
- Juan Zhu und Prof. Dr. Lifeng Chi für die sehr enge und erfolgreiche Kooperation im Rahmen des deutsch-chinesischen Kollaborationsprojektes Transregio 61. Dem gesamten Transregio 61 Projekt danke ich für die finanzielle Unterstützung und das Ermöglichen vieler Auslandsaufenthalte.
- Walter Tewes für die vielen interessanten gemeinsamen Projekte, Diskussionen und Reisen.
- Sebastian Engelnkemper für die spannende Zusammenarbeit an den rutschenden Tropfen.
- Meinen Korrekturlesern Christian Barthel, Svetlana Gurevich, Lukas Ophaus, Sophie Schröder, Felix Tabbert, Walter Tewes, Uwe Thiele und Sarah Trinschek für das Verhindern zahlreicher Fehler in dieser Arbeit.
- Den derzeitigen und ehemaligen Mitgliedern der Arbeitsgruppen Friedrich und Thiele für entspannte Mittagessen und Diskussionen sowie viele gemeinsame Konferenzzreisen, insbesondere Anton Daitche, Christoph Honisch, Johannes Lülff, Cornelia Petrovic und Michael Wilczek.
- Der Mensa-Gruppe zum Fremdgehen für die manchmal nötige Ablenkung.
- Meiner gesamten Familie für die bedingungslose Unterstützung in allen Lebenslagen, seitdem ich denken kann.
- Christina für das gemeinsame Leben, Arbeiten und Urlauben, für ihre Liebe, für Alles.

Lebenslauf

Name	Markus Wilczek
Geburtsdatum	13.11.1987
Geburtsort	Höxter
Staatsangehörigkeit	Deutsch
Familienstand	ledig

Schulausbildung

1994 – 1998	Gemeinschaftsgrundschule Brakel
1998 – 2007	Städtisches Petrus-Legge-Gymnasium Brakel
15.06.2007	Allgemeine Hochschulreife (Note 1,0)

Studium

10/2007 – 08/2010	Bachelorstudium der Physik an der Westfälischen Wilhelms-Universität Münster
23.08.2010	Abschluss Bachelor of Science mit Auszeichnung (Note 1,0) Thema der Bachelorarbeit: Realisierung und Charakterisierung einer galvanometrischen Rasterspiegeleinheit für konfokale, nichtlineare Mikroskopie
10/2010 – 12/2012	Masterstudium der Physik an der Westfälischen Wilhelms-Universität Münster
12.12.2010	Abschluss Master of Science (Note 1,0) Thema der Masterarbeit: Pattern formation in Cahn-Hilliard models for Langmuir-Blodgett transfer

Promotionsstudium

seit 01/2013	Promotion am Institut für Theoretische Physik der Westfälischen Wilhelms-Universität Münster, zunächst unter der Betreuung von Prof. Dr. Andreas Heuer, ab 2014 unter der Betreuung von Prof. Dr. Uwe Thiele
---------------------	--

Berufstätigkeit

06/2007 – 07/2007	Aushilfsmitarbeiter bei der DMA Maschinen- und Anlagenbau GmbH, Höxter
10/2008 – 03/2010	Studentische Hilfskraft am Center for Nonlinear Science der Universität Münster
10/2009 – 03/2011	Studentische Hilfskraft am Mathematischen Institut der Universität Münster
01/2011 – 03/2011	Studentische Hilfskraft am Center for Nonlinear Science der Universität Münster
02/2011 – 03/2011	Studentische Hilfskraft an der Deutschen Hochschule der Polizei, Hiltrup
04/2011 – 12/2012	Wissenschaftliche Hilfskraft an der Deutschen Hochschule der Polizei, Hiltrup
04/2011 – 06/2012	Wissenschaftliche Hilfskraft am Center for Nonlinear Science der Universität Münster
08/2012 – 12/2012	Wissenschaftliche Hilfskraft am Center for Nonlinear Science der Universität Münster
seit 01/2013	Wissenschaftlicher Mitarbeiter am Institut für Theoretische Physik der Universität Münster

Stipendien

11/2007 – 12/2012	Stipendiat der Studienstiftung des Deutschen Volkes
10/2009 – 09/2010	Empfänger eines NRW/WWU-Stipendiums der Universität Münster